The geology of the Beardmore-Geraldton belt, Ontario, Canada: geochronology, tectonic evolution and gold mineralization

By

Zsuzsanna Tóth

A thesis submitted in partial fulfillment
of the requirements for the degree of
Doctor of Philosophy (PhD)
in Mineral Deposits and Precambrian Geology

The Faculty of Graduate Studies
Laurentian University
Sudbury, Ontario, Canada

THESIS DEFENCE COMMITTEE/COMITÉ DE SOUTENANCE DE THÈSE
Laurentian Université/Université Laurentienne
Faculty of Graduate Studies/Faculté des études supérieures

Title of Thesis Titre de la thèse	The geology of the Beardmore-Geraldton belt, Ontario, Canada: geochronology, tectonic evolution and gold mineralization
Name of Candidate Nom du candidat	Tóth, Zsuzsanna
Degree Diplôme	Doctor of Philosophy
Department/Program Département/Programme	Mineral Deposits and Precambrian Geology
Date de la soutenance	November 07, 2018

APPROVED/APPROUVÉ

Thesis Examiners/Examinateurs de thèse:

Dr. Bruno Lafrance
(Co-Supervisor/Co-directeur de thèse)

Dr. Benoît Dubé
(Co-Supervisor/Co-directeur de thèse)

Dr. Phil Thurston
(Committee member/Membre du comité)

Approved for the Faculty of Graduate Studies
Approuvé pour la Faculté des études supérieures
Dr. David Lesbarrères
Monsieur David Lesbarrères
Dean, Faculty of Graduate Studies
Doyen, Faculté des études supérieures

Dr. Shoufa Lin
(External Examiner/Examinateur externe)

Dr. Bruce Jago
(Internal Examiner/Examinateur interne)

ACCESSIBILITY CLAUSE AND PERMISSION TO USE

ABSTRACT

The Beardmore-Geraldton belt (BGB) is a greenstone belt straddling the boundary between the eastern Wabigoon subprovince and the Quetico metasedimentary subprovince. It consists of shear-bounded panels of metavolcanic and metasedimentary rocks which were imbricated during an early thrusting event and regionally folded and sheared during subsequent deformation events. It hosts several historic gold mines with a combined past production exceeding 4 Moz gold. New gold resources were delineated within the last ca. 10 years at the Hardrock deposit in the eastern part of the belt which highlighted the need for a better understanding of the controls on gold mineralization in the belt.

The BGB comprises three panels of metasedimentary rocks, representing a southward transition from fluvial to deltaic to deep oceanic basin plain environments, overlying three panels of older, ca. 2725 Ma, metavolcanic rocks, representing back arc, island arc, and oceanic crust. Detrital zircon geochronology of the BGB and adjacent northern Quetico metasedimentary rocks suggests that these rocks formed from sediments derived by the erosion of ca. 2700 Ma to 2900 Ma source rocks and older >3200 Ma Mesoarchean craton of the eastern Wabigoon subprovince. The emplacement of crosscutting 2694±1 Ma feldspar-quartz porphyry (FQP) dikes, marks the end of sedimentation in the belt. The panels were subsequently imbricated during an early thrusting event (D_1) which ended with the emplacement of the stitching 2690±1 Ma Croll Lake stock. The composition of the FQP dikes and Croll Lake stock (i.e. SiO_2, ferromagnesian oxide and transition element contents, $[La/Yb]_N$ ratio) indicate a shift from tonalite-trondhjemite-granodiorite (TTG) suite to sanukitoid suite magmatism over a 4 Ma period. The formation of the sanukitoid melts, which involves the addition of a mantle melt component, is consistent with their generation during

delamination or slab break-off as the BGB metavolcanic and metasedimentary panels were thrust-imbricated and accreted to the Wabigoon subprovince during closure of the Quetico basin.

D_1 structures are expressed by early, isoclinal, F_1 folds with an axial planar S_1 cleavage. They are folded by regional F_2 folds with an axial planar, regional, S_2 cleavage, which becomes more pronounced along belt-parallel, sinistral, high strain zones characterized by asymmetrical, S-shaped F_2 folds and NE-striking, en echelon, quartz-carbonate veins. The association of regional folds and cleavage with sinistral high strain zones suggest that these structures formed during regional sinistral transpression (D_2) across the belt. During subsequent dextral D_3 transpression, the regional F_2 folds and S_2 cleavage were overprinted by Z-shaped F_3 folds and by a second regional cleavage (S_3), and the D_2 high-strain zones were reactivated as dextral shear zones. Within the reactivated high strain zones, F_1, F_2 and F_3 fold axes are parallel to a strong, shallowly-plunging, stretching lineation that formed during D_2 and was accentuated and rotated towards the orientation of the fabric attractor during D_3. The fabric attractor is oblique to the intersection lineation between the reactivated S_2 cleavage and dextral shear bands, suggesting that the deformation during D_3 had triclinic symmetry.

The Hardrock gold deposit is one of several deposits hosted by the Bankfield-Tombill deformation zone near Geraldton in the eastern part of the BGB. Gold was emplaced during early D_1 thrusting and D_2 sinistral transpression in association with strongly folded, early D_1, quartz-carbonate veins (V_1) and E- to NE-striking, syn-D_2, tourmaline-rich (V_2) and quartz-carbonate veins (V_3) veins. Gold is present in association with inclusion-rich pyrite with elevated Au, Ag, As, Bi, Co, Ni, Pb, Sb, Te concentrations and along fractures and as inclusions in the veins and sulfides. The deposit is surrounded by a broad (≤250 m) alteration envelope of carbonate and sericite with elevated pathfinder S, Te, As, W, and Bi concentrations. Early introduction of gold in the belt during

thrusting and sinistral transpression differs from previous studies which favored late tectonic emplacement of gold in D_3 shear zones and fold hinges.

Keywords: Archean orogenic gold; Beardmore-Geraldton greenstone belt; structural control; LA-ICP-MS pyrite mapping; geochemical footprint; geochronology; TTG and sanukitoid petrogenesis; sinistral transpression; triclinic dextral transpression

CO-AUTHORSHIP STATEMENT

This thesis consists of three manuscripts prepared for publication in peer-reviewed scientific journals and six additional papers in the Appendix which were published by the Ontario Geological Survey and the Geological Survey of Canada. Chapters two to four and the papers in the appendices were co-authored by the candidate and several collaborators. The collaborators provided constructive suggestions, figures and tables for geochronological data. The candidate is the first author on all manuscript except for one Summary of Field Work report published by the Ontario Geological Survey in 2012, whose preparation was supported by the candidate as a second author. Chapter 2 of this dissertation is co-authored with Drs. Vicki McNicoll, Bruno Lafrance and Benoît Dubé. Chapter 3 and 4 are co-authored by Drs. Bruno Lafrance and Dr. Benoît Dubé.

The candidate completed the bulk of the field work including mapping of mechanically stripped outcrops, core-logging and sample collection, as well as sample selection, sample preparation, petrography, SEM analyses, data processing and interpretation under the guidance and supervision of Dr. Bruno Lafrance and Dr. Benoît Dubé.

The samples for detrital zircon geochronology were collected by Drs. Bruno Lafrance, Benoît Dubé, Vicki McNicoll, Phillips Thurston and Patrick Mercier-Langevin in 2011. The preparation and analyses of these samples as well as the U-Pb geochronological data processing were completed by and under the supervision of Dr. Vicki McNicoll of Geological Survey of Canada, Ottawa.

The drill core samples were provided by Premier Gold Mines and Greenstone Gold Mines but were selected and collected by the candidate. The geochemical analyses discussed in Chapters 2

and 4 were executed by the Activation Laboratories Ltd. in Ancaster, Ontario and the Geoscience Laboratories of the Ministry of Northern Developments and Mines in Sudbury, Ontario.

Drs. Matthew Leybourne and Joseph A. Petrus assisted the LA-ICP-MS analytical work and data interpretation at Geochemical Fingerprinting Laboratory of Laurentian University in Sudbury. The Re-Os geochronology (Chapter 4), including the sample preparation, analyses and data processing, was carried out by and under the supervision of Dr. Robert Creaser at the Canadian Centre of Isotopic Microanalysis (CCIM), University of Alberta, AB.

The structural measurements discussed in Chapter 3 were collected by the candidate and Dr. Bruno Lafrance.

Drs. Bruno Lafrance, Benoît Dubé, Vicki McNicoll, Phillips Thurston, Patrick Mercier-Langevin, Daniel Kontak and Matthew Leybourne contributed to this study by providing scientific guidance on various subjects discussed in Chapters 2 to 4 and the Appendices. Drs. Bruno Lafrance, Benoît Dubé and Phillips Thurston helped to improve the manuscripts presented in Chapters 2 to 4. Dr. Bruno Lafrance reviewed Chapters 1 and 5. Dr. Krisztina Pandur also edited the Chapter 1 of the dissertation.

ACKNOWLEDGEMENTS

I thank my primary supervisor, Dr. Bruno Lafrance, for providing me the opportunity to complete this research. I thank Drs. Bruno Lafrance and Benoît Dubé for their expertise, support, guidance and mentorship through this project. I thank my supervisors to help me become a better geologist and scientist. The bulk of the project was funded by the Targeted Geoscience Initiative 4 program of the Geological Survey of Canada. Additional funding was provided by Dr. Bruno Lafrance and Greenstone Gold Mines. I thank Premier Gold Mines, Greenstone Gold Mines and Alto Ventures for providing access to their properties, allowing and assisting mapping and sampling. Premier Gold Mines and Greenstone Gold Mines are also thanked for the in-kind support they provided over the summers I spent in Geraldton. I am grateful to the Ontario Geological Survey for the providing me with transportation for Symposiums in Thunder Bay.

I am grateful to Dr. Phillips C. Thurston for the discussions on Precambrian geology and for the suggestions that improved my manuscripts. I thank Drs. Patrick Mercier-Langevin, Daniel Kontak, Matthew Leybourne, Pedro Jugo, Andrew McDonald, Alessandro Ielpi, John Ayer and Jeremy Richards for the discussions on different topics; these discussions were undoubtedly beneficial for the thesis and my personal growth as a researcher. Dr. Fernando Corfu is thanked for the discussion on his work in the area and for providing thin sections of dated samples.

Willard Desjardins is thanked for his assistance with sample preparation including thin section preparation and cutting my samples of awkward shapes and sizes. Dr. William Zhe is thanked for his assistance with the SEM analyses. Drs. Matthew Leybourne and Joseph Petrus are thanked for their assistance with the LA-ICP-MS analyses. Dr. Vicki McNicoll is thanked for her U-Pb geochronology work and explaining me the details of this method. Dr. Robert Creaser is thanked

for his assistance with the Re-Os geochronology. Dr. William Oswald is thanked for teaching me the use of the “differential GPS”.

Without listing everyone, I would like to thank “*the crew*” in Geraldton, including those who moved on since, for their support and friendship which were essential to keep me going over the years. Thank you all for your kind words, patience and accepting my nerdiness.

I would like to thank my fellow graduate students, particularly Mojgan Adibpour, Marie Létourneau, Chris Kelly, Kate Rubingh and Dr. Katie Hahn, for their support and friendship through this challenging endeavour. Michael Langa is thanked for his love, support and encouragement over the final stretch of my studies.

Köszönet illetti dr. Pandur Krisztinát a barátságáért, segitségéért és tanácsaiért, amit a jelentkezés és Kanadába költözés során nyújtott. Köszönet illetti továbbá Szabadi Adriennt barátságáért és támogatásáért az elmúlt több, mint 12 évben.

Végül, de nem utolsó sorban, végtelenül hálás vagyok szüleimnek, bátyámnak, nagyszüleimnek és keresztszüleimnek, amiért mindvégig támogattak a tanulmányaimban és elviselték, ahogy megtöltöttem a házat *kövekkel*. Köszönöm Édesanyámnak és kései nagypapámnak, hogy javasolták, hogy látogassam meg a Sátorkőpusztai Kristálybarlangot, ami megszerettette velem a *köveket* és elindított a geológiához vezető úton. Köszönöm Édesapámnak, amiért belém nevelte az utazás szeretét, a lelkes támogatást abban, hogy egy új kontinensen próbáljak szerencsét és a 2017-es látogatást, ami erőt adott a fennmaradó nehézségek leküzdésében. Köszönöm, hogy hittetek bennem.

TABLE OF CONTENTS

LIST OF FIGURES

LIST OF TABLES

LIST OF APPENDICES

1. CHAPTER 1 - INTRODUCTION

Introduction to the thesis

Research problem

The Beardmore-Geraldton greenstone belt (BGB) is located along the boundary of two Archean terranes, the granite-greenstone Wabigoon subprovince and the metasedimentary Quetico subprovince of the Archean Superior Province. Over the past century, the BGB produced over 4.1 Moz Au from several deposits across the belt (Mason and McConnell, 1983; Mason and White, 1986). All mining activities ceased in 1970, and during the following ca. 35 years, limited mineral exploration was done in the belt.

Detailed description of the geology of the BGB is presented in numerous Ontario Geological Survey reports (e.g. Pye, 1952; Horwood and Pye, 1955; Mackasey, 1975, 1976; Beakhouse, 1984; Carter, 1987; Williams, 1989; Kresz and Zayachivsky, 1991, 1993; Shanks, 1993; Hart et al., 2002). More detailed studies focused on the geochemistry of the metavolcanic units (Tomlinson et al., 1996), the evolution of the overlying metasedimentary units (Barrett and Fralick, 1985; Devaney and Fralick, 1985; Williams, 1987; Barrett and Fralick, 1989; Devaney and Williams, 1989; Fralick and Kronberg, 1997; Fralick and Pufahl, 2006; Fralick et al., 2006) and the complex structural history of the BGB (Buck, 1986; Kehlenbeck, 1986; Reilly, 1987; Williams, 1987, 1989, 1990; Lafrance et al., 2004). However, studies on the gold mineralization across the BGB were limited to the few available surface exposures and old mine level plans and descriptions (Anglin, 1987; Macdonald, 1988; Lafrance et al., 2004; DeWolfe et al., 2007).

The only comprehensive study describing and discussing the controls on gold mineralization in the Geraldton area was presented by Anglin (1987) as part of her MSc thesis. Another MSc thesis reports on gold enrichment during two distinct mineralization events along the Paint Lake shear zone along the northern boundary of the BGB (DeWolfe et al., 2007).

Renewed exploration in 2007 at the sites of the former Hard Rock and MacLeod-Cockshutt mines in Geraldton, together with a renewed research focus on gold deposits by the Geological Survey of Canada through their Targeted Geoscience Initiative program, provided access to new drill cores, extensive stripped outcrops, and new research funding to revisit the structural and tectonic controls on gold mineralization in the Geraldton camp. The camp has many features of major orogenic gold camps, and with new resources of 6.4 Moz Au at the Hard Rock and MacLeod-Cockshutt deposits (collectively named as the Hardrock deposit by Greenstone Gold Mines; G Mining Services, 2016), new research was deemed necessary to understand better the tectonic environment of these deposits and how they formed.

Thesis objectives

The objectives of the thesis are to:

- Propose a new interpretation of the geodymanic evolution of the BGB based on U-Pb geochronology of detrital zircons in sedimentary sequences in the belt and on whole rock geochemistry and U-Pb zircon geochronology of younger porphyry intrusions;
- Test existing interpretations on the structural evolution of the BGB and present new interpretations on the development of structures during multiple regional transpression events;

- Describe the geologic controls on gold mineralization at the Hardrock deposit and characterize the structural timing of mineralization and the alteration and geochemical footprint of the deposit;
- Compare the geology of the BGB to that of major Archean orogenic gold districts in the Superior Province in Canada and the Yilgarn craton in Australia.

Methodology

Fulfillment of the research objectives required detailed field mapping, core logging, petrography, whole rock and in situ LA-ICP-MS geochemical analyses, U-Pb and Re-Os geochronologic analyses.

Field work

Detailed outcrop mapping was conducted over four summers (2012 to 2015) on the properties of Premier Gold Mines Ltd., Greenstone Gold Mines L.P. and Alto Ventures Ltd. The "Spectra Precision Promark 800" cm-precise surveying devices owned by the Geological Survey of Canada and Greenstone Gold Mines were used to map eight mechanically stripped outcrops and to take precise structural measurements in magnetic banded iron formation-bearing rocks. One outcrop was mapped and some of the structural measurements and photographs presented in Chapter 3 were collected by Dr. Bruno Lafrance between 2000 and 2002 as well as in 2017. The mapping was carried out to improve the understanding of the structural evolution of the BGB, and to define the structural controls on gold mineralization in the belt. Samples for geochemical, geochronological and structural analyses were collected from outcrops during the summers of 2011 to 2016. Nine diamond drill holes were re-logged and sampled during the summers of 2012 and 2013, in order to characterize the mineralogical assemblages, geochemical footprints and Re-

Os radiogenic age of the gold mineralization, as well as to describe the mineral chemistry of auriferous sulfides.

Petrography

Two hundred and thirty-three thin sections were prepared to characterize the host rocks and hydrothermal alteration styles associated with the gold mineralization, as well as to describe fabric elements associated with the deformation events. The thin sections were described using a transmitted and reflected light optical microscope and scanning electron microscope (SEM). Semi-qualitative SEM mineral chemical analyses were done using an Oxford energy-dispersive spectrometer mounted on the JEOL JSM-6400 scanning electron microscope at the Central Analytical Facilities of Laurentian University, Sudbury, ON.

Whole rock geochemistry

Two hundred and thirty-seven samples were submitted for whole rock major and trace element geochemical analyses at Activation Laboratories Ltd. in Ancaster, Ontario (2012, 2013, 2016) and Geoscience Laboratories of the Ministry of Northern Developments and Mines in Sudbury, Ontario (2014). The whole rock geochemistry helped to understand the petrogenesis of the intrusive rocks in the vicinity of the Hard Rock deposit and to determine the geochemical footprints of the mineralization.

Mineral chemical mapping of sulfides

Eleven pyrite and arsenopyrite grains were selected and analyzed *in situ* using the Thermo X Series II inductively coupled plasma mass spectrometer (ICP-MS) interfaced with a Resonetics RESOlution M-50 193 nm ArF excimer laser at the Chemical Fingerprinting Laboratory,

Laurentian University, Sudbury, ON. These analyses were performed to characterize the elemental associations of sulfides in the ore zones of the Hard Rock deposit.

Geochronology

The U-Pb age of over 300 detrital zircons were obtained from metasedimentary units of the BGB and northern part of the Quetico subprovince to assess the provenance and depositional setting of these rocks. The samples were crushed, ground, and heavy mineral concentrates were prepared using the hydrogravimetric Wilfley™ table and heavy liquid separation. Final separation of the zircon grains was completed by magnetic susceptibility using a Frantz™ isodynamic separator and hand-picking using a binocular microscope. SHRIMP II (Sensitive High Resolution Ion MicroProbe) analyses were conducted at the Geological Survey of Canada.

U-Pb geochronology was also performed on a feldspar-quartz porphyry in intrusive contact with the metasedimentary units to provide a minimum age for sedimentation. Re-Os geochronology was performed on arsenopyrite from a gold-rich sample in order to determine the age of the gold mineralization.

The structure of the thesis

This dissertation is divided into five chapters. It comprises an introductory chapter (Chapter 1), three manuscripts that will be submitted to international peer-reviewed scientific journals (Chapters 2 to 4), and a summary chapter (Chapter 5).

Chapter 1 introduces the research problem, the objectives, the methodology, the structure of the thesis and a statement of original contributions.

Chapter 2 is written as a manuscript entitled **"Early depositional and magmatic history of the Beardmore-Geraldton Belt: Formation of a transitional accretionary belt along the Wabigoon-Quetico subprovince boundary in the Archean Superior craton, Canada".** It discusses the U-Pb age of detrital zircons in metasedimentary units in the BGB and the northern Quetico subprovince and provides new data about the provenance of the detritus and the maximum age of sedimentation. It also discusses the petrogenesis of porphyry intrusions, their age, and implications for the tectonic evolution of the BGB.

Chapter 3 is written as a manuscript entitled **"Revisiting the structural evolution of the Beardmore-Geraldton greenstone belt, Superior Province, Canada: Evidence for sinistral transpression predating triclinic dextral transpression".** It presents a new interpretation for the structural evolution of the BGB and discusses the development of structures during two juxtaposed regional transpressive events.

Chapter 4 is written as a manuscript entitled **"The geology of the world-class Hardrock orogenic gold deposit, Geraldton, Ontario, Canada: structural control, mineralogy, geochemistry and geochronology".** It discusses the relative structural timing of gold mineralizing events, and describes the alteration and geochemical footprint of the mineralization, the U-Pb and Re-Os radiogenic age constraints on gold mineralization, as well as the mineral chemistry of sulfides associated with gold mineralization.

Statement of original contributions

The following is a summary of the original contributions presented in this thesis:

1. Documentation of new Meso- and Paleoarchean detrital zircon populations in the metasedimentary rocks of the BGB;

2. The geochemical and geodynamic interpretation of igneous bodies emplaced across the BGB;
3. A new interpretation for the structural evolution of the BGB;
4. New insights on the development of structures during regional transpressive events;
5. Discovery of two separate mineralization events in the Geraldton camp and the interpretation of their relative timing with respect to the structural evolution of the BGB;
6. Characterization and interpretation of the hydrothermal alteration and geochemical footprint associated with gold mineralization in the BGB;
7. The first Re-Os isotopic age on auriferous arsenopyrite in the BGB;
8. The first *in situ* LA-ICP-MS mineral chemical analyses of sulfide minerals in the BGB.

References

Anglin, C.D., 1987. Geology, structure and geochemistry of gold mineralization in the Geraldton area, Northwestern Ontario. Unpublished Master's Thesis. Memorial University of Newfoundland, St. John's, Newfoundland. 283 p.

Barrett, T.J., Fralick, P.W., 1989. Turbidites and iron formations, Beardmore-Geraldton, Ontario: application of a combined ramp/fan model to Archaean clastic and chemical sedimentation. Sedimentology 36, 221–234. doi:10.1111/j.1365-3091.1989.tb00604.x

Barrett, T.J., Fralick, P.W., 1985. Sediment redeposition in Archean Iron Formation: Examples from the Beardmore-Geraldton Belt, Ontario. J. Sediment. Petrol. 55, 205–212.

Beakhouse, G.P., 1984. Geology of the Grenville Lake Area, Thunder Bay District; Ontario Geological Survey Open File Report 5513, 146p.

Buck, S., 1986. Structural studies and gabbro mylonitization within the Barton Bay Deformation Zone, Geraldton, Ontario. Unpublished MSc thesis. Brock University, St. Catharines, Ontario. 171 p.

Carter, M.W., 1987. Geology of McComber and Vincent Townships, District of Thunder Bay; Ontario Geological Survey, Open File Report 5648, 144p.

Devaney, J.R., Fralick, P.W., 1985. Regional sedimentology of the Namewaminikan Group, northern Ontario: Archean fluvial fans, braided rivers, deltas and an aquabasin., in: Current Research, Part B, Paper 85-1B. Geological Survey of Canada, pp. 125–132.

Devaney, J.R., Williams, H.R., 1989. Evolution of an Archean subprovince boundary: a sedimentological and structural study of part of the Wabigoon–Quetico boundary in northern Ontario. Can. J. Earth Sci. 26, 1013–1026.

DeWolfe, J.C., Lafrance, B., Stott, G.M., 2007. Geology of the shear-hosted Brookbank gold prospect in the Beardmore–Geraldton belt, Wabigoon Subprovince, Ontario. Can. J. Earth Sci. 44, 925–946. doi:10.1139/E06-118

Fralick, P.W., Kronberg, B.I., 1997. Geochemical discrimination of clastic sedimentary rock sources. Sediment. Geol. 113, 111–124.

Fralick, P.W., Pufahl, P., 2006. Iron formation in Neoarchean deltaic successions and Microbially mediated depositon of transgessive systems tracts. J. Sediment. Res. 76, 1057–1066.

Fralick, P.W., Purdon, R.H., Davis, D.W., 2006. Neoarchean trans-subprovince sediment transport in southwestern Superior Province: sedimentological, geochemical and geochronological evidence. Can. J. Earth Sci. 43, 1055–1070. doi:10.1139/E06-059

G Mining Services, 2016. NI 43-101 Technical Report - Hardrock Project, Ontario, Canada. 509 p.

Hart, T.R., terMeer, M., and Jolette, C., 2002. Precambrian Geology of Kitto, Eva, Summers, Dorothea and Sandra Townships, Northwestern Ontario: Phoenix Bedrock Mapping Project; Ontario Geological Survey, Open File Report 6095, 206 p.

Horwood, H.C., Pye, E.G., 1955. Geology of Ashmore Township., in: 60th Annual Report of the Ontario Department of Mines, Part 5. Ontario Department of Mines, 139 p.

Kehlenbeck, M.M., 1986. Folds and folding in the Beardmore - Geraldton fold belt. Can. J. Earth Sci. 23, 158–171.

Kresz, D.U., Zayachivsky, B., 1991. Precambrian Geology, northern Long Lake area. Ontario Geological Survey, Report 273, 77 p.

Kresz, D.U. and Zayachivsky, B. 1993. Precambrian geology, Seagram Lake area; Ontario Geological Survey, Report 287, 81 p.

Lafrance, B., DeWolfe, J.C., Stott, G.M., 2004. A structural reappraisal of the Beardmore-Geraldton Belt at the southern boundary of the Wabigoon subprovince, Ontario, and implications for gold mineralization. Can. J. Earth Sci. 41, 217–235. doi:10.1139/E03-090

Macdonald, A.J., 1988. The Geraldton Gold Camp: The role of the banded iron formation. Ontario Geological Survey, Open File Report 5694. 173 p.

Mackasey, W.O., 1975. Geology of Dorothea, Sandra, and Irwin Townships, District of Thunder Bay. Ontario Division of Mines, Geological Report 122, 83 p.

Mackasey, W.O., 1976. Geology of Walters and Leduc Townships, District of Thunder Bay. Ontario Division of Mines, Geoscience Report 149. 58 p.

Mason, J.K., McConnell, C.D., 1983. Gold mineralization in the Beardmore-Geraldton area, In: Colvine, A.C. (Ed.), The Geology of Gold in Ontario, Ontario Geological Survey, Misc. Paper 110. pp. 84–97.

Mason, J.K., White, G., 1986. Gold occurrences, prospects and deposits of the Beardmore-Geraldton area, District of Thunder Bay and Cochrane. Ontario Geological Survey, Open File Report 5630. 680 p.

Pye, E.G., 1952. Geology of Errington Township, Little Long Lac Area, in: 60th Annual Report of the Ontario Department of Mines. Ontario Department of Mines, 140 p.

Reilly, B.A., 1987. Structural analysis of the Paint Lake deformation zone, northern Ontario. Unpublished MSc thesis. Brock University, St. Catharines, Ontario. 189 p.

Shanks, W.S. 1993. Geology of Eva and Summers townships, District of Thunder Bay; Ontario Geological Survey, Open File Report 5821, 93p.

Tomlinson, K.Y., Hall, R.P., Hughes, D.J., Thurston, P.C., 1996. Geochemistry and assemblage accretion of metavolcanic rocks in the Beardmore–Geraldton greenstone belt, Superior Province. Can. J. Earth Sci. 33, 1520–1533.

Williams, H.R., 1987. Ontario Geoscience Research Program, Grant No. 242. Structural Studies in the Wabigoon and Quetico Subprovinces, Open File Report 5668. Ontario Geological Survey, 163 p.

Williams, H.R., 1989. Geological studies in the Wabigoon, Quetico and Abitibi-Wawa subprovinces, Superior Province of Ontario, with emphasis on the structural development of the Beardmore-Geraldton Belt; Ontario Geological Survey, Open File Report 5724. 189 p.

Williams, H.R., 1990. Subprovince accretion in the south-central Superior Province. Can. J. Earth Sci. 27, 570–581.

2. CHAPTER 2: EARLY DEPOSITIONAL AND MAGMATIC HISTORY OF THE BEARDMORE-GERALDTON BELT: FORMATION OF A TRANSITIONAL ACCRETIONARY BELT ALONG THE WABIGOON-QUETICO SUBPROVINCE BOUNDARY IN THE ARCHEAN SUPERIOR CRATON, CANADA

Zsuzsanna Tóth[1,*], Vicki McNicoll[2], Bruno Lafrance[1], Benoît Dubé[3]

[1]Mineral Exploration Research Centre, Harquail School of Earth Sciences, Goodman School of Mines, Laurentian University, Sudbury, ON, Canada P3E 2C6

[2]Geological Survey of Canada, Earth Sciences Sector, Natural Resources Canada, Ottawa, Ontario K1A 0E8

[3]Geological Survey of Canada, Earth Sciences Sector, Natural Resources Canada, Québec City, Québec G1K 9A9

*Corresponding author: Zsuzsanna Tóth, e-mail address: ztoth@laurentian.ca

Abstract

The Beardmore-Geraldton Belt (BGB) is a major gold camp along the boundary between the granite-greenstone eastern Wabigoon subprovince and the metasedimentary Quetico subprovince of the Archean Superior Province, Canada. New detrital zircon geochronology suggests that the metasedimentary rocks of the BGB and northern Quetico subprovince were derived from the erosion of the eastern Wabigoon subprovince to the north. The eastern Wabigoon subprovince is dominated by ca. 2900-2680 Ma rocks but also comprises crust as old as >3200 Ma. Uplift of the eastern Wabigoon subprovince as a result of convergence and compression along its southern margin exposed those rocks to erosion and shed sediments in the Quetico basin to the south, as

indicated by the similarity in the age of detrital zircon populations (2690-2900 Ma) in the BGB and Quetico metasedimentary rocks with the age of the rocks in the eastern Wabigoon subprovince. Sedimentation in the Quetico basin is bracketed between ca. 2700 Ma, the age of the youngest detrital zircon population, and 2694.0 ± 1.0 Ma, the crystallization age of cross-cutting feldspar-quartz porphyries (FQP). Continued convergence facilitated the thrust-imbrication of the metavolcanic rocks of the eastern Wabigoon subprovince with the metasedimentary rocks of the Quetico basin resulting in the assembly of the BGB. This resulted in crustal thickening, the introduction of hydrated mafic rocks at the base of the crust, and partial melting of these rocks to form TTG suite melts at depths greater than 50 km, as suggested by the strong HREE+Y depletion, positive Sr, Al and negative Nb, Ta, Ti anomalies, and lack of an Eu anomaly of the FQP intrusions. Imbrication and thrusting ended with the emplacement of the stitching, 2690±1 Ma Croll Lake Stock, which has the high transition elements and ferromagnesian oxides signature of sanukitoid suite rocks. The Croll Lake magma formed either during delamination or slab break-off from mixing of hot, mantle material with TTG suite melts at depth >50 km. The early geological evolution of the Geraldton gold camp is similar to that of other major Archean gold camps associated with major faults and/or terrane boundaries, where deposition of fluvial conglomerate and turbiditic sandstones in fault-bounded basins overlying older volcanic rocks is followed by magmatic activity and the upward migration of gold-bearing hydrothermal fluids.

Keywords:

Syn-tectonic Archean granitoids; syn-tectonic sedimentation; U-Pb zircon geochronology; geochemistry; Superior Province; Beardmore-Geraldton greenstone belt

Introduction

The Archean Superior craton of Canada and the Yilgarn craton of Western Australia are amongst Earth's richest gold terranes (Poulsen et al., 2000; Goldfarb et al., 2001, 2005; Robert et al., 2005; Bateman and Bierlein, 2007). Gold deposits in these two cratons are typically associated with regional fault zones in close proximity to clastic sedimentary rocks unconformably overlying older volcanic rocks. In the Superior craton, the Abitibi subprovince is well-known for its two major, extremely prolific, fault zones or "breaks", the Destor-Porcupine Fault and the Larder Lake – Cadillac Fault, which extend over 170 km and 250 km, respectively, across the Ontario-Quebec provincial boundary. The Destor-Porcupine Fault occurs along the southern margin of a basin of marine turbidites, the ca. 2690-2685 Ma Porcupine assemblage, which is unconformably overlain by a second, younger basin filled with fluvial to shallow marine conglomerate and sandstone of the <2679 to <2669 Ma Timiskaming assemblage (Mueller et al., 1994; Born, 1995; Ayer et al., 2002a, 2005; Bateman et al., 2008). The latter is also present along the Larder Lake – Cadillac Fault Zone, where conglomerate and sandstone are interleaved with alkaline flows and pyroclastic deposits (Hyde, 1980, Ispolatov et al., 2005, 2008). In the Kalgoorlie camp of the Yilgarn craton, the Boulder-Lefroy fault system occurs along the contact between older volcanic rocks and unconformably overlying clastic metasedimentary and volcanoclastic rocks (2681 Ma to 2655 Ma), which are in turn overlain by younger, ca. <2655 Ma fluvial conglomerate and sandstone that are broadly coeval with ca. 2650-2630 Ma alkaline magmatism (Smithies and Champion, 1999; Krapež et al., 2000). The unconformities are thought to be important regional controls on the formation of Archean gold camps because they represent periods of tectonic instability presumably related to movement along faults that later controlled the upward migration of melts and hydrothermal fluids (Robert et al., 2005).

Broadly coeval with the development of these basins are tonalite, granodiorite, diorite, and feldspar-quartz porphyry intrusions. In the Timmins camp, quartz-feldspar porphyry dikes and stocks span both Porcupine and Timiskaming episodes of sedimentation (Corfu et al., 1989; Macdonald, 2010). The ca. 2687 Ma Krist felsic fragmental rocks, which were erupted at the base of the Porcupine assemblage, are the extrusive equivalents of pre-tectonic, quartz-feldspar porphyry stocks (Ayer et al., 2002b, 2005; Macdonald, 2010). Magmatism continued with the emplacement of alkaline dikes (ca. 2677-2672 Ma albitite and ca. 2673 Ma lamprophyre dikes) along the Destor-Porcupine Fault (Corfu et al., 1989; Ropchan et al., 2002; Ayer et al., 2005; Bateman et al., 2005, 2008), and with the effusion and eruption of alkaline magmas along the Larder Lake-Cadillac fault, coeval with the formation of the Timiskaming basin (Ayer et al., 2002b, 2005 and references therein).

The Geraldton gold camp is similar in many ways to the better known Archean Timmins, Kirkland Lake and Kalgoorlie gold camps (Table 2-1). It is located in the eastern part of the Beardmore-Geraldton Belt (BGB) along the southern margin of the Wabigoon granite-greenstone subprovince immediately north of the Quetico metasedimentary subprovince (Figs. 2-1-2). The belt comprises fluvial polymictic conglomerate and turbidites that were thrust-imbricated, intruded by quartz-feldspar porphyry dikes and various granitoid stocks, and then deformed during regional folding and strike-slip faulting (Devaney and Williams, 1989; Lafrance et al., 2004). Several gold deposits occur along the Bankfield-Tombill deformation zone located along the southern margin of the belt (Tóth et al., 2015 and references therein).

In this study, we present new geochronological and geochemical data to address the following questions about the early evolution of the BGB: 1) When were these rocks deposited? 2) What is the provenance of the clastic sedimentary rocks of the BGB and the northern Quetico? 3) Are the

metasedimentary rocks of the BGB similar to those of the northern Quetico? 4) What petrogenetic and geodynamic processes does the geochemistry of the cross-cutting, early- to syn-tectonic dikes and intrusions indicate? 5) How does the early history of the BGB compare to that of the Abitibi greenstone belt and the Yilgarn craton, which host major orogenic gold camps?

Regional geology

The BGB includes rocks similar to those in the Wabigoon and Quetico subprovinces. Because of this similarity in rock types, the BGB has been described as a transitional belt between the two subprovinces (Fig. 2-1.; Kehlenbeck, 1986; Devaney and Williams, 1989). The Quetico subprovince is a 1200 km long by 70 km wide belt of interlayered sandstone and mudstone that are metamorphosed to upper greenschist grade along the northern and southern margins of the belt and replaced by granulite grade migmatite and leucogranite in the centre of the belt (Fig. 2-1.; Percival, 1989; Williams, 1991). The deposition of the Quetico sediments is bracketed between 2698 ± 3 Ma and 2688 ± 4 Ma in the north (Davis et al., 1990) and <2690 Ma in the south (Zaleski et al., 1999). The Wabigoon subprovince consists of metavolcanic rocks of various compositions and ages surrounded by granitoid batholiths and plutons (Blackburn et al., 1991). It was previously divided into western, central and eastern regions, based on the geographic location of lithologic associations (Blackburn et al., 1991), but has been more recently subdivided into the Winnipeg River, Marmion and Western Wabigoon terranes (Thurston, 1991) based on their Nd model ages (Tomlinson et al., 2004). Granitoids of the Winnipeg River terrane are locally as old as 3.17 Ga and formed by the reworking of older 3.4 Ga crust. The granitoid rocks of the Marmion terrane were emplaced at 3.0 Ga (Tomlinson et al., 2003, 2004) and derived from reworked 3.5-3.2 Ga crust (Lu et al., 2013). The western Wabigoon terrane represent younger 2.7-2.8 Ga juvenile crust (Tomlinson et al., 2004). Although the Winnipeg River Terrane and Marmion terrane are thought

to extend in the eastern Wabigoon region, the exact location of their boundaries have yet to be determined (Fig. 2-1).

The BGB consists of three units of metavolcanic rocks that are fault-bounded and interleaved with three units of metasedimentary rocks (Fig. 2-2). The three metavolcanic units, namely the northern, central, and southern metavolcanic units (NVU, CVU, SVU), have back-arc, island arc, and oceanic crust geochemical signatures, respectively (Tomlinson et al., 1996). The NVU consists of 2724.9±1.1 Ma, predominantly mafic to felsic, pyroclastic rocks and flows of tholeiitic affinity (Pye, 1952; Horwood and Pye, 1955; Mackasey, 1975, 1976; Kresz and Zayachivsky, 1991; Shanks, 1993; Tomlinson et al., 1996; Hart et al., 2002). The CVU comprises mafic to intermediate, massive to pillowed, amygdaloidal flows and pyroclastic rocks of both calc-alkaline and tholeiitic geochemical affinity (Pye, 1952; Horwood and Pye, 1955; Mackasey, 1975, 1976; Carter, 1987; Kresz and Zayachivsky, 1991; Shanks, 1993; Tomlinson et al., 1996; Hart et al., 2002; Lavigne, 2009). A quartz-feldspar porphyry feeder dike was emplaced in wet, unconsolidated tuff breccias and it yielded a U-Pb zircon age of 2724.9±1.2 Ma (Hart et al., 2002) identical to that in the NVU. The SVU consists mainly of massive, pillowed and amygdaloidal andesite and basalt flows of tholeiitic affinity (Carter, 1987; Williams, 1987; Kresz and Zayachivsky, 1991; Shanks, 1993; Tomlinson et al., 1996; Lavigne, 2009).

The northern, central, and southern metasedimentary units (NSU, CSU, SSU) represent a southward-prograding clastic wedge that was unconformably deposited atop the metavolcanic units either prior to, or following their accretion (Devaney and Fralick, 1985; Devaney and Williams, 1989; Tomlinson et al., 1996). The NSU consists of coarse-grained polymictic conglomerate representing an alluvial fan or braid-plain environment (Beakhouse, 1984; Mackasey, 1975, 1976; Devaney and Williams, 1989). The CSU comprises north-younging

polymictic conglomerate, feldspathic and quartz-rich sandstone, mudstone and shallow water iron formation (Pye, 1952; Horwood and Pye, 1955; Mackasey, 1975, 1976; Barrett and Fralick, 1985; Kresz and Zayachivsky, 1991; Fralick and Pufahl, 2006), deposited in a subaqueous fan and/or prodelta setting (Devaney and Williams, 1989). The SSU consists of north-younging turbiditic sandstone and mudstone with minor iron formation and conglomerate (Pye, 1952; Horwood and Pye, 1955; Mackasey, 1975, 1976; Barrett and Fralick, 1985; Carter, 1987), which were deposited in submarine fan and/or basin-plain environments (Devaney and Williams, 1989). Detrital zircons from each unit yielded U-Pb ages of 2889.5 Ma to 2709.6 Ma from 5 zircons in conglomerate of the NSU, 2922 Ma to 2696.3 Ma from 10 zircons in conglomerate of the CSU, and 2827.6 Ma to 2701.1 Ma from 5 zircons in sandstone of the SSU (Hart et al., 2002; Fralick et al., 2006).

A granitic to monzodioritic intrusion, the Croll Lake Stock, was emplaced across the CVU, CSU and NVU in the eastern part of the BGB (Fig. 2-3; Macdonald, 1988; Kresz and Zayachivsky, 1991, 1993). The main granodioritic phase of the intrusion yielded a U-Pb zircon age of 2689.9±1 Ma, and a quartz-feldspar porphyry phase at the western end of the intrusion yielded a U-Pb zircon age of 2689.5±1.2 Ma (Macdonald, 1983, 1988; Corfu, 2000). Other quartz-feldspar and feldspar porphyry dikes across the SSU and CVU are thought to be coeval with the Croll Lake Stock (Macdonald, 1988; Anglin, 1987; Kresz and Zayachivsky, 1991). A feldspar porphyry located 5 km SE of Geraldton was dated at 2691+3/-2 Ma (Anglin, 1987; Anglin et al., 1988) and a feldspar porphyry collected at the Hard Rock mine in the Geraldton camp returned an older U-Pb zircon age of 2698.6±1.3 Ma (Corfu, 2000).

Past-producing gold mines across the BGB produced more than 4 million ounces of gold over the past century (Mason and White, 1986). In the Geraldton camp, most mines are located in the SSU within the kilometre-wide Bankfield-Tombill deformation zone near the contact between the SSU

and the Quetico subprovince (Pye, 1952; Lafrance et al., 2004). Gold mineralization is associated with quartz-carbonate veins hosted by banded iron formation, turbiditic sandstone, polymictic conglomerate and feldspar-quartz porphyry. New indicated resources of 4.87 Moz gold and inferred resources of 2.74 Moz gold have been recently discovered along the Bankfield-Tombill deformation zone (InnovExplo Inc., 2015), which attests to the strong mineral potential of this major ore-controlling structure.

Detrital Zircon Geochronology

Three sandstone samples from the SSU, CSU and Quetico and two conglomerate samples from the SSU and NSU were collected from outcrops closest to the stratigraphic top of each unit (Fig. 2-2). The samples were crushed, ground, and heavy mineral concentrates were prepared using the hydrogravimetric Wilfley™ table and heavy liquid separation. Final separation of the zircon grains was completed by magnetic susceptibility using a Frantz™ isodynamic separator and hand-picking using a binocular microscope. SHRIMP II (Sensitive High Resolution Ion MicroProbe) analyses were conducted at the Geological Survey of Canada (GSC) using analytical procedures described by Stern (1997), with standards and U-Pb calibration methods following Stern and Amelin (2003). Zircons from the samples and fragments of the GSC laboratory zircon standard (z6266 zircon, with $^{206}Pb/^{238}U$ age = 559 Ma) and a secondary zircon standard (M1002)) were cast in an epoxy grain mount (see Table 2-2 for GSC mount#), polished with diamond compound to reveal the grain centers, and photographed in transmitted light. Internal features of the zircons (such as zoning, structures, alteration, etc.) were characterized in back-scattered electron (BSE) and cathodoluminescence (CL) modes using a Zeiss Evo 50 scanning electron microscope (SEM). Mount surfaces were coated with 10 nm of high purity Au. Analyses were conducted using an O^- primary beam, projected onto the zircons with an elliptical spot (ranging in size from 13µm x 16µm

(K100) to 17μm x 23μm (K120); see Table 2-2 for the spot size used for each sample). The count rates of eleven masses including background were sequentially measured over 6 scans with a single electron multiplier and a pulse counting system with deadtime of 23 ns. Off-line data processing was done using customized in-house software. The SHRIMP analytical data is presented in Table 2-2, where the 1σ external errors of $^{206}Pb/^{238}U$ ratios reported in the data table incorporate a 1.0% - 1.5% error in calibrating the standard zircon (Stern and Amelin, 2003). No fractionation correction was applied to the Pb-isotope data; the common Pb correction used the Pb composition of the surface blank (Stern, 1997). In this study, zircon ages with up to 5% discordance were taken into consideration. AgeDisplay (Sircombe, 2004) was used to calculate the major peaks and to plot the data in cumulative probability diagrams with errors at the 2σ level. The maximum depositional age of each metasedimentary unit was defined by the calculated weighted mean average of the youngest detrital zircon population.

All zircon grains from the five samples have similar external features. They are colorless to pale brown, typically subhedral, rarely anhedral, unrounded to well-rounded with stubby and prismatic crystal habits and terminations (aspect ratio=1:1 to 1:5; Fig. 2-4A). Fractured zircon grains are common with the fractures typically perpendicular to the c-axis of the grains. Zircon grains from conglomerate samples are typically 100-250 μm in size, clear to slightly dark and only slightly damaged. Zircon grains from sandstone samples are typically 150 to 250 μm in size with a maximum size of 350 μm, and they are generally darker and more damaged by both radiation and transport than those from conglomerate samples. SEM images of zircon grains from all samples typically show xenocrystic cores and oscillatory zoning (Fig. 2-4C-F).

Polymictic conglomerate of the NSU was sampled along the southern shore of Paint Lake, 500 m east of Road 801, in Walters Township (*1 on Fig. 2-2). Flattened well-rounded clasts of granitoid,

mafic volcanics, iron formation, chert, jasper and vein quartz are surrounded by a medium green, chlorite-rich, sandy matrix (Fig. 2-5A). Fifty-five zircon grains were extracted from the matrix of the conglomerate. They yielded $^{207}Pb/^{206}Pb$ ages between 2930 Ma and 2690 Ma with a statistical peak population (33 zircons; ~55 % of total zircon population) at 2774 Ma. Eight and six zircons (~15% and ~11 %) define peaks at 2711 Ma and 2899 Ma, respectively (Fig. 2-6A; Table 2-2).

Turbiditic sandstone of the CSU was collected from an outcrop along Road 801, east of Pasha Lake in Walters Township (*2 on Fig. 2-2). The rock is greenish grey, medium- to coarse-grained, and is composed of well-rounded quartz, feldspar, and lithic mafic grains (Fig. 2-5B). It yielded $^{207}Pb/^{206}Pb$ ages between 3200 Ma and 2690 Ma. Of 58 analyzed zircons, 37 zircons (~67%) define a statistical population peak at 2700 Ma and 16 zircons (~29%) define secondary statistical peaks at 2896 Ma and 2865 Ma (Fig. 2-6B; Table 2-2).

A SSU sandstone, similar to the previous sandstone sample, was collected 200 m SE of the contact with the CVU along Road 801 (*3 on Fig. 2-2; Fig. 2-5C). $^{207}Pb/^{206}Pb$ ages vary between 3270 Ma and 2690 Ma. Of the 63 analyzed zircons, 46 zircons (73%) define a statistical peak at 2700 Ma, 6 and 4 zircons (~10% and 6%) define secondary peaks at 2771 and 2893 Ma, respectively (Fig. 2-6C; Table 2-2).

Conglomerate of the SSU was sampled under the power line, on the east side of the Old Arena Road in Errington Township, roughly 3 km SW of Geraldton (*4 on Fig. 2-2). The conglomerate contains flattened clasts of granitoid, quartz-feldspar porphyry, mafic volcanic and jasper clasts surrounded by a greenish grey matrix of sandy siltstone (Fig. 2-5D). Zircon grains from the sandy siltstone matrix yielded $^{207}Pb/^{206}Pb$ ages between 2900 Ma and 2690 Ma. Of 63 dated zircons, 55 zircons (~87%) define a peak at 2726 Ma (Fig. 2-6D; Table 2-2).

Sandy siltstone from the Quetico subprovince was collected roughly 3.2 km SW of Beardmore along Highway 11, close to the northern boundary of the Quetico subprovince (*5 on Fig. 2-2). The rock is dark grey, massive, and composed mainly of quartz, biotite and/or chlorite (Fig. 2-5E). The sample yielded $^{207}Pb/^{206}Pb$ ages between 3090 Ma and 2690 Ma. Of 78 dated zircons, 52 zircon grains (~67%) define a statistical population peak at 2711 Ma with a secondary peak at 2734 Ma flanking the dominant peak. Another 7 zircons (~9%) define a minor peak at 2903 Ma (Fig. 2-6E; Table 2-2).

Felsic intrusive rocks

Description

Feldspar-quartz porphyry

Feldspar-quartz porphyry intrusions (Fig. 2-7A) in the Geraldton area (FQP on Fig. 2-2) occur as tabular bodies parallel to lithological contacts. They are dark grey on fresh surface, texturally homogeneous, and strongly foliated. The least altered FQPs (see definition in the Geochemistry section) contain 25-35% albitic feldspar phenocrysts (average grain size of 0.5-3 mm) and rare rounded quartz phenocrysts (<1%, average grain size of 0.3-1 mm), surrounded by a fine-grained matrix of quartz (47-58%), sericite (2-10%), carbonates (3-10%), up to 5% chlorite, up to 1% biotite and opaque minerals.

A dike of feldspar porphyry (Fig. 2-7B) was sampled 6 km east of Geraldton. It differs from the FQP intrusions by the lack of quartz phenocryst and larger plagioclase phenocrysts, which have a maximum grain size of 1 cm and are surrounded by a fine-grained matrix of quartz (50-55%), plagioclase (30%), biotite (15-20%), sericite (1-2%), minor epidote and carbonate.

Croll Lake Stock

The main granodioritic phase of the Croll Lake stock is a massive, homogeneous, light grey intrusion. It is medium- to coarse-grained with an average grain size of 0.5-2 mm and a maximum grain size of 4 mm (Fig. 2-7C). Its modal mineralogy consists of 35-45% plagioclase (generally albite), 20-22% quartz, 10-15% hornblende, 5-10% microcline, up to 5-10% biotite, 5-10% sericite, 2 % epidote, up to 2% chlorite and minor carbonate. Younger tonalite dikes cut across the stock (Fig. 2-7D). They are light grey and fine-grained with an average grain size of 0.1-0.5 mm (locally ranging up to 2 mm; Fig. 2-7E). They consist of 45-60% albite, 25-40% quartz, 5-12% white mica, up to 10% partially chloritized biotite, up to 2% potassic feldspar, and minor epidote, chlorite and carbonate.

Geochemistry

Thirty-two feldspar-quartz porphyry and six Croll Lake stock samples were collected from the Geraldton and Longlac areas. Most samples were crushed using a Cr-free steel mill, fused by lithium metaborate/tetraborate, dissolved using nitric acid digestion, and analyzed for major oxides and trace elements by X-ray fluorescence spectrometry (XRF) and inductively coupled plasma mass spectrometry (ICP-MS), respectively, at Activation Laboratories Ltd. in Ancaster, Ontario. Three samples, which were collected in 2014, were analyzed at the Geoscience Laboratories of the Ministry of Northern Development and Mines in Sudbury, Ontario. They were crushed in an agate mill and were analyzed for major oxides using fusion X-ray fluorescent spectrometry (XRF) and for trace elements using inductively coupled plasma mass spectrometry (ICP-MS) following closed vessel multi-acid digestion. The analytical methods, detection limits, accuracy and precision of each element at both laboratories are shown in Appendix 2-A.

Samples that returned loss of ignition (LOI) contents exceeding 4 wt. % were eliminated from further consideration of their primary composition because of the possible effects of hydrothermal alteration on their composition. To test for major element mobility, the remaining 14 samples were plotted on the chlorite-carbonate-pyrite index (CCPI) versus alteration index (AI) diagram of Large et al. (2001) and on the alkali-alumina (Na/Al vs. K/Al) molar ratio diagram of Davies and Whitehead (2006). On the CCPI versus AI diagram, the granodiorite of the Croll Lake Stock and the feldspar porphyry plot in the least altered dacite field whereas a tonalite dike cutting the Croll Lake Stock and the feldspar-quartz porphyry samples plot in the least altered rhyolite field (Fig. 2-8A). On the binary molar Na/Al versus K/Al diagram of Davies and Whitehead (2006), the samples display similar compositions as those of average Archean granitoid intrusions but the distribution of feldspar-quartz porphyry samples along the muscovite-albite alteration trend is consistent with the albitization and breakdown of feldspar to sericite during hydrothermal alteration and metamorphism (Fig. 2-8B). Thus, although the effects of alteration were minimized by eliminating samples with high LOI, the remaining samples still underwent some degree of alteration. Diagrams that include alkali elements will still be used but, because of the mobility of these elements, they will only be used as means of broadly classifying those rocks.

Feldspar-quartz porphyry

Feldspar-quartz porphyry samples (FQP on Fig. 2-2) have a felsic composition with high SiO_2 (66-70 wt. %), Al_2O_3 (16.2-17.6 wt. %), Na_2O (5.8-6.8 wt. %), and with low MgO (0.6-1.1 wt. %), CaO (2.5-4 wt. %), K_2O (1.6-2.3 wt. %), total ferromagnesian oxide contents (FeO_t+MgO+MnO+TiO_2=3.3-4.4 wt. %) and K_2O/Na_2O ratios (0.24-0.4). They have low transition metal concentrations (Cr≤30 ppm; Ni<20 ppm; V=40-54 ppm) and Zr-contents (<200 ppm), and Zr/Y (>7) and La/Yb (>6) ratios indicative of calc-alkaline rocks (MacLean and Barrett,

1993; Barrett and MacLean, 1999). On the volcanic rock classification diagram of Winchester and Floyd (1977), they plot in the subalkaline rhyodacite-dacite and alkaline trachyandesite fields (Fig. 2-8C). On the chondrite-normalized REE diagram, they display strong REE fractionation [$(La/Yb)_N$=27-40 and ΣREE=60-82 ppm (Fig. 2-9A)]. On the primitive mantle normalized multi-element diagram, they have pronounced negative Ta-, Nb-, and Ti-anomalies (Fig. 2-9B).

The tonalitic feldspar porphyry (9 on Fig. 2-2 and 2-3) is chemically similar to the FQP but it differs by its higher MgO (2.2 wt. %) and total ferromagnesian oxide (FeO_t+MgO+MnO+ TiO_2 =7.6 wt. %) content, and by its lower SiO_2 (64.8 wt. %) and Na_2O (4.3 wt. %) content and lower transition metal concentrations (Cr=60 ppm, Ni=21.8 ppm, V=54 ppm). The feldspar porphyry is more enriched in ΣREEs (135 ppm) than the FQP but has similar REE patterns, and negative Ta-, Nb-, and Ti-anomalies on the primitive mantle-normalized multi-element diagram (Fig. 2-9B).

Croll Lake Stock

Granodioritic samples of the Croll Lake stock (1, 2, 5 on Fig. 2-2 and 2-3) have higher K_2O (2.5-3.2 wt. %), MgO (~2.7-4.5 wt. %), CaO (4.75-7 wt. %), ferromagnesian oxide concentrations (FeO_t+MgO+MnO+TiO_2=6.8-10.4 wt. %) and K_2O/Na_2O ratios (0.68-0.74) than the FQPs. They have similar Al_2O_3 (16.1-16.5 wt. %), but lower SiO_2 (58.9-65 wt. %) and Na_2O concentrations (~3.7-4.2 wt. %; Table 2-3). They have high V (50-90 ppm), Ni (40-52 ppm), Cr concentrations (120-130 ppm). Their Zr concentrations (<200 ppm), Zr/Y (>7) and La/Yb (>6) ratios suggest a calc-alkaline geochemical affinity (MacLean and Barrett, 1993; Barrett and MacLean, 1999). On the volcanic rock classification diagram by Winchester and Floyd (1977), they plot in the rhyodacite/dacite and andesite fields (Fig. 2-8C). They display similar LREE fractionation

($(La/Yb)_N$=20-33) and higher ΣREE concentrations (150-200 ppm) than the FQPs (Fig. 2-9A) as well as similar, pronounced negative Ta-, Nb-, Ti- and positive Sr-anomalies (Fig. 2-9B).

The two analyzed samples of tonalite dike (3-4 on Fig. 2-2 and 2-3) are more similar in composition to the feldspar-quartz porphyry than to the granodioritic phase of the Croll Lake stock. Their composition is summarized in Table 2-3.

Geochronology of feldspar porphyry dike

A sample of feldspar-quartz porphyry was crushed and prepared using the mineral separation procedure described above and analysed using the U-Pb isotope dilution thermal ionization mass spectrometry (ID-TIMS) techniques described in McNicoll and others (2014) and modified after Parrish (1987) and Roddick (1987). U-Pb ID-TIMS analytical results are presented in Table 2-4 and plotted on a concordia plot with errors at the 2σ level (Fig. 2-10) using Isoplot v. 3.0 (Ludwig, 2003).

The sample was collected on Porphyry Hill which is located 600 m east-southeast of the No. 1 headframe of the past-producing Macleod–Cockshutt Mine and 400 m south of the Highway 11 in Ashmore Township, south of Geraldton (*6 on Fig. 2-2). The quartz-feldspar porphyry is typically light pink on weathered surface, and pink to brownish green on fresh surface. It consists of 30-35 % feldspar (up to 6-7 mm in size with an average of 1-2 mm) and 1-2% quartz phenocrysts (1-2 mm in size) surrounded by a strongly to pervasively sericite- and Fe-carbonate-altered, fine-grained matrix with disseminated pyrite.

Four single grain zircon fractions were analyzed (Table 2-4). They are clear, colourless and euhedral (Fig. 2-3B). Three have a prismatic habit with fractures, and the fourth is a stubby grain. Grain size varies from 100 μm to 200 μm with aspect ratio ~1:2. Three zircons are slightly

discordant (≤ ±0.6%), and the fourth zircon is strongly discordant (20.1%). A linear regression through the origin yields an upper intercept of 2694.0 ± 1.0 Ma (2σ error; MSWD=0.6), which is interpreted as the crystallization age of the porphyry (Fig. 2-9).

Discussion

Sources and deposition of the metasedimentary units of the Beardmore-Geraldton belt

Detrital zircon ages and possible sources for the five metasedimentary samples are summarized in Table 2-5. All samples show similar zircon age distributions ranging from 2900 Ma to 2690 Ma, indicating broadly similar provenance of their sediments (Fig. 2-6). The detrital zircon age populations between 2690 Ma and 2900 Ma are represented in variable proportions in the sedimentary panels. Detrital zircons that yielded ages younger than 2690 Ma have high 2σ errors and they overlap in age with the detrital zircons dated around 2700 Ma. Thus, these <2690 Ma zircons do not represent geologically significant ages and cannot be interpreted as the youngest detrital zircon grains marking the maximum age of sedimentation. Peak zircon populations vary from 2774 Ma in the NSU conglomerate to 2726 Ma in the SSU conglomerate, 2711 Ma in the Quetico siltstone and 2700 Ma in both CSU and SSU sandstones. Source rocks with similar ages are present in the eastern Wabigoon subprovince (Table 2-5) to the north of the BGB, but few detrital zircons older than ca. 2800 Ma correspond to exposed source rocks of the same age north of the BGB. The latter may have been completely eroded, or the detrital zircons may have been sourced from the Winnipeg River terrane extending eastward in the eastern Wabigoon subprovince.

The youngest dominant detrital zircon populations have an age of 2711 Ma in the NSU conglomerate and Quetico sandstone, 2700 Ma in the CSU and SSU sandstones and 2726 Ma in

the SSU conglomerate, suggesting a maximum age of ca. 2700 Ma for the deposition of these rocks. Thus, the deposition of the BGB metasedimentary rocks is bracketed between ca. 2700 Ma and 2694.0 ± 1.0 Ma, the U-Pb age of the feldspar-quartz porphyry at Porphyry Hill which crosscuts bedding in the turbiditic sandstone of the SSU. The BGB and Quetico sandstones have similar detrital zircon age populations supporting the interpretation of the BGB as a transitional belt between the granite-greenstone Wabigoon and metasedimentary Quetico subprovinces (Devaney and Williams, 1989; Fralick et al., 2006). Sediments were deposited in the Quetico foreland basin stretching in front of the Wabigoon subprovince as the Wawa-Abitibi terrane migrated northward towards the Wabigoon subprovince uplifting the southern margin of the Wabigoon subprovince and imbricating Quetico sedimentary rocks with Wabigoon volcanic rocks.

Petrogenesis of the intrusive units

The geochemistry of the FQPs differs from that of the granodiorites of the Croll Lake stock, suggesting that they also differ in their petrogenesis. The FQPs are similar in geochemistry to Archean tonalite, trondhjemite and granodiorite (TTG) intrusions, which typically have high SiO_2 content (65-75 wt. %), low total ferromagnesian oxide content (FeO_t+MgO+MnO+TiO_2 < 5 wt. %), and low transition element concentrations (V<20 ppm; Laurent et al., 2014 and references therein). On Archean granitoid discrimination diagrams of Laurent and others (2014), they plot in the TTG field or in the overlapping field between the TTG and sanukitoid groups (Fig. 2-11A-D). On the binary La/Yb versus Yb and Nb versus Ta diagrams, they plot in the TTG high-pressure field (Figs. 2-12A, B), and on the Th versus SiO_2 and Ta versus Yb binary diagrams, they plot in the overlapping field between medium- and high-pressure TTG (Figs. 2-12C-D). Thus, their major and trace element compositions suggest that they formed as high-pressure TTGs.

The main granodiorite phase of the Croll Lake stock and the feldspar porphyry dike have lower SiO_2-, higher ferromagnesian oxide contents, higher transition element and ΣREE concentrations, variable LREE enrichment, and negative Nb and Ta and positive Sr anomalies. Their geochemistry is similar to that of sanukitoid suite intrusions which have a wider range of SiO_2 content (45-70 wt. %) and LREE enrichment [$10<(La/Yb)_N<75$] than the TTG intrusions, as well as higher ferromagnesian oxide content (5-25 wt. %), and higher transition metal (V>50 ppm; Ni=15–200 ppm; Cr=20–500 ppm) and ΣREE concentrations (Laurent et al., 2014). On the discrimination diagrams of Laurent and others (2014) for Archean granitoids, they plot in the sanukitoid field and in the overlapping TTG and sanukitoid fields (Fig. 2-11A-D).

A few geochemical attributes are common to all samples. The positive Sr and Al anomalies and the lack of a pronounced Eu anomaly suggest partial melting of the source rocks in the absence of plagioclase at pressures ≥16 kbar (Rollinson, 1993; Moyen and Stevens, 2006; Moyen, 2011; Laurent et al., 2014). The negative Nb, Ta and Ti anomalies suggest that rutile remained in the restite after partial melting at pressures >16-18 kbar (Rollinson, 1993; Foley et al., 2002; Moyen and Stevens, 2006; Moyen, 2011), and the depletions in HREEs and Y are indicative of garnet-present partial melting at pressures >10-12 kbar (Moyen, 2011). These geochemical characteristics collectively suggest that the FQP, the feldspar porphyry intrusions and Croll Lake stock formed as the result of partial melting of rutile-bearing garnet eclogite (Halla et al., 2009; Moyen, 2011) at depths greater than 50-60 km (Piercey et al., 2008 and references therein). A few FQP samples and the tonalite dike are less fractionated than typical TTGs, suggesting that hornblende may have been the dominant mineral (instead of garnet) present during partial melting causing a more moderate fractionation of the HREEs with respect to the LREEs (Rollinson, 1993). Thus, the

source rocks were likely heterogeneous and had variable proportions of garnet and hornblende at the place of partial melting.

The TTG melts can form either by partial melting of basaltic oceanic crust in subduction zones (e.g. Martin, 1986, 1999; Defant and Drummond, 1990; Martin and Moyen, 2002; Martin et al., 2005, 2009; Moyen and Martin, 2012) or by accretion of hydrated basaltic rocks at the base of a magmatically or tectonically overthickened crust, and delamination and partial melting of these rocks as they sank in the mantle (e.g. Smithies, 2000; Smithies and Champion, 2000; Bédard, 2006; Moyen, 2011; Bédard et al., 2013). The Croll Lake stock has a mantle signature (i.e. high transition element concentrations and high total ferromagnesian oxide content) typical of sanukitoid suite rocks, indicating inputs from both mantle peridotite and TTG melts (e.g. Laurent et al., 2014). This occurred either through melting of mantle peridotite that was formerly metasomatized by incompatible element-rich (TTG) melts or by assimilation of slab-derived TTG melts ascending through depleted mantle peridotites (Martin et al., 2009).

The TTG geochemical character of the late tonalite dike that sharply crosses the Croll Lake Stock suggests a lack of interaction with mantle material. Although the age and spatial importance of these dikes are unknown, they likely formed by similar processes as the earlier TTGs, that is, by partial melting of hydrated basaltic rocks at the base of the crust.

Tectonic implications

The 6 m.y. preceding the emplacement of the 2694 +/- 1 Ma TTG feldspar-quartz porphyries represents an important tectonic period during the evolution of the BGB. During this period, the metasedimentary units were deposited in a fore-arc basin to the north of an accretionary prism defined by imbricated Quetico sedimentary rocks (Percival and Williams, 1989; Fralick et al.,

2006). The accretionary prism was above a shallowly north-dipping subduction zone that formed during convergence of the composite Wabigoon-Winnipeg River terrane and the Abitibi-Wawa greenstone terrane (Percival et al., 2006, 2012). Alternatively, the metasedimentary units were deposited in a foreland basin, the Quetico basin, and were deformed and imbricated as the composite Wabigoon-Winnipeg River terrane migrated southward towards the Abitibi-Wawa terrane due to mantle convection or mantle drag. Either tectonic process caused crustal thickening, the introduction of hydrated mafic rocks into the lower crust, the generation of high-pressure TTG melts, and the emplacement of the FQP intrusions.

As accretion ended, the overthickened >50 km thick crust became unstable and delamination of the lower crust (Bédard, 2006; Halla et al., 2009) or slab break-off (Calvert et al., 2004; Whalen et al., 2004) facilitated the influx of mantle material resulting in the generation of sanukitoid melts and the emplacement of the stitching, post-D_1 accretion, Croll Lake Stock at ca. 2690 Ma (Corfu, 2000; Lafrance et al., 2004). Archean sanukitoid suite intrusions commonly occur as stitching plutons along major terrane boundaries (Thurston, 2015). They mark the collision of terranes and the assembly of the Superior craton that took place at very similar ages (ca. 2700-2685 Ma) across the western Superior Province except for the Wawa-Abitibi terrane where the assembly was completed ca. 10-20 m.y later (Beakhouse and Davis, 2005).

Along strike of the BGB along the Quetico-Wabigoon boundary to the west, fluvial conglomerates of the Seine assemblage were deposited between 2691.8 ±1 Ma and 2686 +2/-1 Ma (Davis et al., 1989; Fralick and Davis, 1999). Models favor the deposition of the Seine conglomerate in a transtensional basin (Blackburn et al., 1991), extensional strike-slip basin (Corcoran and Mueller, 2007), or delta fan environment (Fralick et al., 2006). Whatever the origin of the basin, the Seine conglomerate unconformably overlies early, nappe-like, recumbent folds in a sequence of

Coutchiching turbiditic sandstone (Poulsen et al., 1980; Tabor and Hudleston, 1991), which was deposited between 2704 ±3 Ma and 2692 ±2 Ma (Davis et al., 1989). The post-accretionary deposition of the Seine conglomerate is broadly coeval with the emplacement of the sanukitoid Croll Lake stock in the BGB, suggesting that extension following slab-breakup or delamination resulted in the formation of extensional basins in which younger fluvial molassic sequences were deposited.

Comparisons with other Archean gold camps

During the evolution of the Earth, the late Archean was a period of accelerated continental growth and increased metal endowment (Albarède, 1998; Condie, 1998). Late Archean gold mineralized belts in the Superior and the Yilgarn cratons have similar geologic and gold mineralization histories. The deposition of older volcanic rocks is followed by a 5-25 My "gap" and the onset of compression, facilitating the accumulation of turbiditic sandstone with minor iron formation and conglomerate as synorogenic flysch sequences in marine basins as well as the development of TTG suite "porphyry" intrusions (Table 1; Born, 1995; Ayer et al., 2002a, 2005; Krapež, 1997; Krapež et al., 2000; Corcoran and Mueller, 2007; Krapež and Hand, 2008; Percival et al., 2012).

The presence of linear belts of synorogenic flysch sequence and a later extensional molasse sequence along major faults are regional indicators of long-lived orogenic activity (Robert et al., 2005; Dubé and Gosselin, 2007; Bleeker, 2015). These faults, which either controlled basin sedimentation and/or the preservation of the basins by down-faulting, acted as long-lived pathways for auriferous hydrothermal fluids (Dubé and Gosselin, 2007). For example, Porcupine and/or Timiskaming assemblages in the Timmins gold camp occurs immediately north of the Destor-Porcupine deformation zone. These sedimentary assemblages overlie older volcanic rocks of the

2710 Ma - 2704 Ma Tisdale assemblage (Ayer et al., 2002a, 2005; Robert et al., 2005; Bateman et al., 2008; Bleeker, 2015). It comprises an older 2690 Ma - 2685 Ma marine turbiditic sandstone Porcupine assemblage, which is unconformably overlain by alluvial-fluvial conglomerate and sandstone of the <2679 Ma - <2669 Ma Timiskaming assemblage (Ayer et al., 2005). The Timiskaming assemblage in the Kirkland Lake gold camp also occurs immediately north of a major fault called the Larder Lake - Cadillac deformation zone. The Timiskaming sedimentary rocks unconformably overlie older volcanic rocks of the 2704 Ma - 2696 Ma Blake River assemblage and comprises fluvial conglomerate and sandstone intercalated with alkalic volcanic rock of the <2679 Ma - 2669 Ma Timiskaming assemblage (Corfu et al., 1991; Ayer et al., 2002a, b, 2005). Other Timiskaming assemblage rocks along the Larder Lake - Cadillac deformation zone, such as the Granada basin south of Rouyn-Noranda in Québec (Corcoran and Mueller, 2007; Diop, 2011), directly overlie older marine turbiditic sandstone of the ~2682 Ma Pontiac group (Mortensen and Card, 1993; Davis, 2002; Frieman et al., 2017). In the Yilgarn craton, the predominantly komatiitic and tholeiitic, 2715 Ma to 2692 Ma, Kambalda Sequence is unconformably overlain by turbiditic sandstone of the 2681-2655 Ma Kalgoorlie Sequence, in turn unconformably overlain by <2655 Ma marine to fluvial conglomerates to mudstones of the Kurrawang, Merougil and Jones Creek Sequences (Krapež, 1997; Krapež et al., 2000; Kositcin et al., 2008; Krapež and Hand, 2008).

In the Superior Province and the Yilgarn craton, TTG and locally sanukitoid suite intrusions temporally overlap or follow syn-tectonic successor basin sedimentation with no apparent time gap (Table 2-1; Champion and Sheraton, 1997; Czarnota et al., 2010; Ayer et al., 2002a). The abrupt change from pre- to early tectonic TTG to syn- to post-tectonic sanukitoid suite plutonism is explained by the termination of subduction, terrane accretion and the large heat influx resulting

from the slab break-off (Beakhouse and Davis, 2005; Percival et al., 2012). In the Timmins gold camp, the porphyritic intrusive rocks are dominated by 2690 Ma-2670 Ma TTG suite magmatism (Ayer et al., 2005 and references therein; Macdonald, 2010 and references therein). Sanukitoid suite magmatism occurs outside of the main gold camp between 2675 Ma and 2665 Ma (Ayer et al., 2005 and references therein; Macdonald, 2010 and references therein). Late-tectonic, predominantly sub-alkaline to alkaline intrusions are spatially associated with the Destor-Porcupine and Larder Lake-Cadillac deformation zones and are broadly coeval (2680 to 2672 Ma) with the deposition of the Timiskaming assemblage (Corfu, 1993; Wilkinson et al., 1999; Ropchan et al., 2002; Ayer et al., 2005). The intrusive rocks in the Kirkland Lake camp are dominated by the latter, alkaline suite rocks (Ayer et al., 2002a, 2005; Ispolatov et al., 2005).

In the Kalgoorlie gold camp of the Yilgarn craton, 5 groups of granitoid intrusions and porphyritic dikes were distinguished based on their geochemical composition (Champion and Sheraton, 1997). They include the 2720-2660 Ma high-Ca group that has TTG-like compositions with extreme LILE-enrichment suggesting transition between TTG suite and sanukitoid suite magmatism, and the mafic group, which represent syn-tectonic, subalkaline to alkaline sanukitoid suite magmatism between >2720 Ma and 2650 Ma (Champion and Sheraton, 1997; Champion and Cassidy, 2002, 2007; Vielreicher et al., 2010). Hornblende- and feldspar-bearing porphyry dikes of sanukitoid suite geochemical affinity and feldspar-quartz porphyries of unknown geochemical affinity were intruded along the Boulder-Lefroy fault system at 2670 Ma and between 2680 Ma and 2670 Ma, respectively (Champion and Sheraton, 1997; Vielreicher et al., 2010, 2016 and references therein).

Major gold camps in the Superior craton, such as the Timmins and Kirkland Lake camps, occur along major deformation corridors (Destor-Porcupine- and Larder Lake-Cadillac deformation zones, respectively) associated with linear successor basins (e.g. Bateman et al., 2005, 2008). The

Kalgoorlie gold camp of the Yilgarn craton is spatially associated with the Boulder-Lefroy Fault system that juxtaposes the fluvial Kalgoorlie basin to older mafic volcanic rocks (Bateman and Bierlein, 2007). The BGB is also bounded by major deformation corridors. Both the Paint Lake Fault and the Bankfield-Tombill deformation zone, which border the BGB to the north and south respectively, host gold deposits (Lafrance et al., 2004; DeWolfe et al., 2007). Thus, the BGB is similar in many respects to other major Archean gold camps. It is associated with major faults, synorogenic flysh sequences overlain along strike by a coarse fluvial basin, and late porphyry intrusions, all key features of world-class and giant gold deposits in both the Superior Province and the Yilgarn craton (Robert et al., 2005).

Conclusions

New geochronological and geochemical results suggest the BGB has a similar early geologic history as that of world-class gold camps in the Superior and Yilgarn craton. Convergence between the Wabigoon-Winnipeg River terrane and the Wawa-Abitibi terrane during the Shebandowanian Orogeny (Percival et al., 2006, 2012) resulted in the deposition of the 2700 Ma to 2694 Ma, synorogenic, marine turbiditic sandstone and deltaic-fluvial conglomerate of the BGB in a fore-arc basin or foreland basin extending in front and south of the Wabigoon-Winnipeg River terrane. Accretion of hydrated mafic rocks to the lower crust as the Wabigoon-Winnipeg River terrane migrated southward towards the Wawa-Abitibi generated high-pressure TTG melts at depths >50 km, which rose through the crust and were emplaced in the BGB as 2694 Ma FQP intrusions. As convergence continued, the BGB basin underwent shortening and was imbricated with volcanic rocks of the composite Wabigoon-Winnipeg River terrane, resulting in the formation of major faults, the Paint Lake and Bankfield-Tombill deformation zones, bounding the BGB to the north and south, respectively. As accretion and convergence ceased, delamination of the lower crust or

slab break-off produced sanukitoid melts, the emplacement of the post-accretion 2690 Ma Croll Lake stock, and local extensional basins in which alluvial-fluvial conglomerate of the <2692 Ma to <2686 Ma Seine assemblage was deposited.

These early accretionary and magmatic events foreshadowed the formation of gold deposits in the belt. Similar to the Larder Lake-Cadillac deformation zone and the Destor-Porcupine deformation zone, the Paint Lake and Bankfield-Tombill deformation zones are long-lived structures that acted as conduits for the migration of gold-bearing hydrothermal fluids during later reactivation of the structures (Lafrance et al., 2004, 2012; Tóth et al., 2015). The BGB has many of the key characteristics of world renowned gold districts, such as major long-lived faults and shear zones, synorogenic clastic sedimentary basins, porphyry and sanukitoid intrusions, extensive alteration systems associated with quartz-carbonate veins and historical major gold production (≥4Moz).

References

Albarède, F., 1998. The growth of continental crust. Tectonophysics 296, 1–14. doi:10.1016/S0040-1951(98)00133-4

Anglin, C.D., 1987. Geology, structure and geochemistry of gold mineralization in the Geraldton area, Northwestern Ontario. Unpublished Master's Thesis. Memorial University of Newfoundland, St. John's, Newfoundland. 283 p.

Anglin, C.D., Franklin, J.M., Loveridge, W.D., Hunt, P.A., Osterberg, S.A., 1988. Use of zircon U-Pb ages of felsic intrusive and extrusive rocks in eastern Wabigoon subprovince, Ontario, to place constraints on base metal and gold mineralization. In: Radiogenic Age and Isotopic Studies: Report 2, Geological Survey of Canada, Paper 88-2, 109-115.

Ayer, J., Amelin, Y., Corfu, F., Kamo, S.L., Ketchum, J.W.F., Kwok, K., Trowell, N.F., 2002a. Evolution of the southern Abitibi greenstone belt based on U–Pb geochronology: autochthonous volcanic construction followed by plutonism, regional deformation and sedimentation. Precambrian Res. Volume 115, 63–95. doi:10.1016/S0301-9268(02)00006-2

Ayer, J., Ketchum, J., Trowell, N., 2002b. New geochronological and Nd isotopic results from the Abitibi Greenstone belt, with emphasis on timing and tectonic implications of late Archean sedimentation and volcanism; in: Summary of Field Work and Other Activities 2002; Ontario Geological Survey, Open File Report 6100, pp. 5–1 to 5–16.

Ayer, J.A., Thurston, P.C., Bateman, R., Dubé, B.,Gibson, H.L., Hamilton, M.A., Hathway, B., Hocker, S.M., Houlé, M.G., Hudak, G., Ispolatov, V.O., Lafrance, B., Lesher, C.M., MacDonald, P.J., Péloquin, A.S., Piercey, S.J., Reed, L.E. and Thompson, P.H. 2005. Overview of results from the Greenstone Architecture Project: Discover Abitibi Initiative; Ontario Geological Survey, Open File Report 6154, 146p.

Barrett, T.J., Fralick, P.W., 1985. Sediment redeposition in Archean Iron Formation: Examples from the Beardmore-Geraldton Belt, Ontario. J. Sediment. Petrol. 55, 205–212.

Barrett, T.J., MacLean, W.H., 1999. Volcanic sequences, lithogeochemistry, and hydrothermal alteration in some bimodal volcanic-associated massive sulphide systems, in: Reviews in Economic Geology, Society of Economic Geology, Vol. 8., pp. 101–131.

Bateman, R., Ayer, J., Dubé, B., Hamilton, M.A., 2005. The Timmins–Porcupine gold camp, northern Ontario: the anatomy of an Archaean greenstone belt and its gold mineralization: Discover Abitibi Initiative; Ontario Geological Survey, Open File Report 6158.

Bateman, R., Bierlein, F.P., 2007. On Kalgoorlie (Australia), Timmins–Porcupine (Canada), and factors in intense gold mineralisation. Ore Geol. Rev. 32, 187–206. doi:10.1016/j.oregeorev.2006.08.001Bateman, R., Ayer, J., Dubé, B., 2008. The Timmins-Porcupine Gold Camp, Ontario: Anatomy of an Archean Greenstone Belt and Ontogeny of Gold Mineralization. Econ. Geol. 103, 1285–1308. doi:10.2113/gsecongeo.103.6.1285

Bateman, R., Ayer, J., Dubé, B., 2008. The Timmins-Porcupine Gold Camp, Ontario: Anatomy of an Archean Greenstone Belt and Ontogeny of Gold Mineralization. Econ. Geol. 103, 1285–1308. doi:10.2113/gsecongeo.103.6.1285

Beakhouse, G.P., 1983. Geological, geochemical and Rb–Sr and U–Pb zircon geochronological investigations of granitoid rocks from the Winnipeg River Belt, northwestern Ontario and southeastern Manitoba. Unpubl. Ph.D. thesis. McMaster University, Hamilton. 376 p.

Beakhouse, G.P., 1984. Geology of the Grenville Lake Area, Thunder Bay District; Ontario Geological Survey Open File Report 5513, 146p.

Beakhouse, G.P., 1991. Winnipeg River Subprovince, in: Thurston, P.C., Williams, H.R., Sutcliffe, R.H., Stott, G.M. (Eds.), Geology of Ontario. Ontario Geological Survey, Special Volume 4. Part 1. pp. 279–301.

Beakhouse, G.P., Davis, D.W., 2005. Evolution and tectonic significance of intermediate to felsic plutonism associated with the Hemlo greenstone belt, Superior Province, Canada. Precambrian Res. 137, 61–92. doi:10.1016/j.precamres.2005.01.003

Bédard, J.H., 2006. A catalytic delamination-driven model for coupled genesis of Archaean crust and sub-continental lithospheric mantle. Geochim. Cosmochim. Acta 70, 1188–1214. doi:10.1016/j.gca.2005.11.008

Bédard, J.H., Harris, L.B., 2014. Neoarchean disaggregation and reassembly of the Superior craton. Geology 42, 951–954. doi:10.1130/G35770.1

Bédard, J.H., Harris, L.B., Thurston, P.C., 2013. The hunting of the snArc. Precambrian Res. 229, 20–48. doi:10.1016/j.precamres.2012.04.001

Blackburn, C.E., Johns, G.W., Ayer, J., Davis, D.W., 1991. Wabigoon Subprovince, in: Thurston, P.C., Williams, H.R., Sutcliffe, R.H., Stott, G.M. (Eds.), Geology of Ontario. Ontario Geological Survey, Special Volume 4. Part 1., pp. 303–381.

Bleeker, W., 2015. Synorogenic gold mineralization in granite-greenstone terranes: the deep connection between extension, major faults, synorogenic clastic basins, magmatism, thrust inversion, and long-term preservation, In: Targeted Geoscience Initiative 4: Contributions to the Understanding of Precambrian Lode Gold Deposits and Implications for Exploration, (ed.) B. Dubé and P. Mercier-Langevin; Geological Survey of Canada, Open File 7852, p. 25–47

Born, P., 1995. A sedimentary basin analysis of the Abitibi greenstone belt in the Timmins area, Northern Ontario, Canada. Carleton University, Ottawa, Unpublished PhD thesis, 489 p.

Calvert, A.J., Cruden, A.R., Hynes, A., 2004. Seismic evidence for preservation of the Archean Uchi granite-greenstone belt by crustal-scale extension. Tectonophysics 388, 135–143. doi:10.1016/j.tecto.2004.07.043

Carter, M.W., 1987. Geology of McComber and Vincent Townships, District of Thunder Bay, Ontario Geological Survey, Open File Report 5648. 144 p.

Champion, D.C., Cassidy, K.F., 2002. Granites in the Leonora-Laverton transect area, north eastern Yilgarn, north eastern Yilgarn Craton, with an emphasis on the Leonora-Laverton transect area: Geoscience Australia, Record 2002/18, 13-35.

Champion, D.C., Cassidy, K.F., 2007. An overview of the Yilgarn Craton and its crustal evolution, in: Bierlein, F.P., Knox-Robinson, C.M. (Eds.), Proceedings of Geoconferences (WA) Inc. Kalgoorlie 07' Conference. Geoscience Australia Record 2007/14. p. 13–35.

Champion, D.C., Sheraton, J.W., 1997. Geochemistry and Nd isotope systematics of Archaean granites of the Eastern Goldfields, Yilgarn Craton, Australia: implications for crustal growth processes. Precambrian Res. 83, 109–132. doi:10.1016/S0301-9268(97)00007-7

Condie, K.C., 1998. Episodic continental growth and supercontinents: a mantle avalanche connection? Earth Planet. Sci. Lett. 163, 97–108. doi:10.1016/S0012-821X(98)00178-2

Corcoran, P.L., Mueller, W.U. 2007. Time-transgressive Archean unconformities underlying molasse basin-fill successions of dissected oceanic arcs, Superior Province, Canada. Journal of Geology 115, 655-674.

Corfu, F., 1993. The evolution of the southern Abitibi Greenstone Belt in light of precise U-Pb geochronology. Econ. Geol. 88, 1323–1340. doi:10.2113/gsecongeo.88.6.1323

Corfu, F., 2000. Extraction of Pb with artificially too-old ages during stepwise dissolution expreiments on Archean zircon. Lithos 53, 279–291.

Corfu, F., Jackson, S.L., Sutcliffe, R.H., 1991. U–Pb ages and tectonic significance of late Archean alkalic magmatism and nonmarine sedimentation: Timiskaming Group, southern Abitibi belt, Ontario. Can. J. Earth Sci. 28, 489–503. doi:10.1139/e91-043

Corfu, F., Krogh, T.E., Kwok, Y.Y., Jensen, L.S., 1989. U-Pb zircon geochronology in the southwestern Abitibi greenstone belt, Superior Province. Can. J. Earth Sci. 26, 1747–1763. doi:10.1017/CBO9781107415324.004

Czarnota, K., Champion, D.C., Goscombe, B., Blewett, R.S., Cassidy, K.F., Henson, P.A., Groenewald, P.B., 2010. Geodynamics of the eastern Yilgarn Craton. Precambrian Res. 183, 175–202. doi:10.1016/j.precamres.2010.08.004

Davies, J.F., Whitehead, R.E., 2006. Alkali-alumina and MgO-alumina molar ratios of altered and unaltered rhyolites. Explor. Min. Geol. 15, 75–88. doi:10.2113/gsemg.15.1-2.75

Davis, D.W., 1999. Report for the Ontario Geological Survey on the U–Pb geochronology of rocks from the Onaman Lake belt. Earth Sci. Dep. Royal Ontario Museum, 20 p.

Davis, D.W., 1998. Report for the Ontario Geological Survey on the U–Pb geochronology of rocks from the Onaman Lake belt. Earth Sci. Dep. Royal Ontario Museum, 19 p.

Davis, D.W., 2002. U-Pb geochronology of Archean metasedimentary rocksin the Pontiac and Abitibi subprovinces, Quebec, constraints on timing, provenance and regional tectonics. Precambrian Research 115, 97-117.

Davis, D.W., Jackson, M., 1988. Geochronology of the Lumby Lake greenstone belt: a 3 Ga complex within the Wabigoon Subprovince, northwest Ontario. Geol Soc Am Bull 100, 818–824.

Davis, D.W., Kwok, Y.Y., Amelin, Y., Kamo, S.L., 2000. Report on U-Pb geochronology of rocks from the Onaman greenstone belt 1998 to 2000, Wabigoon Subprovince, Ontario. Jack Satterly Geochronology Lab. Royal Ontario Museum.

Davis, D.W., Pezzutto, F., Ojakansas, R.W., 1990. The age and provenance of metasedimentary rocks in the Quetico Subprovince, Ontario, from single zircon analyses: implications for Archean sedimentation and tectonics in the Superior Province. Eart and Planetary Science Letters 99, 195-205.

Davis, D.W., Poulsen, K.H., Kamo, S.L., 1989. New insights into Archean crustal development from geochronology in the Rainy Lake area, Superior Province, Canada. Journal of Geology 97, 379-398.

Davis, D.W., Sutcliffe, R.H., Trowell, N.F., 1988. Geochronological constraints on the tectonic evolution of a late Archean greenstone belt, Wabigoon Subprovince, northwestern Ontario, Canada. Precambrian Res 39, 171–191.

Defant, M.J., Drummond, M.S., 1990. Derivation of Some Modern Arc Magmas by Melting of Young Subducted Lithosphere. Nature 347, 662–665.

Devaney, J.R., Fralick, P.W., 1985. Regional sedimentology of the Namewaminikan Group, northern Ontario: Archean fluvial fans, braided rivers, deltas and an aquabasin, in: Current Research, Geological Survey of Canada, Part B, Paper 85-1B, pp. 125–132.

Devaney, J.R., Williams, H.R., 1989. Evolution of an Archean subprovince boundary: a sedimentological and structural study of part of the Wabigoon–Quetico boundary in northern Ontario. Can. J. Earth Sci. 26, 1013–1026.

DeWolfe, J.C., Lafrance, B., Stott, G.M., 2007. Geology of the shear-hosted Brookbank gold prospect in the Beardmore–Geraldton belt, Wabigoon Subprovince, Ontario. Can. J. Earth Sci. 44, 925–946. doi:10.1139/E06-118

Diop, A., 2011. Caractéristiques sédimentologiques, volcanologiques et structurales du bassin de Granada dans la ceinture de roches vertes de l'Abitibi (Québec). Unpublished Ph.D. thesis, Université du Québec à Chicoutimi, Chicoutimi, Québec, 348 pp.

Dubé, B., and Gosselin, P., 2007. Greenstone-hosted quartz-carbonate vein deposits, in: Goodfellow, W.D. (Ed.), Mineral Deposits of Canada: A Synthesis of Major Deposit-Types, District Metallogeny, the Evolution of Geological Provinces, and Exploration Methods: Geological Association of Canada, Mineral Deposits Division, Special Publication No. 5, pp. 49–73.

Foley, S.F., Tiepolo, M., Vannucci, R., 2002. Growth of early continental crust controlled by melting of amphibolite in subduction zones. Nature 417, 837–840. doi:10.1038/nature00799

Fralick, P.W., Davis, D.W., 1999. The Seine-Coutchiching problem revisited: Sedimentology, geochronology, and geochemistry of sedimentary units in the Rainy Lake and Sioux Lookout areas. In 1999 Western Superior Transect 5th Annual Workshop. Edited by R.M. Harrap and H.H. Helmstaedt. Lithoprobe Report 70, Lithoprobe Secretariat, The University of British Columbia, Vancouver, B.C., pp. 66-75.

Fralick, P.W., Pufahl, P., 2006. Iron formation in Neoarchean deltaic successions and Microbially mediated depositon of transgessive systems tracts. J. Sediment. Res. 76, 1057–1066.

Fralick, P.W., Purdon, R.H., Davis, D.W., 2006. Neoarchean trans-subprovince sediment transport in southwestern Superior Province: sedimentological, geochemical and geochronological evidence. Can. J. Earth Sci. 43, 1055–1070. doi:10.1139/E06-059

Frieman, B.M., Kuiper, Y.D., Kelly, N.M., Monecke, T., Kylander-Clark, A., 2017. Constraints on the geodynamic evolution of the southern Superior Province: U-Pb LA-ICP-MS analysis of detrital zircon in successor basins of the Archean Abitibi and Pontiac subprovinces of Ontario and Quebec, Canada. Precambrian Research 292, 398-416.

Goldfarb, R.J., Baker, T., Dubé, B., Groves, D.I., Hart, C., Gosselin, P., 2005. Distribution, Character, and Genesis of Gold Deposits in Metamorphic Terranes, in: Economic Geology 100th Anniversary Volume. pp. 407–450.

Goldfarb, R.J., Groves, D.I., Gardoll, S., 2001. Orogenic gold and geologic time: A global synthesis. Ore Geol. Rev. 18, 1–75. doi:10.1016/S0169-1368(01)00016-6

Halla, J., van Hunen, J., Heilimo, E., Hölttä, P., 2009. Geochemical and numerical constraints on Neoarchean plate tectonics. Precambrian Res. 174, 155–162. doi:10.1016/j.precamres.2009.07.008

Hart, T.R., terMeer, M. and Jolette, C. 2002. Precambrian geology of Kitto, Eva, Summers, Dorothea andSandra townships, northwestern Ontario: PhoenixBedrock Mapping Project; Ontario Geological Survey, Open File Report 6095, 206 p.

Henry, P., Stevenson, R.K., Gariépy, C., 1998. Late Archean Mantle Composition and Crustal Growth in the Western Superior Province of Canada: Neodymium and Lead Isotopic Evidence from the Wawa, Quetico, and Wabigoon Subprovinces. Geochim. Cosmochim. Acta 62, 143–157. doi:10.1016/S0016-7037(97)00324-4

Horwood, H.C., Pye, E.G., 1955. Geology of Ashmore Township. In: 60th Annual Report of the Ontario Department of Mines, Part 5. 139 p.

Hyde, R.S., 1980. Sedimentary facies in the Archean Timiskaming Group and their tectonic implications, Abitibi greenstone belt, northeastern Ontario, Canada. Precambrian Res. 12, 161–195.

InnovExplo Inc 2015. Technical Report on the Trans-Canada Property (according to National Instrument 43-101 and Form 43-101F1). 500p.

Ispolatov, V., Lafrance, B., Dubé, B., Hamilton, M.A., Creaser, R.A., 2005. Geology, structure,and gold mineralization, Kirkland Lake and Larder Lake areas (Gauthier and Teck townships): Discover Abitibi Initiative; Ontario Geological Survey, Open File Report 6159. 170p.

Ispolatov, V., Lafrance, B., Dubé, B., Creaser, R., and Hamilton, M., 2008: Geological and structural setting of gold mineralization in the Kirkland Lake-Larder Lake gold belt, Ontario. Economic Geology, volume 103, No. 8, pp. 1309-1340.

Kehlenbeck, M.M., 1986. Folds and folding in the Beardmore - Geraldton fold belt. Can. J. Earth Sci. 23, 158–171.

Kositcin, N., Brown, S.J.A., Barley, M.E., Krapež, B., Cassidy, K.F., Champion, D.C., 2008. SHRIMP U-Pb zircon age constraints on the Late Archaean tectonostratigraphic architecture of the Eastern Goldfields Superterrane, Yilgarn Craton, Western Australia. Precambrian Res. 161, 5–33. doi:10.1016/j.precamres.2007.06.018

Krapež, B., 1997. Sequence-stratigraphic concepts applied to the identification of depositional basins and global tectonic cycles. Aust. J. Earth Sci. 44, 879–886. doi:10.1080/08120099708728360

Krapež, B., Brown, S.J.., Hand, J., Barley, M.E., Cas, R.A.F, 2000. Age constraints on recycled crustal and supracrustal sources of Archaean metasedimentary sequences, Eastern Goldfields Province, Western Australia: evidence from SHRIMP zircon dating. Tectonophysics 322, 89–133. doi:10.1016/S0040-1951(00)00059-7

Krapež, B., Hand, J.L., 2008. Late Archaean deep-marine volcaniclastic sedimentation in an arc-related basin: The Kalgoorlie Sequence of the Eastern Goldfields Superterrane, Yilgarn Craton, Western Australia. Precambrian Res. 161, 89–113. doi:10.1016/j.precamres.2007.06.014

Kresz, D.U., Zayachivsky, B., 1991. Precambrian Geology, northern Long Lake area. Ontario Geological Survey, Report 273, 77 p.

Kresz, D.U. and Zayachivsky, B. 1993. Precambrian geology, Seagram Lake area; Ontario Geological Survey, Report 287, 81 p.

Kwok, Y.Y., Amelin, Y., Kamo, S.L., Davis, D.W., 2000. Report for the Ontario Geological Survey on U–Pb geochronology of rocks from the Onaman greenstone belt. Earth Sci. Dep. R. Ontario Museum, 37 p.

Lafrance, B., DeWolfe, J.C., Stott, G.M., 2004. A structural reappraisal of the Beardmore-Geraldton Belt at the southern boundary of the Wabigoon subprovince, Ontario, and implications for gold mineralization. Can. J. Earth Sci. 41, 217–235. doi:10.1139/E03-090

Lafrance, B., Tóth, Z., Dubé, B., Mercier-Langevin, P., 2012. Targeted Geoscience Initiative 4. Lode Gold Deposits in Ancient Deformed and Metamorphosed Terranes: Geological Setting of Banded Iron Formation–Hosted Gold Mineralization in the Geraldton Area, Northern Ontario. In: Summary of Field Work and Other Activities 2012; Ontario Geological Survey, Open File Report 6280, p.48-1 to 48-10.

Large, R., Gemmell, B., Paulick, H., Huston, D., 2001. The Alteration Box Plot: A Simple Approach to Understanding the Relationship between Alteration Mineralogy and Lithogeochemistry Associated with Volcanic-Hosted Massive Sulfide Deposits. Econ. Geol. 96, 957–971.

Laurent, O., Martin, H., Moyen, J.-F., Doucelance, R., 2014. The diversity and evolution of late-Archean granitoids: Evidence for the onset of "modern-style" plate tectonics between 3.0 and 2.5 Ga. Lithos 205, 208–235. doi:10.1016/j.lithos.2014.06.012

Lavigne, M.J. 2009. Distribution of gold with respect to lithologies, metamorphic facies and strain state in the Beardmore–Geraldton greenstone belt; OntarioGeological Survey, Open File Report 6241, 88p.

Lu, Y., McCuaig, T.C., Hollings, P., Ketchum, K., Kerrich, R., Smyk, M., Cliff, J., Bagas, L., 2013. Zircon multi-isotopic mapping in Wabigoon Subprovince, western Superior Craton: Implications for lithospheric architecture and controls on orogenic gold mineral systems. SGA Bienn. Meet. Proc. 3, 7–11.

Ludwig, K.R., 2003. User's Manual for Isoplot 3.0: a Geochronological Toolkit for Microsoft Excel. Berkeley Geochronological Center, Special Publication 4, 74 p.

Macdonald, A.J., 1983. A Re-Appraisal of the Geraldton Gold Camp, p. 194-197. In: Wood, J., White, O.L., Barlow, R.B. Colvine, A.C. (Eds.) Summary of Field Work, 1983, Ontario Geological Survey, Miscellaneous Paper 116, 313 p.

Macdonald, A.J., 1988. The Geraldton Gold Camp: The Role of Banded Iron Formation; Ontario Geological Survey, Open File Report 5694, 173 p.

Macdonald, P.J., 2010. The geology, lithogeochemistry and petrogenesis of intrusions associated with gold mineralization in the Porcupine gold camp, Timmins, Canada. Laurentian University, Sudbury, Unpublished MSc thesis. 188p.

Mackasey, W.O., 1975. Geology of Dorothea, Sandra, and Irwin Townships, District of Thunder Bay. Ontario Division of Mines, Geological Report 122, 83 p.

Mackasey, W.O., 1976. Geology of Walters and Leduc Townships, District of Thunder Bay. Ontario Division of Mines, Geoscience Report 149. 58 p.

MacLean, W.H., Barrett, T.J., 1993. Lithogeochemical techniques using immobile elements. J. Geochemical Explor. 48, 109–133. doi:10.1016/0375-6742(93)90002-4

Martin, H., 1986. Effect of steeper Archean geothermal gradient on geochemistry of subduction-zone magmas. Geology 14, 753–756. doi:10.1130/0091-7613(1986)14<753:EOSAGG>2.0.CO;2

Martin, H., 1999. Adakitic magmas: Modern analogues of Archaean granitoids. Lithos 46, 411–429. doi:10.1016/S0024-4937(98)00076-0

Martin, H., Moyen, J.-F., 2002. Secular changes in tonalite-trondhjemite-granodiorite composition as markers of the progressive cooling of Earth. Geology 30, 319–322. doi:10.1130/0091-7613(2002)030<0319:SCITTG>2.0.CO

Martin, H., Moyen, J.-F., Rapp, R.P., 2009. The sanukitoid series: magmatism at the Archaean–Proterozoic transition. Earth Environ. Sci. Trans. R. Soc. Edinburgh 100, 15–33. doi:10.1017/S1755691009016120

Martin, H., Smithies, R.H., Rapp, R.P., Moyen, J.-F., Champion, D.C., 2005. An overview of adakite, tonalite-trondhjemiten-granodiorite (TTG), and sanukitoid: Relationships and some implications for crustal evolution. Lithos 79, 1–24. doi:10.1016/j.lithos.2004.04.048

Mason, J.K., White, G., 1986. Gold occurrences, prospects and deposits of the Beardmore-Geraldton area, District of Thunder Bay and Cochrane. Ontario Geological Survey, Open File Report 5630. 680 p.

McDonough, W.F., Frey, F.A., 1989. REE in upper mantle rocks, in: Lipin, B., McKay, G.R. (Eds.), Geochemistry and Mineralogy of Rare Earth Elements. Mineralogical Society of America, Chelsea, Michigan, pp. 99–145.

McDonough, W.F., Sun, S. -s., 1995. The composition of the Earth. Chem. Geol. 120, 223–253. doi:10.1016/0009-2541(94)00140-4

McNicoll, V., Goutier, J., Dubé, B., Mercier-Langevin, P., Ross, P.S., Dion, C., Monecke, T., Legault, M., Percival, J., Gibson, H., 2014. U-Pb geochronology of the Blake River Group, Abitibi greenstone belt, Quebec, and implications for base metal exploration. Econ. Geol. 109, 27–59. doi:10.2113/econgeo.109.1.27

Morris, T.F., 1999. Quaternary geology of the Separation Lake area, northwestern Ontario. Ontario Geological Survey, Open File Report 5980, 86 p.

Mortensen, J.K., Card, K.D., 1993. U-Pb age constraints for the magmatic and tectonic evolution of the Pontiac Subprovince, Quebec. Canadian Journal of Earth Sciences 30, 1970-1980.

Moyen, J.-F., 2011. The composite Archaean grey gneisses: Petrological significance, and evidence for a non-unique tectonic setting for Archaean crustal growth. Lithos 123, 21–36. doi:10.1016/j.lithos.2010.09.015

Moyen, J.-F., Martin, H., 2012. Forty years of TTG research. Lithos 148, 312–336. doi:10.1016/j.lithos.2012.06.010

Moyen, J.-F., Stevens, G., 2006. Experimental constraints on TTG petrogenesis: Implications for Archean geodynamics. Geophys. Monogr. 164, 149–175.

Mueller, W., Donaldson, J.A., Doucet, P., 1994. Volcanic and tectono-plutonic influences on sedimentation in the Archean Kirkland Basin Abitibi greenstone belt, Canada. Precambrian Res. 68, 201–230.

Parrish, R.R., 1987. An improved micro-capsule for zircon dissolution in U-Pb geochronology. Chem. Geol. 66, 99–102.

Pearce, J.A., Harris, N.B.W., Tindle, A.G., 1984. Trace element distribution diagrams for the tectonic interpretation of granitic rocks. J. Petrol. 25, 956–983.

Percival, A.J., 1989. A regional perspective of the Quetico metasedimentary belt, Superior Province, Canada. Can. J. Earth Sci. 26, 677–693.

Percival, A.J., Williams, H.R., 1989. The Quetico accretionary complex, Superior Province, Canada. Geology 17, 23-25.

Percival, A.J., McNicoll, V.J., Brown, J.L., Whalen, J.B., 2004. Convergent margin tectonics, central Wabigoon subprovince, Superior Province, Canada. Precambrian Res. 132, 213–244.

Percival, J.A., Sanborn-Barrie, M., Skulski, T., Stott, G.M., Helmstaedt, H., White, D.J., 2006. Tectonic evolution of the western Superior Province from NATMAP and Lithoprobe studies. Canadian Journal of Earth Sciences 43, 1085-1117.

Percival, J.A., Skulski, T., Sanborn-Barrie, M., Stott, G.M., Leclair, A.D., Corkery, M.T., Boily, M., 2012. Geology and tectonic evolution of the Superior Province, Canada, in: Percival, A.J., Cook, F.A., Clowes, R.M. (Eds.), Tectonic Styles in Canada. Geological Association of Canada, pp. 321–378.

Piercey, S.J., Chaloux, E.C., Shirley, P.A., Hamilton, M.A., Creaser, R.A., 2008. Synvolcanic and younger plutonic rocks from the Blake River Group: Implications for regional metallogenesis. Econ. Geol. 103, 1243–1268. doi:10.2113/gsecongeo.103.6.1243

Poulsen, K.H., Borradaile, G.J., Kehlenbeck, M.M., 1980. An inverted Archean succession at Rainy Lake, Ontario. Canadian Journal of Earth Sciences 17, 1358-1369.

Poulsen, K.H., Robert, F., and Dubé, B., 2000. Geological Classification of Canadian Gold Deposits: Geological Survey of Canada, Bulletin 540, 106 p.

Pye, E.G., 1952. Geology of Errington Township, Little Long Lac Area, in: 60th Annual Report of the Ontario Department of Mines. Ontario Department of Mines, 140 p.

Robert, F., Poulsen, K.H., Cassidy, K.F., Hodgson, J.C., 2005. Gold Metallogeny of the Superior and Yilgarn Cratons, in: Hedenquist, J.W., Thompson, J.F.H., Goldfarb, R.J., Richards, J.P. (Eds.), Economic Geology 100th Anniversary Volume. pp. 1001–1033.

Roddick, J.C., 1987. Generalized numerical analysis with applications to geochronology and thermo-dynamics. Geochim. Cosmochim. Acta 51, 2129–2135.

Rollinson, H.R., 1993. Using geochemical data: evaluation, presentation, interpretation. Routledge, London and New York.

Ropchan, J.R., Luinstra, B., Fowler, A.D., Benn, K., Ayer, J., Berger, B., Dahn, R., Labine, R., Amelin, Y., 2002. Host-rock and structural controls on the nature and timing of gold mineralization at the Holloway Mine, Abitibi Subprovince, Ontario. Econ. Geol. 97, 291–309.

Sanborn-Barrie, M., Skulski, T., 1999. Tectonic assembly of contitental margin and oceanic terranes at 2.7 Ga in the Savant Lake-Sturgeon Lake greenstone belt, Ontario, in: Current Research 1999-C. Geological Survey of Canada, pp. 209–220.

Shanks, W.S. 1993. Geology of Eva and Summers townships, District of Thunder Bay; Ontario Geological Survey, Open File Report 5821, 93p.

Sircombe, K.N., 2004. AgeDisplay: an EXCEL workbook to evaluate and display univariate geochronological data using binned frequency histograms and probability density distributions. Comput. Geosci. 30, 21–31. doi:10.1016/J.CAGEO.2003.09.006

Smithies, R.H., 2000. The Archean tonalite-trondhjemite-granodiorite (TTG) series is not and analogue of Cenozoic adakite. Earth Planet. Sci. Lett. 182, 115–125.

Smithies, R.H., Champion, D.C., 1999. Late Archaean felsic alkaline igneous rocks in the Eastern Goldfields, Yilgarn Craton, Western Australia: a result of lower crustal delamination? J. Geol. Soc. London. 156, 561–576. doi:10.1144/gsjgs.156.3.0561

Smithies, R.H., Champion, D.C., 2000. The Archaean High-Mg Diorite Suite: Links to Tonalite–Trondhjemite–Granodiorite Magmatism and Implications for Early Archaean Crustal Growth. J. Petrol. 41, 1653–1671. doi:10.1093/petrology/41.12.1653

Stern, R.A., 1997. The GSC Sensitive High Resolution Ion Microprobe (SHRIMP): analytical techniques of zircon U-Th-Pb age determinations and performance evaluation, in: Radiogenic Age and Isotopic Studies: Report 10; Current Research 1997-F. pp. 1–31.

Stern, R.A., Amelin, Y., 2003. Assessment of errors in SIMS zircon U-Pb geochronology using a natural zircon standard and NIST SRM 610 glass. Chem. Geol. 197, 111–142.

Stott, G.M., Davis, D.W., 1999. Contributions to the tectonostratigraphic analysis of the Onaman–Tashota greenstone belt, eastern Wabigoon Subprovince., in: Harrap, R.M., Helmstaedt, H. (Eds.), Western Superior Transect Annual Meeting Lithoprobe Report #70. Lithoprobe Secretariat, University of British Columbia, pp. 122–124.

Stott, G.M., Davis, D.W., Parker, J.R., Straub, K.H., Tomlinson, K.Y., 2002. Geology and Tectonostratigraphic Assemblages, eastern Wabigoon Subprovince, Ontario. Scale 1:250 000. Ontario Geological Survey, Preliminary Map P. 3449. 1 sheet

Sutcliffe, R.H., 1991. Proterozoic Geology of the Lake Superior Area, in: Thurston, P.C., Williams, H.R., Sutcliffe, R.H., Stott, G.M. (Eds.), Geology of Ontario. Ontario Geological Survey, Special Volume 4, Part 1. pp. 627–658.

Tabor, J.R., Hudleston, P.J., 1991. Deformation of an Archean subprovince boundary, northern Minnesota. Canadian Journal of Earth Sciences 28, 292-307.

Taylor, S.R. and McLennan, S.M., 1985. The continental crust: its composition and evolution. Blackwell Scientific Publications, Palo Alto, CA, USA.

Thurston, P.C., 1991. Archean Geology of Ontario: Introduction, in: Thurston, P.C., Williams, H.R., Sutcliffe, R.H., Stott, G.M. (Eds.), Geology of Ontario. Ontario Geological Survey, Special Volume 4, Part 1, pp. 73–78.

Thurston, P.C., 2015. Igneous Rock Associations 19. Greenstone Belts and Granite−Greenstone Terranes: Constraints on the Nature of the Archean World. Geosci. Canada 42, 437–484. doi:http://www.dx.doi.org/10.12789/geocanj.2015.42.081

Tomlinson, K.Y., 2000. Neodymium isotopic data from the central Wabigoon subprovince, Ontario: implications for crustal recycling in 3.1 to 2.7 Ga sequences, in: Radiogenic Age and Isotopic Studies: Report 13, Geological Survey of Canada. Current Research 2000-F8, 10 p.

Tomlinson, K.Y., Davis, D.W., Percival, A.J., Hughes, D.J., Thurston, P.C., 2002. Mafic to felsic magmatism and crustal recycling in the Obonga Lake greenstone belt, western Superior Province: evidence from geochemistry, Nd isotopes and U–Pb geochronology. Precambrian Res. 114, 295–325.

Tomlinson, K.Y., Davis, D.W., Percival, A.J., Hughes, D.J., Thurston, P.C., 1999a. Neoarchean supracrustal development in the Central Wabigoon Subprovince: Nd isotope data and U/Pb geochronology; in: Harrap, R.M., Helmstaedt, H. (Eds.), Western Superior Transect 1999 Annual Meeting Lithoprobe Report #70. Lithoprobe Secretariat, University of British Columbia, pp. 147–152.

Tomlinson, K.Y., Davis, D.W., Stone, D., Hart, T.R., 2003. U–Pb age and Nd isotopic evidence for Archean terrane development and crustal recycling in the south-central Wabigoon Subprovince, Canada. Contrib. to Mineral. Petrol. 144, 684–702.

Tomlinson, K.Y., Davis, D.W., Stott, G.M., 2000. Nd isotopes in the eastern Wabigoon subprovince: implications for crustal recycling and correlations with the cetral Wabigoon; in: Harrap, R.M., Helmstaedt, H. (Eds.), 2000 Western Superior Transect Sixth Annual Workshop. Lithoprobe Report #77. Lithoprobe Secretariat, University of British Columbia, pp. 119–126.

Tomlinson, K.Y., Dickin, A.P., 2003. Geochemistry and Neodymium Isotopic Character of Granitoid Rocks in the Lac Seul Region of the Winnipeg River Subprovince, Northwestern Ontario., in: Baker, C.L., Kelly, R.I., Parker, J.R., Ayer, J.A., Easton, R.M. (Eds.), Summary of Field Work and Other Activities 2003; Ontario Geological Survey, Open File Report 6120, p.13-1 to 13-8.

Tomlinson, K.Y., Hall, R.P., Hughes, D.J., Thurston, P.C., 1996. Geochemistry and assemblage accretion of metavolcanic rocks in the Beardmore–Geraldton greenstone belt, Superior Province. Can. J. Earth Sci. 33, 1520–1533.

Tomlinson, K.Y., Hughes, D.J., Thurston, P.C., Hall, R.P., 1999b. Plume magmatism and crustal growth at 2.9 to 3.0 Ga in the Steep Rock and Lumby Lake area, western Superior Province. Lithos 46, 103–136.

Tomlinson, K.Y., Percival, J.A. 2000. Geochemistry and Nd isotopes of granitoid rocks in the Shikag–Garden lakes area, Ontario: recycled Mesoarchean crust in the central Wabigoon Subprovince; Geological Survey of Canada, Current Research 2000-E12; 11 p.

Tomlinson, K.Y., Skulski, T., Whalen, J.B., Stott, G.M., Stone, D., Percival, A.J., 2001. Nd isotope mapping of terrane boundaries in the Wabigoon and Winnipeg River Subprovinces; in: Harrap, R.M., Helmstaedt, H. (Eds.), Western Superior Lithoprobe-Western Superior NATMAP 2001 Annual Meeting Lithoprobe Report #80. Lithoprobe Secretariat, University of British Columbia, pp. 5–7.

Tomlinson, K.Y., Stott, G.M., Percival, A.J., Stone, D., 2004. Basement terrane correlations and crustal recycling in the western Superior Province: Nd isotopic character of granitoid and felsic volcanic rocks in the Wabigoon subprovince, N. Ontario, Canada. Precambrian Res. 132, 245–274.

Tóth, Z., Lafrance, B., Dubé, B., McNicoll, V.J., Mercier-Langevin, P., and Creaser, R.A., 2015. Banded iron formation-hosted gold miner- alization in the Geraldton area, northwestern Ontario: Structural setting, mineralogical characteristics, and geochronology, In: Targeted Geoscience Initiative 4: Contributions to the Understanding of Precambrian Lode Gold Deposits and Implications for Exploration, (ed.) B. Dubé and P. Mercier-Langevin; Geological Survey of Canada, Open File 7852, p. 85–97.

Vielreicher, N.M., Groves, D.I., Snee, L.W., Fletcher, I.R., McNaughton, N.J., 2010. Broad synchroneity of three gold mineralization styles in the Kalgoorlie gold field: SHRIMP, U-Pb, and 40Ar/39Ar geochronological evidence. Econ. Geol. 105, 187–227. doi:10.2113/gsecongeo.105.1.187

Vielreicher, N.M., Groves, D.I., McNaughton, N.J., 2016. The giant Kalgoorlie Gold Field revisited. Geosci. Front. 7, 359–374. doi:10.1016/j.gsf.2015.07.006

Whalen, J.B., Percival, J.A., McNicoll, V.J., Longstaffe, F.J., 2004. Geochemical and isotopic (Nd–O) evidence bearing on the origin of late- to post-orogenic high-K granitoid rocks in the Western Superior Province: implications for late Archean tectonomagmatic processes. Precambrian Res. 132, 303–326.

Wilkinson, L., Cruden, A.R., Krogh, T.E., 1999. Timing and kinematics of post-Timiskaming deformation within the Larder Lake - Cadillac deformation zone, southwest Abitibi greenstone belt, Ontario, Canada. Can. J. Earth Sci. 36, 627–647. doi:10.1139/e99-015

Williams, H.R., 1987. Ontario Geoscience Research Program, Grant No. 242. Structural Studies in the Wabigoon and Quetico Subprovinces, Open File Report 5668. Ontario Geological Survey, 163 p.

Williams, H.R., 1991. Quetico Subprovince, in: Thurston, P.C., Williams, H.R., Sutcliffe, R.H., Stott, G.M. (Eds.), Geology of Ontario. Ontario Geological Survey, Special Volume 4, Part 1, pp. 383–403.

Winchester, J.A., Floyd, P.A., 1977. Geochemical discrimination of different magma series and their differentiation products using immobile elements. Chem. Geol. 20, 325–343. doi:10.1016/0009-2541(77)90057-2

Zaleski, E., van Breemen, O., Peterson, V.L., 1999. Geological evolution of the Manitouwadge greenstone belt and Wawa-Quetico subprovince boundary, Superior Province, Ontario, constrained by U-Pb zircon dates of supracrustal and plutonic rocks. Canadian Journal of Earth Sciences 36, 945-966.

Figures

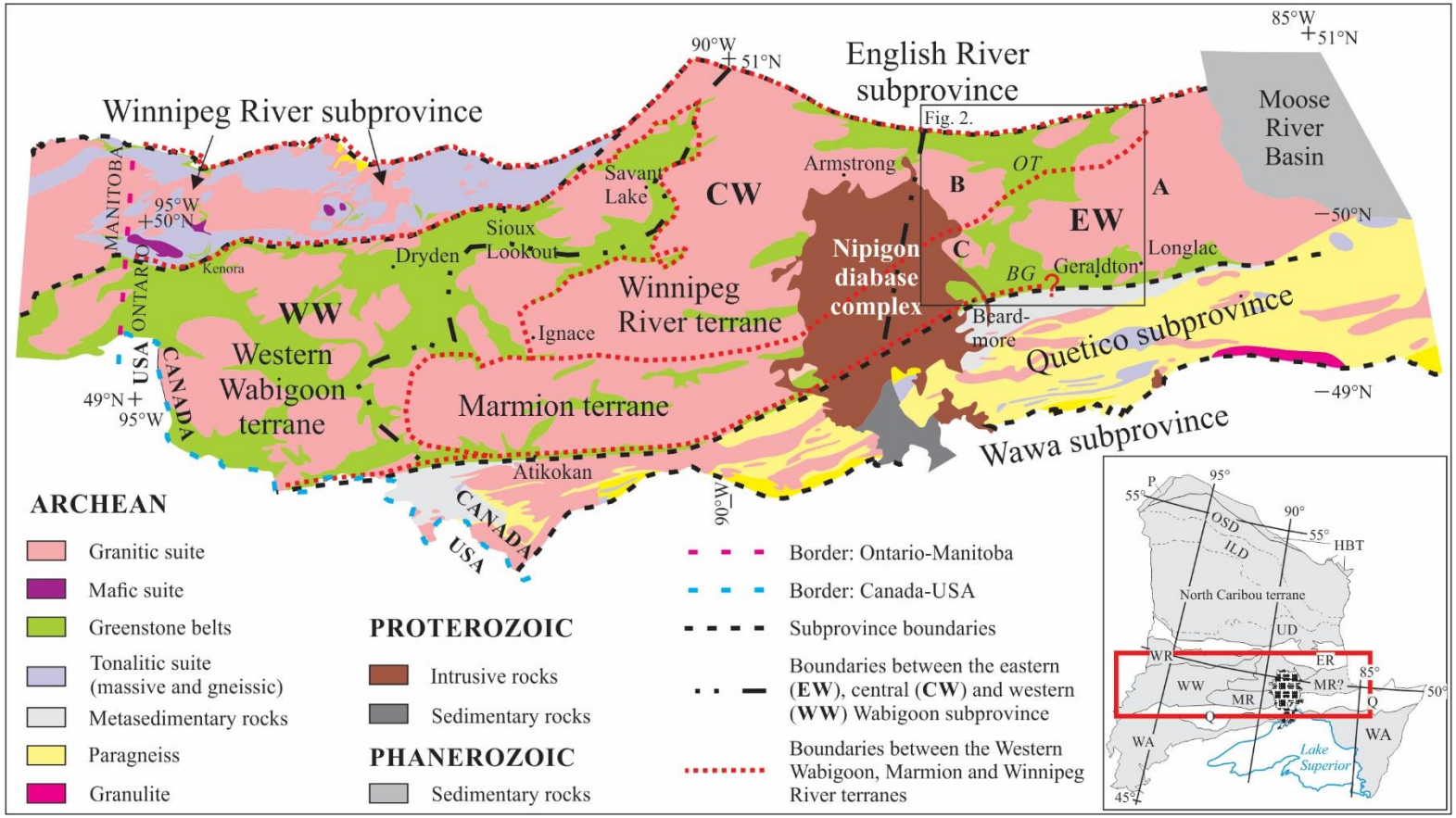

Figure 2-1 Regional geological maps of the Winnipeg River, Wabigoon and Quetico subprovinces showing the historical subdivision (WW: western Wabigoon subprovince; CW: central Wabigoon subprovince; EW: eastern Wabigoon subprovince) and the new subdivision (modified after Beakhouse, 1991; Blackburn et al., 1991; Sutcliffe, 1991; Williams, 1991; Morris, 1999; Tomlinson and Dickin, 2003; Tomlinson et al., 2004; Lu et al., 2013). Abbreviations: Greenstone belts: BG: Beardmore-Geraldton greenstone belt, OT: Onaman-Tashota greenstone belt, Plutons: **A**: Onaman Lake batholith, **B**: Ombabika batholith, **C**: North Wind pluton. The inset map shows the location of the BGB in the western Superior Province (after Percival et al., 2012). Abbreviations of terranes: ER: English River; HBT: Hudson Bay; MR: Marmion; P: Pikwitonei; Q: Quetico; WA: Wawa-Abitibi; WR: Winnipeg River; WW: Western Wabigoon; Domains of North Caribou terrane: ILD: Island Lake Domain; OSD: Oxford-Stull Domain; UD: Uchi Domain.

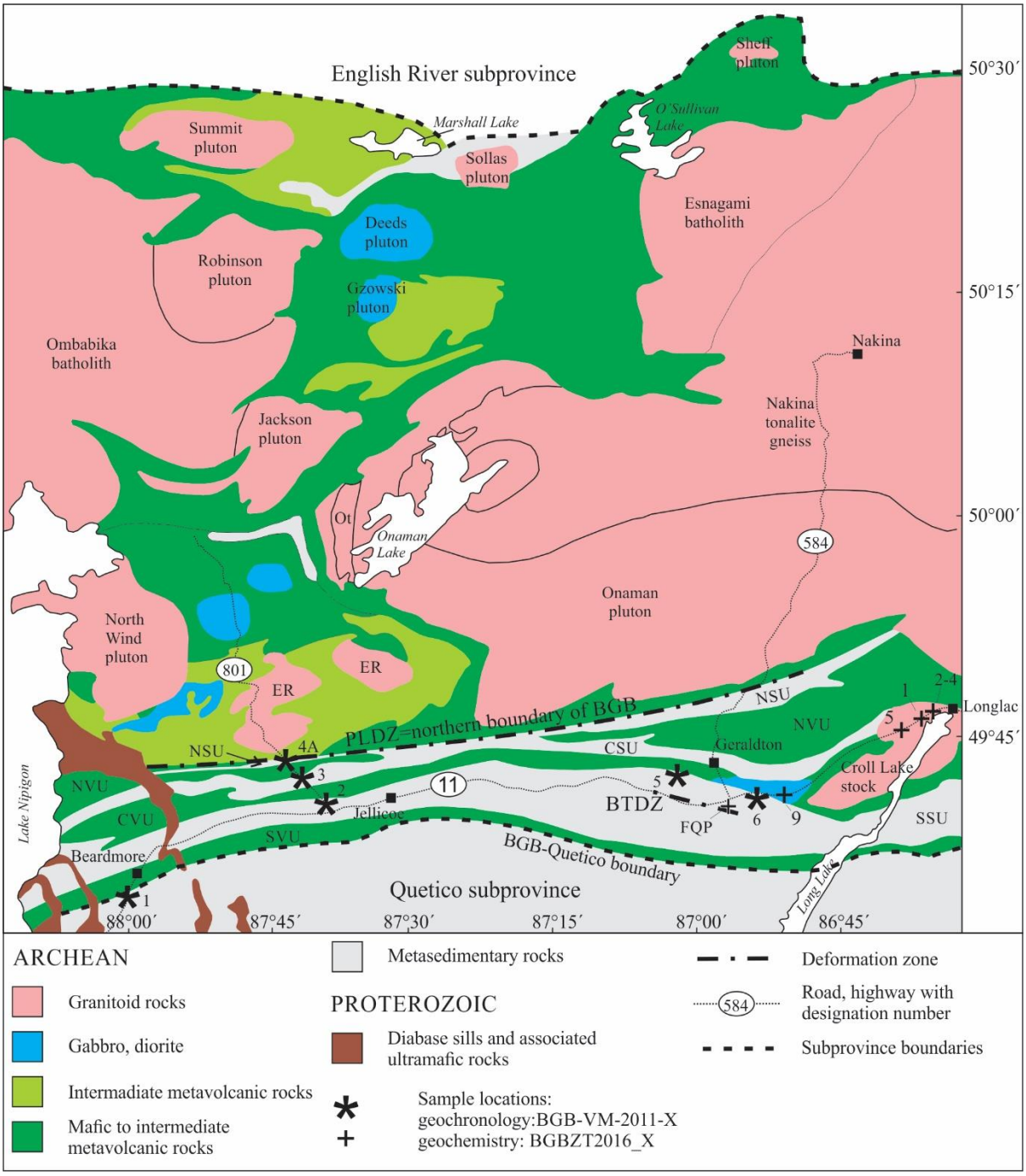

Figure 2-2. Regional geology of the Beardmore-Geraldton Belt and the eastern Wabigoon subprovince (modified after Blackburn et al., 1991; Stott et al., 2002; Lafrance et al., 2004). The map shows the location of the geochronology (*) and geochemistry (+) samples presented in this study. Abbreviations: NVU, CVU, SVU: northern, central and southern metavolcanic unit; NSU, CSU, SSU: northern, central and southern metasedimentary unit; Ot: Onaman tonalite, BTDZ: Bandfield-Tombill deformation zone; PLDZ: Paint Lake deformation zone, ER: Elmhirst-Rickaby complex.

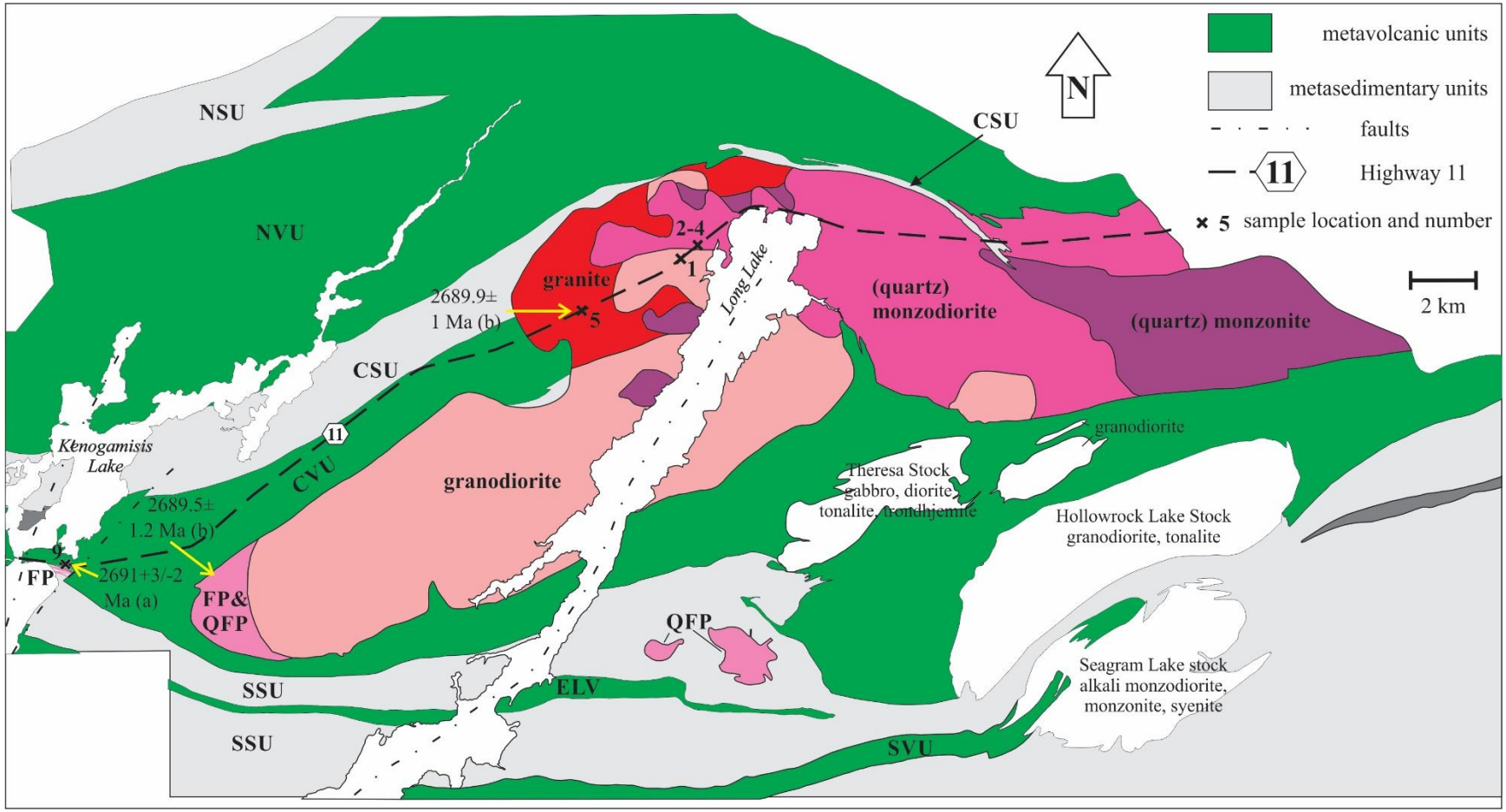

Figure 2-3. Geological map of the Croll Lake Stock (after Horwood and Pye, 1955; Macdonald, 1988; Kresz and Zayachivsky, 1991, 1993). The U-Pb ages are from a) Anglin (1987) and b) Corfu (2000).

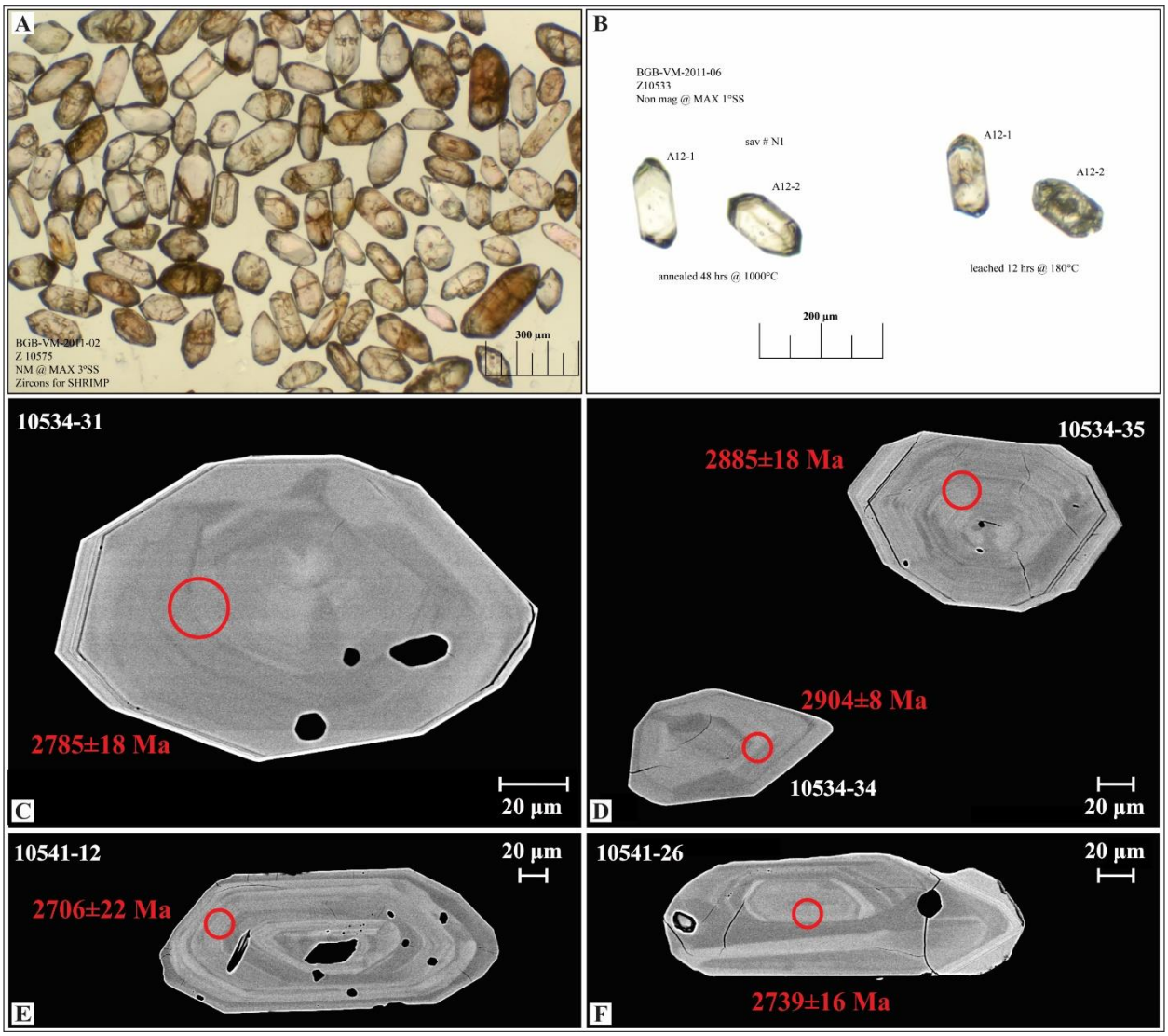

Figure 2-4. Representative examples of A) detrital zircons from the southern sedimentary unit under stereomicroscope; B) magmatic zircons from a quartz-feldspar porphyry in Geraldton following 12 hours leaching (right) and after 48 hours annealing (left). Back-scattered electron images with U-Pb ages of representative detrital zircon grains from the conglomerate of northern (C-D) and the conglomerate of southern sedimentary units (E-F). The errors indicated on the pictures represent 2 sigma error.

Figure 2-5. Field photographs of the dated metasedimentary units: A) NSU conglomerate; B) CSU sandstone; C) SSU sandstone; D) SSU conglomerate; E) Quetico siltstone.

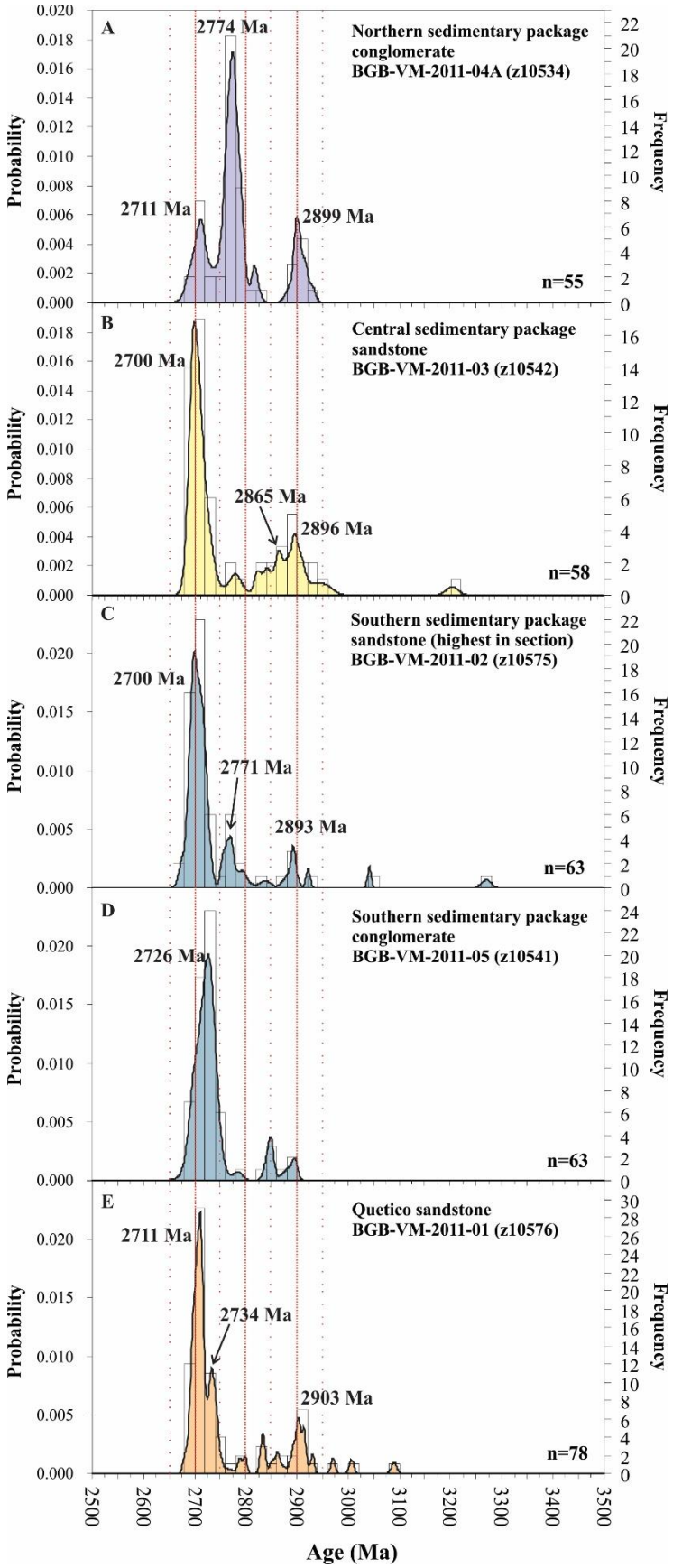

Figure 2-6. Cumulative probability diagram of detrital zircon ages from the A) NSU conglomerate; B) CSU sandstone; C) SSU sandstone; D) SSU conglomerate; E) northern Quetico subprovince siltstone.

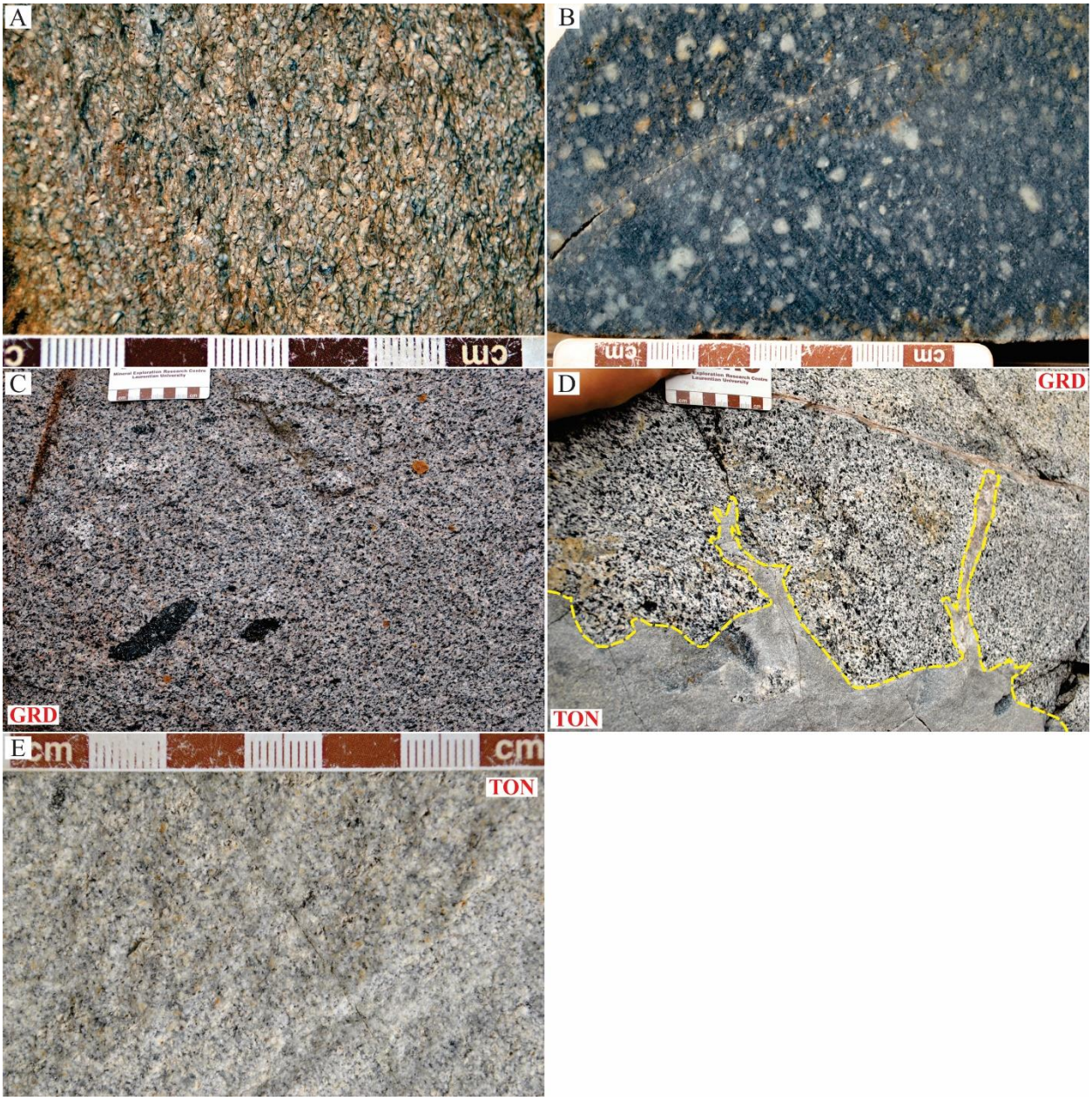

Figure 2-7. Petrography of intrusive rocks. Field photographs of A) feldspar-quartz porphyry; B) tonalitic feldspar porphyry; C) granodiorite; D) granodiorite (GRD) with tonalite dike (TON); E) close-up of tonalite dike shown on Fig. 7D).

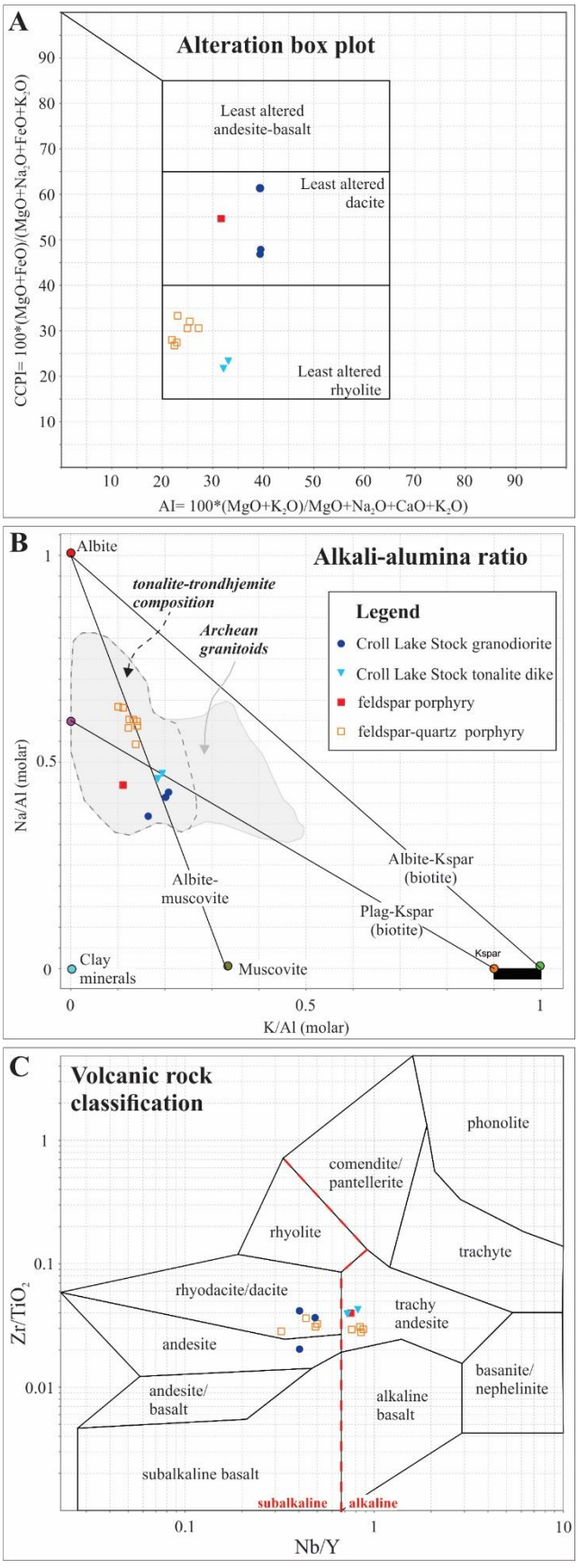

Figure 2-8. Geochemical plots of intrusive rocks. A) Chlorite Carbonate Pyrite Index (CCPI) vs. Alteration Index (AI) diagram (Large et al., 2001). B) Alkali-Alumina (Na/Al vs. K/Al) Molar Ratio diagram modified after Davies and Whitehead (2006). The Archean granitoid and tonalite-trondhjemite fields are taken from Davies and Whitehead (2006) and references therein; C) Volcanic rocks classification diagram after Winchester and Floyd (1977).

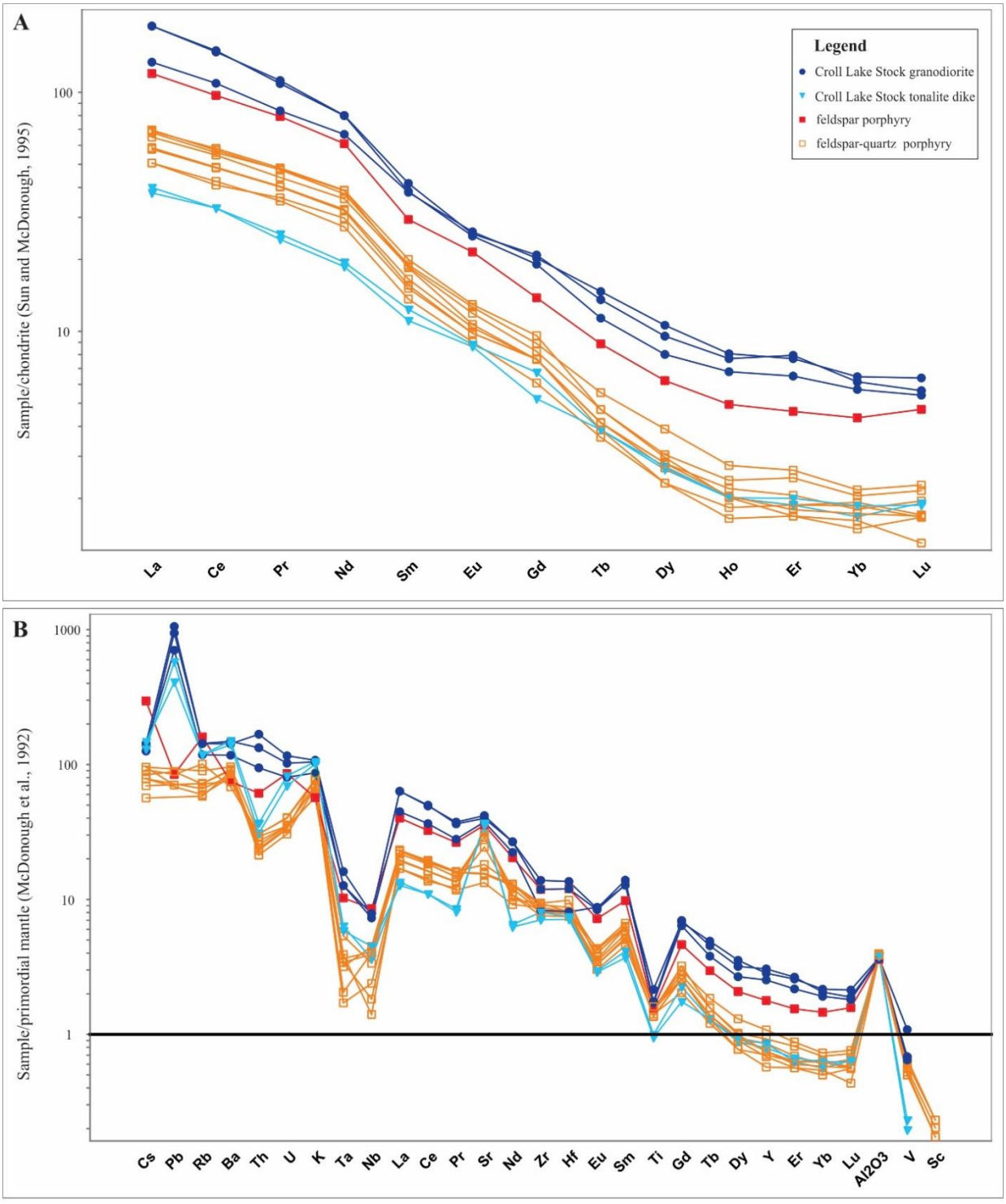

Figure 2-9. A) C1 chondrite-normalized rare earth element diagram using normalization values defined by McDonough and Sun (1995). B) Primordial mantle-normalized extended diagram. Normalization values are from McDonough and Frey (1989) and Rollinson (1993) and references therein.

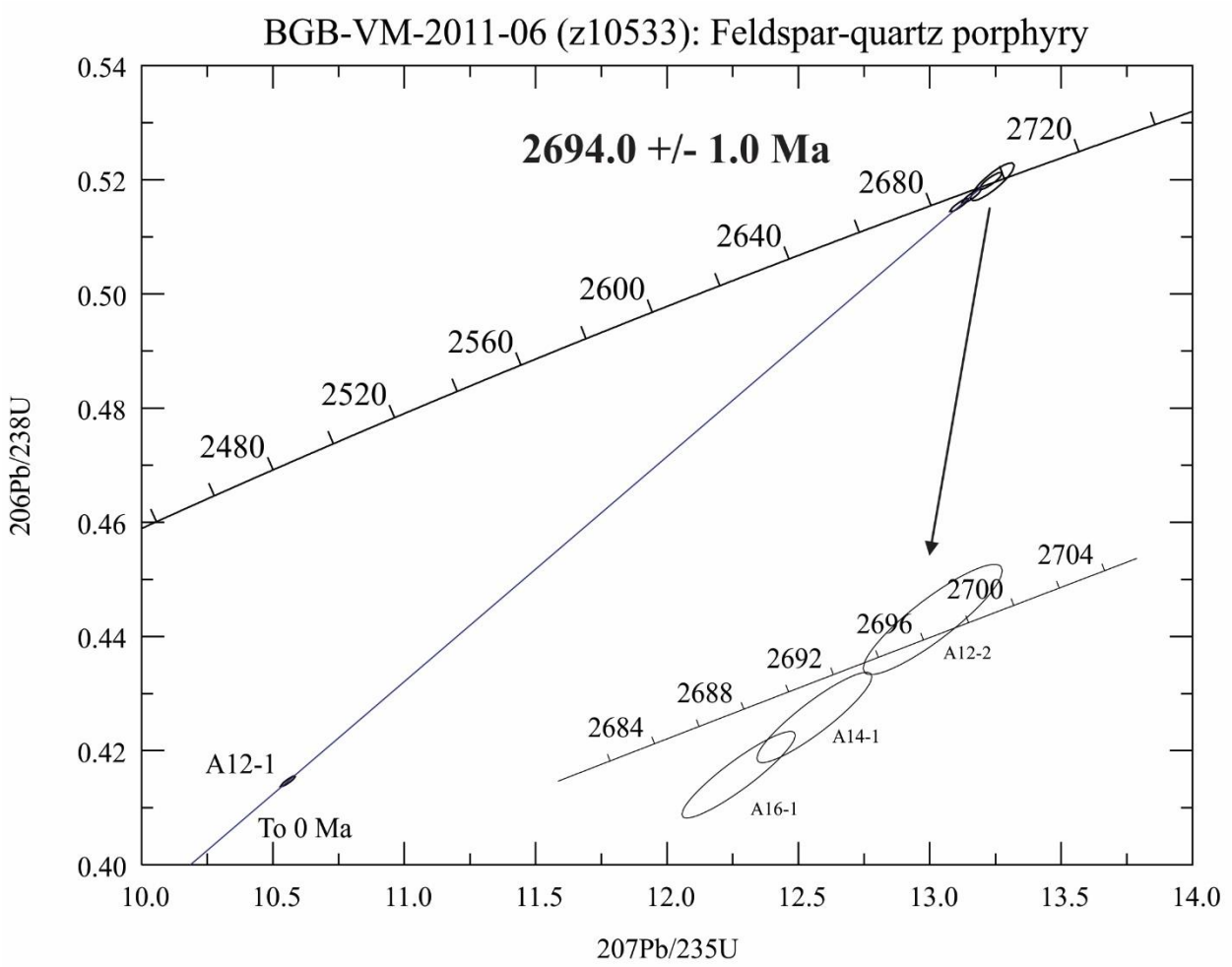

Figure 2-10. U-Pb concordia diagram of zircon analyses from feldspar-quartz porphyry, Porphyry hill, Geraldton.

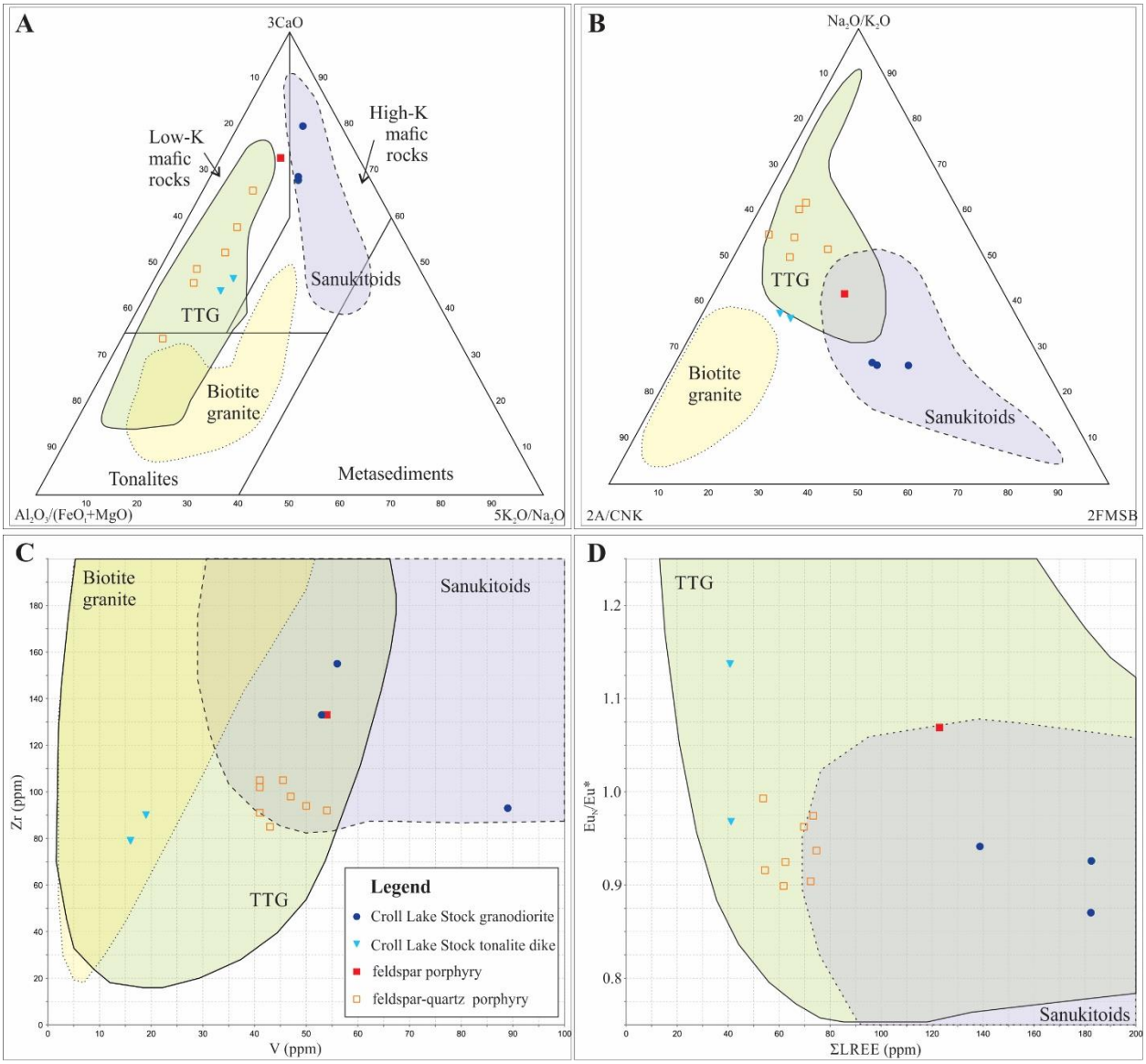

Figure 2-11. Discrimination diagrams for Archean granitoids (after Laurent et al., 2014 and references therein). A) Ternary diagram: $Al_2O_3/(FeO_t+MgO)$ vs. 3*CaO vs. 5*(Na_2O+K_2O); B) Ternary diagram: 2*A/CNK=2*$Al_2O_3/(CaO+Na_2O+K_2O)$ molar ratio vs. (Na_2O+K_2O) vs. 2*FMSB=2*(FeO_t+MgO)wt.% *(Sr+Ba)wt.%; C) Binary diagram: Zr (ppm) vs. V (ppm). D) Binary diagram: Eu_N/Eu^*=(Eu/0.087)/(sqrt((Sm/0.231)*(Gd/ 0.306))) (after Taylor and McLennan, 1985) vs. ΣLREE=La+Ce+Nd+Sm+Gd (ppm)

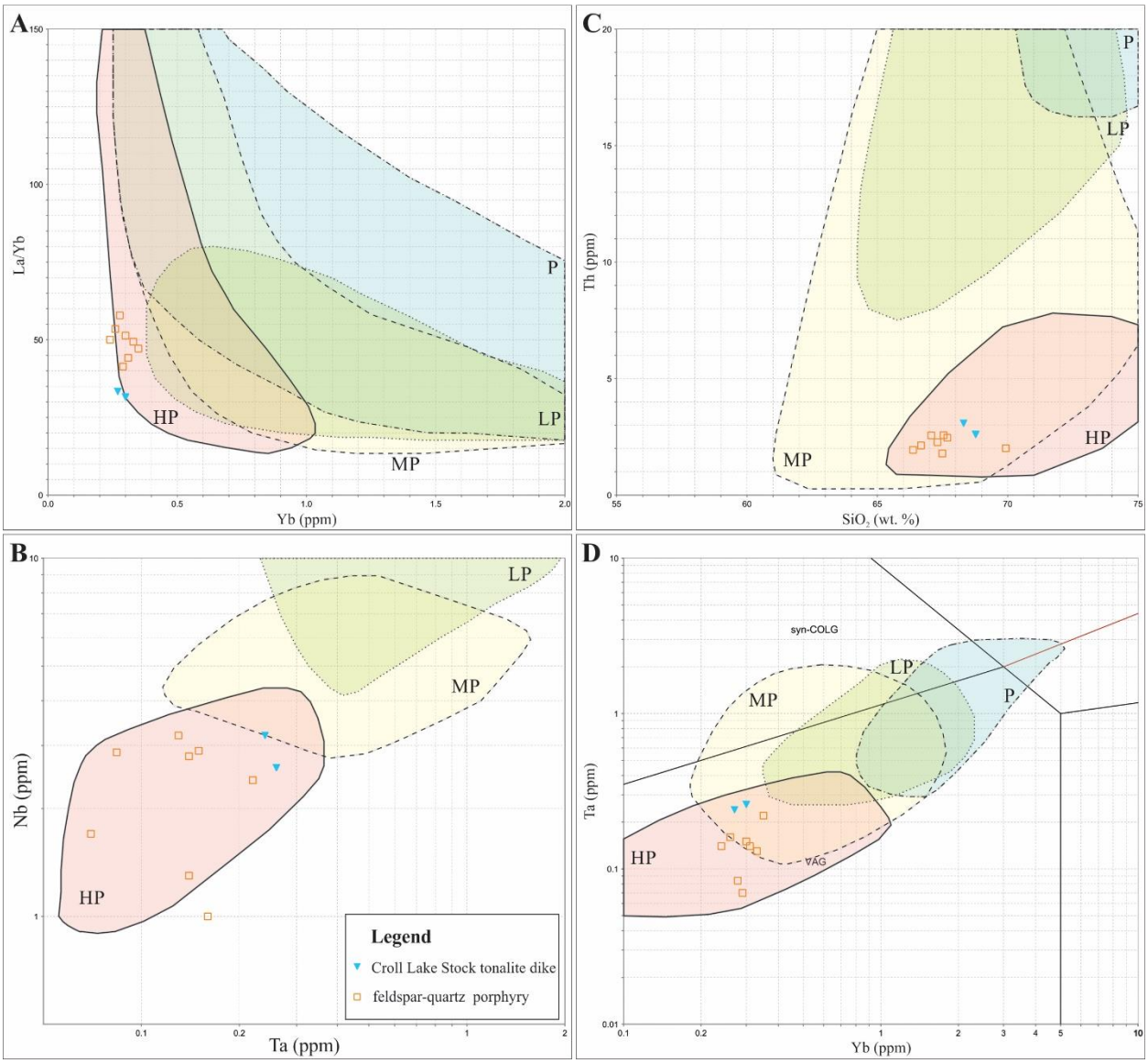

Figure 2-12. Discrimination diagrams for high- (HP), medium- (MP) and low-pressure (LP) and potassic (P) type TTGs after Moyen (2011). A) SiO_2 wt.% vs. Th (ppm); B) Yb (ppm) vs. La/Yb ratio; C) Yb (ppm) vs. Ta (ppm) (after Pearce et al., 1984); D) Ta (ppm) vs. Nb (ppm).

Tables

Table 2-1. Summary of the evolution of greenstone belts in the Eastern Goldfield Province, Abitibi subprovince and Beardmore-Geraldton district

	Beardmore-Geraldton greenstone belt	**Yilgarn craton**	**Abitibi greenstone belt**
Age of volcanism	2740-2720 Ma (Stott et al., 2002; Hart et al., 2002)	2720-2660 Ma	2710-2697 Ma (Ayer et al., 2002a)
Cessation of greenstone belt volcanism	NVU and CVU: ca. 2725 Ma (Hart et al., 2002)	Kalgoorlie: ≤ 2666 Ma (Kositcin et al., 2008)	Tisdale and Blake River assemblages: ca. 2696 Ma (Ayer et al., 2005)
Volcanic-sedimentary gap	**25 m.y.** from 2725 Ma to 2700 Ma	**ca. 11 m.y.** from ≤2666 Ma to <2655 Ma	**6 m.y.** from 2696 Ma to 2690 Ma
Major fault system	Bankfield-Tombill Fault (e.g. Horwood and Pye, 1955; Pye, 1952)	Boulder-Lefroy Fault (e.g. Bateman and Bierlein, 2007)	Destor-Porcupine Fault, Cadillac-Larder Lake Fault (e.g. Ayer et al., 2005; Robert et al., 2005)
Successor basin sedimentation	ca. 2700 Ma - 2694 Ma (this paper)	Kurrawang, Merougil and Jones Creek Seq.: <2655 Ma (Krapež et al., 2000)	Porcupine basin: 2690 - 2685 Ma; Timiskaming basin: 2676-2670 Ma (Ayer et al., 2005)
Sedimentation - porphyry gap	none	none	none
Porphyries	TTG Geraldton FQP 2694 Ma (this paper); sanukitoid Croll Lake Stock and feldspar porphyry: ca. 2690 Ma (Corfu, 2000; this paper)	from 2690 to 2650 Ma; less voluminous until 2600 Ma (Champion and Sheraton, 1997); alkaline magmatism 2650-2630 Ma (Smithies and Champion, 1999)	TTG suite: 2690 - 2670 Ma; sanukitoid suite: 2675 - 2665 Ma (Macdonald, 2010); alkaline plutons: 2685-2672 Ma (Corfu et al., 1989; Corfu, 1993; Wilkinson et al., 1999; Bateman et al., 2008)

Table 2-2. SHRIMP U-Pb detrital zircon results for the NSU conglomerate, CSU sandstone, SSU conglomerate, SSU and Quetico sandstones.

																	Apparent Ages (Ma)				
Spot name	**U (ppm)**	**Th (ppm)**	**Th/U**	**^{206}Pb* (ppm)**	**^{204}Pb/^{206}Pb**	**% ±**	**f(206)^{204} %**	**^{208*}Pb/^{206*}Pb**	**% ±**	**^{207*}Pb/^{235}U**	**% ±**	**^{206*}Pb/^{238}U**	**% ±**	**Corr Coeff**	**^{207*}Pb/^{206*}Pb**	**% ±**	**^{206}Pb/^{238}U**	**±^{206}Pb/^{238}U**	**^{207}Pb/^{206}Pb**	**±^{207}Pb/^{206}Pb**	**Disc. (%)**
Northern Sedimentary unit: polymictic conglomerate UTM NAD 83, zone 16, 446975E, 5507972N																					
10534-87.1	161	142	0.91	71	2.5E-5	35	0.044	0.255	1.9	13.0	1.35	0.514	1.3	0.928	0.184	0.5	2672	27	2689	8	0.8
10534-57.1	107	67	0.64	46	2.1E-5	37	0.037	0.174	3.0	12.8	1.52	0.501	1.4	0.913	0.185	0.6	2619	30	2699	10	3.6
10534-65.1	131	111	0.87	58	-9.9E-6	156	-0.017	0.250	1.5	13.2	1.29	0.517	1.2	0.949	0.186	0.4	2687	27	2705	7	0.8
10534-14.1	43	18	0.42	19	1.9E-4	45	0.332	0.125	4.9	13.3	1.76	0.519	1.4	0.796	0.186	1.1	2693	31	2707	18	0.6
10534-53.1	33	25	0.77	15	-7.6E-5	147	-0.132	0.211	3.7	13.5	1.79	0.525	1.4	0.777	0.186	1.1	2720	31	2709	19	-0.5
10534-26.1	134	67	0.52	60	4.0E-5	79	0.070	0.145	2.1	13.6	1.32	0.527	1.2	0.936	0.187	0.5	2729	27	2712	8	-0.8
10534-66.1	168	112	0.69	76	-5.5E-6	137	-0.009	0.195	1.5	13.5	1.29	0.523	1.2	0.964	0.187	0.3	2711	27	2715	6	0.1
10534-59.1	30	11	0.37	14	-6.5E-5	34	-0.112	0.113	7.0	14.3	2.16	0.555	1.8	0.839	0.187	1.2	2844	42	2715	19	-5.9
10534-63.1	51	25	0.50	23	5.0E-4	26	0.863	0.123	4.1	13.5	1.79	0.523	1.4	0.760	0.187	1.2	2711	30	2717	19	0.3
10534-3.1	68	56	0.86	33	3.6E-4	19	0.619	0.242	2.3	14.5	1.54	0.563	1.3	0.878	0.187	0.7	2878	31	2718	12	-7.3
10534-10.1	35	17	0.49	16	3.6E-4	26	0.630	0.135	4.0	14.0	1.69	0.537	1.4	0.803	0.189	1.0	2770	31	2731	17	-1.7
10534-18.1	56	18	0.32	26	1.8E-4	30	0.313	0.086	4.0	14.0	1.76	0.538	1.4	0.779	0.189	1.1	2776	31	2733	18	-1.9
10534-11.1	23	32	1.42	11	-1.5E-4	55	-0.265	0.401	3.6	14.0	1.96	0.533	1.5	0.775	0.190	1.2	2753	34	2742	20	-0.5
10534-64.1	43	54	1.30	19	1.6E-4	27	0.281	0.365	2.2	13.9	1.50	0.525	1.3	0.872	0.191	0.7	2721	29	2755	12	1.5
10534-22.1	146	113	0.80	67	2.5E-5	88	0.043	0.235	1.9	14.1	1.34	0.531	1.2	0.932	0.192	0.5	2745	28	2760	8	0.7
10534-49.1	116	69	0.61	54	3.4E-5	40	0.058	0.169	1.9	14.3	1.30	0.541	1.2	0.949	0.192	0.4	2786	28	2761	7	-1.1
10534-101.1	157	114	0.75	70	8.6E-5	40	0.149	0.207	1.7	13.8	1.34	0.522	1.3	0.942	0.192	0.5	2707	28	2762	7	2.4
10534-13.1	79	29	0.38	35	2.5E-4	25	0.431	0.099	3.6	13.8	1.47	0.521	1.3	0.869	0.192	0.7	2705	28	2763	12	2.6
10534-60.1	146	105	0.74	68	-2.3E-5	44	-0.040	0.210	1.6	14.4	1.28	0.540	1.2	0.954	0.193	0.4	2784	28	2766	6	-0.8
10534-80.1	54	25	0.48	25	1.2E-4	51	0.208	0.133	4.2	14.4	1.66	0.541	1.4	0.855	0.193	0.9	2786	32	2767	14	-0.8
10534-74.1	59	26	0.46	27	1.3E-4	33	0.222	0.124	3.3	14.3	1.47	0.537	1.3	0.897	0.193	0.6	2772	30	2768	11	-0.1
10534-41.1	109	87	0.83	48	-1.4E-5	171	-0.025	0.234	2.0	13.7	1.48	0.516	1.4	0.939	0.193	0.5	2684	30	2768	8	3.7
10534-56.1	95	51	0.56	43	4.4E-5	24	0.077	0.153	2.3	14.0	1.35	0.526	1.3	0.937	0.193	0.5	2726	28	2769	8	1.9
10534-23.1	68	53	0.80	32	1.6E-5	136	0.028	0.228	2.4	14.3	1.40	0.536	1.3	0.909	0.193	0.6	2766	29	2769	10	0.2
10534-36.1	92	50	0.57	43	6.4E-6	639	0.011	0.156	2.3	14.4	1.36	0.540	1.2	0.920	0.193	0.5	2784	28	2771	9	-0.6
10534-78.1	116	62	0.55	54	4.5E-5	17	0.079	0.150	2.2	14.6	1.35	0.546	1.3	0.944	0.193	0.4	2809	29	2771	7	-1.7

Table 2-2. SHRIMP U-Pb detrital zircon results for the NSU conglomerate, CSU sandstone, SSU conglomerate, SSU and Quetico sandstones (cont'd)

																Apparent Ages (Ma)				
Spot name	**U (ppm)**	**Th (ppm)**	**Th/U**	**^{206}Pb* (ppm)**	**^{204}Pb/^{206}Pb**	**% ±**	**f(206)^{204} %**	**^{208*}Pb/^{206*}Pb**	**% ±**	**^{207*}Pb/^{235}U**	**% ±**	**^{206*}Pb/^{238}U**	**% ±**	**Corr Coeff**	**^{207*}Pb/^{206*}Pb**	**% ±**	**^{206}Pb/^{238}U**	**±^{206}Pb/^{238}U**	**^{207}Pb/^{206}Pb**	**±^{207}Pb/^{206}Pb**	**Disc. (%)**
10534-29.1	229	180	0.81	107	4.0E-6	1	0.007	0.231	1.3	14.5	1.27	0.543	1.2	0.971	0.194	0.3	2796	28	2775	5	-1.0
10534-39.1	269	225	0.86	126	2.9E-5	34	0.050	0.243	1.3	14.6	1.28	0.547	1.2	0.964	0.194	0.3	2812	28	2775	6	-1.7
10534-55.1	107	61	0.58	49	2.4E-5	69	0.041	0.162	2.2	14.2	1.32	0.531	1.2	0.938	0.194	0.5	2747	28	2776	7	1.3
10534-30.1	233	214	0.95	109	2.6E-5	37	0.045	0.268	1.2	14.5	1.25	0.543	1.2	0.969	0.194	0.3	2795	27	2778	5	-0.7
10534-1.1	70	42	0.62	32	4.2E-5	110	0.072	0.178	2.6	14.4	1.42	0.539	1.3	0.898	0.194	0.6	2781	29	2778	10	-0.1
10534-107.1	118	81	0.71	52	6.2E-5	79	0.107	0.194	2.3	13.7	1.44	0.513	1.3	0.912	0.194	0.6	2669	29	2779	10	4.8
10534-61.1	43	23	0.55	20	-1.1E-4	63	-0.189	0.168	3.2	14.2	1.60	0.529	1.4	0.874	0.194	0.8	2737	31	2779	13	1.8
10534-46.1	74	52	0.73	35	1.5E-5	320	0.026	0.203	2.3	14.8	1.42	0.550	1.3	0.907	0.194	0.6	2827	30	2780	10	-2.1
10534-67.1	157	102	0.67	74	4.6E-5	36	0.079	0.180	1.9	14.8	5.73	0.551	5.5	0.962	0.195	1.6	2831	126	2784	26	-2.1
10534-108.1	118	86	0.75	51	8.0E-5	50	0.138	0.215	1.9	13.5	1.55	0.503	1.3	0.827	0.195	0.9	2625	28	2784	14	6.9
10534-31.1	93	48	0.54	43	-1.7E-5	91	-0.030	0.149	2.8	14.6	1.38	0.544	1.3	0.920	0.195	0.5	2802	29	2785	9	-0.7
10534-83.1	119	63	0.55	54	9.3E-5	28	0.162	0.152	2.1	14.2	1.33	0.528	1.3	0.941	0.195	0.5	2735	28	2786	7	2.3
10534-28.1	91	55	0.63	42	-5.9E-6	911	-0.010	0.172	2.7	14.6	1.43	0.541	1.3	0.890	0.195	0.7	2786	29	2788	11	0.1
10534-98.1	186	74	0.41	81	7.2E-5	36	0.124	0.105	2.7	13.6	1.32	0.506	1.2	0.936	0.196	0.5	2639	27	2789	8	6.6
10534-62.1	97	60	0.64	45	4.6E-5	28	0.080	0.173	2.5	14.6	1.44	0.540	1.3	0.931	0.196	0.5	2783	30	2789	9	0.3
10534-73.1	160	147	0.95	71	-3.3E-5	14	-0.057	0.277	1.5	14.0	1.35	0.518	1.3	0.958	0.196	0.4	2690	28	2790	6	4.4
10534-54.1	461	210	0.47	220	3.3E-5	30	0.058	0.130	1.5	15.2	1.24	0.555	1.2	0.973	0.199	0.3	2846	28	2816	5	-1.3
10534-40.1	129	47	0.38	61	5.0E-5	31	0.086	0.105	2.4	15.2	1.29	0.551	1.2	0.950	0.199	0.4	2831	28	2822	7	-0.4
10534-35.1	99	51	0.54	47	7.0E-5	40	0.121	0.147	2.7	15.9	1.37	0.557	1.3	0.922	0.207	0.5	2854	29	2885	9	1.4
10534-25.1	164	32	0.20	78	1.9E-5	174	0.033	0.056	2.9	16.0	1.37	0.554	1.3	0.958	0.209	0.4	2843	30	2897	6	2.3
10534-6.1	561	253	0.47	283	1.4E-5	34	0.024	0.132	1.1	17.0	1.24	0.588	1.2	0.987	0.209	0.2	2983	29	2898	3	-3.7
10534-42.1	72	29	0.42	36	1.1E-4	26	0.195	0.120	2.9	16.7	1.43	0.576	1.3	0.927	0.210	0.5	2933	31	2903	9	-1.3
10534-34.1	402	241	0.62	196	-6.8E-6	44	-0.012	0.172	1.1	16.4	1.22	0.567	1.2	0.982	0.210	0.2	2896	28	2904	4	0.3
10534-24.1	60	17	0.30	28	-2.4E-5	51	-0.041	0.085	3.9	15.8	2.13	0.544	2.1	0.965	0.210	0.6	2802	47	2906	9	4.4
10534-58.1	164	85	0.54	76	1.4E-4	37	0.247	0.145	2.0	15.6	1.34	0.538	1.2	0.930	0.210	0.5	2774	28	2908	8	5.7
10534-21.1	242	164	0.70	121	-3.3E-6	333	-0.006	0.197	1.3	16.9	1.24	0.581	1.2	0.973	0.211	0.3	2954	29	2917	5	-1.6
10534-16.1	117	75	0.66	57	3.5E-5	21	0.061	0.183	1.9	16.6	1.32	0.565	1.3	0.951	0.213	0.4	2889	29	2929	7	1.7

Grain mount IP616; spot size 13µm x 16µm; # of scans = 6; Error in 206Pb/238U calibration = 1.2%

Table 2-2. SHRIMP U-Pb detrital zircon results for the NSU conglomerate, CSU sandstone, SSU conglomerate, SSU and Quetico sandstones (cont'd)

																Apparent Ages (Ma)				
Spot name	**U (ppm)**	**Th (ppm)**	**Th/U**	**^{206}Pb* (ppm)**	**^{204}Pb/^{206}Pb**	**% ±**	**f(206)^{204} %**	**^{208*}Pb/^{206*}Pb**	**% ±**	**^{207*}Pb/^{235}U**	**% ±**	**^{206*}Pb/^{238}U**	**% ±**	**Corr Coeff**	**^{207*}Pb/^{206*}Pb**	**% ±**	**^{206}Pb/^{238}U**	**±^{206}Pb/^{238}U**	**^{207}Pb/^{206}Pb**	**±^{207}Pb/^{206}Pb**	**Disc. (%)**
Central Sedimentary Unit: sandstone UTM NAD 83, zone 16, 449008E, 5505677N																					
10542-56.1	120	71	0.61	52	5.9E-4	23	1.018	0.158	3.4	12.51	2.52	0.505	2.1	0.824	0.1796	1.4	2635	45	*2650*	*24*	0.7
10542-39.2	130	79	0.63	56	8.1E-4	13	1.405	0.159	2.7	12.66	1.88	0.504	1.6	0.874	0.1821	0.9	2631	35	*2672*	*15*	1.8
10542-52.1	61	35	0.59	26	3.9E-4	32	0.681	0.160	3.6	12.59	2.07	0.500	1.7	0.840	0.1826	1.1	2615	37	*2676*	*19*	2.8
10542-39.3	183	106	0.60	79	1.6E-4	26	0.271	0.168	2.4	12.78	1.87	0.505	1.8	0.957	0.1835	0.5	2636	39	*2685*	*9*	2.2
10542-39.1	155	87	0.58	66	1.4E-5	33	0.024	0.159	2.3	12.51	1.90	0.494	1.9	0.973	0.1837	0.4	2587	39	*2687*	*7*	4.5
10542-70.1	164	123	0.78	73	4.2E-5	32	0.072	0.220	1.8	13.09	1.66	0.516	1.6	0.968	0.1839	0.4	2683	35	2689	7	0.3
10542-43.1	414	225	0.56	184	4.1E-5	27	0.070	0.158	1.4	13.17	1.66	0.519	1.6	0.979	0.1841	0.3	2695	36	2690	6	-0.2
10542-8.1	64	38	0.61	29	8.9E-5	34	0.154	0.179	3.2	13.54	1.79	0.533	1.7	0.927	0.1843	0.7	2754	37	*2692*	*11*	-2.8
10542-39.1.2	146	80	0.56	67	4.6E-6	841	0.008	0.159	2.3	13.67	1.68	0.538	1.6	0.956	0.1843	0.5	2775	36	*2692*	*8*	-3.8
10542-39.3_A	294	189	0.66	125	2.6E-4	22	0.442	0.180	2.3	12.62	1.75	0.497	1.6	0.939	0.1843	0.6	2599	35	*2692*	*10*	4.2
10542-37.1	113	60	0.55	52	6.5E-5	40	0.113	0.156	2.6	13.58	1.90	0.534	1.8	0.963	0.1844	0.5	2758	41	2693	8	-3.0
10542-47.1	149	107	0.74	68	9.2E-5	31	0.160	0.201	2.0	13.53	1.67	0.532	1.6	0.962	0.1845	0.5	2749	36	2693	8	-2.5
10542-8.4	124	125	1.04	56	9.3E-5	42	0.162	0.293	1.8	13.38	2.86	0.526	2.5	0.877	0.1846	1.4	2724	56	*2694*	*23*	-1.3
10542-133.1	125	72	0.59	53	-7.0E-6	779	-0.012	0.168	2.6	12.58	1.73	0.494	1.6	0.937	0.1846	0.6	2589	35	2694	10	4.7
10542-56.4	83	50	0.62	38	8.7E-5	32	0.151	0.183	2.2	13.68	1.87	0.537	1.8	0.966	0.1846	0.5	2772	41	*2695*	*8*	-3.5
10542-40.1	256	198	0.80	115	1.6E-4	19	0.274	0.227	1.5	13.26	1.64	0.521	1.6	0.971	0.1846	0.4	2703	35	2695	6	-0.4
10542-56.5	106	61	0.60	49	3.3E-5	34	0.058	0.159	2.9	13.61	1.74	0.534	1.7	0.952	0.1847	0.5	2760	37	*2695*	*9*	-3.0
10542-51.1	78	31	0.41	36	1.3E-4	35	0.228	0.117	4.1	13.63	1.83	0.535	1.7	0.915	0.1847	0.7	2763	38	2696	12	-3.0
10542-14.1	83	26	0.32	38	1.4E-4	33	0.236	0.085	4.0	13.54	1.76	0.532	1.6	0.932	0.1848	0.6	2748	37	2697	11	-2.3
10542-57.1	334	207	0.64	149	1.9E-5	86	0.033	0.180	1.2	13.20	1.60	0.518	1.6	0.987	0.1848	0.3	2690	35	2697	4	0.3
10542-16.1	98	58	0.61	43	4.2E-5	34	0.073	0.179	2.8	12.90	1.74	0.506	1.6	0.947	0.1850	0.6	2639	36	2698	9	2.7
10542-3.1	88	45	0.53	39	4.3E-5	85	0.075	0.144	4.7	13.33	1.75	0.522	1.6	0.937	0.1850	0.6	2709	36	2698	10	-0.5
10542-21.1	286	185	0.67	125	3.4E-5	60	0.058	0.185	1.6	12.95	1.69	0.508	1.7	0.980	0.1850	0.3	2647	36	2698	6	2.3
10542-67.1	154	127	0.85	71	1.1E-5	76	0.019	0.249	1.9	13.70	1.68	0.537	1.6	0.962	0.1850	0.5	2770	36	2699	8	-3.3
10542-15.1	94	51	0.56	43	1.6E-4	30	0.278	0.162	2.7	13.59	1.83	0.532	1.7	0.943	0.1852	0.6	2750	39	2700	10	-2.3
10542-36.1	65	42	0.66	28	1.4E-4	31	0.239	0.184	2.9	12.94	2.01	0.506	1.9	0.944	0.1852	0.7	2642	41	2700	11	2.6

Table 2-2. SHRIMP U-Pb detrital zircon results for the NSU conglomerate, CSU sandstone, SSU conglomerate, SSU and Quetico sandstones (cont'd)

																Apparent Ages (Ma)				
Spot name	**U (ppm)**	**Th (ppm)**	**Th/U**	**^{206}Pb* (ppm)**	**^{204}Pb/^{206}Pb**	**% ±**	**f(206)^{204} %**	**^{208*}Pb/^{206*}Pb**	**% ±**	**^{207*}Pb/^{235}U**	**% ±**	**^{206*}Pb/^{238}U**	**% ±**	**Corr Coeff**	**^{207*}Pb/^{206*}Pb**	**% ±**	**^{206}Pb/^{238}U**	**±^{206}Pb/^{238}U**	**^{207}Pb/^{206}Pb**	**±^{207}Pb/^{206}Pb**	**Disc. (%)**
10542-39.2.2	161	96	0.62	69	1.1E-4	74	0.185	0.173	2.7	12.86	1.93	0.504	1.8	0.922	0.1853	0.7	2629	38	*2701*	*12*	3.2
10542-52.3	91	75	0.86	38	4.6E-5	27	0.080	0.239	2.6	12.44	1.76	0.487	1.7	0.942	0.1853	0.6	2558	35	*2701*	*10*	6.4
10542-136.1	115	62	0.56	52	3.4E-5	55	0.059	0.158	2.6	13.39	1.70	0.523	1.6	0.956	0.1856	0.5	2714	36	2703	8	-0.5
10542-52.2	80	60	0.78	32	9.1E-5	24	0.157	0.220	2.8	12.11	1.78	0.473	1.7	0.936	0.1856	0.6	2498	34	2703	*10*	9.2
10542-33.1	181	135	0.77	78	7.7E-6	87	0.013	0.208	1.8	12.79	1.68	0.500	1.6	0.973	0.1857	0.4	2613	35	2704	6	4.1
10542-39.4	181	133	0.76	85	9.1E-5	36	0.158	0.221	1.8	14.04	1.66	0.548	1.6	0.963	0.1858	0.5	2817	37	2706	*7*	-5.1
10542-50.1	212	210	1.03	94	4.1E-5	26	0.071	0.284	1.4	13.30	1.64	0.519	1.6	0.975	0.1859	0.4	2694	35	2706	6	0.5
10542-30.1	83	52	0.65	35	2.9E-5	324	0.050	0.175	3.0	12.70	1.85	0.495	1.6	0.888	0.1860	0.9	2593	35	2707	14	5.1
10542-52.2.2	94	79	0.87	41	---	100	0.000	0.251	3.0	12.89	1.81	0.502	1.7	0.927	0.1861	0.7	2624	36	2708	*11*	3.8
10542-41.1	107	79	0.77	47	1.0E-4	30	0.177	0.205	2.2	13.27	1.72	0.517	1.6	0.954	0.1861	0.5	2687	36	2708	9	0.9
10542-56.2	86	47	0.57	39	2.8E-5	177	0.049	0.169	2.3	13.67	1.71	0.532	1.6	0.945	0.1863	0.6	2752	36	2709	*9*	-1.9
10542-39.3.2	191	111	0.60	83	8.5E-5	29	0.148	0.164	2.3	12.92	1.74	0.502	1.7	0.963	0.1864	0.5	2624	36	2711	*8*	3.9
10542-39.2_A	280	191	0.71	120	1.1E-4	22	0.199	0.190	1.8	12.81	1.65	0.498	1.6	0.969	0.1864	0.4	2606	34	2711	*7*	4.7
10542-28.1	272	218	0.83	123	8.8E-5	27	0.152	0.235	1.3	13.60	1.62	0.529	1.6	0.978	0.1865	0.3	2736	35	2712	6	-1.1
10542-75.1	100	48	0.49	44	6.4E-5	38	0.110	0.144	2.7	13.06	1.69	0.507	1.6	0.955	0.1867	0.5	2646	35	2713	8	3.0
10542-19.1	169	174	1.06	76	2.7E-5	67	0.048	0.308	1.5	13.45	1.65	0.522	1.6	0.969	0.1870	0.4	2706	35	2716	7	0.5
10542-72.1	71	27	0.40	32	1.5E-5	2	0.026	0.114	3.5	13.44	1.72	0.521	1.6	0.949	0.1870	0.5	2704	36	2716	9	0.5
10542-35.1	83	42	0.53	37	3.8E-5	29	0.066	0.153	3.0	13.53	1.73	0.524	1.6	0.946	0.1872	0.6	2718	36	2718	9	0.0
10542-52.1.2	68	44	0.66	29	-2.1E-5	64	-0.037	0.177	3.1	12.91	2.04	0.500	1.9	0.955	0.1872	0.6	2614	42	2718	*10*	4.6
10542-4.1	134	80	0.62	59	1.8E-5	75	0.031	0.173	2.3	13.36	1.76	0.517	1.6	0.918	0.1873	0.7	2688	35	2718	11	1.4
10542-22.1	156	93	0.61	70	2.4E-3	5	4.237	0.168	1.7	13.57	1.91	0.525	1.6	0.860	0.1876	1.0	2718	36	2721	16	0.1
10542-8.2	88	54	0.63	41	4.4E-5	91	0.076	0.183	3.3	13.81	1.81	0.534	1.7	0.929	0.1877	0.7	2757	38	2722	*11*	-1.6
10542-66.1	108	37	0.36	48	1.0E-4	43	0.178	0.098	3.0	13.33	1.87	0.514	1.8	0.959	0.1879	0.5	2675	39	2724	9	2.2
10542-56.3	109	63	0.60	48	2.5E-5	146	0.044	0.179	2.0	13.31	1.67	0.514	1.6	0.960	0.1879	0.5	2673	35	2724	*8*	2.3
10542-68.1	136	83	0.63	58	2.8E-5	42	0.048	0.160	4.0	12.82	2.02	0.495	1.9	0.934	0.1880	0.7	2591	40	2725	12	6.0
10542-73.1	77	50	0.68	33	2.9E-4	45	0.509	0.188	3.2	13.01	2.00	0.502	1.7	0.835	0.1881	1.1	2621	36	2725	18	4.7
10542-46.1	138	71	0.53	62	1.7E-4	37	0.289	0.153	2.2	13.47	1.89	0.519	1.8	0.952	0.1883	0.6	2694	40	2727	10	1.5
10542-26.1	77	38	0.52	36	---	100	0.000	0.139	3.2	14.07	1.73	0.540	1.6	0.949	0.1891	0.5	2782	37	2734	9	-2.1

Table 2-2. SHRIMP U-Pb detrital zircon results for the NSU conglomerate, CSU sandstone, SSU conglomerate, SSU and Quetico sandstones (cont'd)

																Apparent Ages (Ma)				
Spot name	**U (ppm)**	**Th (ppm)**	**Th/U**	**^{206}Pb* (ppm)**	**^{204}Pb/^{206}Pb**	**% ±**	**f(206)^{204} %**	**^{208*}Pb/^{206*}Pb**	**% ±**	**^{207*}Pb/^{235}U**	**% ±**	**^{206*}Pb/^{238}U**	**% ±**	**Corr Coeff**	**^{207*}Pb/^{206*}Pb**	**% ±**	**^{206}Pb/^{238}U**	**±^{206}Pb/^{238}U**	**^{207}Pb/^{206}Pb**	**±^{207}Pb/^{206}Pb**	**Disc. (%)**
10542-7.1	40	13	0.33	18	3.3E-4	31	0.576	0.089	5.8	13.86	2.05	0.518	1.7	0.848	0.1940	1.1	2691	38	2777	18	3.8
10542-29.1	51	21	0.42	24	1.4E-4	126	0.236	0.107	4.5	14.73	2.18	0.550	1.8	0.807	0.1943	1.3	2824	40	2779	21	-2.0
10542-20.1	92	79	0.89	41	1.1E-4	17	0.185	0.244	2.4	13.83	1.73	0.516	1.6	0.948	0.1945	0.6	2681	36	2780	9	4.3
10542-25.1	203	24	0.12	95	1.6E-5	28	0.027	0.035	4.0	14.95	1.70	0.543	1.7	0.979	0.1995	0.3	2798	38	2822	6	1.1
10542-45.1	37	18	0.49	17	-1.2E-4	32	-0.200	0.143	5.3	15.19	2.00	0.543	1.8	0.888	0.2031	0.9	2795	40	2851	15	2.4
10542-6.1	81	31	0.40	39	1.0E-4	28	0.177	0.121	3.4	15.71	1.74	0.557	1.6	0.946	0.2045	0.6	2854	38	2863	9	0.4
10542-27.1	232	178	0.79	112	4.3E-5	50	0.075	0.218	1.5	15.81	1.69	0.560	1.7	0.980	0.2048	0.3	2866	38	2865	5	-0.1
10542-11.1	91	45	0.51	42	2.6E-4	26	0.445	0.132	3.1	15.48	1.77	0.546	1.6	0.928	0.2057	0.7	2808	37	2872	11	2.7
10542-34.1	101	51	0.52	49	3.1E-5	201	0.053	0.143	2.7	16.11	1.75	0.565	1.6	0.944	0.2070	0.6	2885	38	2882	9	-0.1
10542-135.1	55	15	0.29	26	5.9E-5	35	0.103	0.075	5.1	16.09	1.80	0.561	1.7	0.933	0.2078	0.6	2873	39	2889	11	0.7
10542-9.1	69	35	0.52	32	5.0E-5	34	0.086	0.143	3.4	15.80	1.76	0.551	1.7	0.942	0.2081	0.6	2828	38	2891	10	2.7
10542-59.1	181	99	0.57	90	2.4E-5	75	0.042	0.155	1.6	16.71	1.63	0.581	1.6	0.983	0.2087	0.3	2951	38	2895	5	-2.4
10542-23.1	31	13	0.42	16	7.6E-5	62	0.131	0.127	5.1	16.85	1.96	0.584	1.8	0.896	0.2091	0.9	2967	42	2899	14	-2.9
10542-10.1	105	36	0.36	49	5.5E-5	32	0.095	0.097	3.7	15.64	2.07	0.540	2.0	0.967	0.2101	0.5	2782	45	2906	9	5.3
10542-138.1	119	44	0.38	58	2.5E-5	128	0.044	0.103	3.0	16.39	1.68	0.565	1.6	0.960	0.2102	0.5	2888	38	2907	8	0.8
10542-53.1	39	17	0.44	19	4.1E-4	32	0.711	0.128	5.0	16.64	2.10	0.567	1.8	0.844	0.2130	1.1	2894	41	2928	18	1.4
10542-61.1	57	34	0.61	28	5.1E-5	51	0.088	0.178	3.5	16.74	2.16	0.570	1.7	0.768	0.2132	1.4	2906	39	2930	22	1.0
10542-44.1	202	44	0.23	95	9.5E-6	61	0.016	0.064	3.1	16.31	2.08	0.545	1.9	0.908	0.2170	0.9	2805	43	2958	14	6.4
10542-137.1	388	23	0.06	215	1.0E-5	22	0.017	0.017	3.8	22.49	1.75	0.645	1.6	0.903	0.2530	0.8	3207	40	3204	12	-0.1

Grain mount IP612; spot size 17µm x 23µm; # of scans = 6; Error in 206Pb/238U calibration = 1.5%

Southern Sedimentary unit: conglomerate UTM NAD 83, zone 16, 501413E, 5503166N

10541-18.1	24	1	0.03	10	3.0E-4	39	0.528	0.001	16.5	12.9	1.97	0.508	1.5	0.783	0.184	1.2	2650	34	2688	20	1.8
10541-105.1	53	40	0.77	23	1.7E-6	242	0.003	0.216	2.5	12.8	1.41	0.505	1.3	0.906	0.184	0.6	2637	28	2690	10	2.4
10541-44.1	65	30	0.48	29	9.4E-5	36	0.163	0.140	2.9	13.2	1.40	0.518	1.3	0.904	0.184	0.6	2692	28	2693	10	0.1
10541-106.1	148	147	1.02	64	2.2E-5	107	0.037	0.293	1.3	12.8	1.28	0.503	1.2	0.952	0.184	0.4	2627	26	2694	6	3.0
10541-87.1	76	46	0.63	34	-1.5E-5	320	-0.025	0.176	2.5	13.2	1.42	0.518	1.3	0.903	0.185	0.6	2691	28	2694	10	0.2
10541-104.1	200	118	0.61	91	1.3E-5	80	0.023	0.177	1.4	13.5	1.30	0.529	1.3	0.970	0.185	0.3	2737	28	2698	5	-1.8

Table 2-2. SHRIMP U-Pb detrital zircon results for the NSU conglomerate, CSU sandstone, SSU conglomerate, SSU and Quetico sandstones (cont'd)

																Apparent Ages (Ma)				
Spot name	**U (ppm)**	**Th (ppm)**	**Th/U**	**^{206}Pb* (ppm)**	**^{204}Pb/^{206}Pb**	**% ±**	**f(206)^{204} %**	**^{208*}Pb/^{206*}Pb**	**% ±**	**^{207*}Pb/^{235}U**	**% ±**	**^{206*}Pb/^{238}U**	**% ±**	**Corr Coeff**	**^{207*}Pb/^{206*}Pb**	**% ±**	**^{206}Pb/^{238}U**	**±^{206}Pb/^{238}U**	**^{207}Pb/^{206}Pb**	**±^{207}Pb/^{206}Pb**	**Disc. (%)**
10541-59.1	35	12	0.36	16	---	100	0.000	0.113	4.4	13.3	1.57	0.523	1.4	0.877	0.185	0.8	2711	30	2699	12	-0.6
10541-99.1	74	81	1.13	32	3.4E-4	20	0.590	0.326	2.0	12.9	1.48	0.503	1.3	0.866	0.185	0.7	2628	28	2700	12	3.2
10541-2.1	212	105	0.51	94	-2.2E-5	92	-0.037	0.139	2.0	13.2	1.28	0.517	1.2	0.951	0.186	0.4	2688	27	2703	7	0.7
10541-12.1	70	84	1.25	31	-7.7E-5	73	-0.133	0.362	1.8	13.5	1.42	0.525	1.3	0.888	0.186	0.7	2722	28	2706	11	-0.7
10541-89.1	91	34	0.39	40	-8.4E-6	42	-0.015	0.113	2.8	13.1	1.46	0.512	1.3	0.891	0.186	0.7	2665	28	2708	11	1.9
10541-22.1	155	128	0.85	68	-7.5E-6	63	-0.013	0.241	1.5	13.2	1.30	0.513	1.2	0.955	0.186	0.4	2669	27	2710	6	1.9
10541-69.1	39	20	0.55	17	1.1E-4	44	0.192	0.153	3.5	13.2	1.52	0.515	1.3	0.861	0.186	0.8	2678	29	2710	13	1.5
10541-70.1	61	20	0.34	27	4.2E-5	43	0.072	0.098	3.7	13.4	1.42	0.520	1.3	0.903	0.187	0.6	2701	28	2714	10	0.6
10541-14.1	77	36	0.49	35	4.2E-5	39	0.073	0.134	2.7	13.5	1.55	0.525	1.5	0.942	0.187	0.5	2719	32	2714	9	-0.2
10541-40.1	91	54	0.61	41	3.8E-6	514	0.007	0.175	2.2	13.4	1.33	0.520	1.2	0.933	0.187	0.5	2697	27	2716	8	0.8
10541-10.1	76	36	0.49	34	6.4E-5	58	0.111	0.140	2.8	13.5	1.39	0.523	1.3	0.906	0.187	0.6	2710	28	2716	10	0.3
10541-107.1	55	25	0.47	25	7.9E-5	83	0.137	0.120	3.2	13.8	2.04	0.536	1.9	0.938	0.187	0.7	2768	43	2717	12	-2.3
10541-3.1	219	241	1.13	93	7.3E-5	30	0.126	0.322	1.1	12.8	1.31	0.496	1.2	0.939	0.187	0.5	2596	26	2717	7	5.4
10541-15.1	35	16	0.48	15	1.3E-4	26	0.232	0.115	4.3	13.2	1.56	0.512	1.3	0.858	0.187	0.8	2663	29	2717	13	2.4
10541-56.1	204	99	0.50	91	3.9E-6	91	0.007	0.137	1.7	13.5	1.30	0.521	1.2	0.946	0.187	0.4	2705	27	2719	7	0.6
10541-32.1	53	30	0.58	24	7.5E-5	43	0.130	0.164	2.8	13.7	1.41	0.531	1.3	0.900	0.188	0.6	2744	28	2721	10	-1.1
10541-95.1	148	45	0.31	65	1.2E-4	31	0.203	0.088	2.2	13.3	1.29	0.514	1.2	0.945	0.188	0.4	2675	27	2722	7	2.1
10541-58.1	85	52	0.63	37	1.5E-5	86	0.026	0.181	2.2	13.3	1.39	0.513	1.3	0.936	0.188	0.5	2669	28	2722	8	2.4
10541-74.1	77	41	0.55	34	2.8E-6	184 3	0.005	0.163	2.5	13.4	1.39	0.520	1.3	0.901	0.188	0.6	2697	28	2722	10	1.1
10541-61.1	54	19	0.36	24	-3.0E-6	353	-0.005	0.100	3.8	13.3	1.49	0.512	1.4	0.912	0.188	0.6	2663	30	2725	10	2.8
10541-23.1	144	71	0.51	65	-2.0E-5	85	-0.035	0.145	1.8	13.6	1.27	0.524	1.2	0.957	0.188	0.4	2717	27	2726	6	0.4
10541-52.1	88	42	0.50	40	5.0E-5	43	0.086	0.136	2.6	13.6	1.46	0.525	1.4	0.939	0.188	0.5	2721	30	2726	8	0.3
10541-71.1	83	55	0.68	37	1.6E-5	163	0.028	0.200	2.1	13.5	1.35	0.521	1.2	0.924	0.188	0.5	2705	28	2727	8	1.0
10541-63.1	101	64	0.65	46	6.8E-6	573	0.012	0.181	2.0	13.6	1.35	0.523	1.3	0.928	0.188	0.5	2710	28	2727	8	0.7
10541-46.1	86	47	0.56	39	-3.8E-5	68	-0.066	0.161	2.3	13.7	1.34	0.528	1.2	0.928	0.188	0.5	2732	28	2728	8	-0.2
10541-90.1	69	31	0.47	31	4.4E-5	60	0.076	0.138	2.6	13.5	1.36	0.520	1.3	0.922	0.188	0.5	2699	28	2728	9	1.3
10541-96.1	100	50	0.52	43	6.6E-6	244	0.011	0.145	2.5	12.9	1.38	0.498	1.3	0.936	0.188	0.5	2604	28	2729	8	5.5
10541-27.1	81	39	0.49	37	6.8E-5	32	0.118	0.146	2.4	13.7	1.34	0.527	1.2	0.930	0.188	0.5	2730	28	2729	8	-0.1
10541-39.1	51	24	0.48	23	-9.8E-5	55	-0.171	0.145	3.1	13.7	1.45	0.529	1.3	0.883	0.188	0.7	2736	29	2729	11	-0.3

Table 2-2. SHRIMP U-Pb detrital zircon results for the NSU conglomerate, CSU sandstone, SSU conglomerate, SSU and Quetico sandstones (cont'd)

																Apparent Ages (Ma)				
Spot name	**U (ppm)**	**Th (ppm)**	**Th/U**	**^{206}Pb* (ppm)**	**^{204}Pb/^{206}Pb**	**% ±**	**f(206)^{204} %**	**^{208*}Pb/^{206*}Pb**	**% ±**	**^{207*}Pb/^{235}U**	**% ±**	**^{206*}Pb/^{238}U**	**% ±**	**Corr Coeff**	**^{207*}Pb/^{206*}Pb**	**% ±**	**^{206}Pb/^{238}U**	**±^{206}Pb/^{238}U**	**^{207}Pb/^{206}Pb**	**±^{207}Pb/^{206}Pb**	**Disc. (%)**
10541-75.1	89	59	0.69	38	6.4E-5	69	0.111	0.177	2.3	12.9	1.42	0.496	1.3	0.916	0.189	0.6	2595	28	2731	9	6.0
10541-66.1	122	63	0.54	55	1.8E-5	136	0.030	0.154	2.0	13.7	1.30	0.527	1.2	0.945	0.189	0.4	2729	27	2732	7	0.1
10541-28.1	117	41	0.36	53	2.0E-4	24	0.339	0.100	2.4	13.7	1.38	0.527	1.2	0.893	0.189	0.6	2728	27	2733	10	0.2
10541-94.1	105	57	0.57	47	-5.7E-6	62	-0.010	0.159	2.0	13.6	1.29	0.523	1.2	0.951	0.189	0.4	2712	27	2733	7	1.0
10541-45.1	112	49	0.46	50	3.2E-5	16	0.055	0.128	2.4	13.5	1.31	0.519	1.2	0.944	0.189	0.4	2696	27	2736	7	1.8
10541-17.1	90	45	0.51	40	1.6E-5	60	0.028	0.150	2.3	13.6	1.33	0.520	1.2	0.937	0.189	0.5	2700	27	2737	8	1.6
10541-38.1	46	24	0.54	21	8.8E-5	60	0.152	0.145	3.2	13.7	1.47	0.524	1.3	0.874	0.189	0.7	2718	29	2738	12	0.9
10541-26.1	74	42	0.58	34	-3.6E-5	24	-0.062	0.172	2.4	13.9	1.34	0.531	1.2	0.930	0.190	0.5	2747	28	2739	8	-0.4
10541-36.1	130	75	0.59	59	3.1E-5	69	0.054	0.169	1.8	13.8	1.28	0.527	1.2	0.951	0.190	0.4	2730	27	2740	7	0.5
10541-80.1	51	20	0.41	22	3.1E-5	81	0.054	0.106	4.2	13.1	1.58	0.500	1.4	0.893	0.190	0.7	2612	30	2742	12	5.8
10541-76.1	98	35	0.37	44	4.1E-5	39	0.071	0.105	2.8	13.8	1.48	0.525	1.3	0.906	0.190	0.6	2721	30	2746	10	1.1
10541-35.1	37	16	0.45	16	-1.2E-4	43	-0.211	0.132	3.8	13.6	1.52	0.514	1.3	0.866	0.191	0.8	2675	29	2753	12	3.5
10541-24.1	83	40	0.49	39	1.1E-5	389	0.020	0.137	2.4	14.7	1.40	0.548	1.3	0.925	0.195	0.5	2815	30	2785	9	-1.3
10541-101.1	149	108	0.75	70	6.1E-5	31	0.106	0.211	1.6	15.1	1.28	0.543	1.2	0.956	0.202	0.4	2797	28	2839	6	1.8
10541-31.1	158	75	0.49	75	6.4E-6	393	0.011	0.135	1.7	15.5	1.26	0.553	1.2	0.962	0.203	0.3	2839	28	2848	6	0.4
10541-25.1	115	60	0.54	54	1.6E-5	37	0.028	0.151	2.0	15.3	1.90	0.546	1.9	0.980	0.203	0.4	2809	42	2849	6	1.7
10541-34.1	182	135	0.77	86	1.4E-5	86	0.024	0.218	1.3	15.4	1.26	0.549	1.2	0.971	0.203	0.3	2823	28	2850	5	1.2
10541-8.1	38	30	0.81	18	-4.8E-5	137	-0.083	0.240	3.1	15.6	1.58	0.550	1.3	0.852	0.206	0.8	2823	31	2877	13	2.3
10541-9.1	90	37	0.43	43	1.6E-4	24	0.282	0.118	2.8	16.0	1.37	0.557	1.3	0.920	0.208	0.5	2854	29	2888	9	1.4
10541-72.1	192	103	0.55	91	-1.1E-5	19	-0.019	0.155	1.6	16.0	1.26	0.555	1.2	0.970	0.209	0.3	2844	28	2897	5	2.3

Grain mount IP616; spot size 13µm x 16µm; # of scans = 6; Error in 206Pb/238U calibration = 1.2%

Southern Sedimentary Unit: sandstone UTM NAD 83, zone 16, 450108E, 5504309N

10575-79.1	85	47	0.57	38	2.7E-5	48	0.048	0.157	1.9	13.19	1.13	0.5208	1.1	0.939	0.1837	0.39	2703	24	2686	6	-0.8
10575-34.1	89	50	0.58	40	1.3E-5	344	0.023	0.165	1.8	13.37	1.17	0.5268	1.1	0.912	0.1841	0.48	2728	24	2690	8	-1.7
10575-31.2	140	103	0.76	61	9.8E-5	20	0.171	0.222	1.1	12.82	1.07	0.5053	1.0	0.962	0.1841	0.29	2637	22	2690	5	2.4
10575-22.1	150	105	0.73	67	5.2E-5	25	0.090	0.206	1.3	13.26	1.19	0.5224	1.0	0.876	0.1841	0.57	2709	23	2690	9	-0.9
10575-6.1	208	180	0.90	92	1.8E-5	83	0.032	0.250	0.9	13.02	1.07	0.5128	1.0	0.960	0.1841	0.30	2669	22	2691	5	1.0
10575-75.1	113	67	0.61	50	1.7E-4	18	0.290	0.175	1.5	13.09	1.12	0.5148	1.0	0.939	0.1844	0.38	2677	23	2693	6	0.7

Table 2-2. SHRIMP U-Pb detrital zircon results for the NSU conglomerate, CSU sandstone, SSU conglomerate, SSU and Quetico sandstones (cont'd)

																Apparent Ages (Ma)				
Spot name	**U (ppm)**	**Th (ppm)**	**Th/U**	**^{206}Pb* (ppm)**	**^{204}Pb/^{206}Pb**	**% ±**	**f(206)^{204} %**	**^{208*}Pb/^{206*}Pb**	**% ±**	**^{207*}Pb/^{235}U**	**% ±**	**^{206*}Pb/^{238}U**	**% ±**	**Corr Coeff**	**^{207*}Pb/^{206*}Pb**	**% ±**	**^{206}Pb/^{238}U**	**±^{206}Pb/^{238}U**	**^{207}Pb/^{206}Pb**	**±^{207}Pb/^{206}Pb**	**Disc. (%)**
10575-33.1	157	118	0.78	69	9.8E-5	26	0.170	0.219	1.2	13.05	1.09	0.5122	1.0	0.954	0.1848	0.33	2666	23	2696	5	1.4
10575-72.1	125	45	0.37	55	3.8E-5	96	0.065	0.108	1.8	13.00	1.13	0.5100	1.0	0.924	0.1849	0.43	2657	23	2697	7	1.8
10575-45.1	191	159	0.86	84	3.4E-4	9	0.582	0.242	1.0	13.06	1.08	0.5123	1.0	0.955	0.1849	0.32	2667	22	2697	5	1.4
10575-29.1	242	155	0.66	107	-2.8E-6	84	-0.005	0.184	1.0	13.08	1.05	0.5129	1.0	0.976	0.1849	0.23	2669	22	2697	4	1.3
10575-40.1	164	132	0.84	72	2.1E-6	711	0.004	0.227	2.3	13.04	1.09	0.5112	1.0	0.963	0.1850	0.29	2662	23	2698	5	1.6
10575-24.1	261	97	0.38	117	8.3E-5	16	0.143	0.107	1.3	13.29	1.05	0.5209	1.0	0.968	0.1850	0.27	2703	22	2698	4	-0.2
10575-50.1	58	29	0.52	26	5.1E-5	76	0.088	0.139	2.4	13.19	1.21	0.5170	1.1	0.902	0.1851	0.52	2686	24	2699	9	0.6
10575-3.1	155	103	0.69	69	7.6E-5	27	0.131	0.192	1.3	13.29	1.10	0.5204	1.0	0.943	0.1852	0.37	2701	23	2700	6	0.0
10575-5.2	98	56	0.59	43	4.1E-5	67	0.070	0.172	1.5	13.00	1.11	0.5089	1.0	0.944	0.1853	0.37	2652	23	2701	6	2.2
10575-20.1	89	29	0.34	40	2.2E-5	54	0.038	0.097	2.5	13.22	1.17	0.5174	1.1	0.914	0.1853	0.47	2688	23	2701	8	0.6
10575-64.1	224	149	0.69	100	----	390	-0.002	0.199	1.0	13.32	1.05	0.5213	1.0	0.976	0.1854	0.23	2705	23	2702	4	-0.1
10575-32.1	110	80	0.75	49	1.6E-5	109	0.028	0.210	1.4	13.25	1.11	0.5183	1.1	0.947	0.1854	0.36	2692	23	2702	6	0.4
10575-10.1	125	69	0.57	56	8.7E-5	28	0.152	0.161	1.6	13.24	1.17	0.5168	1.1	0.930	0.1858	0.43	2686	24	2705	7	0.9
10575-15.1	217	65	0.31	95	2.0E-5	63	0.036	0.084	1.6	12.97	1.07	0.5064	1.0	0.960	0.1858	0.30	2641	22	2705	5	2.9
10575-74.1	128	73	0.59	55	5.6E-4	8	0.963	0.163	1.4	12.73	1.21	0.4971	1.0	0.863	0.1858	0.61	2601	22	2705	10	4.7
10575-43.1	79	27	0.35	35	2.1E-5	36	0.036	0.102	2.4	13.40	1.14	0.5218	1.1	0.939	0.1863	0.39	2707	24	2710	6	0.2
10575-23.1	168	135	0.83	74	2.4E-5	51	0.042	0.235	1.1	13.24	1.08	0.5152	1.0	0.954	0.1863	0.32	2679	23	2710	5	1.4
10575-42.1	68	35	0.53	30	-2.5E-5	60	-0.043	0.153	2.2	13.18	1.32	0.5130	1.2	0.944	0.1864	0.44	2669	27	2710	7	1.9
10575-35.1	215	157	0.75	94	2.0E-5	30	0.034	0.210	1.0	13.04	1.08	0.5073	1.0	0.952	0.1864	0.33	2645	22	2711	5	2.9
10575-62.1	113	82	0.75	49	-5.6E-6	97	-0.010	0.215	1.4	13.15	1.09	0.5115	1.0	0.956	0.1864	0.32	2663	23	2711	5	2.2
10575-69.1	99	41	0.43	44	8.9E-5	31	0.154	0.121	1.9	13.26	1.12	0.5159	1.1	0.940	0.1864	0.38	2682	23	2711	6	1.3
10575-88.1	84	43	0.52	37	-2.3E-5	93	-0.041	0.151	1.9	13.14	1.13	0.5106	1.1	0.937	0.1866	0.40	2659	23	2712	7	2.4
10575-27.1	136	126	0.96	61	-1.2E-5	77	-0.021	0.269	1.1	13.39	1.08	0.5202	1.0	0.960	0.1866	0.30	2700	23	2713	5	0.6
10575-53.1	84	50	0.61	37	3.8E-5	77	0.065	0.182	1.8	13.28	1.15	0.5155	1.1	0.928	0.1868	0.43	2680	23	2714	7	1.5
10575-68.1	124	70	0.59	55	6.8E-5	42	0.117	0.167	1.5	13.32	1.10	0.5168	1.0	0.946	0.1870	0.36	2686	23	2716	6	1.4
10575-4.1	53	39	0.76	23	2.2E-5	57	0.038	0.210	2.1	13.26	1.23	0.5143	1.1	0.888	0.1870	0.56	2675	24	2716	9	1.8
10575-73.1	88	48	0.57	40	3.5E-5	57	0.060	0.162	1.7	13.59	1.13	0.5263	1.1	0.942	0.1872	0.38	2726	24	2718	6	-0.4
10575-70.1	157	82	0.54	69	1.3E-4	18	0.219	0.147	1.3	13.15	1.07	0.5093	1.0	0.959	0.1872	0.30	2653	22	2718	5	2.9
10575-13.1	150	89	0.62	66	-1.4E-5	94	-0.025	0.176	1.4	13.29	1.10	0.5144	1.0	0.943	0.1873	0.37	2675	23	2719	6	2.0
10575-77.1	287	256	0.92	126	1.9E-4	13	0.324	0.266	0.7	13.27	1.05	0.5132	1.0	0.969	0.1876	0.26	2670	22	2721	4	2.3

Table 2-2. SHRIMP U-Pb detrital zircon results for the NSU conglomerate, CSU sandstone, SSU conglomerate, SSU and Quetico sandstones (cont'd)

																Apparent Ages (Ma)				
Spot name	**U (ppm)**	**Th (ppm)**	**Th/U**	**^{206}Pb* (ppm)**	**^{204}Pb/^{206}Pb**	**% ±**	**f(206)^{204} %**	**^{208*}Pb/^{206*}Pb**	**% ±**	**^{207*}Pb/^{235}U**	**% ±**	**^{206*}Pb/^{238}U**	**% ±**	**Corr Coeff**	**^{207*}Pb/^{206*}Pb**	**% ±**	**^{206}Pb/^{238}U**	**±^{206}Pb/^{238}U**	**^{207}Pb/^{206}Pb**	**±^{207}Pb/^{206}Pb**	**Disc. (%)**
10575-66.1	54	20	0.37	24	2.1E-5	36	0.036	0.108	2.7	13.44	1.18	0.5195	1.1	0.922	0.1876	0.46	2697	24	2721	8	1.1
10575-63.1	112	56	0.51	50	2.2E-5	48	0.038	0.148	1.6	13.54	1.10	0.5226	1.0	0.955	0.1878	0.33	2710	23	2723	5	0.6
10575-28.1	75	37	0.51	33	4.9E-5	35	0.086	0.145	2.1	13.42	1.22	0.5171	1.1	0.883	0.1882	0.57	2687	24	2726	9	1.8
10575-26.1	97	49	0.52	44	-3.0E-6	214	-0.005	0.145	1.8	13.72	1.12	0.5287	1.1	0.947	0.1883	0.36	2736	24	2727	6	-0.4
10575-86.1	193	55	0.30	84	1.1E-4	14	0.195	0.088	2.0	13.20	1.11	0.5077	1.1	0.948	0.1886	0.35	2647	23	2730	6	3.7
10575-48.1	209	54	0.27	94	-1.4E-5	50	-0.025	0.075	1.7	13.84	1.05	0.5247	1.0	0.974	0.1913	0.24	2719	23	2754	4	1.5
10575-17.1	124	59	0.49	55	-1.0E-5	75	-0.018	0.137	1.7	13.79	1.10	0.5195	1.0	0.943	0.1925	0.37	2697	23	2763	6	2.9
10575-18.1	142	76	0.55	66	4.7E-5	56	0.081	0.154	1.5	14.38	1.72	0.5420	1.7	0.975	0.1925	0.38	2792	38	2763	6	-1.3
10575-9.1	131	74	0.59	60	2.1E-4	16	0.357	0.165	1.6	14.15	1.14	0.5326	1.0	0.923	0.1926	0.44	2753	23	2765	7	0.5
10575-80.1	78	62	0.82	35	1.4E-5	58	0.024	0.237	1.6	14.13	1.14	0.5313	1.1	0.941	0.1929	0.39	2747	24	2767	6	0.9
10575-36.1	267	127	0.49	124	4.2E-5	25	0.073	0.138	1.1	14.40	1.05	0.5395	1.0	0.978	0.1936	0.22	2781	23	2773	4	-0.4
10575-39.1	163	136	0.86	76	4.1E-5	96	0.070	0.245	1.1	14.45	1.10	0.5393	1.0	0.944	0.1944	0.36	2781	23	2780	6	0.0
10575-25.1	121	55	0.47	56	2.9E-4	12	0.505	0.128	1.6	14.66	1.15	0.5422	1.1	0.932	0.1961	0.42	2793	24	2794	7	0.0
10575-19.1	51	23	0.46	24	3.6E-4	18	0.626	0.131	2.9	14.95	1.36	0.5511	1.1	0.831	0.1967	0.76	2830	26	2799	12	-1.4
10575-41.1	72	60	0.85	35	-6.2E-6	39	-0.011	0.241	1.6	16.07	1.14	0.5605	1.1	0.943	0.2079	0.38	2869	25	2889	6	0.9
10575-11.1	321	78	0.25	153	7.3E-5	17	0.127	0.071	1.4	15.90	1.04	0.5533	1.0	0.977	0.2084	0.22	2839	23	2893	4	2.3
10575-61.1	94	45	0.49	47	1.8E-5	195	0.031	0.142	1.7	16.57	1.12	0.5748	1.1	0.942	0.2090	0.38	2928	25	2898	6	-1.3
10575-89.1	187	79	0.43	92	1.7E-5	54	0.030	0.123	1.3	16.70	1.05	0.5710	1.0	0.975	0.2122	0.24	2912	24	2922	4	0.4
10575-30.1	213	114	0.55	111	2.5E-6	440	0.004	0.149	1.1	19.18	1.05	0.6085	1.0	0.978	0.2286	0.22	3064	25	3042	3	-0.9
10575-49.1	27	12	0.46	16	9.7E-5	57	0.168	0.121	3.3	24.31	1.33	0.6680	1.2	0.897	0.2640	0.59	3298	31	3271	9	-1.1

Grain mount IP626; spot size 13µm x 16µm; # of scans = 5; Error in 206Pb/238U calibration = 1.0%

Quetico sandstone UTM NAD 83, zone 16, 429595E, 5492251N

10576-22.1	142	163	1.19	64	-4.4E-6	69	-0.008	0.339	1.0	13.25	1.08	0.5215	1.0	0.964	0.1843	0.28	2705	23	2692	5	-0.6
10576-113.1	107	119	1.15	48	4.9E-5	16	0.085	0.328	1.1	13.17	1.10	0.5182	1.0	0.954	0.1844	0.33	2691	23	2693	5	0.1
10576-90.1	176	129	0.76	77	-3.0E-6	53	-0.005	0.218	1.1	13.03	1.09	0.5121	1.1	0.971	0.1845	0.26	2666	23	2694	4	1.3
10576-109.1	53	36	0.71	23	8.5E-5	31	0.147	0.196	2.0	13.08	1.20	0.5139	1.1	0.911	0.1846	0.50	2673	24	2694	8	1.0
10576-54.1	448	407	0.94	194	8.2E-6	44	0.014	0.259	0.6	12.84	1.07	0.5045	1.0	0.948	0.1847	0.34	2633	22	2695	6	2.8

Table 2-2. SHRIMP U-Pb detrital zircon results for the NSU conglomerate, CSU sandstone, SSU conglomerate, SSU and Quetico sandstones (cont'd)

																Apparent Ages (Ma)				
Spot name	**U (ppm)**	**Th (ppm)**	**Th/U**	**^{206}Pb* (ppm)**	**^{204}Pb/^{206}Pb**	**% ±**	**f(206)^{204} %**	**^{208*}Pb/^{206*}Pb**	**% ±**	**^{207*}Pb/^{235}U**	**% ±**	**^{206*}Pb/^{238}U**	**% ±**	**Corr Coeff**	**^{207*}Pb/^{206*}Pb**	**% ±**	**^{206}Pb/^{238}U**	**±^{206}Pb/^{238}U**	**^{207}Pb/^{206}Pb**	**±^{207}Pb/^{206}Pb**	**Disc. (%)**
10576-104.1	123	108	0.91	54	-7.4E-6	150	-0.013	0.257	1.2	13.07	1.09	0.5132	1.0	0.957	0.1847	0.32	2670	23	2695	5	1.1
10576-103.1	145	93	0.66	65	6.3E-5	35	0.109	0.193	1.3	13.23	1.09	0.5196	1.0	0.956	0.1847	0.32	2698	23	2695	5	-0.1
10576-18.1	166	114	0.71	73	4.2E-6	40	0.007	0.203	1.2	13.12	1.07	0.5143	1.0	0.968	0.1850	0.27	2675	23	2699	4	1.1
10576-83.1	211	207	1.02	92	-4.4E-6	169	-0.008	0.289	0.9	12.89	1.06	0.5053	1.0	0.972	0.1850	0.25	2637	22	2699	4	2.8
10576-96.1	121	109	0.93	54	6.8E-5	35	0.118	0.270	1.2	13.27	1.10	0.5198	1.0	0.949	0.1852	0.35	2698	23	2700	6	0.1
10576-99.1	209	106	0.53	91	1.4E-5	71	0.025	0.152	1.2	12.91	1.05	0.5057	1.0	0.972	0.1852	0.25	2638	22	2700	4	2.8
10576-22.2	127	127	1.03	53	6.6E-5	31	0.114	0.288	1.1	12.36	1.08	0.4838	1.0	0.955	0.1852	0.32	2544	22	2700	5	7.0
10576-4.1	148	69	0.48	66	1.4E-5	156	0.025	0.132	1.5	13.23	1.08	0.5179	1.0	0.957	0.1853	0.32	2690	23	2701	5	0.5
10576-121.1	230	209	0.94	101	4.3E-5	20	0.075	0.265	0.8	13.13	1.05	0.5135	1.0	0.976	0.1855	0.23	2672	22	2703	4	1.4
10576-30.1	150	64	0.44	68	8.1E-6	283	0.014	0.121	1.5	13.40	1.11	0.5236	1.1	0.960	0.1856	0.31	2715	24	2704	5	-0.5
10576-21.1	349	179	0.53	153	9.8E-6	50	0.017	0.149	0.9	13.07	1.03	0.5103	1.0	0.985	0.1857	0.18	2658	22	2704	3	2.1
10576-89.1	186	74	0.41	80	-5.5E-6	87	-0.009	0.119	1.4	12.89	1.08	0.5033	1.1	0.972	0.1858	0.26	2628	23	2705	4	3.5
10576-93.1	105	91	0.89	46	3.1E-6	842	0.005	0.263	1.3	13.16	1.12	0.5133	1.1	0.941	0.1859	0.38	2671	23	2706	6	1.6
10576-100.1	206	76	0.38	91	-8.3E-6	51	-0.014	0.109	1.4	13.16	1.05	0.5133	1.0	0.973	0.1860	0.24	2671	22	2707	4	1.6
10576-59.1	87	106	1.26	38	1.2E-4	27	0.200	0.358	1.3	13.25	1.22	0.5167	1.1	0.931	0.1860	0.45	2685	25	2707	7	1.0
10576-143.1	99	97	1.01	44	8.0E-6	77	0.014	0.286	1.2	13.13	1.10	0.5119	1.0	0.953	0.1861	0.33	2665	23	2708	6	1.9
10576-144.1	190	119	0.65	84	4.2E-6	372	0.007	0.187	1.2	13.20	1.07	0.5140	1.0	0.967	0.1863	0.27	2674	23	2710	5	1.6
10576-47.1	307	222	0.75	137	7.6E-6	101	0.013	0.216	0.8	13.35	1.04	0.5193	1.0	0.981	0.1864	0.20	2696	22	2710	3	0.6
10576-65.1	207	164	0.82	93	2.4E-5	41	0.041	0.239	1.3	13.40	1.07	0.5214	1.0	0.972	0.1864	0.25	2705	23	2711	4	0.2
10576-110.1	353	340	1.00	158	1.7E-5	28	0.029	0.283	1.1	13.46	1.03	0.5233	1.0	0.984	0.1866	0.18	2713	22	2712	3	-0.1
10576-6.1	168	80	0.49	75	8.9E-6	142	0.015	0.140	1.4	13.38	1.07	0.5200	1.0	0.966	0.1866	0.28	2699	23	2712	5	0.6
10576-95.1	105	71	0.70	47	7.3E-6	110	0.013	0.197	1.5	13.29	1.10	0.5165	1.1	0.952	0.1866	0.34	2684	23	2712	6	1.3
10576-119.1	227	150	0.68	101	4.9E-6	391	0.009	0.193	1.0	13.29	1.06	0.5164	1.0	0.969	0.1866	0.26	2684	23	2713	4	1.3
10576-92.1	123	151	1.26	55	2.6E-5	99	0.045	0.361	1.0	13.44	1.10	0.5224	1.0	0.948	0.1866	0.35	2709	23	2713	6	0.2
10576-34.1	63	39	0.64	28	-1.4E-5	74	-0.024	0.176	1.9	13.50	1.15	0.5243	1.1	0.933	0.1867	0.41	2717	24	2713	7	-0.2
10576-35.1	91	101	1.14	41	-2.5E-5	89	-0.044	0.326	1.2	13.53	1.13	0.5258	1.1	0.941	0.1867	0.38	2724	24	2713	6	-0.5
10576-122.1	88	63	0.74	39	2.2E-5	88	0.038	0.204	1.6	13.40	1.13	0.5206	1.1	0.939	0.1867	0.39	2702	23	2714	6	0.5
10576-97.1	105	40	0.39	48	2.5E-5	61	0.044	0.109	1.9	13.64	1.21	0.5299	1.1	0.872	0.1867	0.59	2741	23	2714	10	-1.2

Table 2-2. SHRIMP U-Pb detrital zircon results for the NSU conglomerate, CSU sandstone, SSU conglomerate, SSU and Quetico sandstones (cont'd)

																Apparent Ages (Ma)				
Spot name	**U (ppm)**	**Th (ppm)**	**Th/U**	**^{206}Pb* (ppm)**	**^{204}Pb/^{206}Pb**	**% ±**	**f(206)^{204} %**	**^{208*}Pb/^{206*}Pb**	**% ±**	**^{207*}Pb/^{235}U**	**% ±**	**^{206*}Pb/^{238}U**	**% ±**	**Corr Coeff**	**^{207*}Pb/^{206*}Pb**	**% ±**	**^{206}Pb/^{238}U**	**±^{206}Pb/^{238}U**	**^{207}Pb/^{206}Pb**	**±^{207}Pb/^{206}Pb**	**Disc. (%)**
10576-50.1	143	57	0.41	66	4.0E-5	42	0.069	0.120	1.5	13.95	1.07	0.5416	1.0	0.963	0.1868	0.29	2790	23	2714	5	-3.4
10576-107.1	170	53	0.32	75	4.5E-5	34	0.078	0.092	1.7	13.25	1.07	0.5142	1.0	0.965	0.1868	0.28	2674	23	2715	5	1.8
10576-80.1	297	281	0.98	133	3.2E-5	37	0.056	0.277	0.8	13.47	1.05	0.5229	1.0	0.976	0.1868	0.23	2711	23	2715	4	0.2
10576-10.1	81	91	1.16	37	1.5E-5	331	0.026	0.330	1.4	13.45	1.19	0.5221	1.1	0.904	0.1869	0.51	2708	24	2715	8	0.3
10576-17.1	87	47	0.56	39	5.6E-5	40	0.098	0.165	1.7	13.45	1.13	0.5215	1.1	0.940	0.1871	0.39	2706	23	2717	6	0.5
10576-85.1	150	72	0.50	66	3.5E-6	608	0.006	0.144	1.5	13.23	1.08	0.5116	1.0	0.957	0.1875	0.32	2664	23	2720	5	2.6
10576-46.1	44	21	0.49	20	2.3E-5	79	0.040	0.140	2.6	13.78	1.22	0.5316	1.1	0.910	0.1880	0.51	2748	25	2725	8	-1.1
10576-48.1	167	71	0.44	76	1.3E-5	61	0.023	0.125	1.4	13.75	1.06	0.5299	1.0	0.969	0.1882	0.26	2741	23	2727	4	-0.7
10576-60.1	43	14	0.34	19	2.1E-5	290	0.036	0.096	3.5	13.47	1.33	0.5184	1.1	0.860	0.1885	0.68	2692	25	2729	11	1.6
10576-25.1	211	89	0.43	94	2.7E-6	288	0.005	0.120	1.3	13.52	1.05	0.5195	1.0	0.975	0.1888	0.23	2697	23	2732	4	1.5
10576-15.1	355	235	0.68	161	-1.5E-6	764	-0.003	0.194	0.8	13.77	1.07	0.5288	1.0	0.952	0.1889	0.33	2736	23	2733	5	-0.2
10576-94.1	172	69	0.41	78	2.1E-5	54	0.036	0.118	1.5	13.72	1.06	0.5264	1.0	0.969	0.1890	0.26	2726	23	2733	4	0.3
10576-51.1	116	65	0.58	52	8.0E-6	94	0.014	0.163	1.5	13.57	1.09	0.5208	1.0	0.958	0.1890	0.31	2702	23	2733	5	1.4
10576-36.1	176	62	0.37	79	2.7E-5	43	0.047	0.104	1.5	13.59	1.08	0.5209	1.0	0.972	0.1892	0.25	2703	23	2735	4	1.4
10576-61.1	138	63	0.47	62	1.5E-5	48	0.026	0.131	1.6	13.67	1.08	0.5238	1.0	0.963	0.1892	0.29	2715	23	2735	5	0.9
10576-120.1	69	28	0.42	32	1.4E-5	156	0.025	0.120	2.3	13.96	1.16	0.5351	1.1	0.931	0.1892	0.42	2763	24	2735	7	-1.2
10576-20.1	326	98	0.31	145	8.0E-6	34	0.014	0.085	1.3	13.58	1.31	0.5186	1.3	0.978	0.1899	0.27	2693	28	2741	5	2.1
10576-114.1	193	82	0.44	87	1.3E-5	59	0.022	0.125	1.4	13.65	1.07	0.5212	1.0	0.973	0.1900	0.25	2704	23	2742	4	1.7
10576-87.1	32	15	0.49	15	1.2E-4	57	0.203	0.139	3.1	14.44	1.38	0.5447	1.2	0.847	0.1923	0.73	2803	27	2762	12	-1.8
10576-58.1	273	164	0.62	127	2.3E-5	90	0.040	0.174	1.0	14.61	1.05	0.5424	1.0	0.971	0.1954	0.25	2793	23	2788	4	-0.2
10576-84.1	280	82	0.30	130	6.3E-5	18	0.109	0.084	1.4	14.70	1.04	0.5422	1.0	0.979	0.1967	0.21	2793	23	2799	4	0.3
10576-45.1	123	85	0.71	59	1.1E-5	107	0.019	0.198	1.3	15.48	1.08	0.5595	1.0	0.963	0.2007	0.29	2865	24	2832	5	-1.4
10576-16.1	234	97	0.43	109	1.8E-5	56	0.031	0.119	1.2	15.00	1.05	0.5417	1.0	0.977	0.2008	0.22	2791	23	2833	4	1.8
10576-112.1	162	66	0.42	76	2.8E-5	54	0.049	0.124	1.4	15.18	1.07	0.5470	1.0	0.967	0.2012	0.27	2813	24	2836	4	1.0
10576-43.1	134	60	0.46	64	7.2E-5	22	0.125	0.129	1.5	15.70	1.08	0.5603	1.0	0.964	0.2032	0.29	2868	24	2852	5	-0.7
10576-115.1	197	76	0.40	95	4.9E-6	84	0.009	0.112	1.3	15.80	1.05	0.5604	1.0	0.977	0.2045	0.22	2868	24	2862	4	-0.3
10576-44.1	60	24	0.42	29	7.1E-5	57	0.123	0.116	2.4	15.86	1.18	0.5596	1.1	0.919	0.2055	0.47	2865	25	2871	8	0.2
10576-42.1	60	26	0.45	29	8.6E-6	71	0.015	0.122	2.2	16.26	1.15	0.5659	1.1	0.941	0.2083	0.39	2891	25	2893	6	0.1

Table 2-2. SHRIMP U-Pb detrital zircon results for the NSU conglomerate, CSU sandstone, SSU conglomerate, SSU and Quetico sandstones (cont'd)

																Apparent Ages (Ma)				
Spot name	**U (ppm)**	**Th (ppm)**	**Th/U**	**^{206}Pb* (ppm)**	**^{204}Pb/^{206}Pb**	**% ±**	**f(206)^{204} %**	**^{208*}Pb/^{206*}Pb**	**% ±**	**^{207*}Pb/^{235}U**	**% ±**	**^{206*}Pb/^{238}U**	**% ±**	**Corr Coeff**	**^{207*}Pb/^{206*}Pb**	**% ±**	**^{206}Pb/^{238}U**	**±^{206}Pb/^{238}U**	**^{207}Pb/^{206}Pb**	**±^{207}Pb/^{206}Pb**	**Disc. (%)**
10576-142.1	79	30	0.39	39	1.8E-5	52	0.032	0.117	2.8	16.41	1.12	0.5713	1.1	0.951	0.2084	0.35	2913	25	2893	6	-0.9
10576-7.1	81	25	0.31	40	2.8E-5	127	0.049	0.088	2.3	16.59	1.14	0.5741	1.1	0.938	0.2096	0.40	2924	25	2902	6	-1.0
10576-116.1	446	275	0.64	217	1.5E-4	9	0.254	0.183	1.5	16.40	1.14	0.5672	1.1	0.982	0.2097	0.22	2896	26	2903	3	0.3
10576-23.1	92	29	0.33	44	1.4E-5	98	0.025	0.092	2.2	15.97	1.14	0.5522	1.1	0.954	0.2097	0.34	2834	25	2904	6	2.9
10576-82.1	77	84	1.13	38	4.8E-5	58	0.084	0.317	1.3	16.58	1.15	0.5732	1.1	0.936	0.2098	0.40	2921	25	2904	7	-0.7
10576-29.1	127	71	0.57	61	1.7E-6	425	0.003	0.164	1.4	16.34	1.14	0.5620	1.0	0.914	0.2108	0.46	2875	24	2912	7	1.6
10576-108.1	360	140	0.40	176	6.3E-6	56	0.011	0.114	1.0	16.58	1.04	0.5696	1.0	0.987	0.2111	0.17	2906	24	2914	3	0.3
10576-19.1	78	31	0.42	38	---	100	0.000	0.119	2.0	16.68	1.12	0.5724	1.1	0.952	0.2113	0.34	2918	25	2916	6	-0.1
10576-86.1	268	186	0.72	135	3.2E-5	33	0.056	0.206	0.9	17.25	1.04	0.5865	1.0	0.981	0.2133	0.20	2975	24	2931	3	-1.9
10576-111.1	184	99	0.56	90	1.8E-6	101 5	0.003	0.154	1.2	17.22	1.06	0.5712	1.0	0.973	0.2186	0.24	2913	24	2971	4	2.4
10576-3.1	114	64	0.58	58	-3.9E-6	363	-0.007	0.156	1.4	18.13	1.08	0.5881	1.0	0.965	0.2236	0.29	2982	25	3007	5	1.0
10576-88.1	95	59	0.65	50	3.4E-5	67	0.059	0.180	1.5	19.85	1.11	0.6114	1.1	0.955	0.2355	0.33	3076	26	3090	5	0.6

Grain mount IP626; spot size 13µm x 16µm; # of scans = 5; Error in 206Pb/238U calibration = 1.0%

Notes (see Stern, 1997):

Spot name follows the convention x-y.z; where x = sample number, y = grain number and z = spot number. Multiple analyses in an individual spot are labelled as x-y.z.z

Uncertainties reported at 1s (absolute) and are calculated by numerical propagation of all known sources of error

f206204 refers to mole fraction of total 206Pb that is due to common Pb, calculated using the 204Pb-method; common Pb composition used is the surface blank (4/6: 0.05770; 7/6: 0.89500; 8/6: 2.13840)

* refers to radiogenic Pb (corrected for common Pb)

Discordance relative to origin = 100 * ((207/206 age -206/238 age)/(207Pb/206Pb age))

Calibration standard 6266; U = 910 ppm; Age = 559 Ma; 206Pb/238U = 0.09059

Th/U calibration: F = 0.03900*UO + 0.85600

Table 2-3. Major oxide (wt. %) and trace element (ppm) compositions of the Croll Lake stock, feldspar porphyry and feldspar-quartz porphyry dikes in the BGB

ID	BGBZT2012_82	BGBZT2012_098	BGBZT2012_107	BGBZT2012_108	BGBZT2013_237	BGBZT2013_385	BGBZT2013_387	BGBZT2014_17B
	FQP	FQP	FQP	FQP	FQP	FQP	FQP	FQP
SiO2 (wt. %)	67.49	67.31	67.07	69.93	67.54	66.68	66.37	67.68
Al2O3 (wt. %)	17.10	17.62	17.62	16.20	16.80	16.60	17.60	17.21
Fe2O3(t) (wt. %)	2.35	2.51	2.76	2.26	3.24	3.51	3.49	2.28
MnO (wt. %)	0.03	0.02	0.03	0.02	0.04	0.03	0.02	0.03
MgO (wt. %)	0.90	1.02	1.06	0.85	0.99	0.89	0.63	0.67
CaO (wt. %)	3.54	2.71	3.05	2.51	3.23	3.74	2.56	3.04
Na2O (wt. %)	6.06	6.79	5.81	6.22	6.11	6.08	6.29	6.31
K2O (wt. %)	1.94	1.65	2.25	1.67	2.19	2.05	2.31	1.98
TiO2 (wt. %)	0.29	0.33	0.32	0.29	0.33	0.32	0.30	0.34
P2O5 (wt. %)	0.10	0.12	0.12	0.10	0.18	0.17	0.15	0.13
Cr2O3 (wt. %)	0.02	0.02	0.02	0.01	< 0.01	< 0.01	0.01	<0.002
V2O5 (wt. %)	0.01	0.01	0.01	0.01	0.01	0.01	0.01	n.a.
LOI (wt. %)	3.73	3.52	3.67	3.03	3.37	3.81	3.74	3.62
Total (wt. %)	99.83	100.10	100.10	100.10	100.70	100.10	99.72	99.82
FeOt (wt. %) (1)	2.11	2.26	2.48	2.03	2.91	3.16	3.14	2.05
Ferromagnesian (FeOt+MgO+MnO+TiO2)	3.34	3.63	3.89	3.19	4.28	4.40	4.09	3.10
K2O/Na2O	0.32	0.24	0.39	0.27	0.36	0.34	0.37	0.31
La (ppm)	12	15.4	16.3	13.7	16.5	13.9	12	16.08
Ce (ppm)	25.1	33.5	35.7	29.6	35.1	29.8	26	34.33
Pr (ppm)	3.36	4.09	4.48	3.73	4.4	3.75	3.26	4.415
Nd (ppm)	13.6	16.4	17.8	14.6	17.2	14.8	12.5	17.72
Sm (ppm)	2.24	2.76	2.96	2.31	2.81	2.45	2.02	2.728
Eu (ppm)	0.553	0.67	0.729	0.553	0.711	0.584	0.508	0.6018
Gd (ppm)	1.52	1.64	1.91	1.53	1.77	1.52	1.21	1.517
Tb (ppm)	0.15	0.17	0.17	0.14	0.2	0.15	0.13	0.1494
Dy (ppm)	0.69	0.73	0.75	0.57	0.96	0.66	0.57	0.691
Ho (ppm)	0.12	0.11	0.13	0.1	0.15	0.11	0.09	0.1115
Er (ppm)	0.33	0.3	0.39	0.3	0.42	0.27	0.27	0.287
Tm (ppm)	0.046	0.047	0.056	0.048	0.059	0.043	0.038	0.0407
Yb (ppm)	0.29	0.3	0.33	0.31	0.35	0.26	0.24	0.278
Lu (ppm)	0.048	0.041	0.053	0.042	0.056	0.032	0.041	0.0415
ΣREE (ppm)	60.05	76.16	81.76	67.53	80.69	68.33	58.88	78.99
Ba (ppm)	643	565	672	620	478	631	575	526
Cr (ppm)	<20	20	<20	<20	<20	20	30	30
Cs (ppm)	2.2	1.8	2.2	1.3	2.1	1.6	1.8	1.932
Ga (ppm)	24	25	24	21	24	22	24	23.63
Ge (ppm)	1	1.4	1.2	1.4	1.6	1.1	1.6	n.a.
Hf (ppm)	2.5	2.5	2.5	2.3	2.7	2.4	2.5	3.05
In (ppm)	< 0.1	< 0.1	< 0.1	< 0.1	< 0.1	< 0.1	< 0.1	0.0193
Nb (ppm)	1.7	2.9	3.2	2.8	2.4	1	1.3	2.871
Ni (ppm)	6	7	7	5	9	9	8	7.5
Pb (ppm)	5	< 5	< 5	< 5	6	< 5	< 5	6.3
Rb (ppm)	46	38	57	37	64	46	42	45.51
Sc (ppm)	3	4	4	3	n.a.	n.a.	n.a.	3.5
Sr (ppm)	676	609	383	515	325	663	281	329.6
Ta (ppm)	0.07	0.15	0.13	0.14	0.22	0.16	0.14	0.084
Th (ppm)	1.79	2.27	2.56	2.01	2.57	2.13	1.94	2.46
Tl (ppm)	0.06	0.09	0.14	0.07	0.12	< 0.05	< 0.05	0.184

Table 2-3. Major oxide (wt. %) and trace element (ppm) compositions of the Croll Lake stock, feldspar porphyry and feldspar-quartz porphyry dikes in the BGB (cont'd)

ID	BGBZT2012_82	BGBZT2012_098	BGBZT2012_107	BGBZT2012_108	BGBZT2013_237	BGBZT2013_385	BGBZT2013_387	BGBZT2014_17B
U (ppm)	0.64	0.73	0.85	0.71	0.84	0.73	0.7	0.734
V (ppm)	41	54	50	43	41	41	47	45.5
Y (ppm)	3.9	3.4	4.2	3.2	4.9	3.1	2.6	3.41
Zr (ppm)	105	92	94	85	102	91	98	105
La/Yb	41.38	51.33	49.39	44.19	47.14	53.46	50.00	57.84
Zr/Y	26.92	27.06	22.38	26.56	20.82	29.35	37.69	30.79
$[La/Yb]_N$ (2)	27.96	34.69	33.38	29.86	31.86	36.13	33.79	39.09
Eu_N/Eu^* (3)	0.92	0.96	0.94	0.90	0.97	0.92	0.99	0.90
trace element anomalies	-Ta, Nb, Ti							

ID	BGBZT2016_1	BGBZT2016_2	BGBZT2016_5	BGBZT2016_3	BGBZT2016_4	BGBZT2016_9
	Croll Lake granodiorite			Croll Lake fine tonalite		tonalitic FP
SiO2 (wt. %)	64.84	63.98	58.90	68.31	68.77	64.83
Al2O3 (wt. %)	16.17	16.19	16.46	16.84	17.03	15.99
Fe2O3(t) (wt. %)	4.15	4.08	5.95	1.64	1.44	5.58
MnO (wt. %)	0.06	0.06	0.10	0.01	0.01	0.05
MgO (wt. %)	2.70	2.84	4.49	0.91	0.82	2.16
CaO (wt. %)	4.75	4.90	7.09	3.15	3.14	3.91
Na2O (wt. %)	4.20	4.08	3.69	4.84	4.76	4.32
K2O (wt. %)	3.11	3.02	2.51	3.03	2.92	1.65
TiO2 (wt. %)	0.36	0.37	0.46	0.21	0.20	0.34
P2O5 (wt. %)	0.18	0.20	0.23	0.08	0.08	0.16
Cr2O3 (wt. %)	0.02	0.03	0.02	0.02	0.01	0.01
V2O5 (wt. %)	0.00	0.00	0.01	< 0.003	< 0.003	0.01
LOI (wt. %)	1.34	1.06	1.97	1.13	1.00	1.54
Total (wt. %)	100.60	99.79	99.95	99.06	99.18	99.01
FeOt (wt. %) (1)	3.73	3.67	5.35	1.47	1.30	5.02
Ferromagnesian (FeOt+MgO+ MnO+TiO2)	6.85	6.95	10.40	2.61	2.33	7.57
K2O/Na2O	0.74	0.74	0.68	0.63	0.61	0.38
La (ppm)	44.9	44.9	31.7	9	9.47	28.4
Ce (ppm)	91.6	90.5	66.9	20.1	20.1	59.5
Pr (ppm)	10.1	10.4	7.77	2.37	2.25	7.35
Nd (ppm)	36.5	36.6	30.5	8.89	8.52	27.9
Sm (ppm)	5.7	6.16	5.65	1.83	1.64	4.35
Eu (ppm)	1.41	1.44	1.47	0.496	0.486	1.21
Gd (ppm)	3.8	4.15	4.03	1.34	1.04	2.75
Tb (ppm)	0.41	0.49	0.53	0.14	0.14	0.32
Dy (ppm)	1.97	2.35	2.61	0.67	0.65	1.53
Ho (ppm)	0.37	0.42	0.44	0.11	0.11	0.27
Er (ppm)	1.04	1.27	1.23	0.3	0.32	0.74
Tm (ppm)	0.142	0.168	0.178	0.043	0.044	0.102
Yb (ppm)	0.92	0.99	1.04	0.27	0.3	0.7
Lu (ppm)	0.133	0.139	0.157	0.047	0.046	0.116
ΣREE (ppm)	199.00	199.98	154.21	45.61	45.12	135.24
Ba (ppm)	996	1040	819	1050	979	523
Cr (ppm)	120	130	130	40	40	60
Cs (ppm)	3.3	2.9	3.2	3	3.4	6.8
Ga (ppm)	18	19	18	18	18	17
Ge (ppm)	0.7	0.7	0.7	0.5	< 0.5	1.5
Hf (ppm)	3.7	4.2	2.5	2.3	2.2	3.7
In (ppm)	0.1	< 0.1	< 0.1	< 0.1	< 0.1	< 0.1
Nb (ppm)	5.6	5.6	5.2	3.2	2.6	6.1

Table 2-3. Major oxide (wt. %) and trace element (ppm) compositions of the Croll Lake stock, feldspar porphyry and feldspar-quartz porphyry dikes in the BGB (cont'd)

ID	BGBZT2016_1	BGBZT2016_2	BGBZT2016_5	BGBZT2016_3	BGBZT2016_4	BGBZT2016_9
Ni (ppm)	51.1	51	40.8	21.8	17.8	21.8
Pb (ppm)	75	67	50	41	29	6
Rb (ppm)	91	91	75	75	75	102
Sc (ppm)	n.a.	n.a.	n.a.	n.a.	n.a.	n.a.
Sr (ppm)	842	882	792	744	773	751
Ta (ppm)	0.66	0.52	0.52	0.24	0.26	0.42
Th (ppm)	14.1	11.2	7.94	3.08	2.6	5.15
Tl (ppm)	0.29	0.3	0.28	0.2	0.21	0.55
U (ppm)	2.44	2.15	1.69	1.73	1.46	1.8
V (ppm)	53	56	89	19	16	54
Y (ppm)	11.5	13.9	12.9	3.9	3.6	8.1
Zr (ppm)	133	155	93	90	79	133
La/Yb	48.80	45.35	30.48	33.33	31.57	40.57
Zr/Y	11.57	11.15	7.21	23.08	21.94	16.42
$[La/Yb]_N$ (2)	32.98	30.65	20.60	22.52	21.33	27.42
Eu_N/Eu^* (3)	0.93	0.87	0.94	0.97	1.14	1.07
trace element anomalies	-Ta, Nb, Ti; +Sr			-Ta, Nb, Ti; +Sr		-Ta, Nb, Ti

1) FeOt is calculated from Fe2O3t: FeOt=0.899808*Fe2O3t

2) $[La/Yb]_N$ ratios are normalized to chondtitic values from Taylor and McLennan (1985).

3) EuN/Eu*=(Eu/0.087)/(sqrt((Sm/0.231)*(Gd/0.306))) (normalization values from Taylor and McLennan, 1985)

Table 2-4 U-Pb Zircon ID-TIMS analytical data of a TTG suite quartz-feldspar porphyry from Geraldton.

							Isotopic Ratios[6]								Ages (Ma)[8]						
Fraction[1]	**Description[2]**	**Wt.**	**U**	**Pb[3]**	**206Pb[4]**	**Pb[5]**	**208Pb**	**207Pb**	**±1SE**	**206Pb**	**±1SE**	**Corr.[7]**	**207Pb**	**±1SE**	**206Pb**	**±2SE**	**207Pb**	**±2SE**	**207Pb**	**±2SE**	**%**
		ug	**ppm**	**ppm**	**204Pb**	**pg**	**206Pb**	**235U**	**Abs**	**238U**	**Abs**	**Coeff.**	**206Pb**	**Abs**	**238U**		**235U**		**206Pb**		**Disc**
BGB-VM-2011-06 (Z10533): Quartz-feldspar porphyry (UTM NAD83, zone 16: 504798E - 5502837N)																					
A12-1 (1;CA)	Co,Clr, Eu Pr,Fr,CA12	1.8	35	17	2436	0.7	0.15	10.55803	0.014 28	0.41467	0.000 48	0.926	0.18466	0.00010	2236.2	4.4	2485.0	2.5	2695.2	1.7	20.1
A12-2 (1;CA)	Co,Clr, Eu Pr,Fr,CA12	2.1	23	14	944	1.7	0.14	13.23297	0.021 64	0.51981	0.000 75	0.889	0.18463	0.00014	2698.4	6.4	2696.4	3.1	2695.0	2.5	-0.2
A14-1 (1;CA)	Co,Clr, Eu Pr,Fr,CA14	1.2	68	40	2136	1.2	0.15	13.15941	0.017 88	0.51714	0.000 61	0.905	0.18456	0.00011	2687.0	5.2	2691.2	2.6	2694.2	1.9	0.3
A16-1 (1;CA)	Co,Clr, Eu St,CA14	6.0	20	11	2316	1.7	0.10	13.11231	0.017 64	0.51558	0.000 59	0.915	0.18445	0.00010	2680.4	5.0	2687.8	2.5	2693.3	1.8	0.6

Notes:

[1]Number in bracket refers to the number of zircon grains in the analysis. CA = chemically abraded.

[2]Fraction descriptions: Co=Colourless, Clr=Clear, Eu=Euhedral, Pr=Prismatic, St=Stubby Prism, Fr=Fractures, CA12=Chemically Abraded for 12 hours.

[3]Radiogenic Pb

[4]Measured ratio, corrected for spike and fractionation

[5]Total common Pb in analysis corrected for fractionation and spike

[6]Corrected for blank Pb and U and common Pb, errors quoted are 1 sigma absolute; procedural blank values for this study ranged from <0.1- 0.1 pg for U and 0.5-1 pg for Pb; Pb blank isotopic composition is based on the analysis of procedural blanks; corrections for common Pb were made using Stacey and Kramers (1975) compositions

[7]Correlation Coefficient

[8]Corrected for blank and common Pb, errors quoted are 2 sigma in Ma

Table 2-5. Summary of detrital zircon populations in each sample with possible source rocks identified predominantly in the eastern Wabigoon subprovince contributing to the clastic sedimentary sequence of the BGB and northern Quetico subprovince. The bracketed number in Italics following the name of the sample provides the number of zircon analyzed from given sample. Continuous detrital zircon populations are indicated in the respective time intervals with the number of representing zircons in brackets. The peak within each population is given to the right of each interval. The ages marked by asterisk are Nd model ages. **References:** a) Beakhouse, 1983; b) Bédard and Harris, 2014; c) Davis and Jackson, 1988; d) Davis et al., 1988; e) Davis et al., 2000; f) Davis, 1998; g) Davis, 1999; h) Henry et al., 1998; i) Kwok et al., 2000; j) Percival et al., 2004; k) Sanborn-Barrie and Skulski, 1999; l) Stott and Davis, 1999; m) Stott et al., 2002; n) Tomlinson and Percival, 2000; o) Tomlinson et al., 1999a; p) Tomlinson et al., 1999b; q) Tomlinson et al., 2000; r) Tomlinson et al., 2001; s) Tomlinson et al., 2002; t) Tomlinson et al., 2003; u) Tomlinson et al., 2004; v) Tomlinson, 2000.

Table 2-5.

Age (Ma)	NSU conglomerate *(55)*		CSU sandstone *(58)*		SSU conglomerate *(63)*		SSU sandstone *(63)*		Quetico siltstone *(78)*		Possible source rocks	Regional scale tectonic and petrogenetic events
2680											Deeds monzogranite 2694 Ma (m, e, g); Gzowski monzogranite 2698 Ma (m, e, f); Sheff granite 2698 Ma (f); Sollas granodiorite 2692 Ma (m, e, i); Marshall gabbro 2695 Ma (m, e)	Continental magmatism in the Winnipeg River terrane (2.69-2.74 Ga) and Marmion terrane (2.69-2.73 Ga); voluminous magmatism in the western Wabigoon terrane after 2.74 Ga (u); NE-dipping subduction and collision of the western Wabigoon terrane to the continental margin in the north and east (v, k); **OR** W-dipping subduction beneath the western Wabigoon and concurrent N-dipping subduction beneath the Winnipeg river-Marmion complex at 2.73-2.74 Ga (k); **OR** plume-driven disaggregation of the Superior I propocontinent from 2.78 to 2.72 Ga and its subsequent reassembly from 2.72 to 2.68 Ga (b)
2700		2711 Ma		2700 Ma				2700 Ma		2711 Ma	Marshall Lake QFP 2706 Ma (m, e); Tashota QFP 2701 Ma (m); Elmhirst-Rickaby tuff 2709 Ma (m); Conglomerate Lake porphyry 2706 Ma (m, e); Humboldt Bay dacite 2713 Ma (m, g); Gzowski area quartz porphyry 2701 Ma (m, n)	
2720	2690-2840 Ma *(46)*		2690-2740 Ma *(37)*		2690-2760 Ma *(55)*	2726 Ma	2690-2800 Ma *(55)*		2690-2800 *(59)*	2734 Ma	Crooked Green gabbro 2734, 2732 Ma (m, n); Frank Lake gneiss 2723 Ma (m); Marshall Lake tuff, dacite, porphyry 2739, 2738 Ma (m, e, c); O'Sullivan QFPs, tuff 2734, 2738, 2733 Ma (m, e); Metcalfe dacite 2722 (m); Willet Lake dacite 2738 Ma (m, e); Metcalfe-Venus dacites 2722, 2728, 2735 Ma (m, e); Elmhirst-Rickaby porphyry, quartz diorites 2738, 2734, 2736 Ma (m, e, i); Kaby pluton tonalite 2734 Ma (m, e); Summit Lake trondhjemite, tonalite 2735, 2736, 2737 Ma (m, e, i); Esnagami tonalite, granodiorite 2729, 2723 Ma (m, e, i); Deeds tonalite 2728 Ma (m, e, d); Gzowski pluton F volcanic 2738 Ma (m);	
2740											Elmhirst-Rickaby tuff 2741 Ma (m);	

Table 2-5. (cont'd)

Age (Ma)	NSU conglomerate *(55)*		CSU sandstone *(58)*		SSU conglomerate *(63)*		SSU sandstone *(63)*		Quetico siltstone *(78)*		Possible source rocks	Regional scale tectonic and petrogenetic events
2760	2690-2840 Ma (46)	2774 Ma	2760-2800 Ma *(3)*				2690-2800 Ma (55)	2771 Ma	2690-2800 (59)		Onaman tonalite, dacite 2768, 2769, 2777 Ma (m, e); Conglomerate Lake granodiorite 2774 (m, e); *Jackson monzogranite 2777 Ma (m, u); *Metcalfe granodiorite 2770 Ma (m, u);	2.77-2.78 Ga tonalitic magmatism in the central and eastern Wabigoon subprovince due to plume magmatism (u)
2780				2780 Ma	2780-2800 Ma *(1)*	2785 Ma					Onaman tuff 2781 Ma (m, e); *Metcalfe-Venus dacite 2798 Ma (m); *Deeds monzogranite, tonalite 2794, 2797 Ma (m, u); *Gzowski monzogranite 2785 Ma (m, u); *Esnagami tonalite 2799 Ma (m, u);	subordinate magmatism in the eastern Wabigoon subprovince, Winnipeg River and Marmion terranes (g, m, t, u, o); metamorphism in the Winnipeg River terrane at 2.79 Ga (a)
2800		2817 Ma									*Elmhirst-Rickaby andesite, tuff, dacite, rhyodacite, porphyry 2819, 2813, 2818, 2808, 2819 Ma (m); *Humboldt Bay dacite 2814 Ma (m, u); Gzowski basalt 2815 Ma (h); *monzonite in central Onanan-Tashota greenstone belt 2806 Ma (m, u);	metamorphism in the Marmion terrane at 2.81 Ga (c)
2820			2820-2960 Ma *(17)*		2820-2900 Ma *(7)*		2820-2840 Ma *(1)*	2839 Ma	2820-2940 Ma *(16)*	2833 Ma	*Marshall Lake tuff and dacite 2838, 2833 Ma (m); *O'Sullivan QFP 2826 Ma (m); *Metcalfe-Venus dacite 2831 Ma (m); *Sheff granite 2833 Ma (m, u); *Conglomerate Lake tuff 2832 Ma (m); *Elmhirst diorite 2824 Ma (m, u); *Elmhirst-Rickaby andesite and dacite 2830, 2833, 2828 Ma (m); *Summit Lake tonalite 2827 Ma (m, u);	2.83 Ga plume magmatism in Marmion terrane → continental flood basalt-komatiite volcanism in Lumby Lake and Lac des Mille Lac greenstone belts (o, t, u); 2.84-2.83 Ga tonalitic magmatism in Winnipeg River terrane (t, u, p); early crust formation within the Onaman-Tashota greenstone belt (q, r)
2840						2849 Ma					*Caribou Lake tonalite gneiss 2859 Ma (u); *Kaby quartz diorite 2850 Ma (m, u); *Elmhirst-Rickaby IM to F volcanics 2833, 2852, 2857 Ma (m); *Metcalfe dacite 2842 Ma (m); *Tashota QFP 2855 Ma (m);	

Table 2-5. (cont'd)

Age (Ma)	NSU conglomerate *(55)*		CSU sandstone *(58)*		SSU conglomerate *(63)*		SSU sandstone *(63)*		Quetico siltstone *(78)*		Possible source rocks	Regional scale tectonic and petrogenetic events
2860				2865 Ma	2820-2900 Ma *(7)*		2860-2900 Ma *(4)*				*Garden Lake IM to F volcanics 2863, 2864 Ma (u); *O'Sullivan tuff and QFP 2875, 2879Ma (m);	
2880		2899 Ma		2896 Ma		2895 Ma		2893 Ma			*Marshall Lake QFP 2883 Ma (m); *Willet Lake dacite 2884 (m);	2.88-2.94 Ga Approach and amalgamation of 3.4 Ga Winnipeg River and 3.0 Ga Marmion terrane; subsequent crustal thickening (u)
2900	2880-2940 Ma *(9)*		2820-2960 Ma (17)						2820-2940 Ma (16)	2903 Ma	*Sollace granodiorite 2905 Ma (u);	
2920							2920-2940 Ma *(1)*	2922 Ma			Esnagami tonalite 2921 Ma (f); Toronto Lake rhyolite 2922 Ma (f, l); Obonga Lake area granodiorite 2930, *2937 Ma (u, s)	
2940												2925-3010 Ma formation of juvenile Marmion terrane (u, h)
2960									2960-2980 Ma *(1)*	2971 Ma	Caribou Lake gneiss 2965 Ma (d); *Onaman pluton trondjemite 2974 Ma (u); *Garden Lake anorthosite 2963 Ma (u, n); *Roaring River complex 2962 Ma (u)	
2980												
3000									3000-3020 Ma *(1)*	3007 Ma	Marmion batholith tonalite gneisses 3002 Ma (t, u, c); F volcanics related to the Marmion batholith 2999-3014 Ma (t)	
3020												
3040							3040-3060 Ma *(1)*	3042 Ma			Tashota dacite 3056 Ma (f, u); Tashota feldspar porphyry 3056 Ma (e); *Garden Lake IM lava 3056 Ma (v); *Heaven Lake F volcanics 3054 and 3039 Ma (t, u, v); *Caribou Lake basalt 3049 Ma (v); *Marshall Lake rhyolite 3043 Ma (q, u);	

Table 2-5. (cont'd)

Age (Ma)	NSU conglomerate *(55)*		CSU sandstone *(58)*		SSU conglomerate *(63)*		SSU sandstone *(63)*		Quetico siltstone *(78)*		Possible source rocks	Regional scale tectonic and petrogenetic events
3080									3080-3100 Ma *(1)*	3090 Ma	Caribou Lake assemblage 3075-3100 Ma (d, v); *Esnagami tonalite 3095 Ma (u); * Garden Lake tonalite 3086, 3090 Ma (u, n)	
↓												
3200			3200-3220 Ma *(1)*	3204 Ma							*Garden Lake rhyolite 3221 Ma (t); *Toronto Lake rhyolite 3208 Ma (q, m, u);	
3220												
3240												
3260							3260-3280 Ma *(1)*	3271 Ma			*Tashota dacite 3279 Ma (m, u);	

Appendix

Appendix 2-A. Calculated accuracy and precision of the geochemical analyses.

	Activation Laboratories, Ancaster, Ontario											
	Method 2012/2013	**LOD 2012-2013**	**LOQ 2012-2013 [1]**	**Accuracy 2012 (%RD)**	**Precision 2012 (%RSD)**	**Accuracy 2013 (%RD)**	**Precision 2013 (%RSD)**	**Method 2016**	**LOD 2016**	**LOQ 2016 [1]**	**Accuracy 2016 (%RD)**	**Precision 2016 (%RSD)**
SiO2 (wt. %)	FUS-XRF	0.01	0.033	0.02-1.13	≤1	0.75-1.63	0.24-0.41	FUS-XRF	0.01	0.033	0.78-1.18	0.23
Al2O3 (wt. %)	FUS-XRF	0.01	0.033	≤ 11.76*	0.15-7.43	≤ 3.4	0.27-2.93	FUS-XRF	0.01	0.033	0.15-1.22	0.41
Fe2O3(t) (wt. %)	FUS-XRF	0.01	0.033	≤ 3.07	≤2.82	0.39-2.65	≤ 1.34	FUS-XRF	0.01	0.033	0.39-3.1	0.39
MnO (wt. %)	FUS-XRF	0.001	0.0033	≤ 6.97	≤5.44	≤ 16.67*	≤ 2.32	FUS-XRF	0.001	0.0033	1-1.72	0.00
MgO (wt. %)	FUS-XRF	0.01	0.033	0.24-25*	≤3.93	≤ 4.84	≤ 1.55	FUS-XRF	0.01	0.033	≤ 1.1	0.33
CaO (wt. %)	FUS-XRF	0.01	0.033	≤ 300*	≤12.69	0.75-10	0.22-3.16	FUS-XRF	0.01	0.033	1.35-5.88	0.73
Na2O (wt. %)	FUS-XRF	0.01	0.033	≤ 56.57*	≤6.15	1.1-56.25*	0.45-3.16	FUS-XRF	0.01	0.033	0.94-10	0.50
K2O (wt. %)	FUS-XRF	0.01	0.033	0.11-40*	≤9.42	≤ 33.33*	≤ 1.63	FUS-XRF	0.01	0.033	0.34-33.33*	0.87
TiO2 (wt. %)	FUS-XRF	0.01	0.033	≤ 40*	≤5.51	≤ 28.57*	≤ 1.08	FUS-XRF	0.01	0.033	≤ 3.45	2.18
P2O5 (wt. %)	FUS-XRF	0.01	0.033	≤ 66.67*	≤28.28*	0.9-42.86*	≤ 17.68 *	FUS-XRF	0.01	0.033	≤ 42.86*	4.29
Cr2O3 (wt. %)	FUS-XRF	0.01	0.033	≤ 50*	≤47.14*	n.d.	≤ 28.28 *	FUS-XRF	0.01	0.033	≤ 20	0.00
V2O5 (wt. %)	FUS-XRF	0.003	0.0099	2.32-14.29*	≤6.33	~ 4.17	1.75-6.43	FUS-XRF	0.003	0.0099	≤ 16.67	38.57*
LOI	FUS-XRF			n.d.	≤9.47	n.d.	0.3-1.78	FUS-XRF				0.91
La (ppm)	FUS-MS	0.05	0.165	0.22-9.94	≤6.32	0.28-10	0.26-6.39	FUS-MS	0.05	0.165	≤ 11.11	1.00
Ce (ppm)	FUS-MS	0.05	0.165	0.33-9.92	≤6.06	2.07-7.37	≤ 7.59	FUS-MS	0.05	0.165	0.17-7.83	0.84
Pr (ppm)	FUS-MS	0.01	0.033	0.36-8.65	≤4.82	4.56-8.06	0.24-10.35*	FUS-MS	0.01	0.033	1.27-4.72	1.46
Nd (ppm)	FUS-MS	0.05	0.165	1.27-9.51	0.82-5.43	2.31-9.81	0.84-7.73	FUS-MS	0.05	0.165	0.3-9.57	0.25
Sm (ppm)	FUS-MS	0.01	0.033	≤ 9.64	0.95-7.71	1.21-7	0.2-8.32	FUS-MS	0.01	0.033	1.16-9.09	3.18
Eu (ppm)	FUS-MS	0.005	0.0165	0.51-10.22	0.21-6.6	4.91-8.67	≤ 12.86	FUS-MS	0.005	0.0165	2.16-6.95	0.00
Gd (ppm)	FUS-MS	0.01	0.033	≤ 4.17	≤2.53	1.33-7.5	0.52-6.73	FUS-MS	0.01	0.033	5.33-5.41	0.77
Tb (ppm)	FUS-MS	0.01	0.033	≤ 7.56	≤4.42	0.3-16	≤ 4.88	FUS-MS	0.01	0.033	≤ 7.51	2.18
Dy (ppm)	FUS-MS	0.01	0.033	0.54-10.63	1.27-4.33	0.55-7.33	0.5-12.12	FUS-MS	0.01	0.033	2.16-6.56	1.37
Ho (ppm)	FUS-MS	0.01	0.033	0.84-7.14	≤6.15	0.83-6.67	≤ 20.20*	FUS-MS	0.01	0.033	0.83-6.58	0.00
Er (ppm)	FUS-MS	0.01	0.033	0.1-7.14	0.52-7.32	0.1-7.38	≤ 14.14	FUS-MS	0.01	0.033	3.73-8.11	0.95
Tm (ppm)	FUS-MS	0.005	0.0165	2.12-5.95	≤6.24	2.6-7.19	≤ 10.10*	FUS-MS	0.005	0.0165	0.43-7.52	1.37
Yb (ppm)	FUS-MS	0.01	0.033	≤ 8.97	0.5-6.73	0.22-5.37	0.88-8.32*	FUS-MS	0.01	0.033	≤ 9.4	0.00
Lu (ppm)	FUS-MS	0.002	0.0066	0.33-10.83	0.31-5.8	1.17-8.85	≤ 8.25	FUS-MS	0.002	0.0066	≤ 7.75	0.61
Ba (ppm)	FUS-ICP	3	9.9	2-14.56	≤3.68	7.5-8.79	≤ 2.23	FUS-ICP	3	9.9	≤ 8.47	0.27
Cr (ppm)	FUS-ICP	20	66	± ≤4.58	± ≤ 15.71*	≤ 2.7	≤ 3.82	FUS-ICP	20	66	3.45-11.11	0

Appendix 2-A. Calculated accuracy and precision of the geochemical analyses (cont'd)

Cs (ppm)	FUS-ICP	0.1	0.33	≤5.75	≤4.56	≤ 9.09	≤ 5.66	FUS-ICP	0.1	0.33	1.44-4.35	1.05
Ga (ppm)	FUS-MS	1	3.3	≤4.8	≤20.2*	≤ 6.25	≤ 4.88	FUS-ICP	1	3.3	≤ 6.67	4.29
Ge (ppm)	FUS-MS	0.5	1.65	0.9-44.44*	≤16.64*	≤ 90*	≤ 9.87	FUS-ICP	0.5	1.65	4.46-50*	0.00
Hf (ppm)	FUS-MS	0.1	0.33	≤ 19.29	≤10.88	≤ 7.69	≤ 9.43	FUS-ICP	0.1	0.33	7.69-9.09	0.00
In (ppm)	FUS-MS	0.1	0.33	3.75-8	BDL	0	BDL	FUS-ICP	0.1	0.33	~ 15.38	BDL
Nb (ppm)	FUS-MS	0.2	0.66	0.1-4.83	≤12.86*	0	1.32-23.57*	FUS-ICP	0.2	0.66	≤ 3.29	3.39
Ni (ppm)	TD-MS	1	3.3	1.43-15.15	≤6.37	2.38-13.36	≤ 2.67	TD-MS	**0.5**	1.65	0.81-23.33	n.a.
Pb (ppm)	FUS-MS	5	16.5	~3.5	≤17.68*	n.d.	0	FUS-ICP	5	16.5	3.63-11.11*	12.86*
Rb (ppm)	FUS-MS	1	3.3	0.4-10.53	≤4.04	0.8-8.97	≤ 2.57	FUS-ICP	1	3.3	≤ 4.35	1.40
Sc (ppm)	FUS-ICP	1	3.3	≤ 45*	≤3.63	n.a.	n.a.	n.a.	n.a.	n.a.	n.a.	n.a.
Sr (ppm)	FUS-ICP	2	6.6	1.97-7.5	≤2.62	1.82-6.32	0.39-4.29	FUS-ICP	2	6.6	0.69-6.67	1.62
Ta (ppm)	FUS-MS	0.01	0.033	0.38-12.9	1.1-31.43	4.15-6	≤ 6.43	FUS-ICP	0.01	0.033	1.61-10	1.70
Th (ppm)	FUS-MS	0.05	0.165	0.7-7.81	≤7.44	0.78-11.67	≤ 10.57	FUS-ICP	0.05	0.165	≤ 9.7	0.55
Tl (ppm)	FUS-MS	0.05	0.165	~0.6	2.67-33.1	≤ 60	1.59-21.43*	FUS-ICP	0.05	0.165	8.33-65*	6.15
U (ppm)	FUS-MS	0.01	0.033	≤ 4.93	BDL	≤ 6.96	≤ 20.20*	FUS-ICP	0.01	0.033	4.35-5.19	0.39
V (ppm)	FUS-ICP	5	16.5	5-28.57*	≤1.41	0.68-3.87	0.56-3.75	FUS-ICP	5	16.5	0.32-8.28	5.44
Y (ppm)	FUS-MS	0.5	1.65	0.51-10.24	≤5.81	0.63-8.33	≤ 1.18	FUS-ICP	0.5	1.65	0.92-9.44	1.77
Zr (ppm)	FUS-MS	1	3.3	≤ 7.42	≤4.88	2.13-9.55	≤ 10.52	FUS-ICP	1	3.3	≤ 5.77	0.53

	Geoscience Laboratories, Sudbury, Ontario				
	Method 2014	**LOD 2014**	**LOQ 2014**	**Accuracy 2014 (%RD)**	**Precision 2014 (%RSD)**
SiO2 (wt. %)	XRF-M01	0.04	0.132	0.18-0.48	0.31
Al2O3 (wt. %)	XRF-M01	0.02	0.066	0.29-1.38	0.37
Fe2O3(t) (wt. %)	XRF-M01	0.01	0.033	0.6-1.43	0.3
MnO (wt. %)	XRF-M01	0.002	0.0066	1.59-3.33	1.89
MgO (wt. %)	XRF-M01	0.01	0.033	0.88-1.68	0.21
CaO (wt. %)	XRF-M01	0.006	0.0198	0.08-0.11	0.15
Na2O (wt. %)	XRF-M01	0.02	0.066	1.13-50*	0.24
K2O (wt. %)	XRF-M01	0.01	0.033	0-0.74	0.78
TiO2 (wt. %)	XRF-M01	0.01	0.033	0	0
P2O5 (wt. %)	XRF-M01	0.002	0.0066	1.56-87.5*	1.33
Cr2O3 (wt. %)	XRF-M01	0.002	0.0066	1.14-60.68*	0
V2O5 (wt. %)		n.a.	-	n.a.	n.a.
LOI	XRF-M01	0.05	0.165	0.08-2.24	1.78

Appendix 2 A. Calculated accuracy and precision of the geochemical analyses (cont'd)					
La (ppm)	IMC-100	0.1	0.33	1.11-3	3.03
Ce (ppm)	IMC-100	0.12	0.396	0.46-6.44	3.04
Pr (ppm)	IMC-100	0.014	0.0462	1.16-2.93	2.87
Nd (ppm)	IMC-100	0.06	0.198	2.70-4.23	3.52
Sm (ppm)	IMC-100	0.026	0.0858	1.39-3.63	2.08
Eu (ppm)	IMC-100	0.0031	0.01023	0.11-2.71	2.89
Gd (ppm)	IMC-100	0.009	0.0297	0.61-0.64	2.76
Tb (ppm)	IMC-100	0.0023	0.00759	2.22-4.4	1.69
Dy (ppm)	IMC-100	0.009	0.0297	0.17-0.56	1.4
Ho (ppm)	IMC-100	0.0025	0.00825	5.34-5.39	0.29
Er (ppm)	IMC-100	0.007	0.0231	2.9-5.87	1.94
Tm (ppm)	IMC-100	0.0019	0.00627	2.81-4.88	1.59
Yb (ppm)	IMC-100	0.009	0.0297	2.92-6.12	3.34
Lu (ppm)	IMC-100	0.002	0.0066	3.48-3.81	3.7
Ba (ppm)	IMC-100	0.8	2.64	0.82-3.66	13.37
Cr (ppm)	IMC-100	3	9.9	≤ 6.19	0.69
Cs (ppm)	IMC-100	0.013	0.0429	4.57-9.77	2.47
Ga (ppm)	IMC-100	0.04	0.132	1.9-3.91	0.59
Ge (ppm)	IMC-100	n.d.	n.d.	n.d.	n.d.
Hf (ppm)	IMC-100	0.14	0.462	0-6.1	1.93
In (ppm)	IMC-100	0.0018	0.00594	n.d.	n.d.
Nb (ppm)	IMC-100	0.028	0.0924	10.53-21.87	0.31
Ni (ppm)	IMC-100	0.7	2.31	2.63-5.73	1.7
Pb (ppm)	IMC-100	0.18	0.594	≤ 6.75	1.4
Rb (ppm)	IMC-100	0.11	0.363	6.34-8.04	23.21
Sc (ppm)	IMC-100	1.1	3.63	5.38-5.72	4.08
Sr (ppm)	IMC-100	0.6	1.98	3.8-6.5	0.28
Ta (ppm)	IMC-100	0.007	0.0231	21.93-26.74	1.11
Th (ppm)	IMC-100	0.018	0.0594	0.8-4.44	3.85
Tl (ppm)	IMC-100	0.002	0.0066	1.11-23.53	0.22
U (ppm)	IMC-100	0.011	0.0363	1.72-3.94	2.81
V (ppm)	IMC-100	0.8	2.64	5.43-6.92	0.48
Y (ppm)	IMC-100	0.05	0.165	3.75-9.25	3.05
Zr (ppm)	IMC-100	6	19.8	1.7-2.17	1.13
Limit of detection (LOD)					
(1) Limit of quantification (LOQ)~3.3*LOD (after Piercey,2014 and references therein)					
%RD: percent relative difference					
%RSD: percent relative standard deviation					
* the poor precision at concentrations below or near LOQ					
BDL: below detection limit in each analyses					

3. CHAPTER 3: REVISITING THE STRUCTURAL EVOLUTION OF THE BEARDMORE-GERALDTON GREENSTONE BELT, SUPERIOR PROVINCE, CANADA: EVIDENCE FOR SINISTRAL TRANSPRESSION PREDATING TRICLINIC DEXTRAL TRANSPRESSION

Zsuzsanna Tóth[a,*], Bruno Lafrance[a], Benoît Dubé[b]

[a]Mineral Exploration Research Centre, Harquail School of Earth Sciences, Goodman School of Mines, Laurentian University, 935 Ramsey Lake Road, Sudbury, ON, Canada P3E 2C6

[b]Geological Survey of Canada, Earth Sciences Sector, Natural Resources Canada, 490 rue de la Couronne, Québec, QC, Canada G1K 9A9

*Corresponding author: Zsuzsanna Tóth, e-mail address: ztoth@laurentian.ca; 1-705-6628740; 935 Ramsey Lake Road, Sudbury, ON, Canada P3E 2C6

Abstract

The Beardmore-Geraldton Belt (BGB) is a polydeformed transitional zone straddling the boundary between the eastern Wabigoon granite-greenstone subprovince and the Quetico metasedimentary subprovince of the Archean Superior Province, Ontario, Canada. The BGB consists of interleaved panels of metasedimentary and metavolcanic rocks that were thrust-imbricated, folded and foliated during an early D_1 event. The latter is bracketed between 2694 ± 1 Ma, the age of D_1-deformed feldspar-quartz porphyry dikes, and 2690±1 Ma, the age of the stitching Croll Lake Stock that intersects the boundary between the thrusted metavolcanic and metasedimentary units. During a D_2 deformation event, the panels were internally folded by regional F_2 folds and overprinted by steeply-dipping high strain zones. The D_2 event also produced a regional S_2 cleavage which

becomes more pronounced within two major high strain zones bounding the belt to the south (Bankfield-Tombill deformation zone) and to the north (Paint Lake fault). The two high strain zones contain several major gold deposits including the Hardrock and Brookbank deposits. Regional F_2 folds along the Bankfield-Tombill deformation zone have S-asymmetry and the S_2 cleavage along both high strain zones is transected by anticlockwise, en échelon, quartz veins, suggesting that the folds, cleavage, high strain zones, and quartz veins formed during a regional sinistral transpression event. During a belt-wide D_3 deformation event, the S_2 cleavage was dextrally reactivated and a second regional cleavage (S_3) and Z-shaped F_3 folds formed within lower strain panels bounded by the D_2 high strain zones. Within the latter, the axes of F_1 and F_2 folds, as well as the axes of F_3 drag folds, are parallel to a strong stretching lineation that formed during D_2 and was rotated and accentuated during D_3. The fold axes and the stretching lineation were rotated into the orientation of a fabric attractor, which is oriented oblique to the direction of the intersection lineation between the reactivated S_2 cleavage and dextral shear bands, suggesting that the deformation during D_3 had triclinic symmetry. Thus, D_3 is a regional dextral transpression event during which deformation was partitioned into lower strain panels dominated by pure shear and reactivated higher strain shear zones dominated by simple shear and triclinic deformation symmetry. The tectonic evolution of the BGB, which began by D_1 thrusting followed by D_2 sinistral transpression and D_3 dextral transpression, shares analogies with other major gold-hosting deformation zones in the Abitibi greenstone belt and Rice Lake greenstone belt (Uchi subprovince, western Superior Province).

Introduction

Boundaries between subprovinces of the Archean Superior craton are complex deformation zones that typically underwent thrust accretion followed by transcurrent strike-slip faulting (e.g. Percival

and Williams, 1989; Daigneault et al., 2002; Bethune et al., 2006; Percival et al., 2012 and references therein). The study area is the Beardmore-Geraldton Belt (BGB) which represents the boundary zone between the Wabigoon subprovince and Quetico subprovince in the western Superior Province. The belt underwent both regional sinistral transpression followed by dextral transpression and thus offers a unique opportunity to study how slip reversal along a transpression zone influenced the orientation of the older structures, the formation of new structures, and the symmetry of the later transpressive event.

Transpressional deformation zones are steeply-dipping or subvertical high strain corridors that underwent simultaneous compression (pure shear component) and strike-slip transcurrent movement (simple shear component) during convergence of their bounding blocks (e.g. Harland, 1971; Sanderson and Marchini, 1984; Dewey et al., 1998). For monoclinic transcurrent transpression, the slip direction is horizontal and the vorticity vector is vertical and parallel to a finite principal strain rate axis of the pure shear component (Lin et al., 1998 and references therein). The stretching lineation is either vertical or horizontal depending on the angle of convergence (simple shear/pure shear ratio), the total accumulated strain (finite strain), and the degree of strain partitioning (Fossen et al., 1994; Robin and Cruden, 1994; Tikoff and Greene, 1997). However, even the smallest deviations from ideal monoclinic transpression result in the non-coaxiality of the pure shear and simple shear components of the transpression, and the stretching lineations will vary in orientation from horizontal to vertical as they track the changes in orientation of the maximum principal finite strain axes (Jiang, 2005, 2007).

Models of oblique transpression with triclinic symmetry describe the strain and orientations of structures in high strain zones with oblique simple shear directions and vorticity vectors that do not coincide with any of the principal strain rate axes of the pure shear component (Fossen and

Tikoff, 1993; Fossen et al., 1994; Robin and Cruden, 1994; Jones and Holdsworth, 1998; Jones and Tanner, 1995; Tikoff and Greene, 1997; Jones et al., 1997; Fossen and Tikoff, 1998; Jiang and Williams, 1998; Lin et al., 1998; Jiang et al., 2001; Czeck and Hudleston, 2004; Jones et al., 2004; Jiang, 2007; Fernández and Díaz-Azpiroz, 2009; Fernández et al., 2013). Consequently, the stretching lineations vary gradually in orientation from horizontal to vertical depending on the obliquity of the transpression (angle between simple shear and pure shear components), the obliquity of the pure shear extrusion component, simple shear to pure shear ratio, finite strain, and strain partitioning and localization of the simple shear component along pre-existing planar anisotropies (Jones and Tanner, 1995; Lin et al., 1998; Jones and Holdsworth, 1998; Jiang and Williams, 1998; Jiang et al., 2001; Jones et al., 2004; Fernández and Díaz-Azpiroz, 2009).

In this paper, we discuss the formation of structures within shear zones and reactivated high strain zones. More specifically, we explore how older structures in the high strain zones influenced the formation of new structures during later transpression, how the orientation of folds can be used to predict the orientation of the stretching lineation, and how the relative orientations of shear bands and stretching lineation can be used to deduce the geometry and symmetry of transpression.

Regional geology

The BGB stretches over 120 km from Lake Nipigon to the west to Long Lake to the east. It consists of six shear zone-bounded and interleaved units of metavolcanic and metasedimentary rocks (Fig. 3-1; Ayres, 1969; Kehlenbeck, 1986; Devaney and Williams, 1989). The three metavolcanic units, namely, the northern (NVU), central (CVU) and southern (SVU) metavolcanic units, consist of mafic to felsic, massive and amygdaloidal flows to pyroclastic volcanic rocks with interflow iron formation, argillaceous layers and graphitic shale (Pye, 1952; Horwood and Pye, 1955; Mackasey,

1975, 1976; Carter, 1987; Williams, 1987; Kresz and Zayachivsky, 1991; Shanks, 1993; Tomlinson et al., 1996). They formed at ca. 2725 Ma (Hart et al., 2002) prior to the deposition of an overlying, southward-prograding clastic wedge in unconformable contact with the volcanic rocks (Devaney and Fralick, 1985; Devaney and Williams, 1989). The clastic wedge is represented by three metasedimentary units (NSU: northern, CSU: central, SSU: southern metasedimentary unit), which were deposited in progressively deeper depositional environments from clast-supported polymictic conglomerate in an alluvial fan or braid-plain system to the north, to graded, turbiditic mudstone to sandstone with thin layers of iron formation and lenses of conglomerate in a submarine fan and/or basin plain environment to the south (Pye, 1952; Horwood and Pye, 1955; Mackasey, 1975, 1976; Barrett and Fralick, 1985, 1989; Williams, 1987; Carter, 1987; Devaney and Williams, 1989). The three metasedimentary units are bracketed in age between ca. 2700 Ma, the U-Pb ages of detrital zircons (Fralick et al., 2006; Chapter 2 of this thesis), and 2694±1.0 Ma, the age of crosscutting porphyry dikes (Chapter 2 of this thesis).

Two similar models were proposed to explain the early tectonic history of the BGB. Devaney and Williams (1989) suggested that the BGB represents an accretionary prism of interleaved metasedimentary rocks and oceanic crust that formed during north-directed subduction below the southern margin of the eastern Wabigoon subprovince. Tomlinson et al., (1996) favored a similar arc-accretion model involving the accretion of back-arc, island arc and ocean floor crust represented by the NVU, CVU and SVU, respectively. They further suggested that the metasedimentary rocks were deposited following the accretion of the metavolcanic rocks to the southern margin of the eastern Wabigoon subprovince and that they were folded and imbricated due to continuing shortening caused by the approaching Wawa arc to the south.

The metavolcanic-metasedimentary panels were subsequently intruded by feldspar-quartz porphyry dikes and granitic to monzodioritic intrusions such as the Croll Lake Stock (Anglin, 1987; Macdonald, 1988; Kresz and Zayachivsky, 1991, 1993; Chapter 2 of this thesis). The 2694±1.0 Ma feldspar-quartz porphyry dikes have tonalite-trondhjemite-granodiorite (TTG) geochemical affinities whereas the 2690±1.0 Ma Croll Lake stock (Corfu, 2000) has a sanukitoid geochemical signature (Chapter 2 of this thesis). Although these dikes and intrusions were generated by broadly similar petrogenetic processes at depths greater than 50 km, the shift from TTG to sanukitoid magmatism indicates the incorporation of a mantle component during the generation of the sanukitoid magmas (Chapter 2 of this thesis).

Early D_1 thrust accretion thickened the crust and led to partial melting, the generation of TTG and sanukitoid magmas, and the emplacement of the Croll Lake stock across several units (SVU, SSU, CVU) of the BGB (Chapter 2 of this thesis). The post-accretion D_2 deformation produced regional, upright and west-plunging, tight F_2 folds and a steeply-dipping S_2 cleavage, which typically parallels bedding across the belt (Devaney and Williams, 1989; Lafrance et al., 2004). D_3 dextral transpression resulted in the formation of a second regional cleavage (S_3) which is axial planar to Z-shaped, map-scale and outcrop-scale, F_3 folds (Williams, 1987, 1989; Devaney and Williams, 1989; Lafrance et al., 2004). The S_3 cleavage is oriented anticlockwise to bedding and to the S_2 cleavage in low strain domains represented by the metasedimentary and metavolcanic units, and it is more pronounced in higher strain domains represented by dextral shear zones at the contact between units. Two major dextral shear zones, the Bankfield-Tombill deformation zone and the Paint Lake fault, bound the BGB to the south and north, respectively (Pye, 1952; Buck, 1986; Reilly, 1987; Williams, 1987; Lafrance et al., 2004). Although these shear zones presently display strike-slip rather than dip-slip shear sense indicators (Williams, 1989; Lafrance et al., 2004), they

likely initially formed as D_1 thrust faults during the accretion of the metavolcanic-metasedimentary units to the southern margin of the eastern Wabigoon subprovince (Lafrance et al., 2004). The paper focuses on the complex structural history of shear zones within the belt, including the Bankfield-Tombill deformation zone and the Paint Lake fault.

Structural Geology

Bankfield-Tombill deformation zone

The Bankfield-Tombill deformation zone (BTDZ; also referred to as the Barton Bay deformation zone) is a kilometre-wide high strain zone along the southern margin of the BGB near the town of Geraldton in the eastern part of the belt (Fig. 3-2; Williams, 1987, Lafrance et al., 2004). Turbiditic sandstone, banded iron formation, polymictic conglomerate, and feldspar-quartz porphyry of the SSU have been strongly folded, transposed, and sheared within this deformation zone. Structures are very well exposed on mechanically stripped outcrops, namely the F Zone, Headframe, OPP and Portal, which are described below.

D_1 structures

On the Headframe outcrop (Fig. 3-3), shallowly (~18°-45°) W- to NW-plunging tight to isoclinal, F_1 folds are outlined by folded, thinly-laminated, banded iron formation and by reversals in stratigraphic facing in graded turbiditic sandstone beds (Fig. 3-4A-B). F_1 folds have amplitudes varying from decimetres to tens of metres. A sericitic cleavage (S_1) is axial planar to the folds and is parallel to bedding along the limb of the folds. Although it could be mistaken for a primary sedimentary lamination, a continuous chloritic foliation (S_1) is axial planar to an F_1 fold defined by a folded mafic dike (Fig. 3-4B-C), and a sericitic S_1 cleavage is preserved in the hinge of a F_2 folded porphyry dike at the OPP outcrop (Fig. 3-5A, B), indicating that S_1 is tectonic in origin.

D_2 structures

At the Headframe and OPP outcrops, the F_1 folds are refolded by open to tight F_2 folds with an axial planar S_2 foliation (Fig. 3-3 and 3-5C). The folds plunge shallowly to the W-WNW parallel to F_1 fold hinges and to a strong stretching mineral lineation (L_2) defined by elongated clasts in conglomerate on the Portal exposure (Fig. 3-6) and by preferentially oriented minerals and mineral aggregates i.e. Fe-carbonate chlorite and sericite streaks along the S_2 cleavage. The superposition of F_1 and F_2 folds result in a coaxial Type 3 fold interference pattern (Fig. 3-4A; Ramsey, 1967). The S_2 cleavage strikes east, dips steeply to the north or south, and is expressed as a spaced (0.5-2 mm) planar fabric defined by laminae of sericite ± chlorite ± carbonate ± biotite. All F_2 folds within the deformation zone have S-shaped asymmetry from outcrop-scale folds (Fig. 3-3,3-5,3-7), which have amplitudes of a few centimeters to a few meters, to the map-scale Hardrock anticline which has an amplitude of 400 metres (Fig. 3-2). The latter is defined by folded feldspar-quartz porphyry intrusions, conglomerate, banded iron formation, and turbiditic sandstone. The folds are transposed parallel to the S_2 cleavage which forms a strong penetrative cleavage across the deformation zone. At the Headframe outcrop, the S_2 cleavage is folded by another set of open to tight, S-shaped folds (F_2') with a strong, steeply-dipping, axial planar crenulation cleavage (S_2') defined by sericite, green mica and chlorite (Fig. 3-4D-F). The F_2' terminology reflects that these folds are only local in occurrence as opposed to the ubiquitous F_2 folds. The F_2' folds have plunges similar to the F_2 folds and their axial planar S_2' cleavage strikes up to 20-25° clockwise of F_2 fold axial planes and the S_2 cleavage. Southwest-trending tourmaline-quartz veins (Fig. 3-7A, B) and southwest- to west-trending quartz-carbonate veins cut across the F_2 folds from one limb, across their axial plane, to the other limb of the folds (Fig. 3-7A, C). The veins are oriented anticlockwise

to the axial plane of the F_2 folds. They are folded by small, asymmetrical S-shaped folds (Fig. 3-7D) similar in orientation to the F_2' folds.

D_3 structures

The D_3 deformation event produced the youngest ductile structures along the BTDZ. At the Headframe outcrop, excellent overprinting relationships are exposed between F_2 and F_2' folds and an E-trending, steeply-dipping cleavage (S_3), which transects the hinge of the folds (Fig. 3-4E-F). The S_3 cleavage is a continuous or spaced foliation (0.1-5 mm spacing) defined by sericite and chlorite as well as by alternating felsic and mafic microlithons of green mica/chlorite and quartz/carbonate. It strikes 10°-30° anticlockwise to the penetrative S_2 cleavage along the deformation zone (Fig. 3-4C). It is axial-planar to shallowly W- to SW-plunging (6°-32°), open to tight, asymmetrical and Z-shaped, F_3 folds (Fig. 3-4E). The folds typically occur as a series of outcrop-scale Z-shaped folds with amplitudes of a few centimeters to meters but they are also present on map-scale with amplitudes of hundred or more metres (Fig. 3-2). A lineation (L_{3c}) is present as a crinkle or as a fine ridge-and-groove corrugation imprinted on the S_2 cleavage. It plunges very shallowly (~6°) to the east and is oblique to F_3 fold axes, which plunge 10° to 34° to the west. Dextral shear sense indicators are present in localized narrow zones along the deformation zone. These include asymmetrical strain shadows around clasts in sheared conglomerate (Fig. 3-8A), extensional quartz tension gashes oriented clockwise to the S_2 cleavage, and dextral shear fractures (Fig. 3-8B) and shear bands oriented clockwise to the S_2 cleavage (Fig. 3-8C).

The Bankfield-Tombill fault is a narrow brittle-ductile fault zone along the southern boundary of both the BTDZ and the BGB. It is roughly parallel to S_2 foliation and is filled with multiple smoky

black quartz-carbonate veins totaling ~1 m in width (Fig. 3-8D) that are boudinaged along SW-trending antithetic sinistral and SE-trending synthetic dextral shear fractures (Fig. 3-8E). Asymmetric strain shadows surrounding small pillow fragments also indicate dextral shear sense along the fault zone (Fig. 3-8F)

Paint Lake Fault

The eastern extension of Paint Lake Fault is exposed at the Missing Link outcrop along the Kinghorn Road, ~9 km northeast of Jellicoe (Fig. 3-1). The outcrop exposes strongly flattened and attenuated pillows in deformed mafic metavolcanic rocks. The pillows are flattened parallel to the regional S_2 foliation (Fig. 3-9), which strikes ENE and dips steeply. Northeast-trending quartz-ankerite veins with fibrous and laminated textures (set 1) extend up to 2 m across the S_2 foliation (Fig. 3-10A). Other lensoid quartz-ankerite veins are oriented at a higher angle to the S_2 foliation (5°-20° anticlockwise of the NE-trending veins) whereas still others are boudinaged parallel to the foliation (Fig. 3-10B). The NE-trending quartz-ankerite veins are fringed by Z-shaped flanking folds (Fig. 3-10C) and by cm-long, NW-trending, quartz-ankerite tension gashes (Set 2; Fig. 3-9). The flanking folds have similar orientation to Z-shaped F_3 folds overprinting the S_2 foliation. A continuous chloritic S_3 cleavage is axial planar to the F_3 folds.

Road 801 exposure

The Road 801 exposure consists of several stripped outcrops located immediately west of Road 801, 2.3 km northwest of its intersection with TransCanada Highway #11 (Fig. 3-1). Several high strain zones are exposed in weak mudstone horizons within a continuous, N-younging sequence of turbiditic sandstone, pebbly sandstone and banded iron formation. Beds are steeply-dipping to the north or south and ENE-striking. Layers of banded iron formation are folded by west-plunging,

open to tight, S-shaped F_2 folds (Fig. 3-11, 3-12A-B). The folds have an axial plane S_2 foliation which is parallel to bedding along the long limbs of the folds. They are overprinted by a SW-trending S_3 foliation defined by sericite and chlorite (Fig. 3-12B), which is oriented ca. 15-20° anticlockwise to bedding-parallel S_2. The S_3 foliation is axial-planar to open, mm- to dm-scale, Z-shaped, F_3 folds. The folds are spatially associated with straight, NE-trending quartz-carbonate veins (Fig. 3-12C). The veins are oriented parallel to the S_3 cleavage and the axial plane of the F_3 folds, and thus they are oriented anticlockwise to the S_2 cleavage, similar to those described at the F Zone and Missing Link.

In the high strain zones, the S_3 foliation is deflected in clockwise manner into the orientation of the ENE-striking, bedding-parallel S_2 cleavage, forming a composite S_2-S_3 foliation. The S_2-S_3 foliation is folded by Z-shaped F_3' folds with a NE-striking axial-planar S_3' foliation (Fig. 3-11, 3-12D-E). The latter is expressed as a closely-spaced crenulation cleavage in sandstone and as a differentiated sericitic and chloritic cleavage in mudstone. The composite S_2-S_3 foliation is sinistrally offset along S_3' foliation planes, which acted as antithetic slip surfaces during their clockwise rotation towards the composite S_2-S_3 foliation (Fig. 3-12E). The SW-trending quartz-carbonate veins are also deflected in clockwise manner within the high strain zones, where they are boudinaged, overprinted by W- to NW-trending dextral shear bands, and folded by small, Z-shaped, F_3' folds. The orientation of the F_3' folds is similar to that of the F_3 folds but they differ slightly by their generally steeper, more southwesterly plunge (Fig. 3-12A).

Discussion

Early D_1 thrusting

The imbrication and interleaving of metasedimentary and metavolcanic units in the belt have been attributed to an early thrusting event (Devaney and Williams, 1989; Williams, 1990; Tomlinson et al., 1996; Lafrance et al., 2004). Although this interpretation is supported by regional tectonic observations (Lafrance et al., 2004), few D_1 structures have been described in those studies. Unit-bounding faults are typically reactivated as late transcurrent shear zones, thus internal structures within these fault zones reflect their latest movement. Additionally, no axial plane cleavage has been described in association with the few, previously reported, F_1 folds. Although these folds are interpreted as thrust-related tectonic structures, the lack of an associated axial plane cleavage is equally consistent with their formation as soft-sediment slump folds within a tectonically active depositional basin (Elliott and Williams, 1988).

Mechanical excavation and overburden removal in the Geraldton area has produced large new outcrops exposing multiple F_1 folds overprinted by younger structures. These outcrops also expose an early tectonic S_1 cleavage within igneous mafic dikes and porphyry intrusions. The S_1 cleavage is parallel to bedding in surrounding sandstone and banded iron formation and is folded within the hinge of F_2 folds. The presence of this early ductile fabric within igneous intrusions suggests that the F_1 folds and S_1 cleavage formed by ductile plastic processes consistent with early tectonic thrust-imbrication of the belt. The chronology of the D_1 event is bracketed between 2694 ± 1 Ma, the U-Pb zircon crystallization age of the feldspar-quartz porphyry dikes (Chapter 2 of this thesis), and ca. 2690 Ma, the U-Pb zircon crystallization age of the Croll Lake Stock (Corfu, 2000) which

was emplaced across the CVU, CSU and NVU (Kresz and Zayachivsky, 1991, 1993) after the juxtaposition and thrust-imbrication of these units.

D_2 sinistral transpression

The Bankfield-Tombill deformation zone is characterized by a strong and straight S_2 cleavage. The latter is axial planar to the Hard Rock anticline which represents the most prominent map-scale structure along the zone. The Hard Rock anticline and its axial plane cleavage correlate with other regional, km-scale folds and their axial planar cleavage in the SSU in the Geraldton area (e.g. Ellis and Barton Bay synclines, Talmora anticline) and Beardmore area (e.g. Beardmore syncline; Pye, 1952; Horwood and Pye, 1955; Lafrance et al., 2004). S_2 is present as a penetrative, bedding-parallel, regional cleavage within all units across the BGB and is accentuated in the two deformation zones bounding the belt to the north (Paint Lake) and south (Bankfield-Tombill), where it is expressed as an intense transposition foliation in the Geraldton area, by flattened pillows at Missing Link, and by flattened pebbles and clasts along Paint Lake (Reilly, 1987; Lafrance et al., 2004). The Hard Rock anticline differs from the other regional map-scale F_2 folds by its asymmetrical S-shape, which is repeated on outcrop-scale by the S-shaped asymmetry of the F_2 folds and that of overprinting F_2' folds which formed later during the same deformation event

The F_2 and F_2' folds are interpreted to have formed during the same progressive deformation event because of their similar orientations implying the same shear sense and their overprinting by younger D_3 structures. Northeast- to east-trending extensional veins transect the F_2 folds at the F Zone and the S_2 cleavage at the 801 stripping and Missing Link. The veins predate the D_3 event because they are boudinaged within D_3 dextral shear zone at the 801stripping and acted as a planar anisotropy that localized buckling and the formation of D_3 flanking folds at the 801 stripping,

Missing Link and F Zone. The veins formed during NE-SW bulk shortening, which is consistent with the formation of S-shaped F_2 and F_2' folds during sinistral shear along the Bankfield-Tombill deformation zone. Therefore, the map-scale F_2 folds and the regional S_2 cleavage formed to accommodate the bulk shortening across the belt as sinistral shearing became localized along the Paint Lake and Bankfield-Tombill deformation zones during regional sinistral transpression across the belt.

Alternatively, the formation of S-shaped F_2' folds, which overprint the S_2 cleavage and F_2 folds, could be explained by the syn-D_3 back-rotation of the S_2 foliation in decimeter-wide domains bounded by dextral shear bands that formed during D_3 dextral shearing. Thus, the F_2' folds may represent antithetic sinistral drag folds in a dextral shear zone. Antithetic drag folds are thought to form where shear zones merge reversing or perturbing the flow of the rocks (Harris, 2002; Carreras et al., 2005). Although the F_2' folds could have formed as antithetic drag folds during dextral shear, antithetic drag folds generally do not have an axial planar crenulation cleavage (Harris, 2002). Therefore, it is more likely that the F_2' folds formed as synthetic drag folds during D_2 sinistral shearing. More pronounced antithetic dextral shearing occurred along S_2' cleavage planes as S_2' rotated in anticlockwise manner during D_2 sinistral shearing, back-rotated the S_2 cleavage and bedding resulting in the formation of sinistral folds (Fig. 3-13).

D_3 dextral transpression

The BGB was first described as a D_3 regional dextral transpression zone by Devaney and Williams (1989) and Lafrance et al. (2004). Regional transpression involves a component of *transcurrent* movement along faults parallel to the trend of an orogenic belt concurrent with a component of *compression* across the belt (Harland, 1971; Robin and Cruden, 1994). Lafrance et al. (2004)

suggested that the strain during transpression was partitioned between the lithological panels and the panel-bounding shear zones. The metasedimentary and metavolcanic units were subjected to mainly pure shear, whereas the dextral strike-slip shear zones underwent simple shear. As all metavolcanic and metasedimentary units were steeply dipping by the end of the D_2 deformation event, bulk NW-directed shortening across the belt resulted in the formation of a regional S_3 cleavage, which refracts in dextral manner as it passes from mudstone beds to more competent sandstone beds in the metasedimentary units, and in the formation of dextral shear zones along contacts between units and in reactivated D_2 high strain zones (Lafrance et al., 2004).

The BTDZ is defined by a pronounced S_2 cleavage, several generations of folds, a strong westerly-plunging stretching lineation, and multiple dextral shear sense indicators. Although S_3 and S_3' cleavages are present, the S_2 cleavage is more pronounced than the S_3 or S_3'cleavages. The presence of dextral shear sense indicators (Fig. 3-8A, Fig. 9e in Lafrance et al., 2004), suggest that the S_2 cleavage controlled the flow of the rocks during D_3 dextral shearing. The S_2 cleavage acted as a planar anisotropy that accommodated the shearing during dextral movement along the BTDZ. The slip direction can be obtained from the orientation of the S_2 cleavage, which acted as the C-plane during dextral shearing, and the dextral shear bands (C'). The latter are typically straight and uniform in orientation suggesting that they formed late and did not rotate during progressive D_3 dextral shearing. The slip direction is perpendicular to the intersection between the shear bands (C') and the S_2 cleavage. As the intersection between the two foliations is sub-vertical, the slip direction (SDG) is sub-horizontal and parallel to the orientation of the striation and crinkle lineation (L_{3c}) along the S_2 cleavage plane (Fig. 3-14). This suggests that the L_{3c} lineation represents a ridge-in-groove ductile slickenline (Lin and Williams 1992), which formed parallel to the slip direction during dextral shearing.

All fold generations (F_1, F_2, F_3) along the BTDZ plunge 20°-30° to the west roughly parallel to the stretching lineation (Fig. 3-2). This suggests that the fold axes and the stretching lineation, which approximates the orientation of the maximum finite principal axis of strain (λ_1; e.g. Tikoff and Greene, 1997), were rotated and attained a stable orientation, represented by the fabric attractor of Passchier (1997). This also indicates that although the stretching lineation initially formed during the D_2 deformation, it likely underwent more rotation and became more accentuated during the D_3 deformation. Thus, the stretching lineation represents the sum of the bulk strain during both D_2 and D_3 deformations. As F_2 and F_3 folds roughly have the same westerly plunge in other areas across the BGB (Lafrance et al., 2004; this study), their trend and plunge can be used in the absence of a stretching lineation as the approximate orientation of λ_1.

Despite the lack of a stretching lineation at the 801 exposure, the orientation of λ_1 and the fabric attractor can be deduced from the orientation of F_2 and F_3 fold axes, which have similar trends and plunges. F_3' drag folds have a wider range of plunges varying from steep to parallel to the plunge of F_2 and F_3 folds (Fig. 3-12A). F_3 and F_3' folds likely nucleated with steeply SW-plunging fold axes oriented roughly perpendicular to the slip direction and, together with older F_2 fold axes, rotated with increasing strain towards a shallower, west-plunging orientation, representing the fabric attractor (Fig. 3-12A, 3-14). Fold axes first rotated by hinge migration and then acted as passive material lines (Lafrance and Williams, 1992) that tracked λ_1 and rotated towards the fabric attractor during the progressive D_3 deformation.

In transpressional shear zones, the pure shear component of the deformation controls the orientation of fabrics at high strains (Fossen and Tikoff, 1998; Teyssier and Tikoff, 1999). The fabrics rotate towards the fabric attractor which is the direction of the maximum principal strain rate of the pure shear component of the transpression (Kuiper et al., 2007; Fernández and Díaz-

Azpiroz, 2009). During a transpressional deformation with monoclinic symmetry, the maximum principal strain rate of the pure shear component of the deformation is either parallel or perpendicular to the vorticity vector (rotation axis) and to the shear direction (Sanderson and Marchini, 1984; Tikoff and Greene, 1997). If it is oblique to the vorticity vector and shear direction, the symmetry of the deformation is triclinic (Lin et al., 1998; Fossen and Tikoff, 1998). Along both the BTDZ and shear zones at the 801 stripped outcrops, the fold axes and λ_1, representing the fabric attractor, plunge westerly ~20° steeper than the slip or shear direction (Fig. 3-14). This suggests that the symmetry of the D_3 transpressional shear zones is triclinic and that the orientations of the fold axes and stretching lineation were stabilized at high strain by shallowly-plunging lateral extrusion parallel to the fabric attractor and maximum principal strain rate of the pure shear component (Teyssier and Tikoff, 1999).

Tectonic correlations

Geochronological, geochemical and aeromagnetic characteristics suggest that the lithological units of the BGB can be correlated with those of the Lac des Iles greenstone belt across the Mesoproterozoic Nipigon diabase complex (Pye, 1968; Blackburn et al., 1991; Tomlinson, 1996; Tomlinson et al., 1999, 2003; Ketchum, 2002). The metavolcanic rocks of the Lac des Iles greenstone belt are high Fe-tholeiites, calc-alkaline basalts and andesites with LREE and Th-enrichments and negative Nb and Ti anomalies that are similar in geochemistry to the CVU of the BGB (Tomlinson, 1996, 1997). In the northern part of the Lac des Iles greenstone belt, a dacitic tuff yielded an age of 2727.8±1.3 Ma (Tomlinson et al., 2003). Therefore, arc related volcanism was active in both the Lac des Iles and the CVU of the BGB (Tomlinson, 1996, 1997). The supracrustal rocks of the Lac des Iles were intruded by a sanukitoid suite intrusion at 2690 Ma (Kamo, 2004; Stone 2010). Thus, the volcanic and intrusive history of the Lac des Iles greenstone

belt are similar to that of the BGB. However, detailed structural mapping is not available for the Lac des Iles greenstone belt; therefore, the comparison of its tectonic evolution to that of the BGB is not possible.

The Fort Frances-Rainy Lake area is located ca. 500 km west of the BGB along the Wabigoon-Quetico boundary. Its depositional and structural history is similar to that of the BGB. It comprises ca. 2725 Ma metavolcanic rocks which are similar in age to those in the BGB and which are overlain by ca. 2704-2692 Ma deep-water turbidites of the Coutchiching Group and by ca. 2695-2686 Ma alluvial conglomerates and arenites of the Seine Group (Poulsen et al., 1980; Davis et al., 1989). These two groups correlate with the turbiditic sandstones and conglomerate of the BGB. Early D_1 thrusting and folding occurred prior to the deposition of the Seine Group and produced a bedding-parallel S_1 cleavage (Poulsen et al., 1980; Davis et al., 1989; Tabor and Hudleston, 1991; Fralick and Davis, 1999). D_1 structures and the Seine Group were then overprinted by regional-scale folds during N-S D_2 compression and by transcurrent shear zones during later D_3 dextral transpression (Poulsen et al., 1980; Davis et al., 1989; Tabor and Hudleston, 1991). The broad range of mineral lineation orientations, plunging from vertical to horizontal and trending either east or west, has been explained by D_3 transpression with triclinic asymmetry (Czeck and Hudleston, 2003).

Other major tectonic boundaries of the Superior craton have undergone a tectonic history similar to the BGB. The southern tectonic boundary of the predominantly metasedimentary English River subprovince with the dominantly granitoid Winnipeg River terrane (previously Winnipeg River subprovince) underwent an early D_1 deformation event, which resulted in the formation of a bedding-parallel S_1 foliation, followed by D_2 sinistral transpression anzxd D_3 dextral transpression (Sanborn-Barrie, 1988; Beakhouse, 1991). The northern tectonic boundary of the English River

subprovince with the Mesoarchean North Caribou terrane comprises a narrow corridor of supracrustal rocks, called the Rice Lake greenstone belt, which is bounded by two major crustal-scale faults: the Wanipigow fault zone to the north and the Manigotagan fault zone to the south (Anderson, 2008, 2013 and references therein). The belt consists of mafic to felsic metavolcanic rocks and clastic and chemical metasedimentary rocks that accumulated between ca. 2750 Ma and <2700 Ma in a back arc basin. The basin was later thrusted and accreted to the southern margin of the North Caribou terrane and then unconformably overlain by <2705 Ma turbiditic metasedimentary rocks (Anderson, 2013). These turbiditic rocks are the low metamorphic-grade equivalents of the metasedimentary rocks of the English River subprovince to the south, which were deposited as a southward prograding clastic wedge along the southern margin of the Mesoarchean North Caribou terrane (Walker, 1987; Meyn and Palonen, 1980; Anderson, 2013). Terminal collision between the North Caribou terrane and English River subprovince began with major folding of the metavolcanic rocks and overlying turbidites during sinistral transpression and ended with the formation of Z-shaped folds, a regional axial planar cleavage, and a shallowly-plunging stretching lineation during dextral transpression (Anderson, 2013). The tectonic evolution of these two tectonic boundaries is very similar to that of the BGB which as many other tectonic boundaries in the Superior craton underwent a prolonged and complex tectonic evolution involving early thrusting followed by transcurrent transpressional events.

The BGB is a major past-producing gold belt with a past production of over 4.1 Moz Au (Mason and McConnell, 1983; Mason and White, 1986) as are several other major deformation corridors in the Superior craton. Two very prolific deformation corridors in the Abitibi subprovince, the Porcupine-Destor and Larder Lake-Cadillac deformation zones, are long-lived, major, crustal-scale faults which produced over 175 Moz Au over the last 110 years (Gosselin and Dubé, 2005;

Bleeker, 2015). Although the Porcupine-Destor deformation zone lies away from a terrane or subprovince boundary, it is similar to structures in the Geraldton camp because it post-dates the early folding of the Porcupine sedimentary package (Bateman, 2008; Bleeker, 2012; Monecke et al., 2017).

The faults bound basins in which younger turbiditic sandstone (ca. 2690-2685 Ma Porcupine assemblage) and/or fluvial conglomerates (ca. 2680 Ma – 2670 Ma Timiskaming assemblage), were deposited over older metavolcanic rocks (Ayer et al., 2005; Thurston et al., 2008). Following their deposition, these rocks were thrusted and folded during collisional closure of the basins and further deformed during transcurrent sinistral and dextral transpression at ca. 2660 Ma to ca. 2600 Ma (Robert, 1989; Bleeker, 1995, 1999, 2015 and references therein). Faulting during the deformation of the basins provided the conduits for the ascent of gold-bearing hydrothermal fluids and the formation of gold deposits in second- and third-order structures (Robert, 1989, Robert et al., 2005 and references therein). Such tectonic history is similar to that of the BGB and may explain, at least in part, why the BGB as other belts along major tectonic boundaries in the Superior craton host major gold deposits.

Conclusions

Early structural studies explained the tectonic evolution of the BGB by two deformation events, an early thrusting and regional folding event followed by a dextral transpressive event (Williams, 1987; Percival and Sullivan, 1988; Devaney and Williams, 1989). This interpretation was later refined and the regional folding was attributed to a N-S compressive event that took place after the early thrusting event but before the dextral transpressive event (Lafrance et al., 2004). In this study,

we propose that the early thrusting and folding event was followed by sinistral and dextral transpressive events.

The tectonic evolution of the BGB began with early D_1 thrust imbrication of the metavolcanic and metasedimentary units during closure of the Quetico basin between 2694±1 Ma, the crystallization age of S_1-foliated feldspar-quartz porphyry dikes, and 2690±1 Ma, the crystallization age of the stitching Croll Lake Stock. Early D_1 thrusting was followed by a D_2 sinistral transpressive event which is expressed by the formation of regional folds, a regional cleavage, and two major belt-bounding deformation zones: the BTDZ and Paint Lake Fault to the south and north, respectively. Within the two high strain zones, bedding was transposed parallel to the regional cleavage, folded by two generations of S-shaped folds, and overprinted by extensional tourmaline-rich and quartz-carbonate veins oriented anticlockwise of bedding and cleavage. During a subsequent regional D_3 dextral transpression event, the belt-bounding high strain zones were reactivated as dextral shear zones, as indicated by the presence of Z-shaped folds, dextral shear bands and other dextral shear sense indicators, and a second regional cleavage oriented anticlockwise to bedding formed across the metavolcanic and metasedimentary units. The shear direction is near horizontal and oblique to the fabric attractor defined by the plunge of 20° to the west of the stretching lineation and F_1 to F_3 fold axes. This obliquity between the slip direction and the maximum principal strain rate of the pure shear component (fabric attractor) of the deformation suggests that the D_3 shear zones have triclinic deformation symmetry.

The tectonic evolution of the BGB is similar to that of other major terrane boundaries and gold camps such as the Abitibi and Rice Lake greenstone belts. These gold camps are associated with major crustal-scale faults in high-strain deformation corridors which underwent early thrusting followed by sinistral and dextral transpression. Thus, multiple tectonic events leading to the

reactivation of older structures is likely a key factor in facilitating the migration of hydrothermal fluids and the formation of gold deposits.

References

Allmendinger, R.W., Cardozo, N.C., Fisher, D., 2013. Structural Geology Algorithms: Vectors & Tensors. Cambridge University Press, Cambridge, England. 289 p.

Anderson, S.D. 2013. The Rice Lake mine trend, Manitoba: regional setting, host rock stratigraphy and structural evolution of a classical Archean orogenic gold system; Geological Association of Canada–Mineralogical Association of Canada Joint Annual Meeting, Field Trip Guidebook FT-A1; Manitoba Innovation, Energy and Mines, Manitoba Geological Survey, Open File OF2013-4, 47 p.

Anderson, S.D. 2008. Geology of the Rice Lake area, Rice Lake greenstone belt, southeastern Manitoba (parts of NTS 52L13, 52M4); Manitoba Science, Technology, Energy and Mines, Manitoba Geological Survey, Geoscientific Report GR2008-1, 97 p.

Anglin, C.D., 1987. Geology, structure and geochemistry of gold mineralization in the Geraldton area, Northwestern Ontario. Unpublished Master's Thesis. Memorial University of Newfoundland, St. John's, Newfoundland. 283 p.

Ayer, J., Thurston, P.C., Bateman, R., Dubé, B., Gibson, H.L., Hamilton, M.A., Hathway, B., Hocker, S.M., Houlé, M., Hudak, G.J., Ispolatov, V., Lafrance, B., Lesher, C.M., MacDonald, P.J., Péloquin, A.S., Piercey, S.J., Reed, L.E., Thompson, P.H., 2005. Overview of results

from the Greenstone Architecture Project: Discover Abitibi Initiative, Ontario Geological Survey.

Ayres, L.D., 1969. Early Precambrian stratigraphy of part of Lake Superior Provincial Park, Canada, and its implication for the origin of the Superior Province. Unpublished Ph.D thesis. Princeton University, Princeton, NJ. 798 p.

Barrett, T.J., Fralick, P.W., 1985. Sediment redeposition in Archean Iron Formation: Examples from the Beardmore-Geraldton Belt, Ontario. J. Sediment. Petrol. 55, 205–212.

Barrett, T.J., Fralick, P.W., 1989. Turbidites and iron formations, Beardmore-Geraldton, Ontario: application of a combined ramp/fan model to Archaean clastic and chemical sedimentation. Sedimentology 36, 221–234. doi: 10.1111/j.1365-3091.1989.tb00604.x

Bateman, R., Ayer, J., Dubé, B., 2008. The Timmins-Porcupine Gold Camp, Ontario: Anatomy of an Archean Greenstone Belt and Ontogeny of Gold Mineralization. Econ. Geol. 103, 1285–1308. doi:10.2113/gsecongeo.103.6.1285

Beakhouse, G.P., 1991. Winnipeg River Subprovince, in: Thurston, P.C., Williams, H.R., Sutcliffe, R.H., Stott, G.M. (Eds.), Geology of Ontario. Special Volume 4. Part 1. Ontario Geological Survey, pp. 279–301.

Bethune, K.M., Helmstaedt, H.H., McNicoll, V.J., 2006. Structural analysis of the Miniss River and related faults, western Superior Province: post-collisional displacement initiated at terrane boundaries. Can. J. Earth Sci. 43, 1031–1054. doi:10.1139/E06-017

Blackburn, C.E., Johns, G.W., Ayer, J., Davis, D.W., 1991. Wabigoon Subprovince, in: Thurston, P.C., Williams, H.R., Sutcliffe, R.H., Stott, G.M. (Eds.), Geology of Ontario. Ontario Geological Survey, Special Volume 4, Part 1, pp. 303–381.

Bleeker, W., 1995. Day 1: Surface geology of the Porcupine camp, In: Tectonics and metallogeny of Archean crust in the Abitibi–Kapuskasing–Wawa region, field trip guidebook; Geological Survey of Canada, Open File 3141, p. 13–37.

Bleeker, W., 1999. Structure, stratigraphy, and primary setting of the Kidd Creek volcanogenic massive sulphide deposit: a semiquantitative reconstruction, In: The Giant Kidd Creek Volcanogenic Massive Sulfide Deposit, western Abitibi Subprovince, Canada, (ed.) M.D. Hannington and C.T. Barrie; Society of Economic Geologist, Economic Geology Monograph 10, p. 71–121.

Bleeker, W., 2012. Targeted Geoscience Initiative 4. Lode Gold Deposits in Ancient Deformed and Metamorphosed Terranes: The Role of Extension in the Formation of Timiskaming Basins and Large Gold Deposits, Abitibi Greenstone Belt—A Discussion, in Summary of Field Work and Other Activities 2012, Ontario Geological Survey, Open File Report 6280, p.47-1 to 47-12.

Bleeker, W., 2015. Synorogenic gold mineralization in granite-greenstone terranes: the deep connection between extension, major faults, synorogenic clastic basins, magmatism, thrust inversion, and long-term preservation, in: Dubé, B., Mercier-Langevin, P. (Eds.), Targeted Geoscience Initiative 4: Contributions to the Understanding of Precambrian Lode Gold Deposits and Implications for Exploration, Open File 7852. pp. 25–47. doi:10.4095/296624

Buck, S., 1986. Structural studies and gabbro mylonitization within the Barton Bay Deformation Zone, Geraldton, Ontario. Unpublished MSc thesis. Brock University, St. Catharines, Ontario. 171 p.

Cardozo, N., Allmendinger, R.W., 2013. Spherical projections with OSXStereonet. Comput. Geosci. 51, 193–205. doi:10.1016/j.cageo.2012.07.021

Carter, M.W., 1987. Geology of McComber and Vincent Townships, District of Thunder Bay; Ontario Geological Survey, Open File Report 5648, 144p.

Carreras, J., Druguet, E., Griera, A., 2005. Shear zone-related folds. J. Struct. Geol. 27, 1229–1251. doi:10.1016/j.jsg.2004.08.004

Corfu, F., 2000. Extraction of Pb with atrificially too-old ages during stepwise dissolution experiments on Archean zircon. Lithos 53, 279–291.

Czeck, D.M., Hudleston, P.J., 2003. Testing models for obliquely plunging lineations in transpression: A natural example and theoretical discussion. J. Struct. Geol. 25, 959–982. doi:10.1016/S0191-8141(02)00079-2

Czeck, D.M., Hudleston, P.J., 2004. Physical experiments of vertical transpression with localized nonvertical extrusion. J. Struct. Geol. 26, 573–581. doi:10.1016/j.jsg.2003.07.002

Daigneault, R., Mueller, W.U., Chown, E.H., 2002. Oblique Archean subduction: Accretion and exhumation of an oceanic arc during dextral transpression, Southern Volcanic Zone, Abitibi Subprovince Canada. Precambrian Res. 115, 261–290. doi:10.1016/S0301-9268(02)00012-8

Davis, D.W., Poulsen, K.H., Kamo, S.L., 1989. New Insights into Archean Crustal Development from Geochronology in the Rainy Lake Area, Superior Province, Canada. J. Geol. 97, 379–398.

Devaney, J.R., Fralick, P.W., 1985. Regional sedimentology of the Namewaminikan Group, northern Ontario: Archean fluvial fans, braided rivers, deltas and an aquabasin., in: Current Research, Part B, Paper 85-1B. Geological Survey of Canada, pp. 125–132.

Devaney, J.R., Williams, H.R., 1989. Evolution of an Archean subprovince boundary: a sedimentological and structural study of part of the Wabigoon–Quetico boundary in northern Ontario. Can. J. Earth Sci. 26, 1013–1026.

Dewey, J.F., Holdsworth, R.E., Strachan, R.A., 1998. Transpression and transtension zones. Geol. Soc. London, Spec. Publ. 135, 1–14. doi:10.1144/GSL.SP.1998.135.01.01

Elliott, C.G., Williams, P.F., 1988. Sediment slump structures: a review of diagnostic criteria and application to an example from Newfoundland. J. Struct. Geol. 10, 171–182. doi:10.1016/0191-8141(88)90114-9

Fernández, C., Czeck, D.M., Díaz-Azpiroz, M., 2013. Testing the model of oblique transpression with oblique extrusion in two natural cases steps and consequences. J. Struct. Geol. 54, 85–102. doi:10.1016/j.jsg.2013.07.001

Fernández, C., Díaz-Azpiroz, M., 2009. Triclinic transpression zones with inclined extrusion. J. Struct. Geol. 31, 1255–1269. doi:10.1016/j.jsg.2009.07.001

Fossen, H., Tikoff, B., 1993. The deformation matrix for simultaneous simple shearing, pure shearing and volume change, and its application to transpression-transtension tectonics. J. Struct. Geol. 15, 413–422. doi:10.1016/0191-8141(93)90137-Y

Fossen, H., Tikoff, B., 1998. Extended models of transpression and transtension, and application to tectonic settings. Geol. Soc. London, Spec. Publ. 135, 15–33. doi:10.1144/GSL.SP.1998.135.01.02

Fossen, H., Tikoff, B., Teyssier, C., 1994. Strain modeling of transpressional and transtensional deformation. Nor. Geol. Tidsskr. 74, 134–145.

Fralick, P.W., Davis, D.W., 1999. The Seine-Coutchiching problem revisited: Sedimentology, geochronology, and geochemistry of sedimentary units in the Rainy Lake and Sioux Lookout areas, In: Harrap, R.M., Helmstaedt, H.H. (Eds.), 1999 Western Superior Transect 5th Annual Workshop. Lithoprobe Report 70, Lithoprobe Secretariat, The University of British Columbia, Vancouver, B.C. p. 66–75.

Fralick, P.W., Purdon, R.H., Davis, D.W., 2006. Neoarchean trans-subprovince sediment transport in southwestern Superior Province: sedimentological, geochemical and geochronological evidence. Can. J. Earth Sci. 43, 1055–1070. doi:10.1139/E06-059

Gosselin, P., Dubé, B., 2005. Gold deposits of Canada: distribution, geological parameters and gold content; Geological Survey of Canada, Open File 4896; doi:10.4095/220380; 105 p.

Harland, W.B., 1971. Tectonic transpression in the Caledonian Spitsbergen. Geol. Mag. 108, 27–42.

Harris, L.B., 2002. Folding in high-grade rocks due to back-rotation between shear zones. J. Struct. Geol. 25, 223–240. doi:10.1016/S0191-8141(02)00024-X

Hart, T.R., terMeer, M., and Jolette, C., 2002. Precambrian Geology of Kitto, Eva, Summers, Dorothea and Sandra Townships, Northwestern Ontario: Phoenix Bedrock Mapping Project; Ontario Geological Survey, Open File Report 6095, 206 p.

Horwood, H.C., Pye, E.G., 1955. Geology of Ashmore Township., in: 60th Annual Report of the Ontario Department of Mines, Part 5. Ontario Department of Mines, 139 p.

Jiang, D., 2005. Problems of transpression and transtension. Geol. Assoc. Canada-Mineral Assoc. Canada Abstr. 30, 97. doi:10.1029/2004JB003124

Jiang, D., Lin, S., Williams, P.F., 2001. Deformation path in high-strain zones, with reference to slip partitioning in transpressional plate-boundary regions. J. Struct. Geol. 23, 991–1005. doi:10.1016/S0191-8141(00)00170-X

Jiang, D., 2007. Sustainable transpression: An examination of strain and kinematics in deforming zones with migrating boundaries. J. Struct. Geol. 29, 1984–2005. doi:10.1016/j.jsg.2007.09.007

Jiang, D., Williams, P.F., 1998. High-strain zones: a unified model. J. Struct. Geol. 20, 1105–1120. doi:10.1016/S0191-8141(98)00025-X

Jones, R.R., Holdsworth, R.E., 1998. Oblique simple shear in transpression zones. Geol. Soc. London, Spec. Publ. 135, 35–40. doi:10.1144/GSL.SP.1998.135.01.03

Jones, R.R., Holdsworth, R.E., Bailey, W., 1997. Lateral extrusion in transpression zones: the importance of boundary conditions. J. Struct. Geol. 19, 1201–1217. doi:10.1016/S0191-8141(97)00034-5

Jones, R.R., Holdsworth, R.E., Clegg, P., McCaffrey, K., Tavarnelli, E., 2004. Inclined transpression. J. Struct. Geol. 26, 1531–1548. doi:10.1016/j.jsg.2004.01.004

Jones, R.R., Tanner, P.W.G., 1995. Strain partitioning in transpression zones. J. Struct. Geol. 17, 793–802. doi:10.1016/0191-8141(94)00102-6

Kamo, S.L. 2004. U-Pb geochronological investigations of rocks from the Lac des Iles area, northwestern Ontario, the Michipicoten greenstone belt, Wawa, and the Tomiko terrane, Mattawa, Ontario; unpublished report of the Jack Satterly Geochronology Laboratory, Department of Geology, University of Toronto, Earth Sciences Centre, 22 Russell Street, Toronto, Ontario.

Kehlenbeck, M.M., 1986. Folds and folding in the Beardmore - Geraldton fold belt. Can. J. Earth Sci. 23, 158–171.

Ketchum, J.W.F., 2002. Report for the Ontario Geological Survey on U–Pb geochronological results from the Beardmore–Geraldton greenstone belt, Superior Province, Ontario. Earth Sci. Dep. Royal Ontario Museum, 7 p.

Kresz, D.U. and Zayachivsky, B., 1991. Precambrian Geology, northern Long Lake area; Ontario Geological Survey, Report 273, 77 p.

Kresz, D.U. and Zayachivsky, B. 1993. Precambrian geology, Seagram Lake area; Ontario Geological Survey, Report 287, 81 p.

Kuiper, Y.D., Jiang, D., Lin, S., 2007. Relationship between non-cylindrical fold geometry and the shear direction in monoclinic and triclinic shear zones. Journal of Structural Geology 29, 1022-1033.

Lafrance, B., DeWolfe, J.C., Stott, G.M., 2004. A structural reappraisal of the Beardmore-Geraldton Belt at the southern boundary of the Wabigoon subprovince, Ontario, and implications for gold mineralization. Can. J. Earth Sci. 41, 217–235. doi:10.1139/E03-090

Lafrance, B., Williams, P.F., 1992. Oblique-cleavage folds: A critical discussion with examples from the Canadian Appalachians. Tectonophysics 207, 315–330. doi:10.1016/0040-1951(92)90393-K

Lavigne, M.J. 2009. Distribution of gold with respect to lithologies, metamorphic facies and strain state in the Beardmore–Geraldton greenstone belt; Ontario Geological Survey, Open File Report 6241, 88p.

Lin, S., Jiang, D., Williams, P.F., 1998. Transpression (or transtension) zones of triclinic symmetry: natural example and theoretical modelling. Geol. Soc. London, Spec. Publ. 135, 41–57. doi:10.1144/GSL.SP.1998.135.01.04

Lin, S., Williams, P.F., 1992. The origin of ridge-in-groove slickenside striae and associated steps in an S-C mylonite. J. Struct. Geol. 14, 315–321. doi:10.1016/0191-8141(92)90089-F

Macdonald, A.J., 1988. The Geraldton Gold Camp: The role of the banded iron formation. Ontario Geological Survey, Open File Report 5694. 173 p.

Mackasey, W.O., 1975. Geology of Dorothea, Sandra, and Irwin Townships, District of Thunder Bay. Ontario Division of Mines, Geological Report 122, 83 p.

Mackasey, W.O., 1976. Geology of Walters and Leduc Townships, District of Thunder Bay. Ontario Division of Mines, Geoscience Report 149. 58 p.

Mason, J.K., McConnell, C.D., 1983. Gold mineralization in the Beardmore-Geraldton area, In: Colvine, A.C. (Ed.), The Geology of Gold in Ontario, Ontario Geological Survey, Misc. Paper 110. pp. 84–97.

Mason, J.K., White, G., 1986. Gold occurrences, prospects and deposits of the Beardmore-Geraldton area, District of Thunder Bay and Cochrane. Ontario Geological Survey, Open File Report 5630. 680 p.

Meyn, H.D. and Palonen, P.A. 1980. Stratigraphy of an Archean submarine fan. Prec. Res., v. 12, p. 257-285.

Monecke, T., Mercier-Langevin, P., Dube, B. and Frieman, B.M., 2017. Geology of the Abitibi Greenstone Belt, in: Monecke, T., Mercier-Langevin, P., Dubé, B. (Eds.), Archean Base and Precious Metal Deposits, Southern Abitibi Greenstone Belt, Canada. Society of Economic Geologists, Reviews in Economic Geology, v. 19, pp. 7-49.

Passchier, C.W., 1997. The fabric attractor. J. Struct. Geol. 19, 113–127. doi:10.1016/S0191-8141(96)00077-6

Percival, J.A., Skulski, T., Sanborn-Barrie, M., Stott, G.M., Leclair, A.D., Corkery, M.T., and Boily, M. 2012. Geology and tectonic evolution of the Superior Province, Canada. Chapter 6 In: Tectonic Styles in Canada: The LITHOPROBE Perspective. Edited by J.A. Percival, F.A. Cook, and R.M. Clowes. Geological Association of Canada, Special Paper 49, pp. 321–378.

Percival, J.A., Sullivan, R.W., 1988. Age constraints on the evolution of the Quetico Belt, Superior Province, Ontario, in: Radiogenic and Isotopic Studies: Report 2; Geological Survey of Canada, Paper 88-2. pp. 99–107.

Percival, J.A., Williams, H.R., 1989. Late Archean Quetico accretionary complex, Superior province, Canada. Geology 17, 23–25. doi:10.1130/0091-7613(1989)017<0023:LAQACS>2.3.CO;2

Poulsen, K.H., Borradaile, G., Kehlenbeck, M.M., 1980. An inverted Archean succession at Rainy Lake, Ontario. Can. J. Earth Sci. 17, 1358–1369.

Pye, E.G., 1952. Geology of Errington Township, Little Long Lac Area, in: 60th Annual Report of the Ontario Department of Mines. Ontario Department of Mines, 140 p.

Pye, E.G., 1968. Geology of Lac des Iles Area, District of Thunder Bay. Ontario Department of Mines, Geological Report 64, 47 p.

Ramsay, J.G., 1967. Folding and Fracturing of Rocks. McGraw-Hill, New York. 568 p.

Reilly, B.A., 1987. Structural analysis of the Paint Lake deformation zone, northern Ontario. Unpublished MSc thesis. Brock University, St. Catharines, Ontario. 189 p.

Robert, F., 1989. Internal structure of the Cadillac tectonic zone southeast of Val d'Or, Abitibi greenstone belt, Quebec. Can. J. Earth Sci. 26, 2661–2675. doi:10.1139/e89-226

Robert, F., Poulsen, K.H., Cassidy, K.F., Hodgson, J.C., 2005. Gold Metallogeny of the Superior and Yilgarn Cratons, in: Hedenquist, J.W., Thompson, J.F.H., Goldfarb, R.J., Richards, J.P. (Eds.), Economic Geology 100th Anniversary Volume. pp. 1001–1033.

Robin, P.-Y.F., Cruden, A.R., 1994. Strain and vorticity patterns in ideally ductile transpression zones. J. Struct. Geol. 16, 447–466. doi:10.1016/0191-8141(94)90090-6

Sanborn-Barrie, M., 1988. Project Number 88-21. Geology of the Tectonic Boundary Zone Between the English River and Winnipeg River Subprovinces, Northwestern Ontario, in: Colvine, A.C., Cherry, M.E., Dressler, B.O., Thurston, P.C., Baker, C.L., Barlow, R.B., Riddle, C. (Eds.), Summary of Field Work and Other Activities 1988, Ontario Geological Survey, Miscellaneous Paper 141, pp. 98–107.

Sanderson, D.J., Marchini, W.R.., 1984. Transpression. J. Struct. Geol. 6, 449–458. doi:10.1016/0191-8141(84)90058-0

Shanks, W.S. 1993. Geology of Eva and Summers townships, District of Thunder Bay; Ontario Geological Survey, Open File Report 5821, 93p.

Stone, D. 2010. Precambrian geology of the centralWabigoon Subprovince area, northwestern Ontario; Ontario Geological Survey, Open File Report 5422, 130p.

Tabor, J.R., Hudleston, P.J., 1991. Deformation at an Archean subprovince boundary, northern Minnesota. Can. J. Earth Sci. 28, 292–307.

Teyssier, C., Tikoff, B., 1999. Fabric stability in oblique convergence and divergence. J. Struct. Geol. 21, 969–974. doi:10.1016/S0191-8141(99)00067-X

Thurston, P.C., Ayer, J.A., Goutier, J., Hamilton, M.A., 2008. Depositional gaps in Abitibi greenstone belt stratigraphy: A key to exploration for syngenetic mineralization. Econ. Geol. 103, 1097–1134. doi:10.2113/gsecongeo.103.6.1097

Tikoff, B., Greene, D., 1997. Stretching lineations in transpressional shear zones: an example from the Sierra Nevada Batholith, California. J. Struct. Geol. 19, 29–39. doi:10.1016/S0191-8141(96)00056-9

Tomlinson, K.Y., Davis, D.W., Percival, A.J., Hughes, D.J., Thurston, P.C., 1999. Neoarchean supracrustal development in the Central Wabigoon Subprovince: Nd isotope data and U/Pb geochronology., in: Harrap, R.M., Helmstaedt, H. (Eds.), Western Superior Transect 1999 Annual Meeting Lithoprobe Report #70. Lithoprobe Secretariat, University of British Columbia, pp. 147–152.

Tomlinson, K.Y., Davis, D.W., Stone, D., Hart, T.R., 2003. U–Pb age and Nd isotopic evidence for Archean terrane development and crustal recycling in the south-central Wabigoon Subprovince, Canada. Contrib. to Mineral. Petrol. 144, 684–702.

Tomlinson, K.Y., Hall, R.P., Hughes, D.J., Thurston, P.C., 1996. Geochemistry and assemblage accretion of metavolcanic rocks in the Beardmore–Geraldton greenstone belt, Superior Province. Can. J. Earth Sci. 33, 1520–1533.

Tomlinson, K.Y., Hughes, D.J., Thurston, P.C., Davis, D.W., Keays, R.R., 1997. The greenstone belts of the central Wabigoon Subprovince: geochemistry, petrogenesis and tectonic setting; *in* 1997 Western Superior Transect, Third Annual Workshop, Lithoprobe Secretariat, University of British Columbia, Vancouver, British Columbia, Lithoprobe Report #63, p. 83-90.

Walker, R.G. 1978. Deep water sandstone facies and ancient submarine fans: models for exploration and stratigrapic traps; American Association of Petroleum Geologists, Bulletin 62, 932-966.

Williams, H.R., 1989. Geological studies in the Wabigoon, Quetico and Abitibi-Wawa subprovinces, Superior Province of Ontario, with emphasis on the structural development of the Beardmore-Geraldton Belt; Ontario Geological Survey, Open File Report 5724. 189 p.

Williams, H.R., 1990. Subprovince accretion in the south-central Superior Province. Can. J. Earth Sci. 27, 570–581.

Williams, H.R., 1987. Ontario Geoscience Research Program, Grant No. 242. Structural Studies in the Wabigoon and Quetico Subprovinces, Open File Report 5668. Ontario Geological Survey, 163 p.

Figures

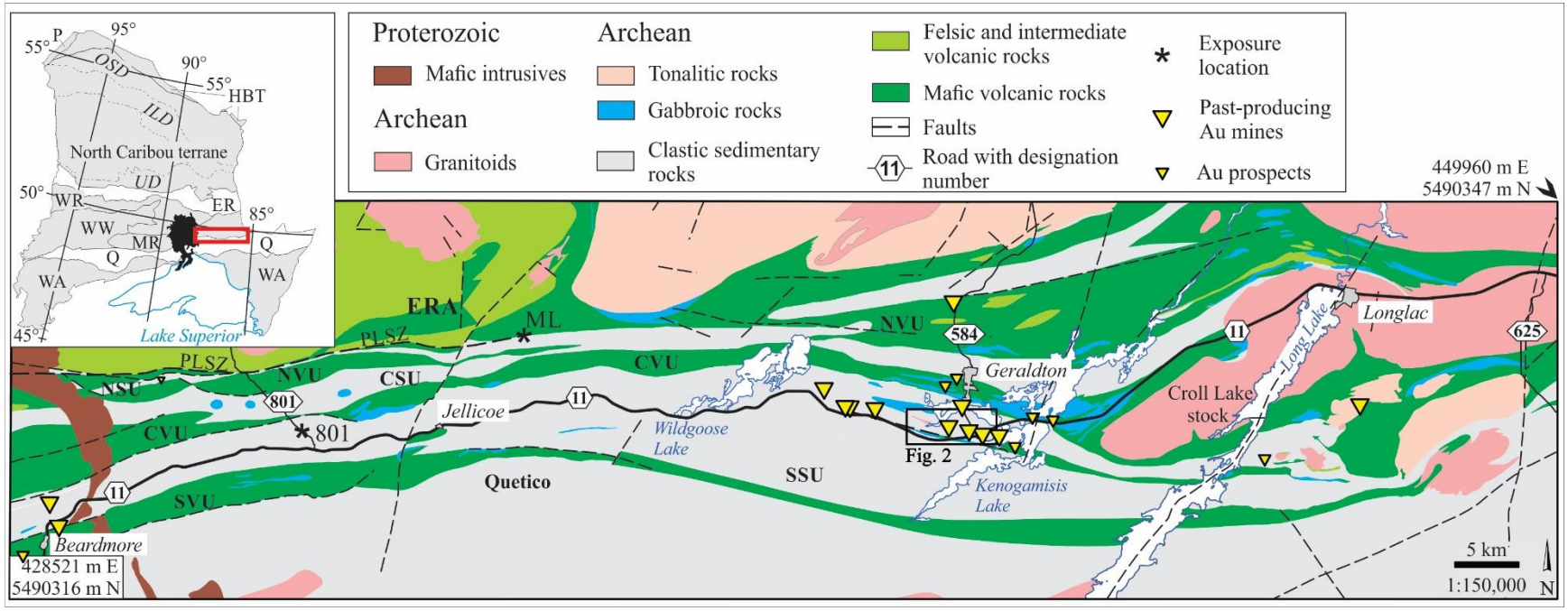

Figure 3-1. Geological map of the Beardmore-Geraldton greenstone belt (modified after Lavigne, 2009). ERA: Elmhirst-Rickaby Assemblage; JF: Jellicoe Fault; ML: Missing Link exposure; PLSZ: Paint Lake Shear Zone. Refer to text for abbreviations of the units in the BGB. The inset map shows the location of the BGB in the western Superior Province (after Percival et al., 2012). The Lake Nipigon and the Proterozoic rocks of the Lake Superior area are coloured black. Abbreviations of terranes: ER: English River; HBT: Hudson Bay; MR: Marmion; P: Pikwitonei; Q: Quetico; WA: Wawa-Abitibi; WR: Winnipeg River; WW: Western Wabigoon; Domains of North Caribou terrane: ILD: Island Lake Domain; OSD: Oxford-Stull Domain; UD: Uchi Domain. Map coordinates in UTM NAD 83, Zone 16.

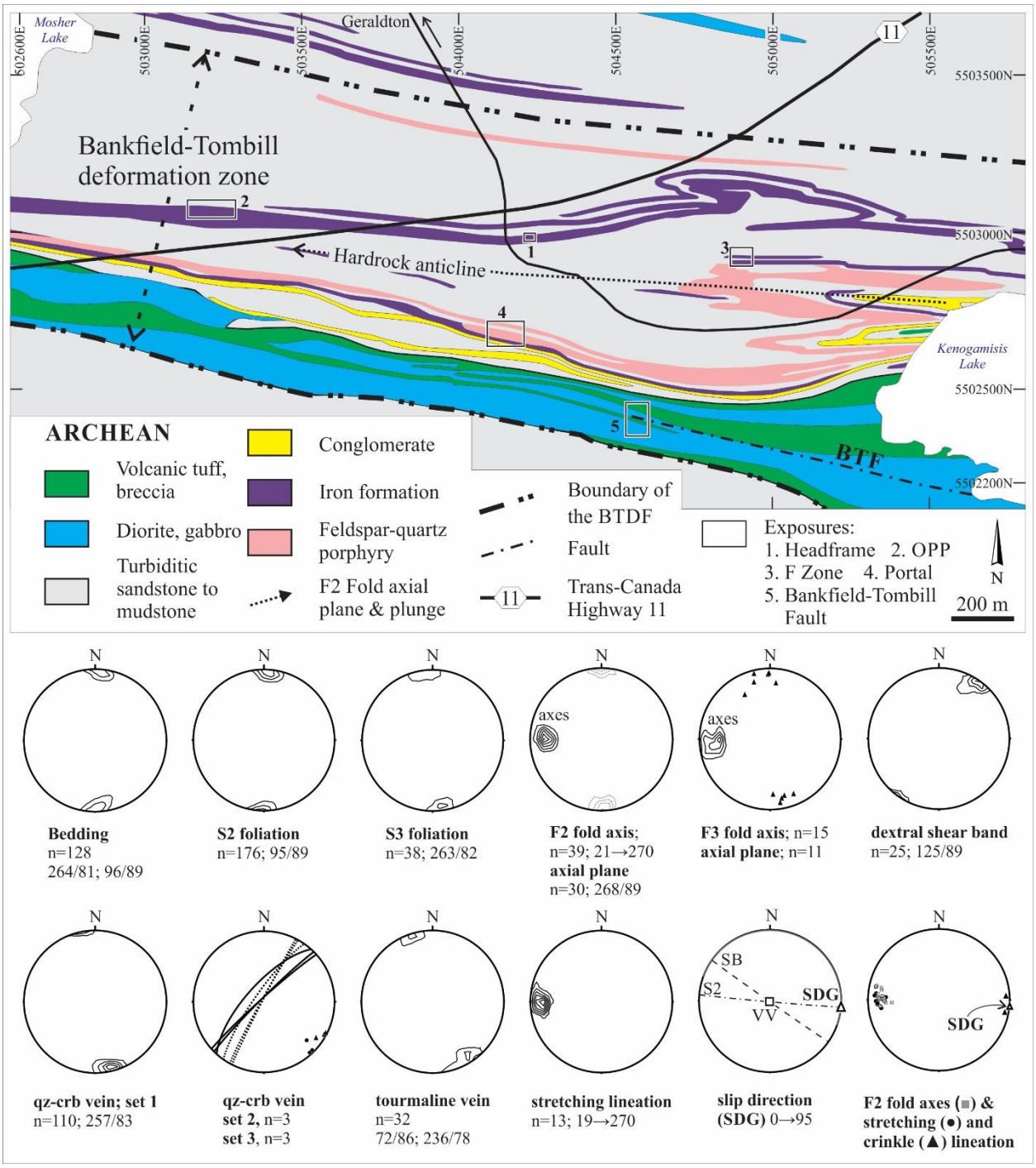

Figure 3-2. Geological map of the Geraldton area (modified after Pye, 1952; Horwood and Pye, 1955). Structures plotted on equal-area, lower hemisphere projections (n: number of measurements; average measurement to the right of the number of measurements; plotted using Stereonet software of Allmendinger et al., 2013; Cardozo and Allmendinger, 2013). Contour intervals in 10% contour intervals per 1% area of the net. Map coordinates are provided in UTM NAD 83, Zone 16. SB: dextral shear band; S2: S_2 foliation; SD: shear direction; VV: vorticity vector.

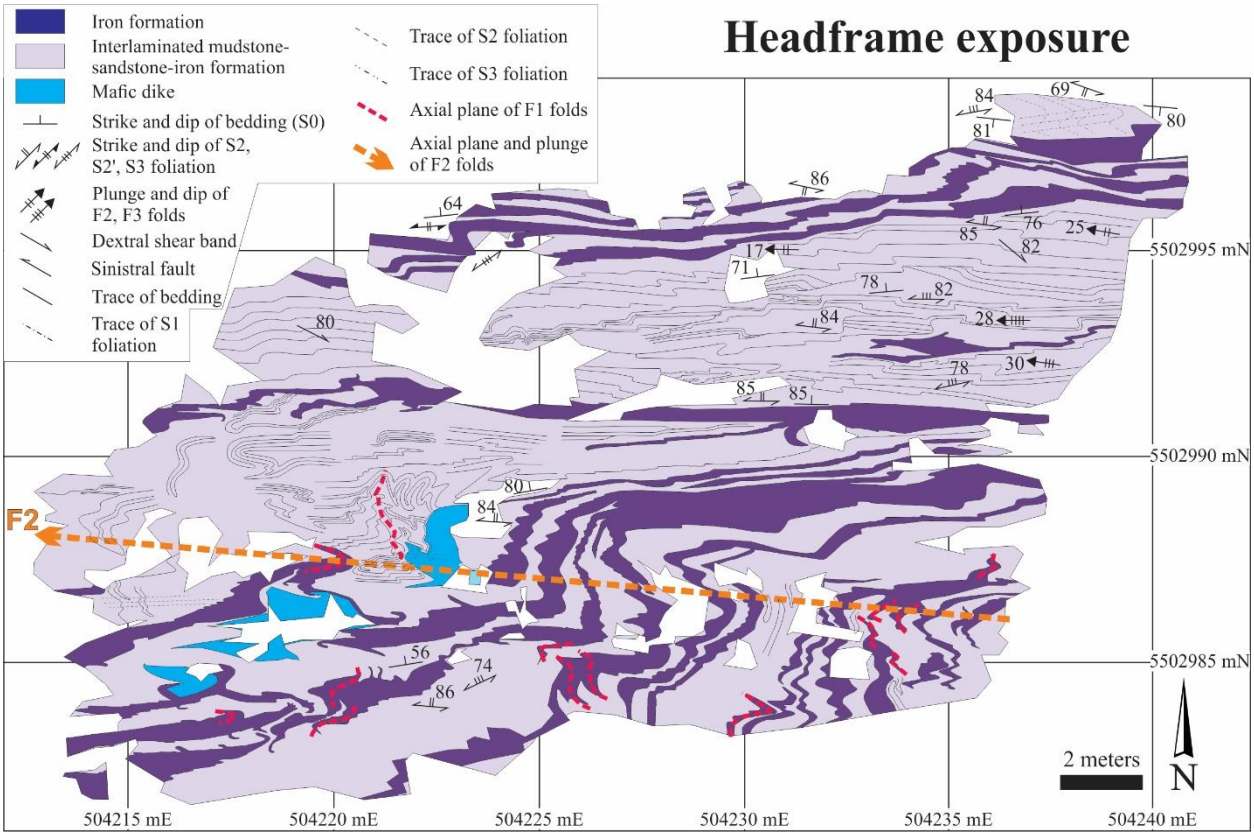

Figure 3-3. Geological map of the Headframe stripped outcrop (Location 1 in Fig. 2). Map coordinates in UTM NAD 83, Zone 16.

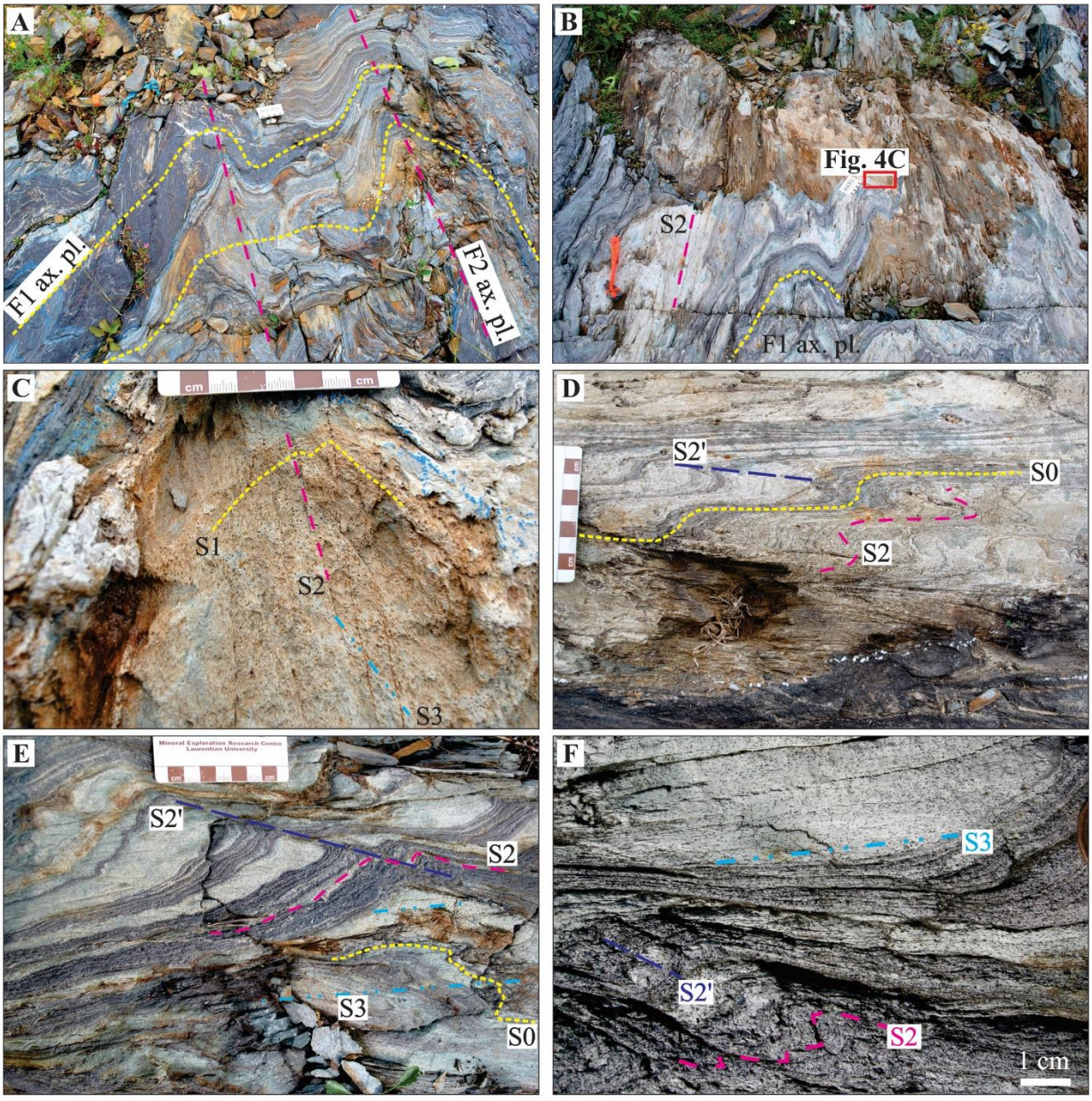

Figure 3-4. Field photographs at the Headframe stripped outcrop. A) F_1 folds refolded by S-shaped F_2 folds in banded iron formation. B) Mafic dike and banded iron formation are folded by F_1 and refolded by F_2 folds with axial-planar S_2 foliation. C) Close up on F_2 fold hinge in mafic dike displaying a folded chloritic S_1 foliation axial-planar to F_1 fold, overprinted by an axial-planar S_2 and an oblique S_3 foliation. D) S-shaped F_2' folds with strong, axial-planar S_2' foliation folding S_2 foliation in banded iron formation. E) S_3 foliation overprints F_2' fold and is axial-planar to Z-shaped F_3 folds in banded iron formation. F) Zoom in on fold hinge shown on Fig. 4E. S-folded S_2 foliation with axial planar S_2'. S_3 foliation overprints F_2' folds as it crosses from one limb to the other. 8.6 cm scale card.

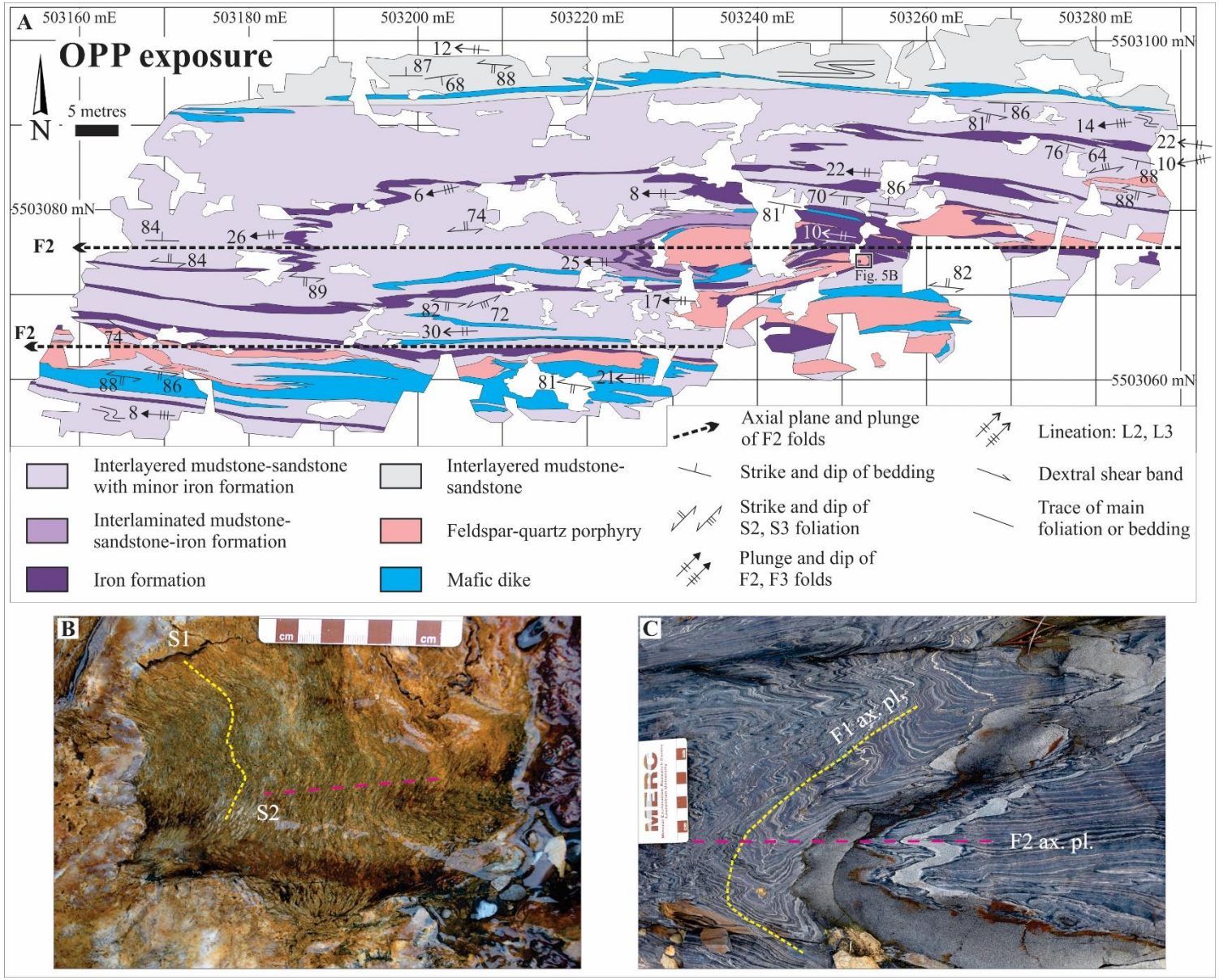

Figure 3-5. A) Geological map of the OPP stripped outcrop (Location 2 in Fig. 2). Map coordinates in UTM NAD 83, Zone 16. Field photographs from the OPP stripped outcrop: B) Strong sericitic S_1 foliation folded by F_2 fold with axial-planar S_2 foliation in feldspar-quartz porphyry. C) F_1 fold folded by F_2 fold in banded iron formation. 8.6 cm scale card.

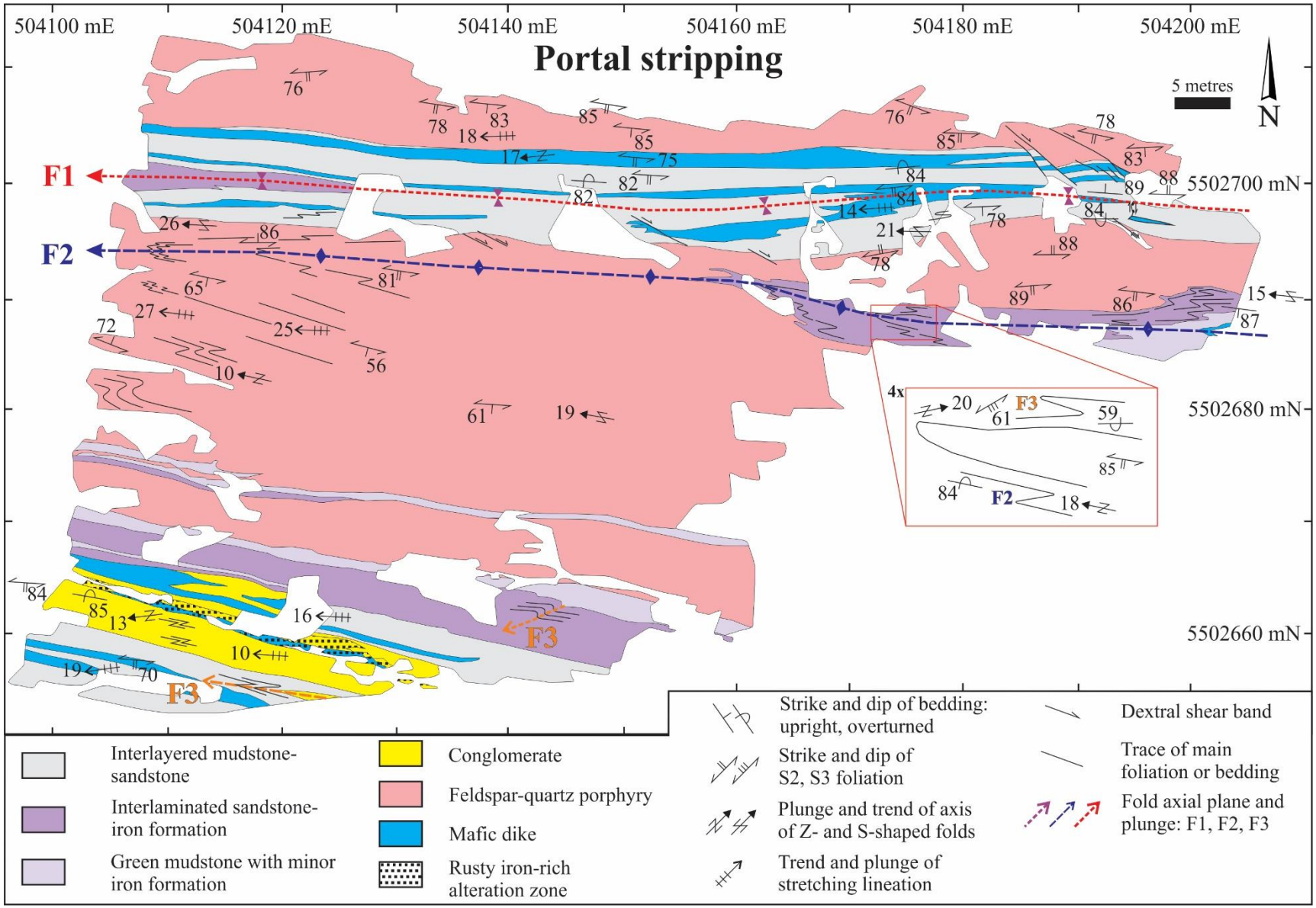

Figure 3-6. Geological map of the Portal stripped outcrop (Location 4 in Fig. 3-2). Map coordinates in UTM NAD 83, Zone 16.

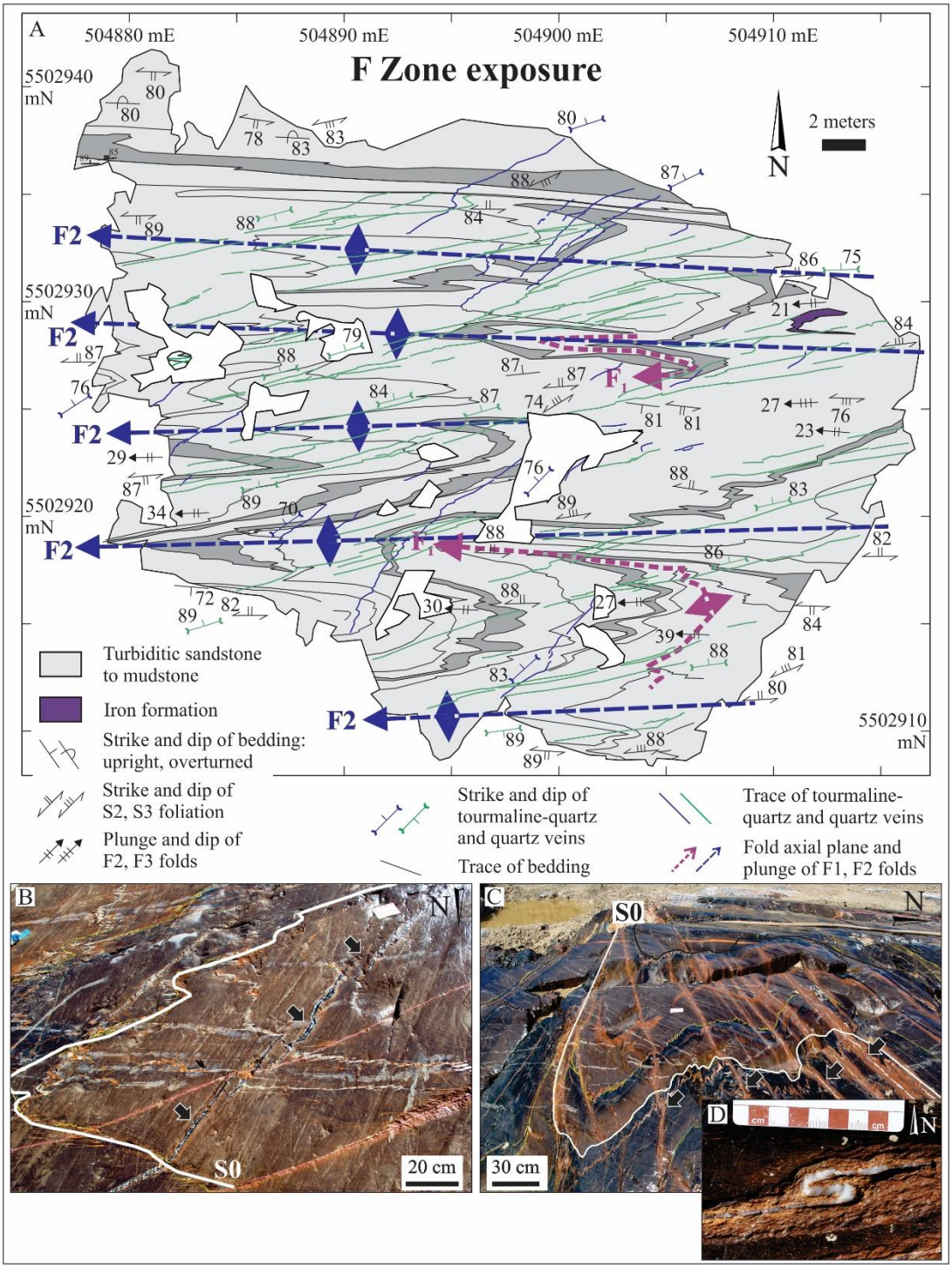

Figure 3-7. A) Geological map of the F Zone stripped outcrop (Location 3 in Fig. 3-2). Map coordinates in UTM NAD 83, Zone 16. Beds of turbiditic sandstone have been highlighted in dark grey in order to outline the outcrop-scale folding pattern. Field photographs from the F Zone exposure: B) S-folded northeast-trending tourmaline-quartz vein cutting across F_2 fold from one limb, across the axial plane to the other limb of the fold. C) Long, narrow E-NE-trending quartz-carbonate veins transecting F_2 fold in graded mudstone to sandstone. D) S-folded E-NE-trending quartz-carbonate vein. 8.6 cm scale card.

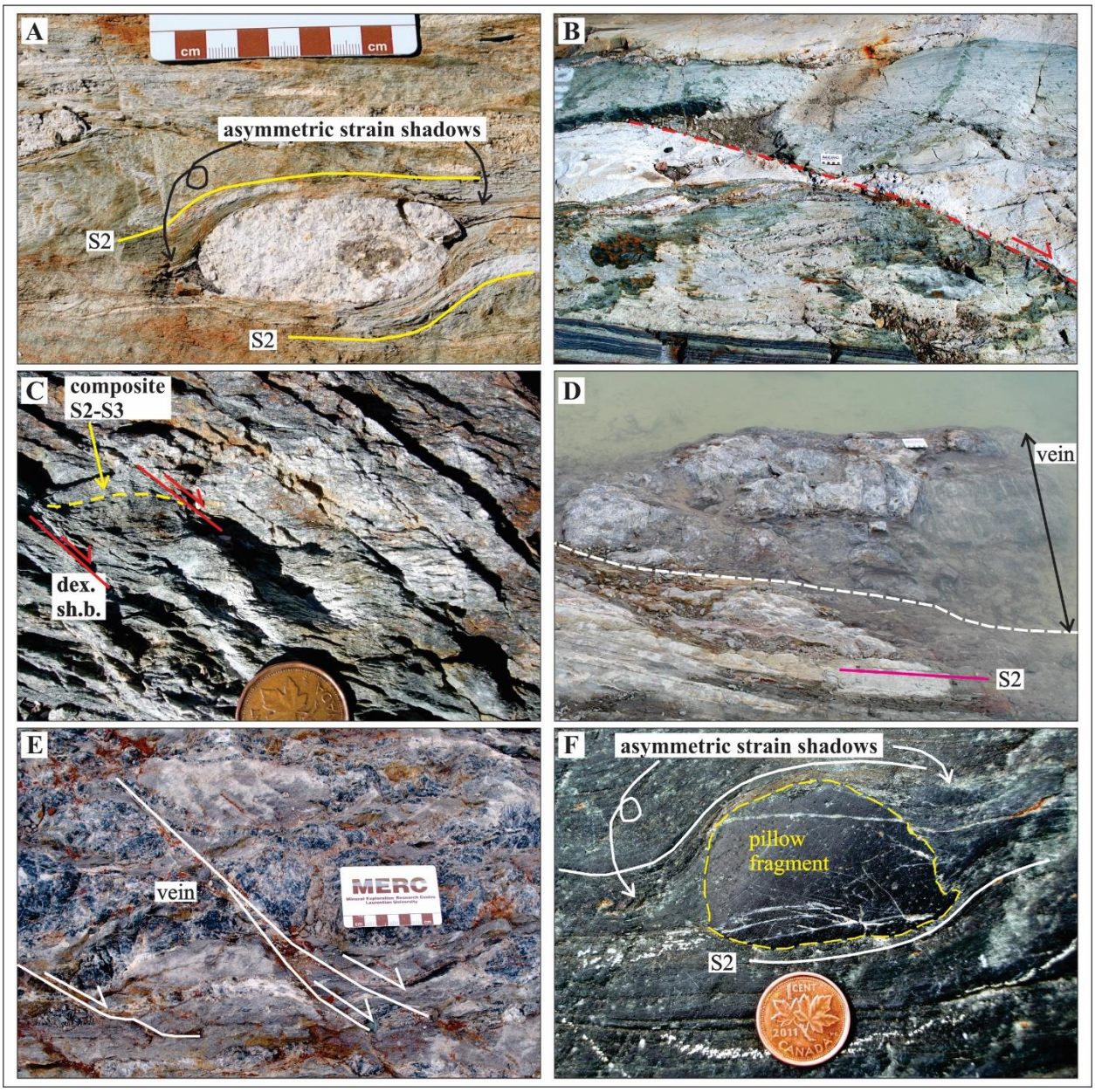

Figure 3-8. Field photographs from the Portal stripped outcrop: A) Rigid granitoid clast surrounded by asymmetric strain shadows indicating dextral sense of shear. B) Northwest-trending dextral shear fracture displacing feldspar-quartz porphyry and fine-grained metasedimentary units. C) Northwest-trending dextral shear bands causing the clockwise rotation of composite S_2-S_3 foliation. The coin for scale has 19 mm diameter. Field photographs from the Bankfield-Tombill stripped outcrop: D) East-trending fault-filling smoky black quartz-carbonate veins oriented roughly parallel to S_2 foliation are intersected by E) dextral shear fractures. F) Small pillow fragment surrounded by asymmetrical strain shadow indicating dextral movement. The coin for scale has 19 mm diameter.

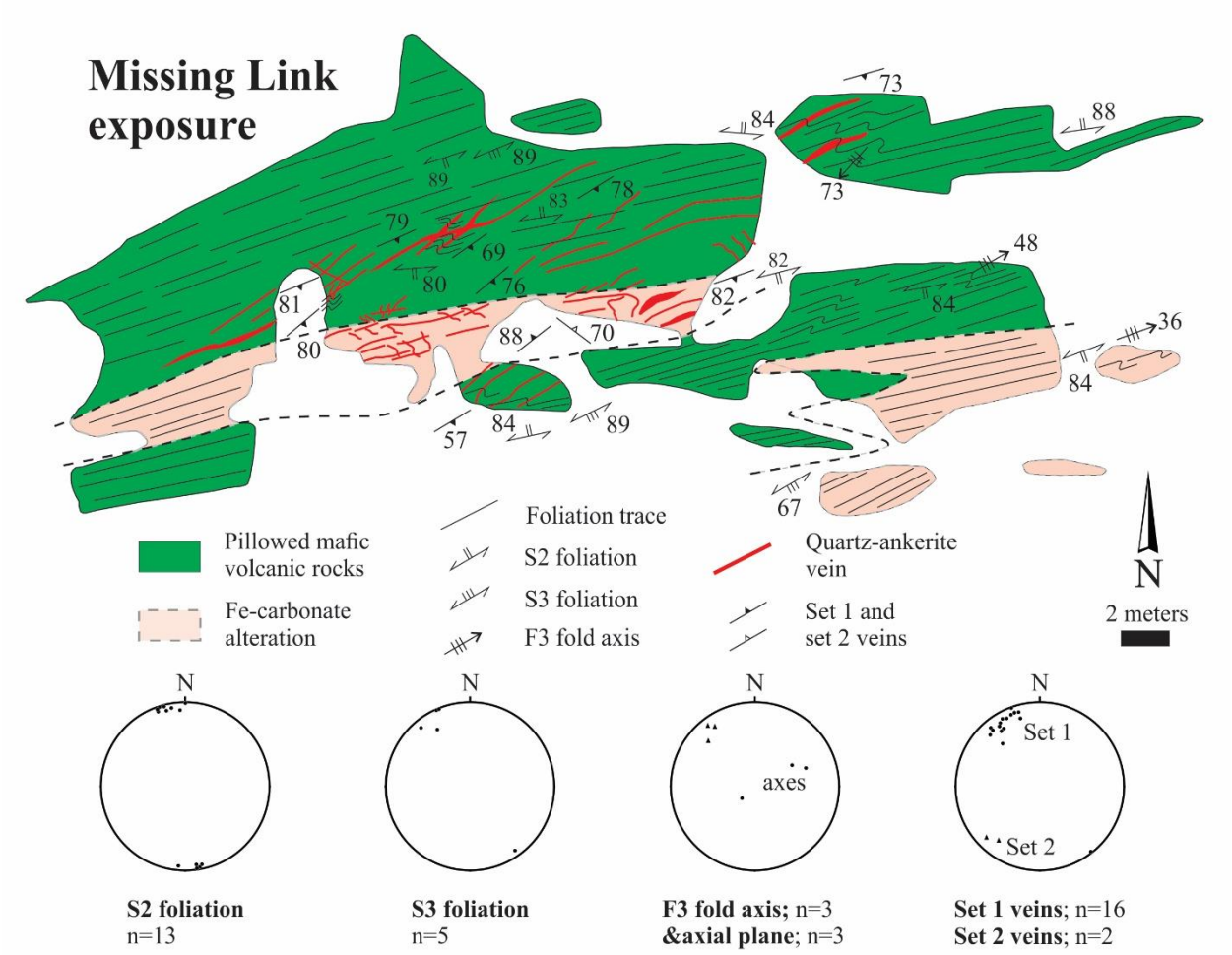

Figure 3-9. A) Geological map of the Missing Link extension stripped outcrop, Jellicoe area (*ML on Fig. 3-1). Structures plotted on equal-area, lower hemisphere projections (n: number of measurements; average measurement to the right of the number of measurements; plotted using Stereonet software of Allmendinger et al., 2013; Cardozo and Allmendinger, 2013). Map coordinates are provided in UTM NAD 83, Zone 16.

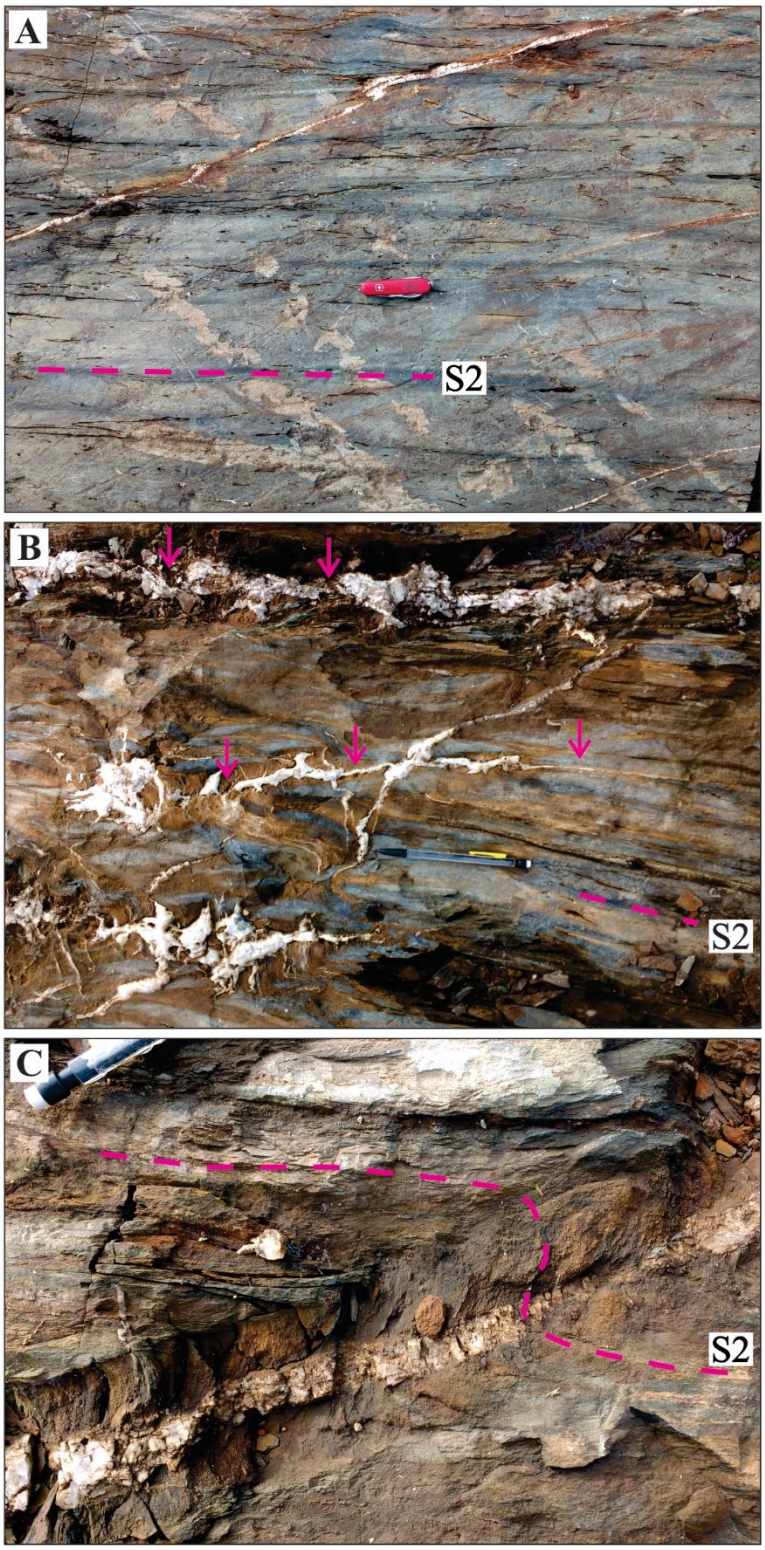

Figure 3-10. Field photographs from the Missing Link stripped outcrop: A) Southwest-trending vein crosscutting S_2 foliation highlighted by flattened pillows. Pocket knife for scale is ca. 9 cm long. B) Different sets of quartz-carbonate veins associated with strong Fe-carbonate alteration. C) Z-shaped flanking structure along the margin of northeast-trending quartz-carbonate veins. Pencil head for scale is ca. 8 mm thick.

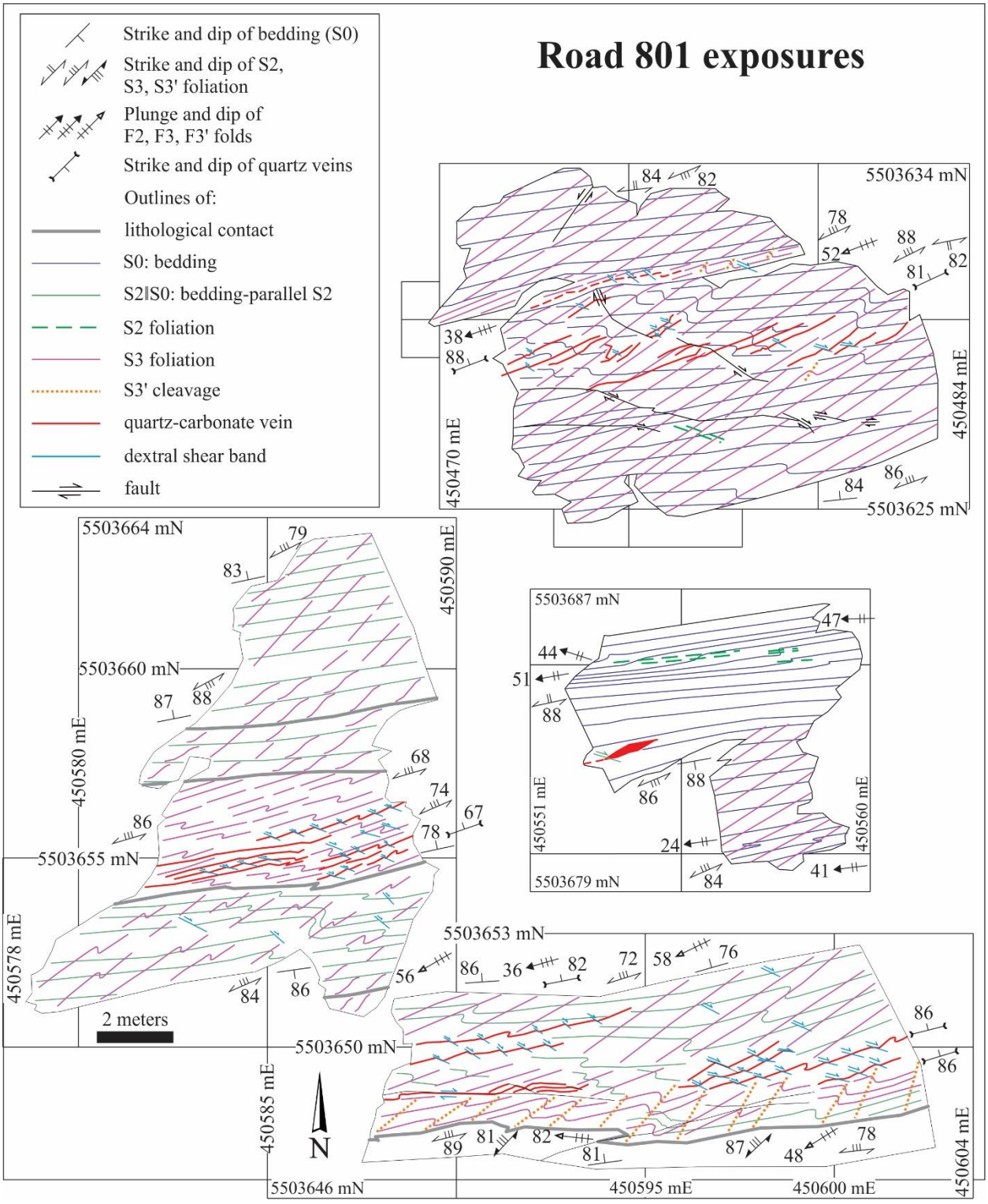

Figure 3-11. Geological map of the Road 801 stripped outcrop (*Road 801 on Fig. 3-1). Coordinates in UTM NAD 83, Zone 16.

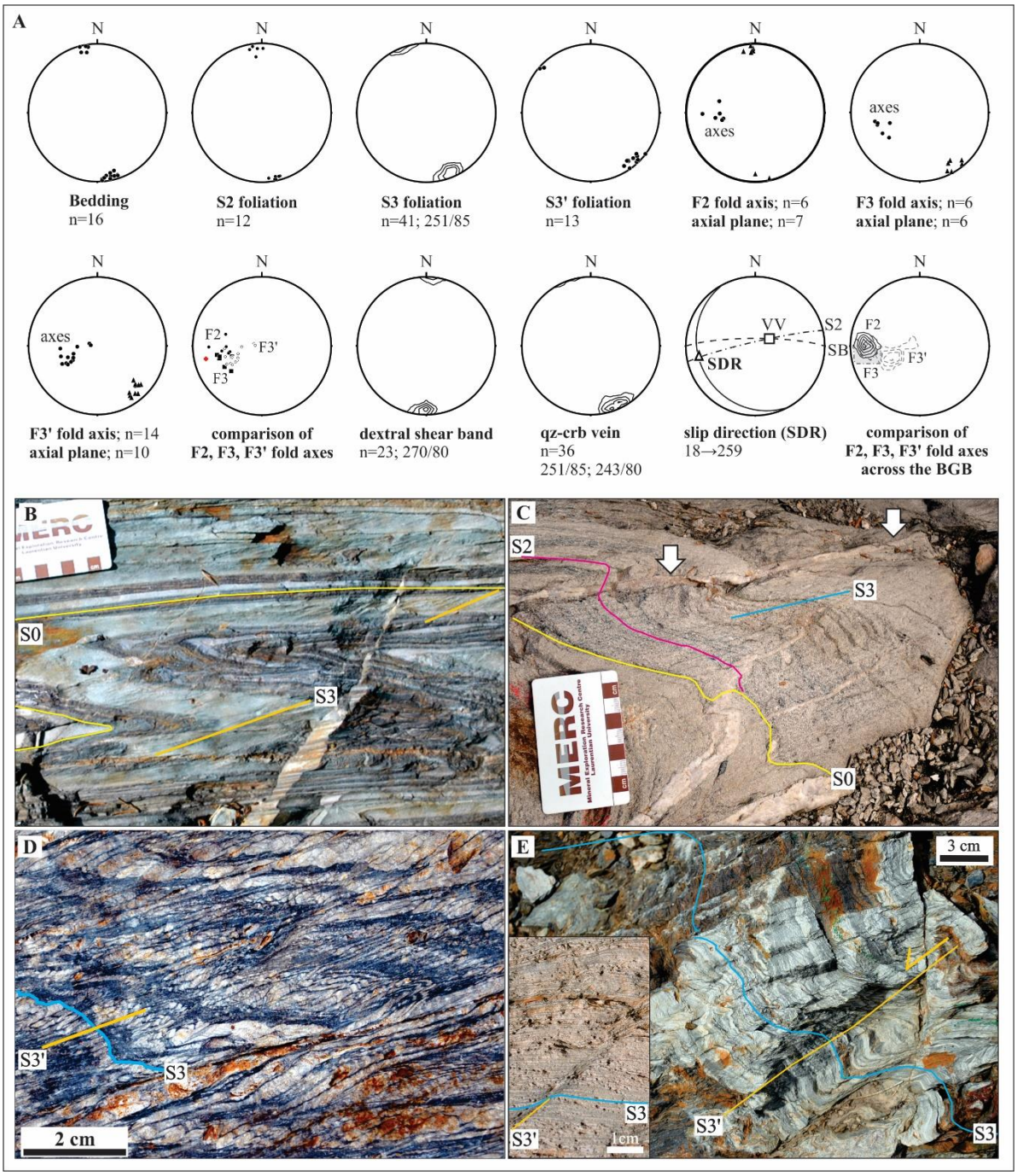

Figure 3-12. A) Equal-area, lower hemisphere plots of structures at the Road 801 stripped outcrop (n: number of measurements; average measurement to the right of the number of measurements; plotted using Stereonet software of Allmendinger et al., 2013; Cardozo and Allmendinger, 2013). 10% contour intervals per 1% area of the net. SB: dextral shear band; SD: shear direction; VV: vorticity vector. Field photographs from the Road 801 stripped outcrop: B) S-shaped F_2 fold with in banded iron formation overprinted by S_3 foliation. C) Z-shaped F_3 folds in sandstone folding S_2. D) S_3 foliation folded by Z-shaped F_3' folds with axial-planar S_3' cleavage. E) Sinistral slip along S_3' cleavage. The inset shows a close-up of S_3' sinistral slip cleavage. 8.6 cm scale bar.

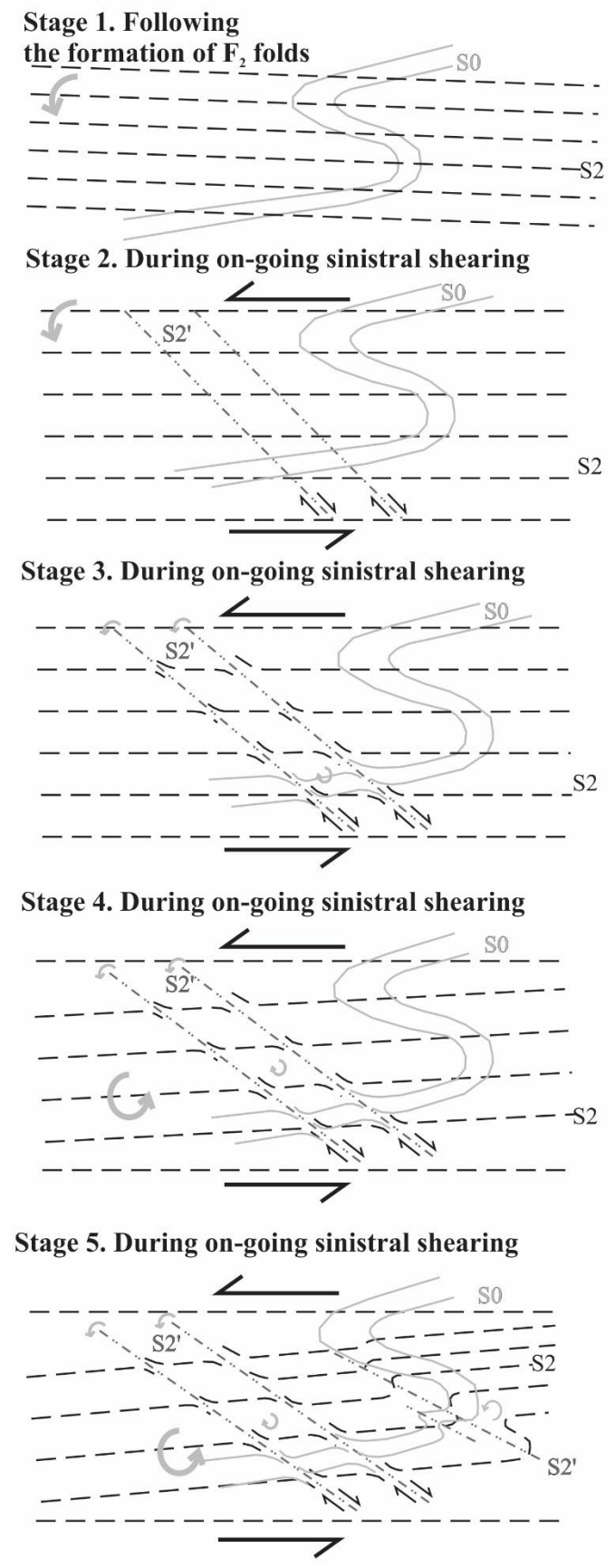

Figure 3-13. Stages of the formation of S-shaped folds during D_2 sinistral transpression.

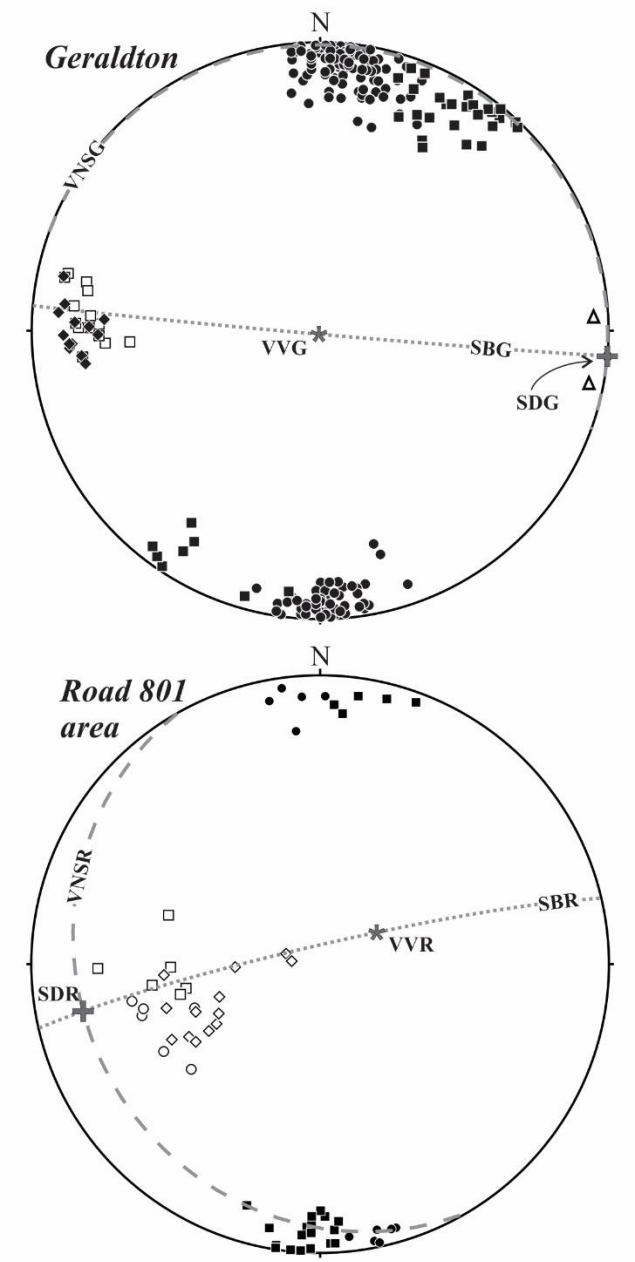

Legend		F3' fold axis	◇
C-fabric	●	Stretching lineation	◆
C'-fabric	■	Crinkle lineation	△
F2 fold axis	□	Vorticity vector	*
F3 fold axis	○	Slip direction	✚

Figure 3-14. Equal-area lower-hemisphere projections showing the relationships between measured and calculated structures in the Geraldton (G), Road 801 area (J; plotted using Stereonet software of Allmendinger et al., 2013; Cardozo and Allmendinger, 2013). Abbreviations: C-fabric=S_2 foliation; C'-fabric=dextral shear bands; SB: average orientation of shear zone boundary; VNS: vorticity normal section; VV: vorticity vector.

4. CHAPTER 4: THE GEOLOGY OF THE WORLD-CLASS HARDROCK OROGENIC GOLD DEPOSIT, GERALDTON, ONTARIO, CANADA: STRUCTURAL CONTROL, MINERALOGY, GEOCHEMISTRY AND GEOCHRONOLOGY

Zsuzsanna Tóth[a,*], Bruno Lafrance[a], Benoît Dubé[b]

[a]Mineral Exploration Research Centre, Harquail School of Earth Sciences, Goodman School of Mines, Laurentian University, 935 Ramsey Lake Road, Sudbury, ON, Canada P3E 2C6

[b]Geological Survey of Canada, Earth Sciences Sector, Natural Resources Canada, 490, rue de la Couronne, Québec, QC, Canada G1K 9A9

*Corresponding author: Zsuzsanna Tóth, e-mail address: ztoth@laurentian.ca;

Abstract

The Hardrock orogenic gold deposit is located in the Beardmore-Geraldton belt (BGB) along the boundary between the granite-greenstone Wabigoon subprovince and the metasedimentary Quetico subprovince of the Archean Superior craton. The deposit is hosted by ca. 2700-2694 Ma turbiditic sandstone, banded iron formation, and ca. 2694 Ma feldspar-quartz porphyry, which underwent strong deformation within the 1 km-wide Bankfield-Tombill deformation zone along the southern margin of the BGB. The deformation zone includes folds and cleavage that formed during early D_1 thrust imbrication of the BGB, S-shaped folds and fabrics that formed during D_2 sinistral transpression, and Z-shaped folds, fabrics and localized shear zones that formed during D_3 dextral reactivation of the deformation zone. Gold mineralization is associated with folded, early-D_1, quartz-carbonate veins (V_1) and with NE- to E-striking, syn-D_2, tourmaline-rich veins (V_2) as well as quartz-carbonate veins (V_3). The V_1 and V_3 veins are surrounded by sericite-

carbonate-pyrite ± albite–rutile alteration halos, and the V_2 veins are surrounded by carbonate-tourmaline- pyrite ± pyrrhotite-chalcopyrite alteration halos. Gold was deposited during fluid-rock sulfidation reactions that resulted in the formation of inclusion-poor pyrite with Ni-Co-As primary crystallographic zoning and inclusion-rich pyrite enriched in Au and other metals (Ag-As-Bi-Co-Ni-Pb-Sb-Te). Hydrothermal alteration associated with the deposition of the veins produced a broad, up to 250 m wide, sericite-carbonate alteration envelope, with S, Te, As, W, and Bi as the best pathfinder indicators to Au mineralization. Contrary to previous studies which attributed the formation of gold deposits in the BGB to late D_3 dextral transpression, our results suggest that gold was emplaced during early D_1 thrusting and D_2 sinistral regional transpression and involved multiple hydrothermal fluid pulses during several deformation events, as suggested for other major Archean orogenic gold camps associated with major fault zones such as the Timmins and Kirkland Lake camps in the Superior craton and the Kalgoorlie and Laverton camps in the Yilgarn craton.

Introduction

The Hardrock gold deposit is an orogenic gold deposit associated with major, crustal scale faults, porphyry intrusions, and linear belts of fluvial to shallow marine sedimentary rocks. These features are also common to the Timmins-Porcupine, Kirkland Lake, Malartic, and Val d'Or camps of the Abitibi greenstone belt (Dubé and Gosselin, 2007; Robert et al., 2005). On a regional scale, gold deposits in these districts and other world-class districts, such as the Kalgoorlie and Laverton camps in the Yilgarn craton, share these features. On the deposit scale, the deposits are characterized by shear-hosted quartz-carbonate veins, iron-rich host rocks (Fe-rich tholeiites and banded iron formation), intense hydrothermal alteration (carbonate, sericite, chlorite ±albite), and disseminated sulfide (pyrite, arsenopyrite, pyrrhotite) mineralization (Groves et al., 1998, 2003; Goldfarb et al., 2005; Robert et al., 2005; Phillips and Powell, 2010). Depletions in Na_2O and

additions of CO_2, K_2O and S characterize the alteration envelopes surrounding the deposits, which are typically enriched in the following pathfinder metals: Ag, As, W, B, Mo, Sb, Te and sometimes Bi (Groves et al., 1998; Dubé and Gosselin, 2007; Lafrance, 2015). Less commonly, albitisation dominates instead of sericite alteration, and consequently the alteration halos are enriched in Na_2O and depleted in K_2O (e.g. Kerr-Addison deposit; Kishida and Kerrich, 1987; Groves et al., 1998).

Gold deposits in the Geraldton camp have regional and deposit scale features similar to large orogenic gold deposits and, even in the 1980's and 1990's as the syngenetic versus epigenetic origin of gold in banded iron formation-hosted gold deposits was being debated, the Hard Rock gold deposit in Geraldton was interpreted as a type end-member example of epigenetic, now orogenic, gold deposits (Kerswill, 1993 and references therein). Access to large new mechanically stripped outcrops and to new exploration drill core across the past-producing Hard Rock and MacLeod-Cockshutt mines (that collectively form the new Hardrock deposit of Greenstone Gold Mines) provide an opportunity to reassess the structural setting and footprint of the Geraldton deposits. In this paper, we: (1) define their structural setting and the relative timing of gold mineralization; (2) describe their alteration envelope and associated sulfide minerals; (3) characterize their geochemical footprint; and (4) present an interpretation for the emplacement of gold mineralization and formation of the deposits. Our results suggest that the Geraldton deposits are syn-deformational as previously suggested but formed during older gold mineralization and structural events than previously recognized.

Geological Background

Regional geology

The Beardmore-Geraldton Belt (BGB) is a transitional terrane along the boundary between the granite-greenstone Wabigoon subprovince and the metasedimentary Quetico subprovince of the Archean Superior craton (Fig. 4-1). It extends for roughly 120 km from Lake Nipigon to the west to Long Lake to the east. The BGB comprises six alternating, shear-zone bounded, generally north-younging, metavolcanic and metasedimentary panels, which are similar to the rocks of the Wabigoon and Quetico subprovinces, respectively (Ayres, 1969; Devaney and Williams, 1989). The 2724.9 +/- 1.1 Ma (Hart et al., 2002) pyroclastic and volcanic flow rocks of the northern metavolcanic unit (NVU) have felsic to intermediate composition and predominantly tholeiitic geochemical affinity (Carter, 1987; Kresz and Zayachivsky, 1991; Shanks, 1993; Tomlinson et al., 1996). The central metavolcanic unit (CVU) consists of 2724.9±1.2 Ma (Hart et al., 2002), mafic to intermediate, pyroclastic rocks as well as massive, pillowed and amygdaloidal flows with calc-alkaline or tholeiitic geochemical affinity (Carter, 1987; Kresz and Zayachivsky, 1991; Shanks, 1993; Tomlinson et al., 1996; Lavigne, 2009). The southern volcanic unit (SVU) comprises pillowed and massive, mafic to intermediate, flows with tholeiitic affinities (Carter, 1987; Williams, 1987; Kresz and Zayachivsky, 1991; Shanks, 1993; Tomlinson et al., 1996; Lavigne, 2009). The metavolcanic rocks of the NVU, CVU and SVU formed in geodynamic environments with trace element attributes similar to modern back-arc, island arc and oceanic crust settings respectively (Tomlinson et al., 1996).

The three panels of metasedimentary rocks, that is, the northern, central and southern metasedimentary units (NSU, CSU, SSU), represent a single, southward-prograding, syn-tectonic

clastic foreland wedge that was deposited between ca. 2700 Ma and 2694±1.0 Ma from detritus derived from the erosion of the eastern Wabigoon subprovince (Devaney and Williams, 1989; Fralick and Pufahl, 2006; Chapter 2 of this thesis). The NSU consists of clast-supported fluvial conglomerate with minor sandstone (Mackasey, 1975, 1976; Devaney and Williams, 1989) unconformably deposited above the back-arc-like metavolcanic rocks of the NVU (Devaney and Fralick, 1985). The CSU comprises conglomerates, sandstones, interlayered mudstones and sandstones with shallow water iron formation, representing subaqueous fan and/or prodelta environments (Pye, 1952; Horwood and Pye, 1955; Mackasey, 1975, 1976; Barrett and Fralick, 1985; Devaney and Williams, 1989; Fralick and Pufahl, 2006). The SSU is dominated by turbiditic mudstone, siltstone and sandstone with minor iron formation and conglomerate lenses that were deposited in a submarine fan and/or basin plain environment (Pye, 1952; Horwood and Pye, 1955; Mackasey, 1975, 1976; Barrett and Fralick, 1985; Devaney and Williams, 1989).

Deformation of the BGB began as the southern Wawa-Abitibi greenstone terrane drifted northward and collided with the Wabigoon subprovince during the ca. 2690 Ma Shebandowanian orogeny (Devaney and Williams, 1989; Percival et al., 2012). This resulted in the closure of the Quetico oceanic basin and the accretion of the metavolcanic-metasedimentary panels of the BGB to the southern margin of the Wabigoon subprovince during early D_1 thrusting and folding. The ca. 2694 Ma tonalite-trondhjemite-granodiorite (TTG) suite dikes are syn-tectonic with the D_1 event, which ended with the emplacement of the stitching 2690±1 Ma sanukitoid Croll Lake stock (Corfu, 2000; Lafrance et al., 2004; Chapter 2 of this thesis). This early accretionary event was followed by D_2 sinistral transpression and the formation of regional W-plunging F_2 folds, a regional W-plunging L_2 stretching lineation, an E-striking and steeply-dipping S_2 foliation, and D_2 high strain zones (Lafrance et al., 2004; Chapter 3 of this thesis). Subsequent reactivation of the S_2 foliation and D_2

high strain zones during a late D_3 dextral transpression event resulted in the development of W-plunging Z-shaped F_3 folds, a W-SW-striking S_3 foliation, and dextral shear bands within localized dextral shear zones (Lafrance et al., 2004; Chapter 3 of this thesis). The BGB is metamorphosed to greenschist facies, with the metamorphic grade increasing to amphibolite grade along the margins of intrusions (Kresz and Zayachivsky, 1991; Lavigne, 2009).

Deposit Geology

Gold was discovered in the 1880's (Wilson, 1910) and the first mines, the Little Longlac mine in Geraldton and the Northern Empire mine in Beardmore, went in production in 1934 (Mason and McConnell, 1983; Mason and White, 1986). Over the following 30 to 40 years, the BGB produced over 4.1 Moz Au until mining ended in 1970 (Mason and McConnell, 1983; Mason and White, 1986). The host rocks, structural controls, and gold-silver production of the main mines are summarized in Table 4-1.

In the Geraldton camp (Fig. 4-2), most major past-producing gold mines are located in the Bankfield-Tombill deformation zone, which was interpreted as a major dextral fault (the Bankfield-Tombill fault; Fig. 4-2) along the boundary between the BGB and the Quetico metasedimentary subprovince (Pye, 1952; Buck, 1986; Williams, 1987; Lafrance et al., 2004). The Bankfield-Tombill deformation zone has been more recently reinterpreted as a dextrally reactivated D_2 high strain zone hosting late, parallel, dextral D_3 shear zones including the Bankfield-Tombill fault (Chapter 3 of this thesis). Although gold deposits in the Geraldton area are known for their association with iron formation (e.g. Kerswill, 1996), significant production came from clastic metasedimentary rocks, felsic porphyritic and mafic intrusive igneous rocks (Table 4-1; Pye, 1952; Horwood and Pye, 1955). Gold mineralization occurs in quartz veins and

their altered wallrocks along sheared contacts between metasedimentary rocks and intrusions, and in strongly folded quartz veins in F_3 fold hinges. As ore shoots plunge 20°-65° to the west parallel to F_3 fold hinges, gold mineralization was attributed to the late D_3 dextral transpression event (Pye, 1952; Horwood and Pye, 1955; Anglin, 1987; Macdonald, 1988; Lafrance et al., 2004). Over the past decade, systematic drilling of the Hardrock deposit by Premier Gold Mines Ltd. and then Greenstone Gold Mines GP Inc. has delineated new resources of 6.4 Moz gold (Fig. 4-2; G Mining Services, 2016).

The Hardrock deposit in the Bankfield-Tombill deformation zone

Mineralogy and chronology of auriferous veins

Gold mineralization and gold-bearing veins are hosted by the following main rock types: sandstone and mudstone-siltstone, banded iron formation, feldspar-quartz porphyry. Their characteristics in each rock types are summarized in Table 4-2. Unaltered sandstone consists of detrital quartz, albite and micas, and secondary sericite, chlorite and minor magnetite and hematite. Unaltered mudstone-siltstone is similar in mineralogy but contains more chlorite and less sericite, detrital quartz and feldspar. Banded iron formation (BIF) occurs as decimeter-thick layers consisting of interlayered millimetre-thick chert and iron oxide (magnetite and hematite) laminae alternating with chlorite- and biotite-rich siltstone and sandstone beds. Feldspar-quartz porphyry (FQP) comprises primary quartz and plagioclase (albite) and secondary sericite, carbonate, metamorphic chlorite and biotite as well as disseminated sulfides.

Mineralization is exposed on 3 stripped outcrops on the proposed Hardrock mine site. The stripped outcrops are located within the Bankfield-Tombill deformation zone and are informally named the OPP, F Zone, Porphyry Hill outcrops (Fig. 4-2). The hydrothermal ore system is characterized by

early Fe-carbonate alteration and by three sets of auriferous veins. Early Fe-carbonate veins and alteration are present at the F Zone (Fig. 4-3, 4-6A), OPP (Fig. 4-4, 4-6B), and Porphyry hill (Fig. 4-5, 4-6C) outcrops where it is characterized by orange or rusty discoloration of sandstone beds and BIF and by the presence of massive Fe-carbonate veins crossed by quartz ladder veins. The Fe-carbonate veins and Fe-carbonatized beds are folded by F_1 folds at the F Zone (Fig. 4-6B) and are completely transposed parallel to the S_2 foliation on the OPP outcrop (Fig. 4-6C), where they are deformed into discontinuous S_2-parallel lenses tapering to a wedge at both ends. This suggests that the veins and early carbonate alteration formed before or early during the D_1 deformation event.

An early set of bedding-parallel quartz-carbonate (±pyrite, chalcopyrite, tourmaline) veins (V_1) is folded by F_1 and F_2 folds at the Porphyry Hill and F zone outcrops (Fig. 4-6D-E). At the OPP outcrop, the veins are oriented slightly clockwise to S_2 and bedding. They are deformed into boudins with narrow pinched boudin necks. The pinched boudin necks are folded within the hinge of F_2 folds (Fig. 4-6F), suggesting that the veins were emplaced and deformed prior to the D_2 event, likely during the D_1 event. V_1 veins are surrounded by strong alteration halos of sericite-carbonate-pyrite (±rutile) in sandstone (Fig. 4-7A), sericite-pyrite-arsenopyrite (±chlorite, biotite, carbonate) in BIF (Fig. 4-7B-C), and sericite-pyrite-carbonate-albite (±rutile) in quartz-feldspar porphyry. The latter is pervasively altered to sericite, carbonate and disseminated pyrite, which increase in abundance towards the veins. In thin section, two textural types of pyrite are present: inclusion-rich pyrite rimmed by inclusion-poor pyrite (Fig. 4-7D). Chalcopyrite and native gold (±ilmenite, rutile, tetrahedrite, galena, pyrrhotite, sphalerite, monazite, Au-Ag-tellurides) are present as inclusions predominantly in the inclusions-rich pyrite and fill fractures in both pyrite types. Rutile inclusions may contain finer-grained inclusions of Ag-Bi±Pb-telluride and native

gold (Fig. 4-7E), and inclusions of Au-Ag-tellurides are present in ilmenite grains within the matrix of quartz-feldspar porphyry. Arsenopyrite grains in BIF contain inclusions similar to those present in pyrite but no native gold. Assays of V_1 veins yielded gold values ranging from nil in quartz-feldspar porphyry to a maximum of 65.1g/t in BIF.

A second set of quartz-tourmaline veins (V_2) cuts across sandstone and quartz-feldspar porphyry. V_2 veins are steeply-dipping and NE to ENE-trending (Figs. 4-2, 4-3). At the F zone, V_2 veins cut both limbs of F_2 folds (Fig. 4-8A). The veins overprint the F_2 folds and are in turn overprinted by gentle folds with the same S-shaped asymmetry as the F_2 folds (Fig. 4-8B). Other V_2 veins cut across the S_2 foliation on the south limb of the Hard Rock anticline exposed at Porphyry Hill (Fig. 4-8C). Adjacent to the veins, tourmaline has infiltrated the S_2 foliation and has replaced minerals in sandstone and mudstone beds and the veins are overprinted by asymmetrical Z-shaped F_3 folds (Fig. 4-8D) that formed as flanking structures next to the veins, suggesting pre-D_3 emplacement of the veins. V_2 veins are surrounded by a carbonate-albite-pyrite alteration halo (Fig. 4-8E). In thin section, the veins locally contain molybdenite and monazite as well as pyrite, pyrrhotite and chalcopyrite intimately intergrown with tourmaline. Inclusions of native gold are present in tourmaline and inclusion-poor pyrite (Fig. 4-8F, 4-9A; Table 4-2), which is surrounded by inclusion-rich pyrite intergrown with molybdenite (Fig. 4-9B). Microfractures in inclusion-rich pyrite are filled with micron-sized Au-Ag-Pb-As-telluride grains (Fig. 4-9C) and galena.

A third set of steeply-dipping, NE- to E-trending, quartz-carbonate veins (V_3) overprint the hinge of F_2 folds (Figs. 4-2, 4-3, 4-5, 4-9D). At the F zone, V_3 veins contain flakes of visible gold (Fig. 4-9E), cut across S-shaped F_2 fold hinges (Fig. 4-9D) and are folded by S-shaped folds (Fig. 4-9F). In banded iron formation at the OPP outcrop, V_3 veins and their strong sulfide-rich alteration halos strike 5° to 45° anticlockwise to bedding (Fig. 4-10A) and are oblique to roughly parallel to

the axial plane of later Z-shaped F_3 drag folds. Quartz-carbonate V_3 veins locally contain tourmaline, pyrite, chalcopyrite, xenotime, and monazite and are surrounded by alteration halo of sericite-carbonate-pyrite (±arsenopyrite, rutile, ilmenite) in sandstone (Fig. 4-9E) and quartz-feldspar porphyry (Fig. 4-10B), and sericite-pyrite-arsenopyrite (±carbonate, chlorite, biotite, monazite, pyrrhotite, chalcopyrite) in BIF (Fig. 4-10C). In thin section, pyrite is elongate parallel to the S_2 foliation and has inclusion-rich cores and inclusion-poor rims (Fig. 4-10D). Native gold occurs as inclusions in pyrite (Fig. 4-10E), infills fractures and cavities in pyrite and arsenopyrite (Fig. 4-10F), and fills fractures cutting through ferrodolomite along the margins of the quartz-carbonate veins. Chalcopyrite, pyrrhotite, ilmenite and rutile (±magnetite, galena, monazite, fluor-apatite, Au-Ag-, Ag- and Pb-Bi-tellurides, thorite) also occurs as inclusions in pyrite (Fig. 4-10G) and arsenopyrite grains.

Geochemical footprint of the gold mineralization

The geochemical footprint of the mineralization is described for V_1 to V_3 veins at the F Zone and Porphyry Hill, where the structural relationship between the veins, fabrics, and fold generations can be the most clearly demonstrated, and in two drill holes across high grade intervals in BIF and interlayered sandstone and mudstone at the Hardrock gold deposit.

One hundred and eighty-six drill core samples and 18 surface samples at the F Zone and Porphyry Hill were analyzed for major oxide and trace element compositions using X-ray fluorescence spectrometry (XRF) and inductively coupled plasma mass spectrometry (ICP-MS) methods, respectively. The analytical techniques are described in detail in Appendix 4-A. The precision and accuracy values were calculated based on analyses of reference materials and duplicates, and are

presented in Appendix 4-B. The geochemical composition of representative samples is presented in Table 4-3.

Geochemical footprint of mineralization at the F Zone and Porphyry hill

Following Grant's (1986) isocon method, major and trace element compositions of altered samples were plotted against least-altered precursors to determine elemental changes in altered wallrocks of V_1 and V_3 veins emplaced in sandstone and quartz-feldspar porphyry. Elemental mobility and mass changes were assessed using three of the following five generally immobile elements Zr, Th, Hf, Y, TiO_2, and Al_2O_3. This assessment suggests no to negligible mass changes associated with V_1 and V_3 vein mineralization in sandstone and quartz-feldspar porphyry. Elemental concentrations of altered samples and least-altered precursors were scaled and plotted on isocon diagrams and % elemental mass changes were corrected using the mass factor and plotted as histograms. The results are displayed on Figures 4-11 and 4-12 and summarized in Table 4-4. Alteration halos associated with V_1 and V_3 veins in sandstone and siltstone show major gains in Au, Ag, S, As and Sb (±Se, Te, Bi, CO_2). Alteration haloes associated with the same veins in quartz-feldspar porphyry show significant gains in Au, As, Te, Cu (±W, Se) and losses in Ag, In, Cd, Li (±Mo).

Diamond drill core sections across mineralized intervals

Spearman correlation coefficients were calculated to establish what elements are associated with and were enriched during gold mineralizing processes. Correlations between gold and other elements from 186 drill core samples are estimated using Spearman correlation coefficient and presented in Table 4-5. Major oxide and trace element geochemical profiles are presented in Figs. 4-13 to 4-16. Positive correlations ($r > 0.5$), which are listed in order of decreasing Spearman

correlation coefficients, are observed between Au and (1) S (r=0.9), W, Te, Mo, Bi, Se, As (r=0.66) in 78 sandstone samples; (2) Pb (r=0.79), S, FeO, Bi, Ag, As, Te (r=0.6) in 33 BIF samples; and (3) W (r=0.64), As, Te, S (r=0.47) in 30 porphyry samples. Collectively, Au grades have strong positive correlation with S (r=0.89), W, As, Bi and Te (r=0.59) in all lithologies. Weaker positive correlations ($0.29<r<0.4$) are observed between Au and Pb, Sb, FeO, Mo and Se.

Similar enrichments in Sb, W, Pb, Bi, Te, As are observed in drill hole profiles through mineralized intervals and are plotted in Figures 4-14 and 4-16. The concentration of the pathfinder metals closely resembles the distribution of gold and remains slightly elevated for a few tens to 120 m beyond the mineralized zone. Hydrothermal alteration indices, which monitor the intensity and type of alteration, are also plotted and their Spearman correlation coefficient with Au is presented in Table 4-6. Those providing the best vectors towards gold mineralization are the sulfidation indices such as $S/(SiO_2+Na_2O)$, $SSI=S/(S+Na_2O)$, $KSI=S/(S+K)$, which emphasize the gains in total sulfur relative to other elements, and the sulfidation-carbonation index $(LOI+CO_2+S)/ SiO_2$ (Gemmell, 2006, 2007). At the deposit scale, the sulfidation and sulfidation-carbonation indices only show elevated values within the ore zone (≥0.3 g/t), therefore they best delineate the contour of the ore body.

Table 4-5 shows that the sericitization (MSI=3K/Al molar ratio, Kishida and Kerrich, 1987; EPAI=K/(Al+Na) molar ratio, Whitbread and Moore, 2004) and carbonation (CO_2/Ca; Eilu et al., 2001) indices show weak to moderate positive correlation with Au. This is consistent with diamond drill hole profiles (Figs. 4-16 and 4-16) that outline an up to 250 m wide sericite and carbonate alteration envelope around the gold deposit. None of the alteration indices correlates strongly with Au in porphyry ($0.3<r<0.5$; Table 4-5), which is attributed to its strong to pervasive sericite-carbonate alteration irrespective of the presence of veins. Although the correlation between Au

and carbonate or sericite alteration is weaker than that with sulfidation, these alteration indices can be used as vectors towards Au on district or regional scale.

Laser-ablation ICP-MS trace element geochemistry of pyrite

Turbiditic sandstone is the most voluminous gold mineralized lithology at the Hardrock deposit, thus the most common sulfide mineral in this lithology, pyrite was chosen to establish the crystallographic distribution of gold and other trace elements. Trace element maps of V_1 to V_3 pyrites collected from sandstone samples display complex metal distributions. A pyrite grain associated with a V_1 vein is characterized by an inclusion-rich core and an inclusion-free idioblastic rim (Fig. 4-17). The latter exhibits a crude primary crystallographic zoning defined by variations in As, Co, Ni concentrations, and these metals, together with Au, Ag, Bi, Cr, Cu, Pb, Sb, Te, Ti, V, W, are enriched in the inclusion-rich core of the grain (Fig. 4-17). V_2 pyrite is inclusion-poor with a discontinuous, irregular, inclusion-rich rim (Fig. 4-18). Arsenic, Co and Ni define a crude primary crystallographic zoning within the inclusion-poor centre of the grain, whereas Au, Ag, Bi, Cu, Pb, Sb and Te are concentrated in the inclusion-rich rim of the grain (Fig. 4-18). V_3 pyrite is similar to V_1 pyrite with an inclusion-rich core defined by enrichments in Au, As, Co, Ni, Pb, Sb, Te (and to a lesser extent Ag, Bi) and an inclusion-free rim with a well-developed primary crystallographic zoning defined by variations in As, Co, Ni and possibly Au concentration (Fig. 4-19). All three pyrite generations show inclusions in or fractures crosscutting the inclusion-poor pyrite with elevated Au-Ag-Bi-Te-Pb-Sb concentrations. In summary, inclusion-rich cores or rims of V_1 to V_3 pyrite are typically enriched in Au, Ag, As, Bi, Co, Ni, Pb, Sb, Te, whereas inclusion-free or –poor cores or rims of the grains have a well-defined to crude primary crystallographic Co, Ni, As zoning.

Re-Os geochronology

A gold-mineralized, arsenopyrite-rich, feldspar-quartz porphyry sample (BGBZT2013_362C; Fig. 4-20A-B) with high Re content was chosen for arsenopyrite Re-Os dating. The feldspar-quartz porphyry sample consists of 35% plagioclase and minor quartz phenocrysts (grain size: 0.5-2.5 mm; average: 1-2 mm) in a recrystallized, fine-grained matrix of quartz (58%; average grain size: 30-50 μm), carbonates (7%), and minor sericite, arsenopyrite and pyrite (Fig. 4-20C). Arsenopyrite and pyrite occur as aggregates of multiple grains and as discrete, subhedral to euhedral, grains within quartz-carbonate veins along the contact between the porphyry and sandstone. They also occur as disseminations in both rock types (Fig. 4-20A-D). Six analyses were done (method described in Appendix 4-A) and they define an isochron yielding a model age of 2579±25 Ma (2σ) with an initial $^{187}Os/^{188}Os$=0.58±0.11 (MSWD=0.63; Table 4-7; Figure 4-20E).

Discussion

Structural control of the gold mineralization

Previous studies on structural controls on gold mineralization in the Geraldton area concluded that gold was introduced late during the structural evolution of the belt. Anglin (1987) described the presence of mineralized veins within sheared rock units, along sheared lithological contacts, and parallel to an earlier folded S_1 and a later S_2 cleavage (S_2 and S_3 in this study), and suggested that gold mineralization was introduced both prior to and after the formation of S_2 cleavage and postdated the emplacement of the porphyry dikes by 130 m.y. (Anglin, 1987).

Macdonald (1988) argued for the deposition of gold in conjugate Riedel fractures and P shear fractures during late dextral shearing. Lafrance and others (2004) explained the plunge of the ore shoots parallel to F_3 fold axes by the emplacement of gold-mineralized veins in dextral shear zones

and along the axial planes of F_3 folds during D_3 dextral transpression. Lavigne (2009) described a gabbro xenolith with C-C' shear fabric in a gold mineralized porphyry dike, and suggested that regional dextral shear zones acted as conduits for the emplacement of the dikes and later deposition of gold.

One of these shear zones, the Bankfield-Tombill fault, is located along the southern margin of the Bankfield-Tombill deformation zone. Mechanical stripping of an outcrop exposed the fault as a late brittle-ductile structure hosting mineralization. Dextral shear bands and asymmetric strain shadows around volcanic fragments suggest that the fault formed during the D_3 deformation event. Sulfide minerals occupy Riedel shear fractures along the brittle-ductile fault, which is consistent with previous interpretations about the late deposition of at least some of the gold along brittle fractures (Macdonald, 1988) and within dextral ductile shear zones during the D_3 deformation event (Anglin, 1987; Macdonald, 1988; Williams, 1989; Lafrance et al., 2004).

Located 65 km west of Geraldton, the Brookbank gold deposit is another example of syn-D_3 mineralization. The deposit lies along a splay of the Paint Lake deformation zone at the northern margin of the BGB. Gold is associated with quartz-carbonate veins, ankerite-sericite-chlorite-epidote-pyrite alteration zones, and quartz-orthoclase-pyrite alteration patches within dextrally sheared metabasalts (DeWolfe et al., 2007).

In the Geraldton area, recently stripped outcrops investigated as part of this study provide new information on the relative chronology and structural controls on mineralization. Our observations suggest that the bulk of the gold mineralization was introduced before the D_3 deformation event. Early Fe-carbonate altered beds and veins are folded by F_1 and F_2 folds, and where deformation has been more intense, the beds have been completely transposed parallel to the S_2 cleavage. As

deformation facilitates fluid flow, fluid-rock interaction and alteration, the Fe-carbonate alteration likely occurred early during the D_1 event as strain became localized along the Bankfield-Tombill deformation zone during early thrust imbrication of the belt (Fig. 4-21A-C; Chapter 3 of this thesis). Auriferous V_1 quartz-carbonate veins are also folded by F_1 and F_2 folds, and some veins were boudinaged prior to F_2 folding, suggesting that they were also emplaced early during D_1 thrusting (Fig. 4-21A-C).

Auriferous V_2 tourmaline-quartz and V_3 quartz-carbonate veins cut across the axial plane of F_2 folds as arrays of extensional veins oriented anticlockwise to bedding and to F_2 fold axial planes (Fig. 4-21D-F). Their orientation suggests that the veins were emplaced during NE-SW shortening, which is consistent with sinistral shearing along the ESE-striking Bankfield-Tombill deformation zone. As the veins cut across the S-shaped F_2 folds but are also S-folded, these observations collectively suggest that the veins were emplaced during sinistral shear along the Bankfield-Tombill deformation zone as the shear component of regional D_2 transpression became localized along the deformation zone (Chapter 3 of this thesis). The older V_2 veins, which are oriented at a higher angle to bedding and to S_2 than the V_3 veins (Fig. 4-21F), were emplaced first, underwent anticlockwise rotation during sinistral shear, and were then overprinted by the V_3 veins which were emplaced later during the same shearing event. Subsequent dextral shear during the D_3 event reversed the rotation of the veins and produced flanking structures adjacent to the veins. The latter acted as planar anisotropies that impeded shearing along the S_2 cleavage and bedding, and facilitated buckling and the formation of F_3 flanking folds (Fig. 4-21G; Chapter 3 of this thesis). F_3 flanking structures adjacent to arrays of V_3 extensional veins are also present at Missing Link (Fig. 3-10C in Chapter 3 of this thesis) along the Paint Lake fault and in shear zones at the 801 stripping near Jellicoe (Fig. 3-12C in Chapter 3 of this thesis).

The ore zones have shallow westerly plunges similar to those of other linear structural elements (L_2 stretching lineation, F_1, F_2 and F_3 fold axes) in the Bankfield-Tombill deformation zone. These structures and the ore zones formed before or during the dextral D_3 event and were rotated towards the shear direction during D_3 shearing (Chapter 3 of this thesis). Thus, although the main ore zones formed early during the D_1 and D_2 events, their geometry reflects the total strain history of the Bankfield-Tombill deformation zone.

Hydrothermal alteration and geochemical footprint at the Hardrock gold deposit

Similar sericite-carbonate-pyrite alteration halos are associated with quartz-carbonate V_1 and V_3 veins although they were emplaced during separate deformation events and in different rock types, i.e. sandstone and quartz-feldspar porphyry. The presence of pyrite in the vein alteration halos explains the mass gains in S and Se, which substitutes for S in sulfide minerals. Mass gains in CO_2 and CaO in sandstone are represented by the formation of carbonates and mass gains in K_2O is due to potassic sericitic alteration adjacent to the veins. In quartz-feldspar porphyry, the inconsistent enrichment in both CO_2 and K_2O in the alteration halos of the veins, the pervasive sericite and carbonate alteration across the porphyry, and the poor correlation between Au and alteration indices, reflect the emplacement of the gold-bearing veins within a much broader sericite-carbonate alteration envelope that extends for as much as 250 metres beyond the mineralized zones. This extensive sericite-carbonate alteration may explain the lack of unaltered protoliths near the gold deposit.

Pathfinder metals with high Au Spearman correlation coefficients (S, W, Te, Mo, Bi, Se, As in sandstone; W, As, Te, S in porphyry) generally correspond with major mass gains of those elements in isocon diagrams and % mass change histograms of V_1 and V_3 veins. Enrichments in

Au, Ag, As, Bi, Co, Ni, Pb, Sb, Te are also present in inclusion-rich pyrites on trace element maps. Point concentrations of Au, Bi, Cr, Pb, Te, Sb, Ti, As within zones of more uniform enrichments of those elements suggest that they represent inclusions in pyrites, which also incorporated those metals either as submicroscopic particles or as elements within their crystal lattice during their growth. Inclusion-poor pyrite with primary crystallographic Ni-Co-As zoning contains no or negligible gold concentrations, which is consistent with the lack of correlation between Au and Ni-Co in whole rock samples. Elevated Au, Ag, Bi, Pb, Sb, Te concentrations along late fractures intersecting both pyrite types indicate that Au was remobilized during an event that postdates both the early-D_1 and the syn-D_2 gold episodes. The strong Au-W correlation in whole rock samples and the low concentrations of W in both inclusion-rich and inclusion-poor pyrite suggest that W was included in other minerals (scheelite?) that formed during gold deposition.

In BIF, sulfide-rich alteration halos surrounding quartz-carbonate veins yielded gold grades as high as 89.9 g/t (Tóth et al., 2018). The alteration halos formed by replacement of magnetite-rich laminae by pyrite and arsenopyrite (± chalcopyrite, pyrrhotite). Sulfidation reactions between magnetite/ilmenite and the hydrothermal fluids destabilized Au-bisulfide complexes in the fluids, precipitating gold (Groves et al., 1998, 2003; Phillips and Powell, 2010) and rutile as a by-product of the sulfidation reactions (Clark and Williams-Jones, 2004). In quartz-feldspar porphyry and sandstone, the replacement of ilmenite and/or titanomagnetite by pyrite and rutile (Fig. 4-10G), and the presence of rutile inclusions in pyrite (Fig. 4-10E), further suggest that host rock sulfidation was one of the processes by which gold precipitated. The alternation of auriferous inclusion-rich pyrites and barren inclusion-poor pyrites indicates that they grew from pulses of metal-rich and metal-poor fluids. Gold was subsequently redistributed as suggested by the infilling of fractures in pyrite and quartz-carbonate veins by native gold, Au-Ag-tellurides and galena (Fig. 4-10F), and

by the presence of Ag-Bi±Pb-telluride and native gold in rutile inclusions in pyrite (Figs. 4-7B, 4-7D, 4-9C). The late gold remobilization is further supported by Au-rich fractures that crosscut barren inclusion-poor pyrite (e.g. Fig. 4-19).

In summary, the similarity in the mineralogy and mass changes in alteration halos of V_1 and V_3 quartz-carbonate veins suggest that they were deposited from hydrothermal fluids similar in composition. The deposition of tourmaline-rich V_2 veins indicates a transient influx of more boron-rich hydrothermal fluids. Textural relationships reveal complex hydrothermal alteration histories involving early stages of sulfides, and possibly gold deposition, during sulfidation reactions between iron-rich oxide minerals and hydrothermal fluids that infiltrated the wall rocks of the veins. Metal-rich and metal-poor pyrites reflect the metal content of the reacting hydrothermal fluids. This was followed by the redistribution and/or introduction of gold and other metals by metal-rich late fluids which percolated along fractures in earlier-formed pyrite and precipitated gold and other metal-rich mineral phases along these fractures. Hydrothermal alteration produced a broad sericite-carbonate footprint, which extends as far as 250 meters from the deposits, in which S, Te, As, W, and Bi are the best indicators of the presence of Au.

Chronology of gold mineralization events

The 2579±25 Ma (2σ) Re-Os arsenopyrite model age for gold mineralization at the Hardrock deposit is significantly younger than that of other mineralization events in gold camps across the Superior Province. In the Red Lake gold camp in the Uchi domain, the main stage of gold mineralization occurred synchronously with D_2 regional deformation at ca. 2723 to ca. 2712 Ma (Dubé et al., 2004). In the Timmins camp in the Abitibi subprovince, it occurred later and is coeval with <2672±7Ma Ma to ca. 2660 Ma D_3 and D_4 deformation events (Ayer et al., 2005; Bateman

and Bierlein, 2007; Bateman et al., 2008). Circa 100 km to the southeast in the Kirkland Lake - Larder Lake camp area, gold was deposited between 2672±2 Ma and 2665±4 Ma during D_2 regional folding and shearing (Wilkinson et al., 1999), but was later remobilized during the Paleoproterozoic in hematite-quartz-carbonate veins (1730±5 Ma, U-Pb monazite), which overprint the main mineralized veins at the Young-Davidson deposit (Zhang et al., 2014). Closer to the BGB, gold at the Hemlo deposit in the Wawa subprovince was deposited and/or remobilized during a short, contracted, regional D_2 deformation, magmatic and mineralization event (Lin, 2001; Muir, 2002, 2003), which is bracketed between 2680±1 and 2677±1 Ma (Davis and Lin, 2003).

In the Geraldton camp, the maximum age of gold mineralization is 2694±1 Ma, which is the crystallization age of the pre-or early-D_1, altered porphyry at the Hardrock deposit (Chapter 2 and 3 of this thesis). The gold mineralization is deposited in second-order structures adjacent to the crustal-scale Bankfield-Tombill fault that was initiated and reactivated during deformation events related to the ca. 2690 Ma Shebandovanian orogeny, a major tectonic process responsible for the assembly of the Superior craton (Percival et al., 2012). The 2579±25 Ma Re-Os model age is broadly similar to Pb model ages (2474-2563 Ma) obtained from galena collected at the Bankfield mine (#1 on Fig. 4-1; Anglin, 1987). As these ages are significantly younger than those of other major mineralization events in the Superior craton and much postdate the Shebandovanian orogeny, the Re-Os and Pb model ages likely represent disturbed ages which were partially reset either during the emplacement of the Matachewan diabase dike swarm at 2452+3/-2 Ma (Heaman, 1988), or during the emplacement of the Nipigon diabase complex at 1108.8+4/-2 Ma (Davis and Sutcliffe, 1985) as even younger Pb model ages (ca. 1100-1600 Ma) were previously obtained from pyrite from the Hardrock deposit (Anglin, 1987).

Comparison with other major orogenic gold camps

The superimposition and recurrence of mineralization events associated with major faults or shear zones occur in other Archean orogenic gold camps. In the Timmins camp, ca. 2672±7 Ma (Ayer et al., 2005) Cu-Au-Ag-Mo stockwork mineralization is spatially associated with the 2691±3 Ma Millerton and 2689±1 Ma Pearl Lake porphyries (Corfu et al., 1989), which are located within ca. 5 km north of the Porcupine-Destor deformation zone (Burrows et al., 1993; Dubé et al., 2018). This early style of mineralization is overprinted by gold-bearing quartz-carbonate veins that were emplaced during D_3 sinistral and D_4 dextral transpression along the Hollinger shear zone, a second-order structure parallel to the Porcupine – Destor deformation zone (Davies and Luhta, 1978; Mason and Melnik, 1986; Corfu et al., 1989; Burrows et al., 1993; Bleeker, 1995, 1999; Dubé et al., 2003; Ayer et al., 2005; Bateman et al., 2005, 2008; Dubé et al., 2018). In the Kirkland Lake – Larder Lake camp, orogenic gold mineralization was emplaced during D_2 south-side-up shearing along the Larder Lake-Cadillac deformation zone (Ayer et al., 2005; Ispolatov et al., 2008; Lafrance, 2015) and during D_4 reverse-dextral displacement along the Kirkland Lake fault (Ispolatov et al., 2008), which is one of several narrow brittle-ductile faults located 2 – 3 km north of the Larder Lake - Cadillac deformation zone. The tectonic evolution of both the Porcupine – Destor and the Larder Lake-Cadillac deformation zones and the gold events in the Timmins and Kirkland Lake camps are associated with a craton scale contraction caused by the amalgamation of the Wawa-Abitibi and Minnesota River Valley terranes and the closure of the Pontiac basin (Bateman et al., 2008; Percival et al., 2012; Dubé et al., 2018).

In the Eastern Goldfields province of Australia, deposits of the Kalgoorlie and Laverton camps cluster along the Boulder-Lefroy fault and the Laverton tectonic zone, respectively (Hallberg, 1986; Clout et al., 1990; Goldfarb et al., 2001, 2005; Salier, 2003; Robert et al., 2005). The gold

deposition at the Kalgoorlie and Laverton camps is associated with tectonic processes resulting in the amalgamation of the Kalgoorlie, Kurnalpi and Burtville Terranes (Vielreicher et al., 2015). In the Laverton camp, gold mineralization at the Granny Smith and Sunrise Dam deposits was emplaced during progressive D_2 and D_3 ENE-WSW compression and dextral-reverse faulting (i.e. D_4 of Swager, 1997; Brown, 2002; Salier, 2003; Vielreicher et al., 2015). Alternatively, Henson et al. (2010) linked gold mineralization at the Wallaby and Sunrise Dam deposits to D_{4b} NW-SE compression (sinistral transpression) and/or D_5 NE-SW compression (dextral strike slip faulting; Blewett et al., 2010). Although the two interpretations differ, in both cases, gold mineralization was emplaced during multiple overprinting events. In the Kalgoorlie camp, mineralization spanned three deformation events. Gold-tellurium Fimiston style mineralization at the Golden Mile deposit was emplaced during late-D_1 thrusting, the Oroya shoots at the same deposit formed during D_2 regional folding and reverse faulting, and the veins at the Mt. Charlotte deposit, which is located at roughly 5 km north of the Golden Mile deposit, were emplaced during late D_4 dextral strike-slip faulting (Bateman and Hagemann, 2004). More recently, other interpretations of the structural and mineralization history of the camp have been proposed by Blewett et al. (2010), Vielreicher et al. (2015) and Mueller (2017) but all involve the juxtaposition of multiple ore-forming events.

In summary, as for other major orogenic gold camps in Archean cratons, gold deposits in the Geraldton camp formed during multiple mineralization events along a reactivated major deformation zone or fault associated with contractional deformation during the assembly of the Superior craton. Gold was deposited from several syntectonic gold-bearing fluid pulses which contributed to and culminated in the formation of the Geraldton gold camp.

Conclusions

Previous interpretations invoked orogen-parallel dextral transcurrent faulting as the main structural control on the emplacement of gold mineralization in the BGB (Anglin, 1987; Macdonald, 1988; Williams, 1989; Lafrance et al., 2004; DeWolfe et al., 2007; Lavigne, 2009). Gold mineralization was thought to be coeval with the formation of structures and dilational zones during regional dextral transcurrent faulting, such as the hinge of Z-shaped folds, dextral shear zones at the contact between rock units, and reactivated thrust faults at the contact between panels of metasedimentary and metavolcanic rocks. Our results suggest that gold was emplaced earlier during the structural history of the belt and involved two stages of gold mineralization. The hydrothermal mineralization history of the Geraldton camp began with the formation of quartz-carbonate veins and early bedding-parallel Fe-carbonate alteration during D_1 faulting and thrust imbrication of the belt. These veins and early Fe-carbonate alteration were folded and transposed along the Bankfield-Tombill deformation zone as panels in the belt were regionally folded and shear became localized along higher strain deformation zone during regional D_2 sinistral transpression. Hydrothermal fluids flowed into the Bankfield-Tombill deformation zone which acted as a conduit for the migration of hydrothermal fluids, and auriferous quartz-tourmaline and quartz-carbonate veins were deposited across S-shaped folds that formed during sinistral shearing along the deformation zone. Reactivation of the deformation zone during regional D_3 dextral transpression rotated and boudinaged these veins and redistributed or introduced new gold and other metals into localized dextral faults and shear zones.

The complex hydrothermal fluid history of the Geraldton camp is recorded by the textures of pyrite grains and their chemical composition. Inclusion-poor pyrites and metal-rich, inclusion rich pyrites are associated with both syn-D_1 and syn-D_2 vein generations. They formed during fluid-rock

sulfidation reactions with their metal content reflecting that of the hydrothermal fluids. Gold was then redistributed, or new gold and other metals were introduced, during the infiltration of late fluids along microfractures cutting across sulfide minerals and other alteration minerals. As this process occurred at different times during the formation of the Geraldton gold deposits, our study exemplifies how the juxtaposition of multiple mineralization events and the redistribution of metals during the prolonged structural history of a major deformation zone can result in the formation of complex ore deposits.

References

Allmendinger, R.W., Cardozo, N.C., Fisher, D., 2013. Structural Geology Algorithms: Vectors & Tensors. Cambridge University Press, Cambridge, England. 289 p.

Anglin, C.D., 1987. Geology, structure and geochemistry of gold mineralization in the Geraldton area, Northwestern Ontario. Unpublished Master's Thesis. Memorial University of Newfoundland, St. John's, Newfoundland. 283 p.

Ayer, J.A., Thurston, P.C., Bateman, R., Dubé, B.,Gibson, H.L., Hamilton, M.A., Hathway, B., Hocker, S.M., Houlé, M.G., Hudak, G., Ispolatov, V.O., Lafrance, B., Lesher, C.M., MacDonald, P.J., Péloquin, A.S., Piercey, S.J., Reed, L.E. and Thompson, P.H. 2005. Overview of results from the Greenstone Architecture Project: Discover Abitibi Initiative; Ontario Geological Survey, Open File Report 6154, 146p.

Ayres, L.D., 1969. Early Precambrian stratigraphy of part of Lake Superior Provincial Park, Canada, and its implication for the origin of the Superior Province. Unpublished Ph.D thesis. Princeton University, Princeton, NJ. 798 p.

Barrett, T.J., Fralick, P.W., 1985. Sediment redeposition in Archean Iron Formation: Examples from the Beardmore-Geraldton Belt, Ontario. J. Sediment. Petrol. 55, 205–212.

Bateman, R., Ayer, J., Dubé, B., 2008. The Timmins-Porcupine Gold Camp, Ontario: Anatomy of an Archean Greenstone Belt and Ontogeny of Gold Mineralization. Econ. Geol. 103, 1285–1308. doi:10.2113/gsecongeo.103.6.1285

Bateman, R., Ayer, J., Dubé, B., Hamilton, M.A., 2005. The Timmins–Porcupine gold camp, northern Ontario: the anatomy of an Archaean greenstone belt and its gold mineralization: Discover Abitibi Initiative; Ontario Geological Survey, Open File Report 6158.

Bateman, R., Bierlein, F.P., 2007. On Kalgoorlie (Australia), Timmins–Porcupine (Canada), and factors in intense gold mineralisation. Ore Geol. Rev. 32, 187–206. doi:10.1016/j.oregeorev.2006.08.001

Bateman, R., Hagemann, S., 2004. Gold mineralisation throughout about 45 Ma of Archaean orogenesis: Protracted flux of gold in the Golden Mile, Yilgarn craton, Western Australia. Miner. Depos. 39, 536–559. doi:10.1007/s00126-004-0431-2

Bleeker, W., 1995. Day 1: Surface geology of the Porcupine camp, In: Heather, K.B., Percival, A.J., Moser, D., Bleeker, W. (Eds.), Tectonics and Metallogeny of Archean Crust in the Abitibi–Kapuskasing–Wawa Region, Field Trip Guidebook; Open File 3141. Geological Survey of Canada, pp. 13–37.

Bleeker, W., 1999. Structure, Stratigraphy and Primary Setting of the Kidd Creek Volcanogenic Massive Sulfide Deposit: A Semiquantitative Reconstruction, in: Hannington, M.D., Barrie,

C.T. (Eds.), The Giant Kidd Creek Volcanogenic Massive Sulfide Deposit, Western Abitibi Subprovince, Canada, Economic Geology Monographs 10. Society of Economic Geologists, pp. 71–122. doi:10.5382/Mono.10

Blewett, R.S., Czarnota, K., Henson, P.A., 2010. Structural-event framework for the eastern Yilgarn Craton, Western Australia, and its implications for orogenic gold. Precambrian Res. 183, 203–229. doi:10.1016/j.precamres.2010.04.004

Brown, S.M., 2002. Structural and temporal evolution of a complex ore system: Cleo Gold Deposit, Eastern Goldfields Province, Western Australia. Unpublished PhD thesis. University of Western Australia. 337 pp.

Buck, S., 1986. Structural studies and gabbro mylonitization within the Barton Bay Deformation Zone, Geraldton, Ontario. Unpublished MSc thesis. Brock University, St. Catharines, Ontario. 171 p.

Burrows, D.R., Spooner, E.T.C., Wood, P.C., Jemielita, R.A., 1993. Structural controls on formation of the Hollinger-McIntyre Au quartz vein system in the Hollinger shear zone, Timmins, southern Abitibi greenstone belt, Ontario. Econ. Geol. 88, 1643–1663. doi:10.2113/gsecongeo.88.6.1643

Cardozo, N., Allmendinger, R.W., 2013. Spherical projections with OSXStereonet. Comput. Geosci. 51, 193–205. doi:10.1016/j.cageo.2012.07.021

Carter, M.W., 1987. Geology of McComber and Vincent Townships, District of Thunder Bay; Ontario Geological Survey, Open File Report 5648, 144p.

Clark, J.R., Williams-Jones, A.E., 2004. Rutile as a potential indicator mineral for metamorphosed metallic ore deposits. Rapport Final de DIVEX, Sous-projet SC2, Montréal, Canada. 17 pp.

Clout, J.M.F., Cleghorn, J.H., P.C., E., 1990. Geology of the Kalgoorlie goldfield, in: Hughes, F.E. (Ed.), Geology of the Mineral Deposits of Australia and Papua New Guinea. Australasian Institute of Mining and Metallurgy, pp. 411–431.

Corfu, F., 2000. Extraction of Pb with atrificially too-old ages during stepwise dissolution experiments on Archean zircon. Lithos 53, 279–291.

Corfu, F., Krogh, T.E., Kwok, Y.Y., Jensen, L.S., 1989. U-Pb zircon geochronology in the southwestern Abitibi greenstone belt, Superior Province. Can. J. Earth Sci. 26, 1747–1763. doi:10.1017/CBO9781107415324.004

Davies, J.F., Luhta, L.E., 1978. An Archean "Porphyry-type" Disseminated Copper Deposit, Timmins, Ontario. Econ. Geol. 73, 383–396.

Davis, D.W., Lin, S., 2003. Unraveling the geologic history of the Hemlo Archean gold deposit, superior province, Canada: A U-Pb geochronological study. Econ. Geol. 98, 51–67. doi:10.2113/gsecongeo.98.1.51

Davis, D.W., Sutcliffe, R.H., 1985. U-Pb ages from the Nipigon plate and northern Lake Superior (Canada). Geol. Soc. Am. Bull. 96, 1572–1579. doi:10.1130/0016-7606(1985)96<1572:UAFTNP>2.0.CO;2

Devaney, J.R. and Fralick, P.W., 1985. Regional sedimentology of the Namewaminikan Group, northern Ontario: Archean fluvial fans, braided rivers, deltas, and an aquabasin; Current Research, Part B, Geological Survey of Canada, Paper 85-18, p. 125-132.

Devaney, J.R., Williams, H.R., 1989. Evolution of an Archean subprovince boundary: a sedimentological and structural study of part of the Wabigoon–Quetico boundary in northern Ontario. Can. J. Earth Sci. 26, 1013–1026.

DeWolfe, J.C., Lafrance, B., Stott, G.M., 2007. Geology of the shear-hosted Brookbank gold prospect in the Beardmore–Geraldton belt, Wabigoon Subprovince, Ontario. Can. J. Earth Sci. 44, 925–946. doi:10.1139/E06-118

Dubé, B. and Gosselin, P., 2007. Greenstone-hosted quartz-carbonate vein deposits, In: Mineral deposits of Canada: A Synthesis of Major Deposit Types, District Metallogeny, the Evolution of Geological Provinces, and Exploration Methods, (ed.) W.D. Goodfellow; Geological Association of Canada, Mineral Deposits Division, Special Publication no. 5, p. 49–73.

Dubé, B., Mercier-Langevin, P., Ayer, J.A., Atkinson, B., Monecke, T., 2018. Orogenic greenstone-hosted quartz-carbonate gold deposits of the Timmins-Porcupine camp, in: Monecke, T., Mercier-Langevin, P., Dubé, B. (Eds.), Archean Base and Precious Metal Deposits, Southern Abitibi Greenstone Belt, Canada. Society of Economic Geologists, Reviews in Economic Geology, v. 19, pp. 51–79.

Dubé, B., Williamson, K., and Malo, M., 2003: Gold mineralization within the Red Lake mine trend: example from the Cochenour-Willans mine area, Red Lake, Ontario, with new key

information from the Red Lake mine and potential analogy with the Timmins camp; Geological Survey of Canada, Current Research 2003-C21, 15 p.

Dubé, B., Williamson, K., McNicoll, V.J., Malo, M., Skulski, T., Twomey, T., Sanborn-Barrie, M., 2004. Timing of gold mineralization at Red Lake, northwestern Ontario, Canada: New constrainsts from U-Pb geochronology at the Goldcorp High-Grade zone, Red Lake mine, and the Madsen mine. Econ. Geol. 99, 1611–1641. doi:10.2113/gsecongeo.99.8.1611

Eilu, P., Mikucki, E.J., Dugdale, A.L., 2001. Alteration zoning and primary geochemical dispersion at the Bronzewing lode-gold deposit, Western Australia. Miner. Depos. 36, 13–31. doi:10.1007/s001260050283

Ferguson, S.A., 1965. Leitch Gold Mines Limited Surface Plan of Eastern Part of Property, Parts of Eva and Summers Townships, District of Thunder Bay; Preliminary Geological map no. P.484.

Fralick, P.W., Pufahl, P., 2006. Iron formation in Neoarchean deltaic successions and Microbially mediated depositon of transgessive systems tracts. J. Sediment. Res. 76, 1057–1066.

Gemmell, J.B., 2006. Exploration implications of hydrothermal alteration associated with epithermal Au-Ag deposits. ASEG Ext. Abstr. 2006, 1. doi:10.1071/ASEG2006ab048

Gemmell, J.B., 2007. Hydrothermal alteration associated with the Gosowong epithermal Au-Ag deposit, Halmahera, Indonesia: Mineralogy, geochemistry, and exploration implications. Econ. Geol. 102, 893–922. doi:10.2113/gsecongeo.102.5.893

G Mining Services 2016. NI 43-101 Technical Report, Hardrock Project, Ontario, Canada. 509p.

Goldfarb, R.J., Baker, T., Dubé, B., Groves, D.I., Hart, C.J.R., and Gosselin, P., 2005. Distribution, character, and genesis of gold deposits in metamorphic terranes, In: Economic Geology 100th Anniversary Volume, (ed.) J.W. Hedenquist, J.F.H. Thompson, R.J. Goldfarb, and J.P. Richards; Society of Economic Geologists, Littleton, Colorado, p. 407–450.

Goldfarb, R.J., Groves, D.I., Gardoll, S., 2001. Orogenic gold and geologic time: A global synthesis. Ore Geol. Rev. 18, 1–75. doi:10.1016/S0169-1368(01)00016-6

Grant, J.A., 1986. The isocon diagram-a simple solution to Gresens' equation for metasomatic alteration. Econ. Geol. 81, 1976–1982. doi:10.2113/gsecongeo.81.8.1976

Groves, D.I., Goldfarb, R.J., Gebre-Mariam, M., Hagemann, S.G., Robert, F., 1998. Orogenic gold deposits: a proposed classification in the context of their crustal distribution and relationship to other gold deposit types. Ore Geol. Rev. 13, 7–27. doi:10.1016/S0169-1368(97)00012-7

Groves, D.I., Goldfarb, R.J., Robert, F., Hart, C.J.R., 2003. Gold deposits in metamorphic belts: Overview of current understanding, outstanding problems, future research, and exploration significance. Econ. Geol. 98, 1–29. doi:10.2113/gsecongeo.98.1.1

Hallberg, J.A., 1986. Archaean basin development and crustal extension in the northeastern Yilgarn Block, western Australia. Precambrian Res. 31, 133–156. doi:10.1016/0301-9268(86)90071-9

Hart, T.R., terMeer, M. and Jolette, C. 2002. Precambrian geology of Kitto, Eva, Summers, Dorothea and Sandra townships, northwestern Ontario: PhoenixBedrock Mapping Project; Ontario Geological Survey, Open File Report 6095, 206 p.

Heaman, L.M., 1988. A precise U-Pb zircon age for a Hearst dike;, In: Program with Abstracts, Annual Meeting Geological Association of Canada- Mineralogical Association of Canada, v.13. p. A53.

Henson, P.A., Blewett, R.S., Roy, I.G., Miller, J.M., Czarnota, K., 2010. 4D architecture and tectonic evolution of the Laverton region, eastern Yilgarn Craton, Western Australia. Precambrian Res. 183, 338–355. doi:10.1016/j.precamres.2010.08.003

Horwood, H.C., Pye, E.G., 1955. Geology of Ashmore Township. In: 60th Annual Report of the Ontario Department of Mines, Part 5. 139 p.

Ishikawa, Y., Sawaguchi, T., Iwaya, S., Horiuchi, M., 1976. Delineation of Prospecting Targets for Kuroko Deposits Based on Modes of Volcanism of Underlying Dacite and Alteration Haloes. Min. Geol. 26, 105–117.

Ispolatov, V., Lafrance, B., Dubé, B., Creaser, R.A., Hamilton, M.A., 2008. Geologic and structural setting of gold mineralization in the Kirkland Lake-Larder Lake gold belt, Ontario. Econ. Geol. 103, 1309–1340. doi:10.2113/gsecongeo.103.6.1309

Kerswill, J.A., 1993. Models for iron-formation-hosted gold deposits, In Mineral Deposit Modeling, (eds.) R.V. Kirkham, W.D. Sinclair, R.I. Thorpe and J.M. Duke, Geological Association of Canada, Special Paper 40, p. 171-199.

Kerswill, J.A., 1996. Iron-formation-hosted stratabound gold, in: Eckstrand, O.R., Sinclair, W.D., Thorpe, R.I. (Eds.), Geology of Canadian Mineral Deposit Types. Geological Survey of Canada, pp. 367–382.

Kishida, A., Kerrich, R., 1987. Hydrothermal alteration zoning and gold concentration at the Kerr-Addison Archean lode gold deposit, Kirkland Lake, Ontario (Canada). Econ. Geol. 82, 649–690. doi:10.2113/gsecongeo.82.3.649

Kresz, D.U., Zayachivsky, B., 1991. Precambrian Geology, northern Long Lake area. Ontario Geological Survey, Report 273, 77 p.

Kretz, R., 1983. Symbols for rock-forming minerals. Am. Mineral. 68, 277–279. doi:10.1016/0016-7037(83)90220-X

Lafrance, B., 2015. Geology of the orogenic Cheminis gold deposit along the Larder Lake – Cadillac deformation zone, Ontario. Can. J. Earth Sci. 52, 1093–1108. doi:dx.doi.org/10.1139/cjes-2015-0067

Lafrance, B., DeWolfe, J.C., Stott, G.M., 2004. A structural reappraisal of the Beardmore-Geraldton Belt at the southern boundary of the Wabigoon subprovince, Ontario, and implications for gold mineralization. Can. J. Earth Sci. 41, 217–235. doi:10.1139/E03-090

Lavigne, M.J. 2009. Distribution of gold with respect to lithologies, metamorphic facies and strain state in the Beardmore–Geraldton greenstone belt; OntarioGeological Survey, Open File Report 6241, 88p.

Lin, S., 2001. Stratigraphic and structural setting of the Hemlo gold deposit, Ontario, Canada. Econ. Geol. 96, 477–507. doi:10.2113/gsecongeo.96.3.477

Macdonald, A.J. 1988. The Geraldton Gold Camp: The Role of Banded Iron Formation; Ontario Geological Survey, Open File Report 5694, 173p.

Mackasey, W.O., 1975. Geology of Dorothea, Sandra, and Irwin Townships, District of Thunder Bay. Ontario Division of Mines, Geological Report 122, 83 p.

Mackasey, W.O., 1976. Geology of Walters and Leduc Townships, District of Thunder Bay. Ontario Division of Mines, Geoscience Report 149. 58 p.

Mason, J.K., McConnell, C.D., 1983. Gold mineralization in the Beardmore-Geraldton area, In: Colvine, A.C. (Ed.), The Geology of Gold in Ontario, Ontario Geological Survey, Misc. Paper 110. pp. 84–97.

Mason, J.K., White, G., 1986. Gold occurrences, prospects and deposits of the Beardmore-Geraldton area, District of Thunder Bay and Cochrane. Ontario Geological Survey, Open File Report 5630. 680 p.

Mason, J.K., White, G., McConnell, C.D., 1985. Field Guide to the Beardmore-Geraldton Metasedimentary-Metavolcanic Belt; Ontario Geological Survey, Open File Report 5538. p. 73

Mason, R., Melnik, N., 1986. The McIntyre-Hollinger investigation, Timmins, Ontario: a gold-dominated porphyry copper system; In: Current Research, Part B, Geological Survey of Canada, Paper 1986-1B. pp. 577–583.

Mueller, A.G., 2017. Structural setting of Fimiston- and Oroya-style pyrite-telluride-gold lodes, Paringa South mine, Golden Mile, Kalgoorlie: 1. Shear zone systems, porphyry dykes and deposit-scale alteration zones. Miner. Depos. doi:10.1007/s00126-017-0747-3

Muir, T.L., 2002. The Hemlo gold deposit, Ontario, Canada: Principal deposit characteristics and constraints on mineralization. Ore Geol. Rev. 21, 1–66. doi:10.1016/S0169-1368(02)00066-5

Muir, T.L., 2003. Structural evolution of the Hemlo greenstone belt in the vicinity of the world-class Hemlo gold deposit. Earth 430, 395–430. doi:10.1139/E03-004

Percival, J.A., Sanborn-Barrie, M., Skulski, T., Stott, G.M., Helmstaedt, H., White, D.J., 2006. Tectonic evolution of the western Superior Province from NATMAP and Lithoprobe studies. Can. J. Earth Sci. 43, 1085–1117.

Percival, J.A., Skulski, T., Sanborn-Barrie, M., Stott, G.M., Leclair, A.D., Corkery, M.T., and Boily, M. 2012. Geology and tectonic evolution of the Superior Province, Canada. Chapter 6; In: Tectonic Styles in Canada: The LITHOPROBE Perspective. Edited by J.A. Percival, F.A. Cook, and R.M. Clowes. Geological Association of Canada, Special Paper 49, pp. 321–378.

Phillips, G.N., Powell, R., 2010. Formation of gold deposits: A metamorphic devolatilization model. J. Metamorph. Geol. 28, 689–718. doi:10.1111/j.1525-1314.2010.00887.x

Pye, E.G., 1952. Geology of Errington Township, Little Long Lac Area, in: 60th Annual Report of the Ontario Department of Mines. Ontario Department of Mines, 140 p.

Robert, F., Poulsen, K.H., Cassidy, K.F., Hodgson, J.C., 2005. Gold Metallogeny of the Superior and Yilgarn Cratons, in: Hedenquist, J.W., Thompson, J.F.H., Goldfarb, R.J., Richards, J.P. (Eds.), Economic Geology 100th Anniversary Volume. pp. 1001–1033.

Saeki Y. and Date J., 1980 Computer application to the alteration data of the footwall dacite lava at the Ezuri Kuroko deposits, Akita prefecture, Mining Geology 30, 241-250

Salier, B., 2003. The timing and source of gold-bearing fluids in the Laverton Greenstone Belt, Yilgarn Craton, with emphasis on the Wallaby gold deposit. PhD thesis, University of Western Australia, Perth, WA, Australia, 379 p.

Shanks, W.S. 1993. Geology of Eva and Summers townships, District of Thunder Bay; Ontario Geological Survey, Open File Report 5821, 93p.

Siivola, J., Schmid, R., 2007. A systematic nomenclature for metamorphic rocks: 12. List of mineral abbreviations. [https://www.bgs.ac.uk/downloads/start.cfm?id=3197].

Swager, C.P., 1997. Tectono-stratigraphy of late Archaean greenstone terranes in the southern Eastern Goldfields, Western Australia. Precambrian Res. 83, 11–42. doi:10.1016/S0301-9268(97)00003-X

Tomlinson, K.Y., Hall, R.P., Hughes, D.J., Thurston, P.C., 1996. Geochemistry and assemblage accretion of metavolcanic rocks in the Beardmore–Geraldton greenstone belt, Superior Province. Can. J. Earth Sci. 33, 1520–1533.

Tóth, Z., Lafrance, B., Dubé, B., Bécu, V., Lauzière, K., 2018. Whole-rock lithogeochemistry of the Archean Hardrock orogenic gold deposit, Ontario, Canada; Geological Survey of Canada, Open File; in prep.

Vielreicher, N.M., Groves, D.I., McNaughton, N.J., Fletcher, I.R., 2015. The timing of gold mineralization across the eastern Yilgarn craton using U–Pb geochronology of hydrothermal phosphate minerals. Miner. Depos. 50, 391–428. doi:10.1007/s00126-015-0589-9

Whitbread, M.A., Moore, C.L., 2004, Two lithogeochemical approaches to the identification of alteration patterns at the Elura Zn–Pb–Ag deposit, Cobar, New South Wales, Australia: use of Pearce Element Ratio analysis and Isocon analysis, GEEA, May 1 2004, Volume 4, Issue 2

Wilkinson, L., Cruden, A.R., Krogh, T.E., 1999. Timing and kinematics of post-Timiskaming deformation within the Larder Lake - Cadillac deformation zone, southwest Abitibi greenstone belt, Ontario, Canada. Can. J. Earth Sci. 36, 627–647. doi:10.1139/e99-015

Williams, H.R., 1987. Ontario Geoscience Research Program, Grant No. 242. Structural Studies in the Wabigoon and Quetico Subprovinces, Ontario Geological Survey, Open File Report 5668. 163 p.

Williams, H.R., 1989. Geological studies in the Wabigoon, Quetico and Abitibi-Wawa subprovinces, Superior Province of Ontario, with emphasis on the structural development of the Beardmore-Geraldton Belt, Ontario Geological Survey. Open File Report 5724. 189 p.

Wilson, A.W.G., 1910. Geology of the Nipigon Basin, Ontario. Geological Survey of Canada, Memoir no. 1, 1910, 177 pages, 1 sheet; doi:10.4095/100476

Zhang, J., Linnen, R., Lin, S., Davis, D., Martin, R., 2014. Paleoproterozoic hydrothermal reactivation in a Neoarchean orogenic lode-gold deposit of the southern Abitibi subprovince:

U-Pb monazite geochronological evidence from the Young-Davidson mine, Ontario. Precambrian Res. 249, 263–272. doi:10.1016/j.precamres.2014.05.015

Figures

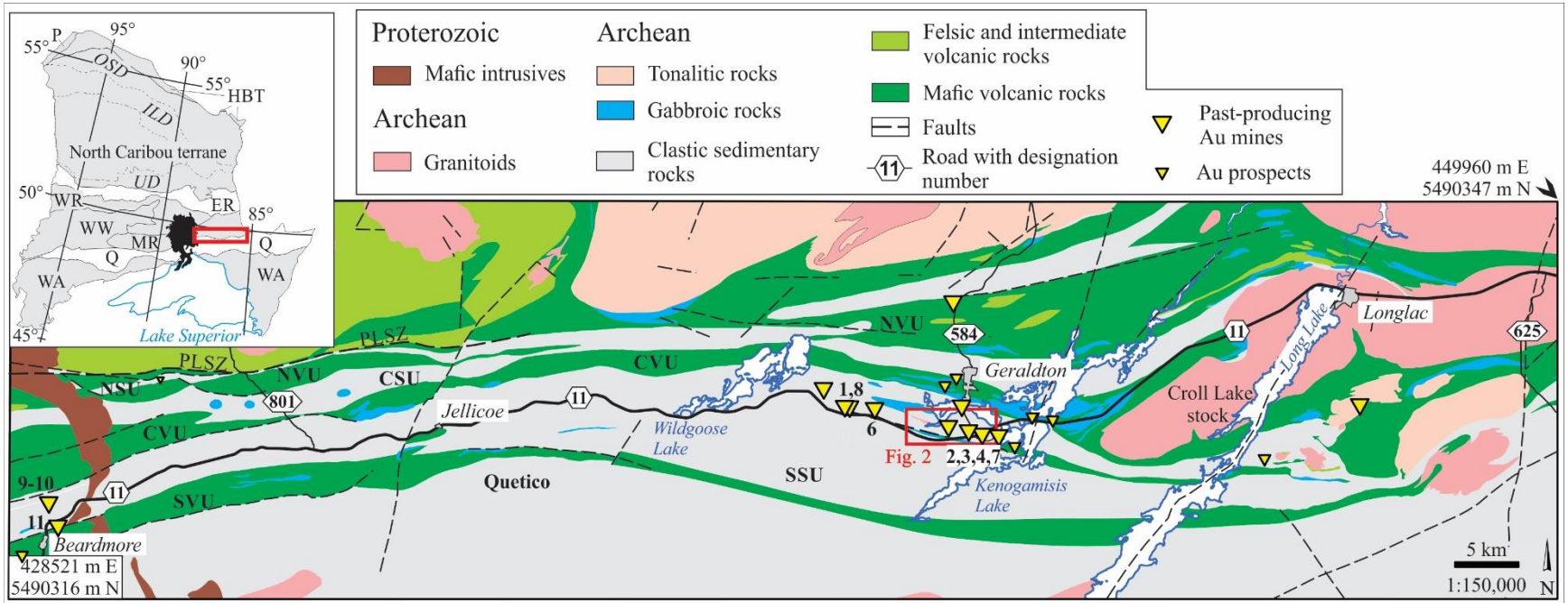

Mine sites: ***Geraldton camp:*** 1) Bankfield, 2) Hard Rock, 3) Little Longlac, 4) MacLeod-Cockshutt, 5) MacLeod-Mosher, 6) Magnet Consolidated, 7) Mosher Longlac, 8) Tombill; ***Beardmore area:*** 9) Leitch, 10) Sand River, 11) Northern Empire

Figure 4-1. Simplified geological map of the Beardmore-Geraldton belt (modified after Lavigne, 2009). PLSZ: Paint Lake Shear Zone. Inset map showing the location of the BGB in the western Superior Province (after Percival et al., 2006). Lake Nipigon and Proterozoic rocks of the Lake Superior area in black. Abbreviations: NVU, CVU, SVU: northern, central and southern metavolcanic unit; NSU, CSU, SSU: northern, central and southern metasedimentary unit; Terranes: ER: English River; HBT: Hudson Bay; MR: Marmion; P: Pikwitonei; Q: Quetico; WA: Wawa-Abitibi; WR: Winnipeg River; WW: Western Wabigoon; Domains of North Caribou terrane: ILD: Island Lake Domain; OSD: Oxford-Stull Domain; UD: Uchi Domain. Map coordinates in UTM NAD 83, Zone 16.

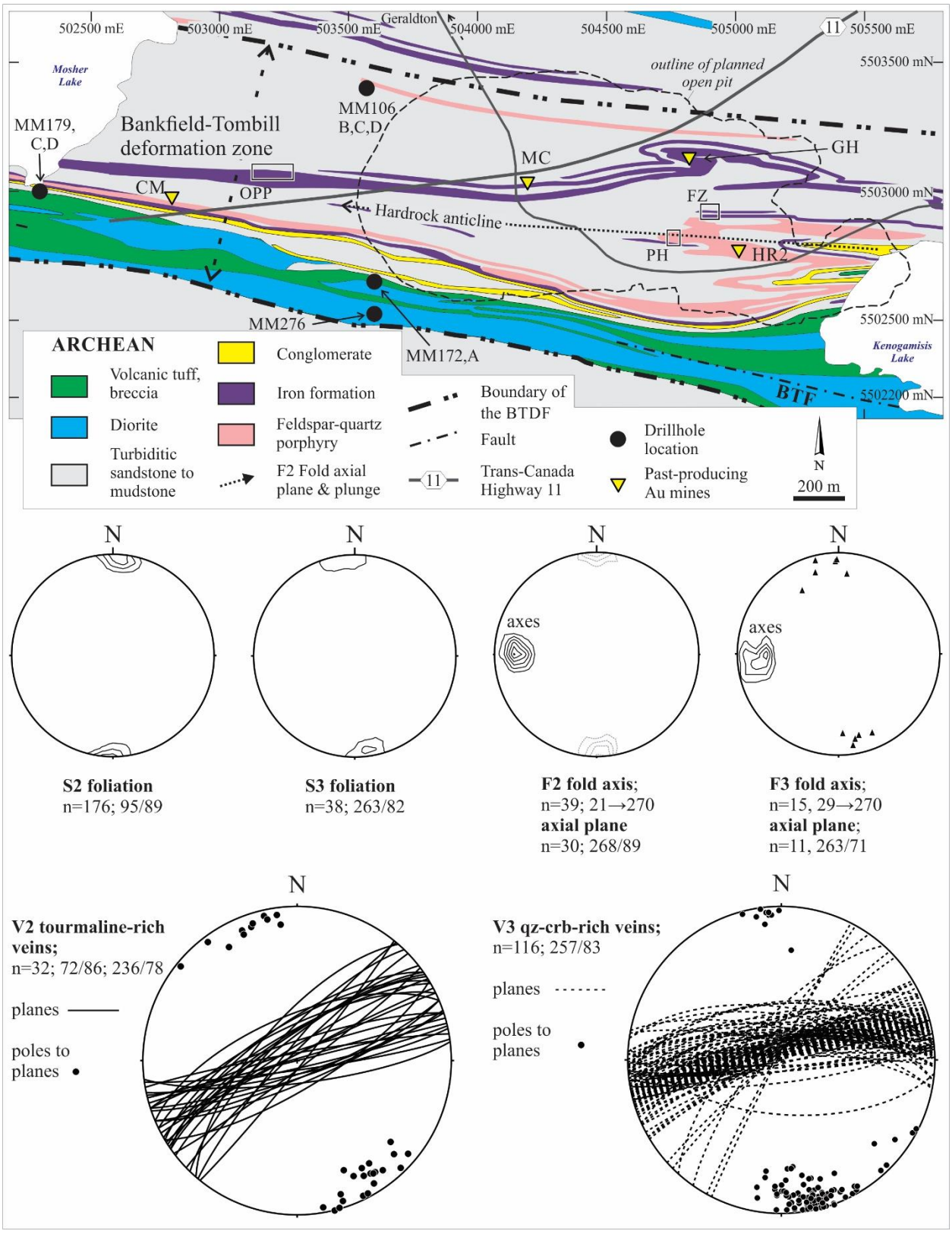
502500 mE
503000 mE
503500 mE
Geraldton
504000 mE
504500 mE
505000 mE
11
505500 mE
Mosher Lake
outline of planned open pit
5503500 mN
MM179, C,D
Bankfield-Tombill deformation zone
MM106 B,C,D
MC
GH
CM
OPP
FZ
5503000 mN
Hardrock anticline
PH
HR2
MM276
MM172,A
5502500 mN
Kenogamisis Lake
BTF
5502200 mN
ARCHEAN
Volcanic tuff, breccia
Diorite
Turbiditic sandstone to mudstone
Conglomerate
Iron formation
Feldspar-quartz porphyry
F2 Fold axial plane & plunge
Boundary of the BTDF
Fault
Trans-Canada Highway 11
Drillhole location
Past-producing Au mines
N
200 m
N
axes
S2 foliation
n=176; 95/89
S3 foliation
n=38; 263/82
F2 fold axis;
n=39; 21→270
axial plane
n=30; 268/89
F3 fold axis;
n=15, 29→270
axial plane;
n=11, 263/71
V2 tourmaline-rich veins;
n=32; 72/86; 236/78
planes
poles to planes
V3 qz-crb-rich veins;
n=116; 257/83
planes
poles to planes

← Figure 4-2. Geological map of the Geraldton area (modified after Pye, 1952; Horwood and Pye, 1955). The outline of the planned open pit is taken from G Mining Services, 2016. Outcrop Abbreviations: PH, Porphyry hill; FZ, F Zone; OPP, OPP exposure. Past-producing mine sites: MC, MacLeod-Cockshutt; CM, Consolidated Mosher; GH, Glory Hole – Hard Rock open stope; HR2, Hard Rock shaft #2. Structures plotted on equal-area, lower hemisphere projections (n: number of measurements; average measurement to the right of the number of measurements; plotted using Stereonet software of Allmendinger et al., 2013; Cardozo and Allmendinger, 2013). Contour intervals in 10% contour intervals per 1% area of the net.

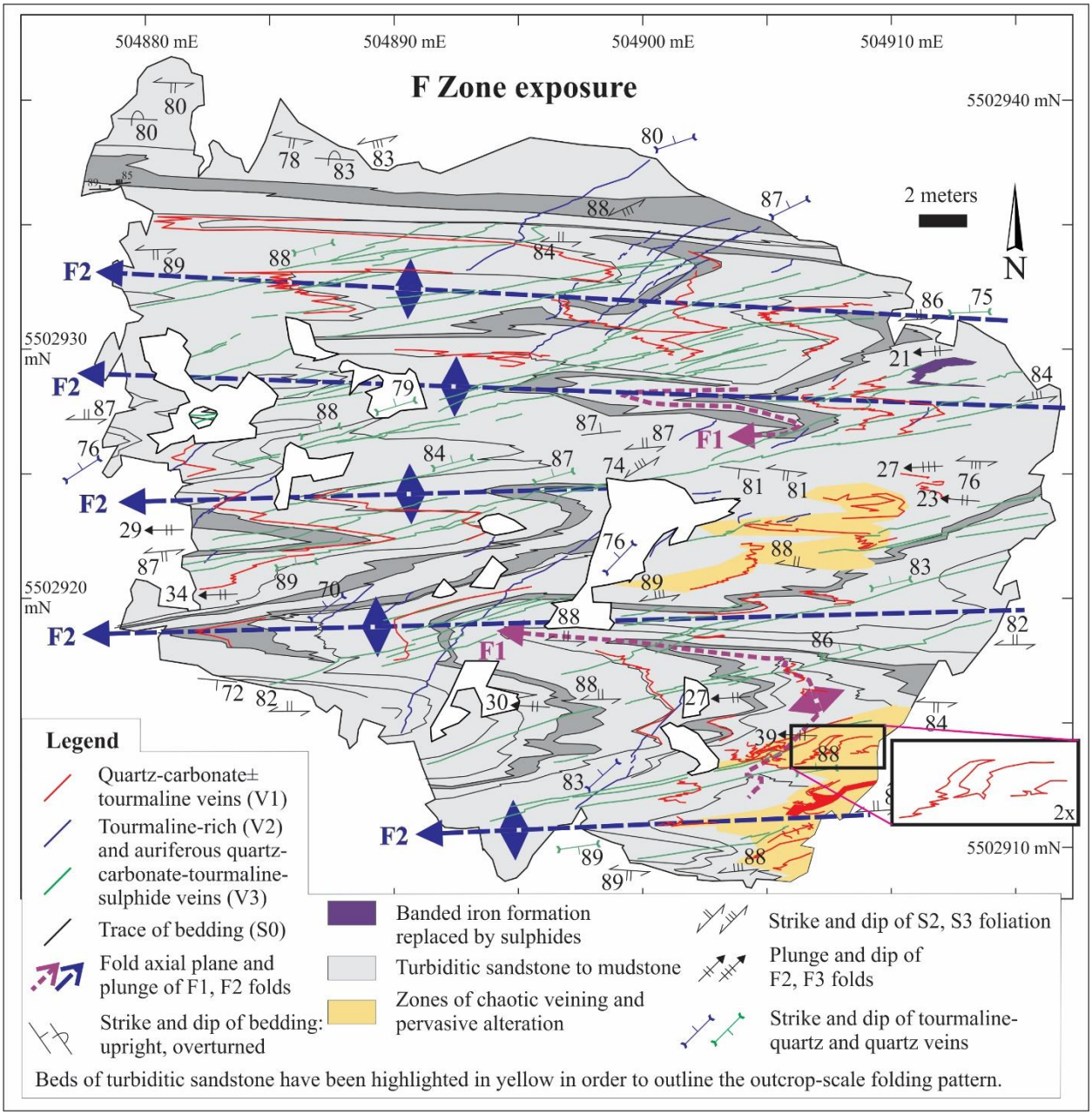

Figure 4-3. Geological map of the F Zone outcrop. Map coordinates in UTM NAD 83, Zone 16. Beds of turbiditic sandstone have been highlighted in yellow in order to outline the outcrop-scale folding pattern.

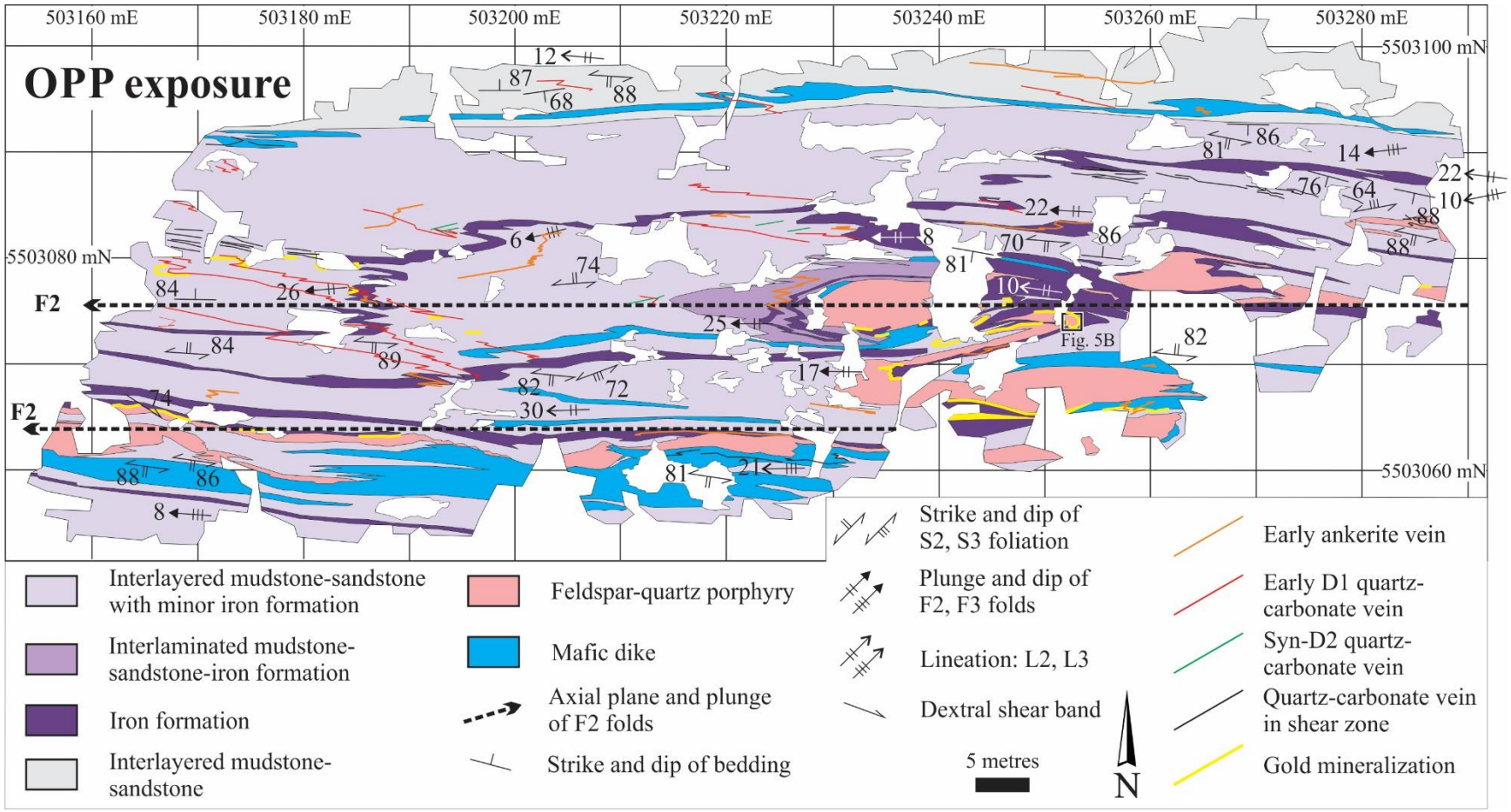

Figure 4-4. Geological map of the OPP outcrop. Map coordinates in UTM NAD 83, Zone 16.

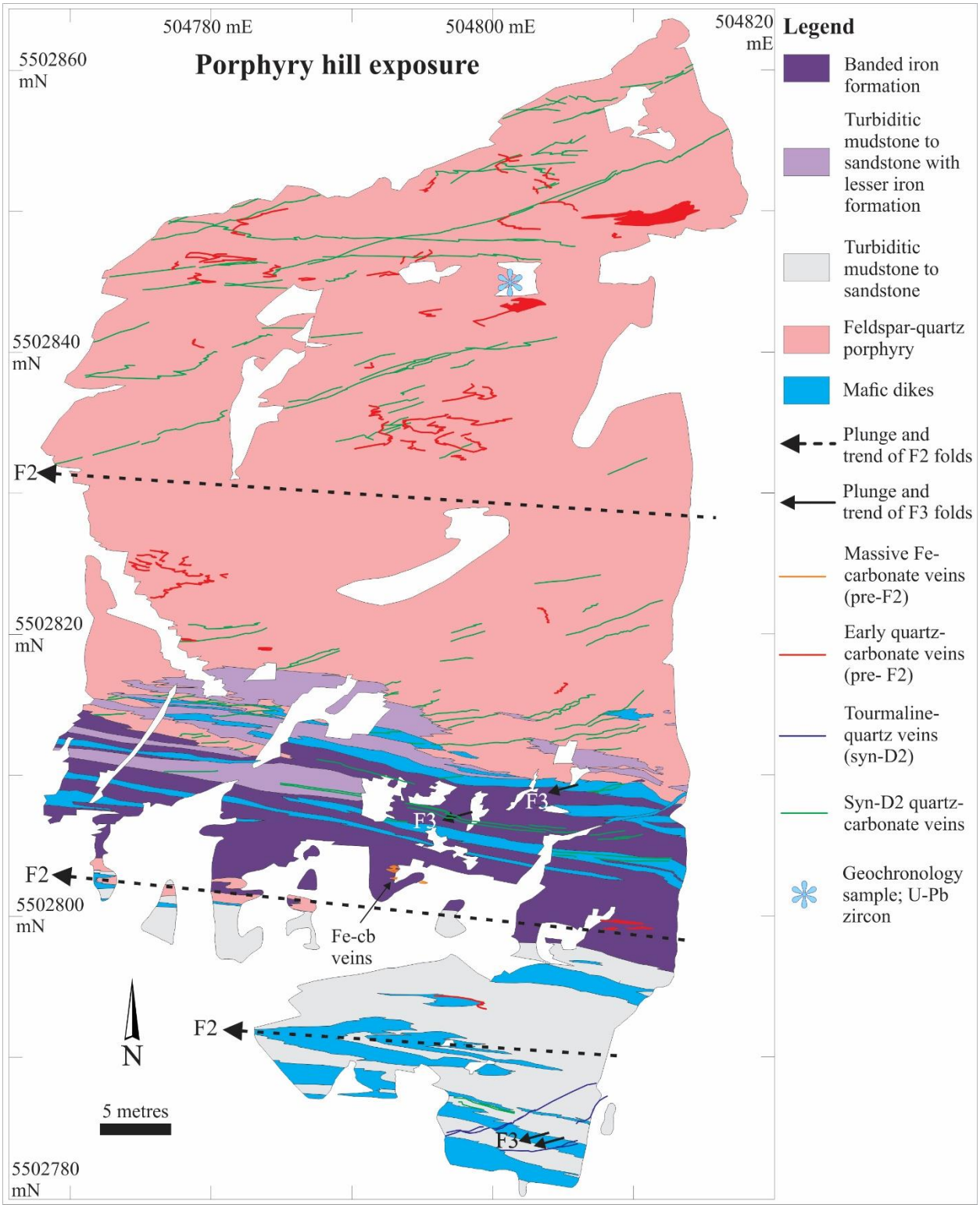

Figure 4-5. Geological map of the Porphyry Hill outcrop. Map coordinates in UTM NAD 83, Zone 16.

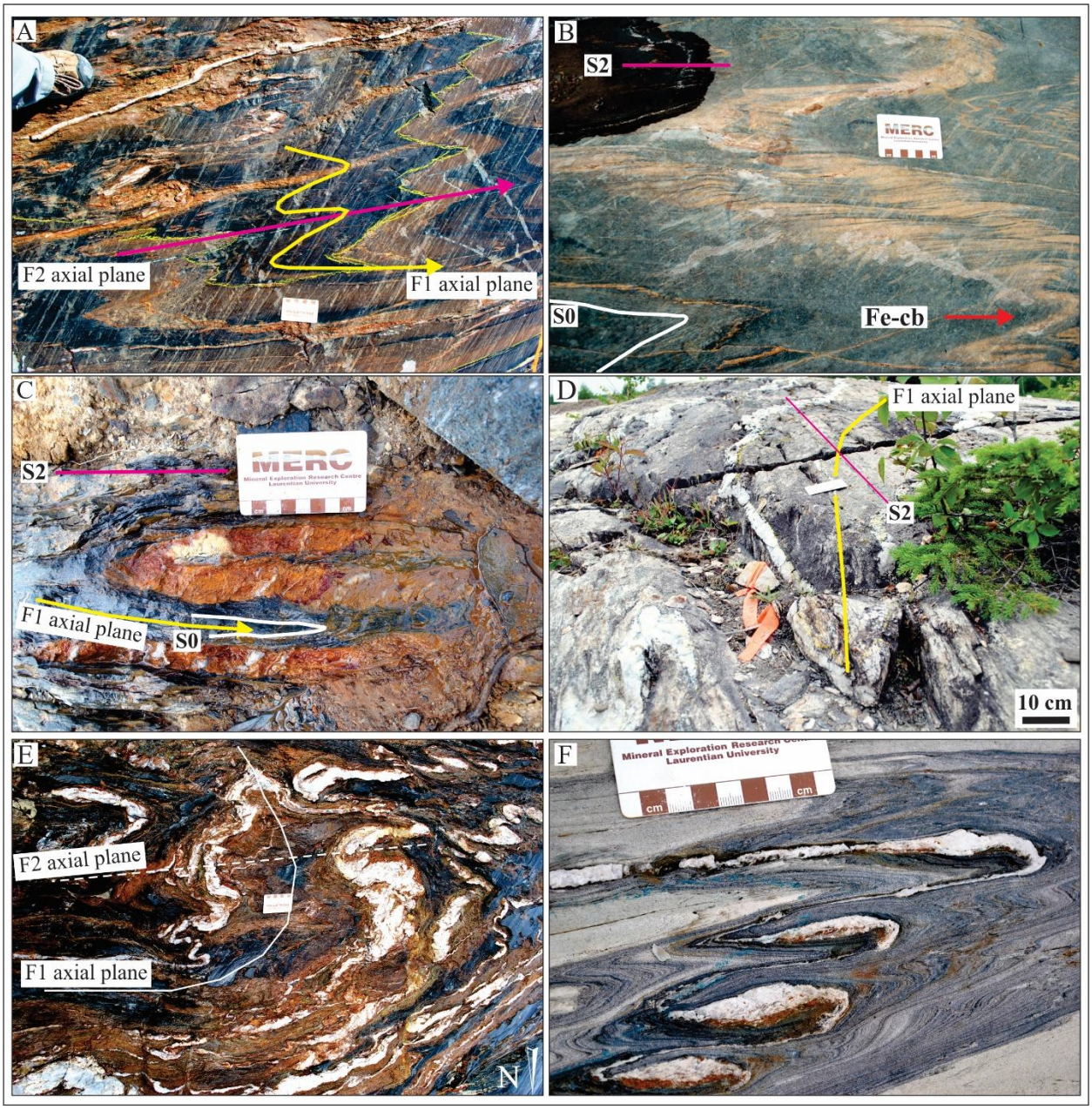

Figure 4-6. Field photographs from the Hardrock mine site. A) Field photograph of bedding-parallel iron carbonate alteration folded by F_1 and F_2 folds in turbiditic sandstone at the F Zone outcrop; B) Field photograph of bedding-parallel Fe-carbonate veins folded by F_2 fold and transposed parallel to S_2 cleavage at the OPP outcrop; C) Field photograph of bedding-parallel Fe-carbonate vein folded by F_1 folds in BIF at the Porphyry Hill outcrop; D) Field photograph of V_1 vein folded by F_1 and F_2 folds in feldspar-quartz porphyry the at the Porphyry Hill outcrop. Photo card (9 cm in length) for scale; E) Field photograph V_1 vein folded by F_1 and F_2 folds in sandstone at the F Zone outcrop. Photo card (9 cm in length) for scale; F) Field photograph of boudinaged V_1 veins folded within F_2 fold hinge at the OPP outcrop. Photo card (9 cm in length) for scale. Abbreviations: S_0: bedding.

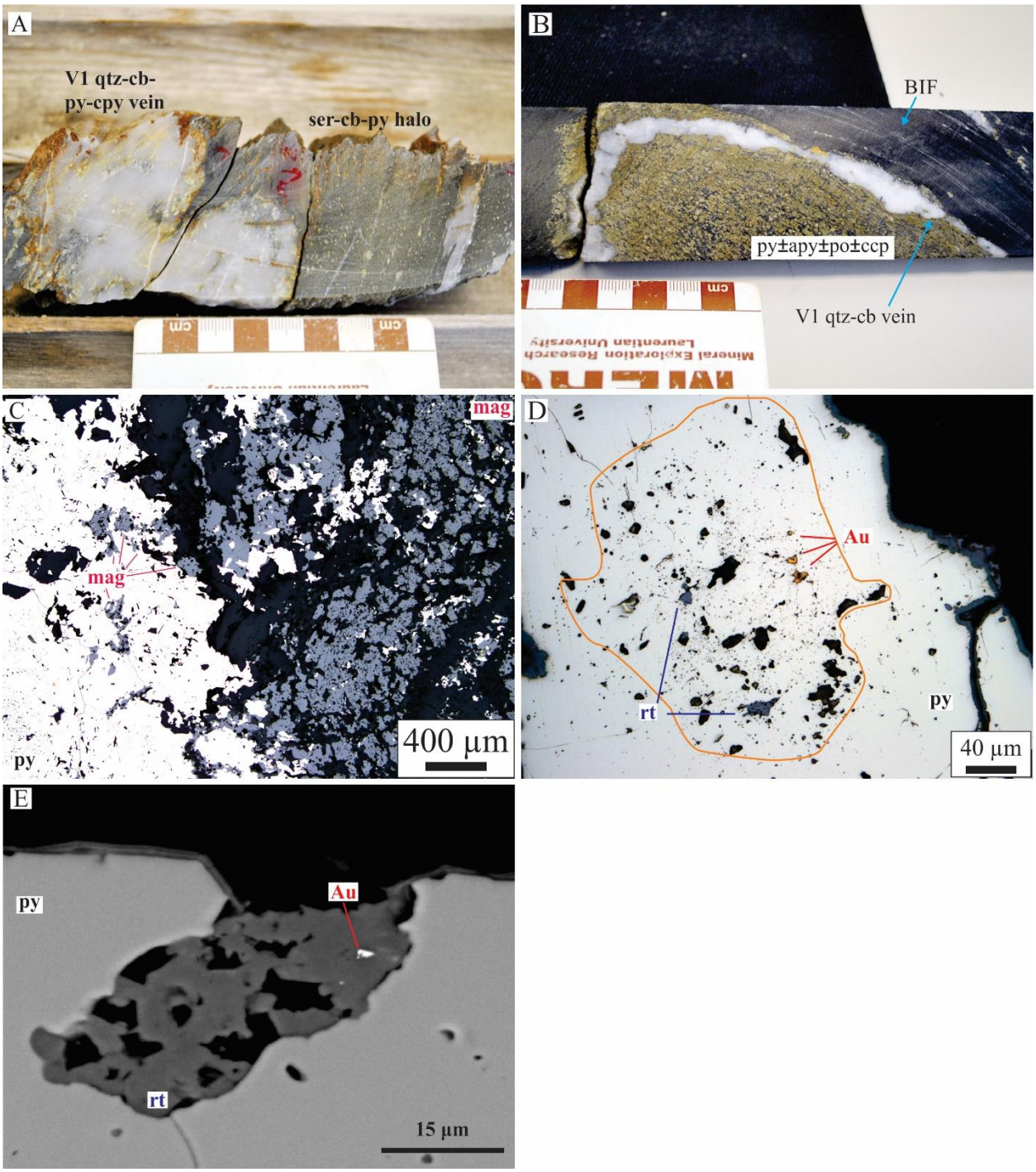
A
V1 qtz-cb-
py-cpy vein
ser-cb-py halo
B
BIF
py±apy±po±ccp
V1 qtz-cb vein
C
mag
mag
400 µm
py
D
Au
rt
py
40 µm
E
py
Au
rt
15 µm

← Figure 4-7. Photographs of samples from the Hardrock mine site. A) Sample photograph of sericite-carbonate-pyrite alteration halo surrounding V_1 quartz-carbonate–pyrite-chalcopyrite ±tourmaline vein in turbiditic sandstone; B) Sample photograph of V_1 vein surrounded by sulfide-rich replacement alteration halo in BIF; C) Reflected light photomicrograph of sulfide alteration halo shown in Fig. 4-7B. D) Reflected light photomicrograph of pyrite grain associated with V_1 veins in feldspar-quartz porphyry with an inclusion-rich (encircled in orange) core containing rutile (rt) and gold (Au) inclusions; E) SEM backscattered image of rutile with native gold inclusion within pyrite from the wallrocks of V_1 veins in feldspar-quartz porphyry. Abbreviations: cb: carbonate; qtz: quartz; py: pyrite; ccp: chalcopyrite; ser: sericite; apy: arsenopyrite; po: pyrrhotite; mag: magnetite; BIF: banded iron formation; Au: native gold; rt: rutile (Kretz, 1983; Siivola and Schmid, 2007).

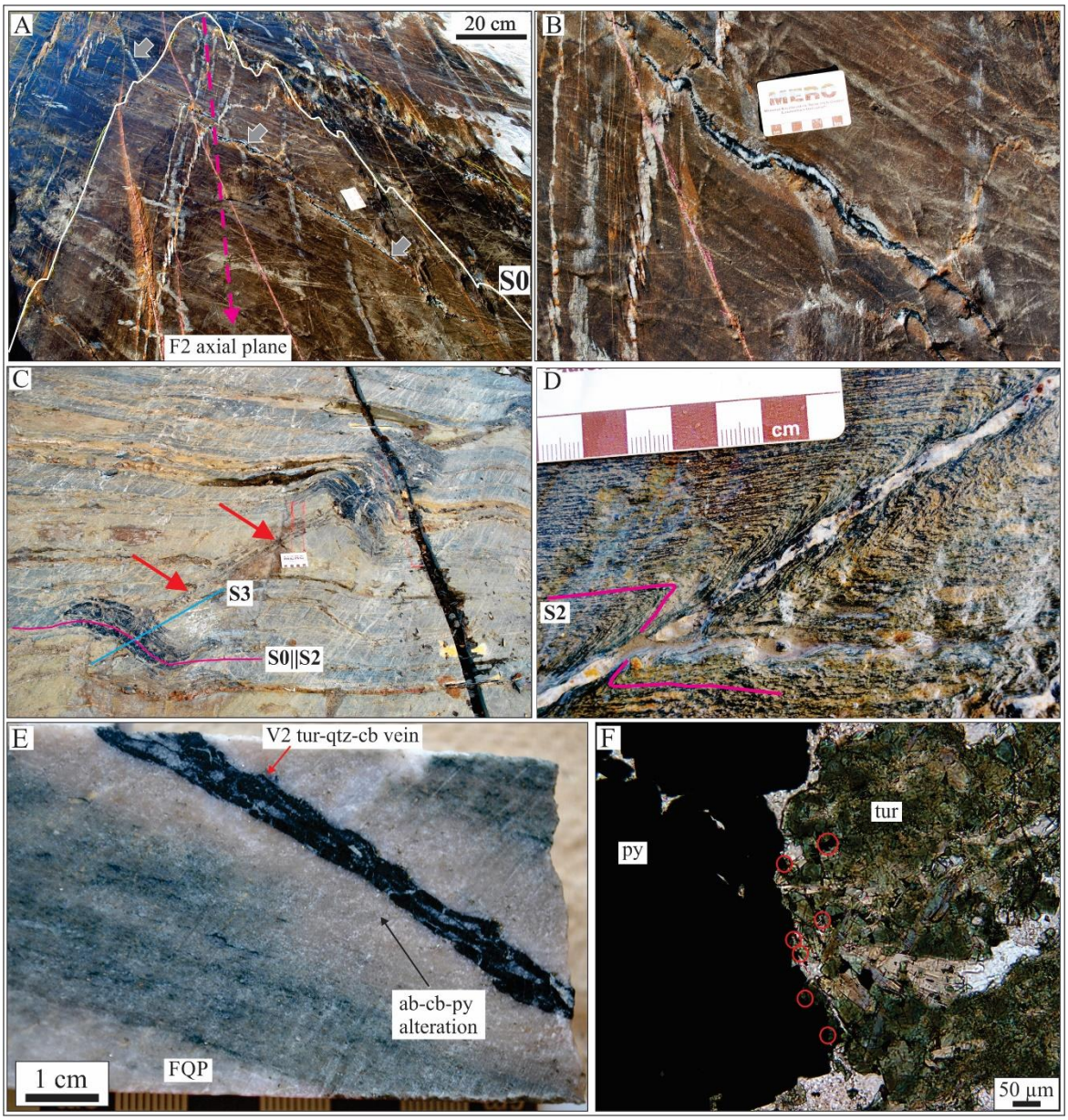

Figure 4-8. A) Field photograph of V_2 vein cutting across the axial plane of F_2 fold in sandstone at the F Zone outcrop. Photo scale (9 cm in length) for scale; B) Close-up of Fig. 4-8A). Note the small S-shaped folds overprinting the vein. Photo scale (9 cm in length) for scale; C) Field photograph of tourmaline-rich V_2 vein at the Porphyry Hill outcrop. Note replacement of wallrocks parallel to S_2 cleavage by tourmaline and the F_3 flanking fold along the margin of the vein. The red arrows highlight the location of V_2 vein. Red arrows mark the location of V_2 vein. Photo card (9 cm in length) for scale; D) Field photograph of Z-shaped F_3 flanking folds adjacent to tourmaline-rich V_2 vein in a mafic dike at the Porphyry Hill outcrop. Note the pinch-and-swell structures along vein. Photo card (9 cm in length) for scale; E) Drill core photograph of V_2 tourmaline-rich vein surrounded by albite (ab)-carbonate (cb)-pyrite (py)-rutile (rt) alteration halo in feldspar-quartz porphyry. F) Plane polarized transmitted light photomicrograph of tourmaline-dominated V_2 vein with native gold inclusions (encircled in red) in pyrite (py) and tourmaline (tur).

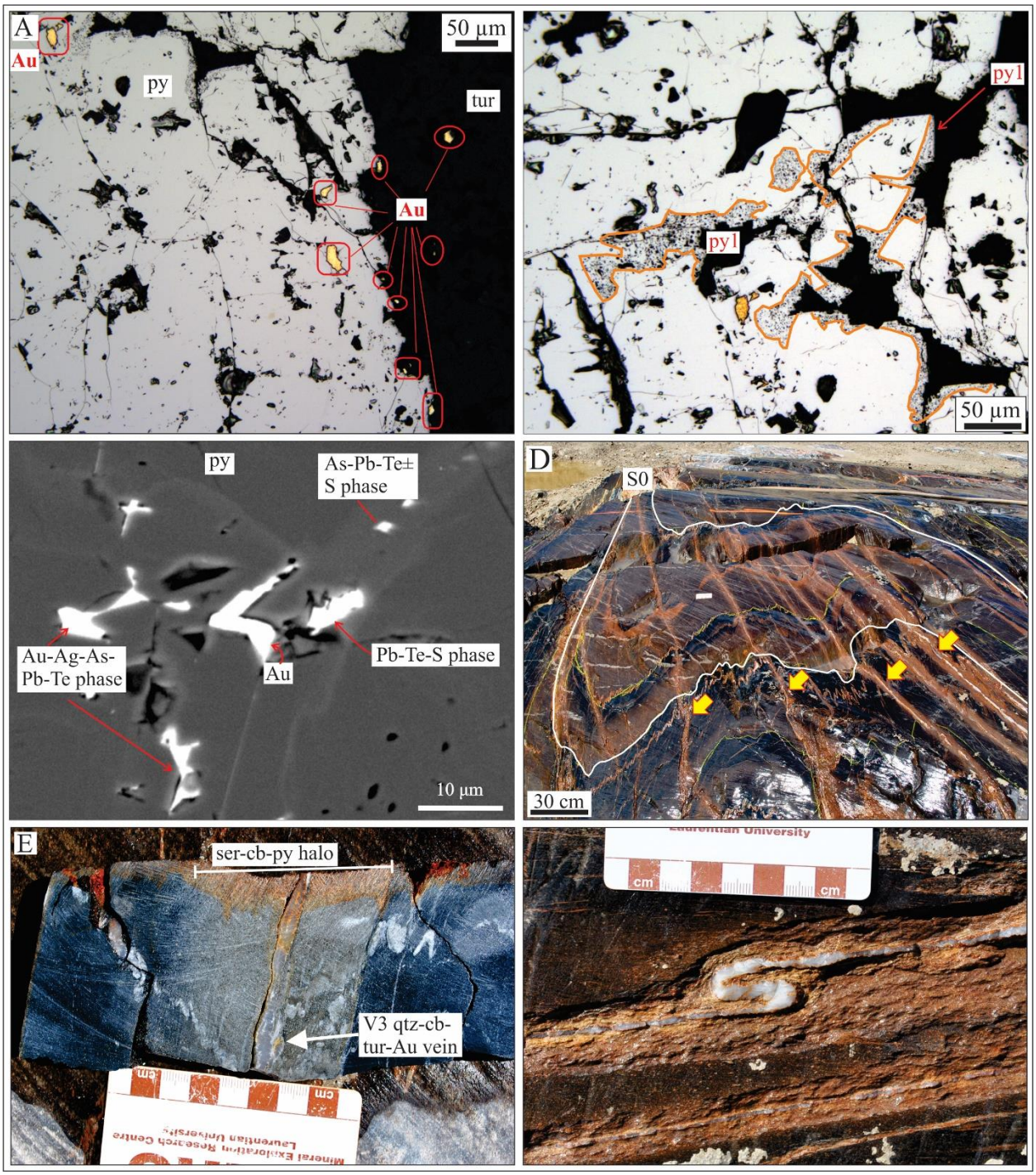
A
Au
50 µm
py
tur
Au
py1
py1
50 µm
py
As-Pb-Te±
S phase
Au-Ag-As-
Pb-Te phase
Au
Pb-Te-S phase
10 µm
D
S0
30 cm
E
ser-cb-py halo
V3 qtz-cb-
tur-Au vein
cm
cm

← Figure 4-9. A) Reflected light photomicrograph of tourmaline (tur) and pyrite (py) grains shown in Fig. 4-8F. Native gold (Au) inclusions within red circles and rectangles; B) Reflected light microphotograph of inclusion-poor pyrite hosting native gold inclusions rimmed by inclusion-rich pyrite (py1) in V_2 vein in sandstone; C) SEM backscatterred image of fracture-fill Au±Ag±As±Pb-tellurides in As-Pb-rich pyrite surrounded by inclusion-poor pyrite in sandstone wallrocks of V_2 vein; D) Field photograph of quartz-carbonate V_3 veins (indicated by arrows) cutting across the axial plane of F_2 folds in sandstone of the F Zone outcrop. Photo card (9 cm in length) for scale; E) Sample photograph of quartz-carbonate V_3 vein surrounded by sericite-carbonate-pyrite alteration halo in sandstone of the F Zone outcrop. Photo card (9 cm in length) for scale. F) Field photograph of quartz-carbonate V_3 vein overprinted by S-shaped F_2 fold at the F Zone outcrop. Photo card (9 cm in length) for scale.

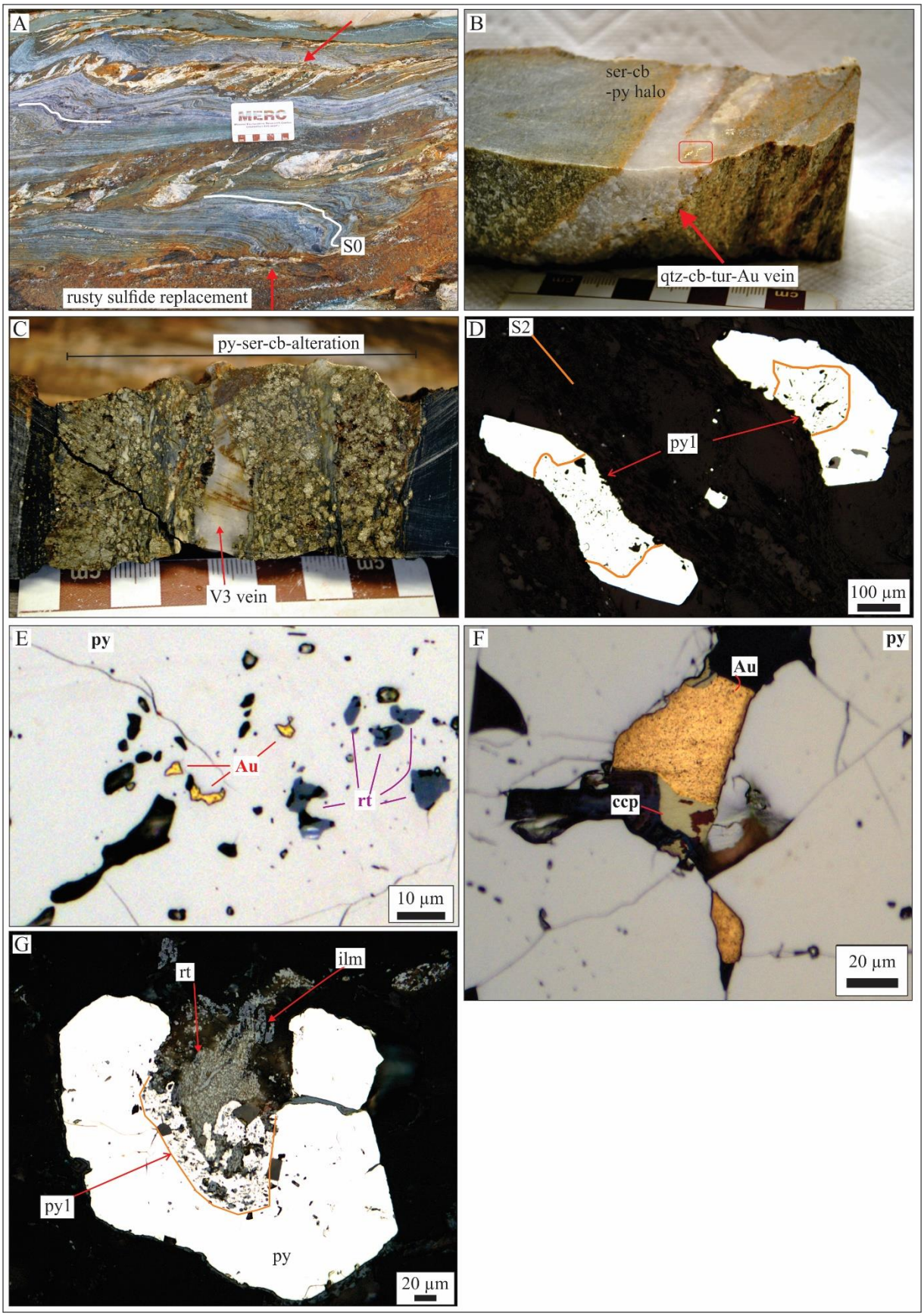
A
S0
rusty sulfide replacement
B
ser-cb
-py halo
qtz-cb-tur-Au vein
C
py-ser-cb-alteration
V3 vein
D
S2
py1
100 µm
E
py
Au
rt
10 µm
F
py
Au
ccp
20 µm
G
rt
ilm
py1
py
20 µm

← Figure 4-10. A) Field photograph of en échelon quartz-carbonate V_3 veins surrounded by sulfide-rich alteration halo in BIF at the OPP outcrop. Photo card (9 cm in length) for scale. B) Sample photograph of quartz-carbonate V_3 vein with sericite-carbonate-pyrite alteration halo in feldspar-quartz porphyry. Photo card (9 cm in length) for scale; C) Sample photograph of quartz-carbonate V_3 vein with pyrite-sericite alteration halo in BIF. Photo card (9 cm in length) for scale; D) Reflected light photomicrograph of inclusion-poor pyrite with inclusion-rich core (py1) in sandstone. Pyrite is elongate parallel to the S_2 foliation and is surrounded by pressure shadows filled with quartz; E) Reflected light photomicrograph of inclusion-rich pyrite (py) with native gold (Au) and rutile (rt) inclusions in py1 in sandstone wallrock of quartz-carbonate V_3 vein. F) Reflected light photomicrograph of visible gold and chalcopyrite filling fracture in pyrite in BIF wallrock of quartz-carbonate V_3 vein; G) Reflected light photomicrograph of pyrite and rutile replacing ilmenite or titanomagnetite in quartz-feldpar porphyry wall rocks of quartz-carbonate V_3 vein.

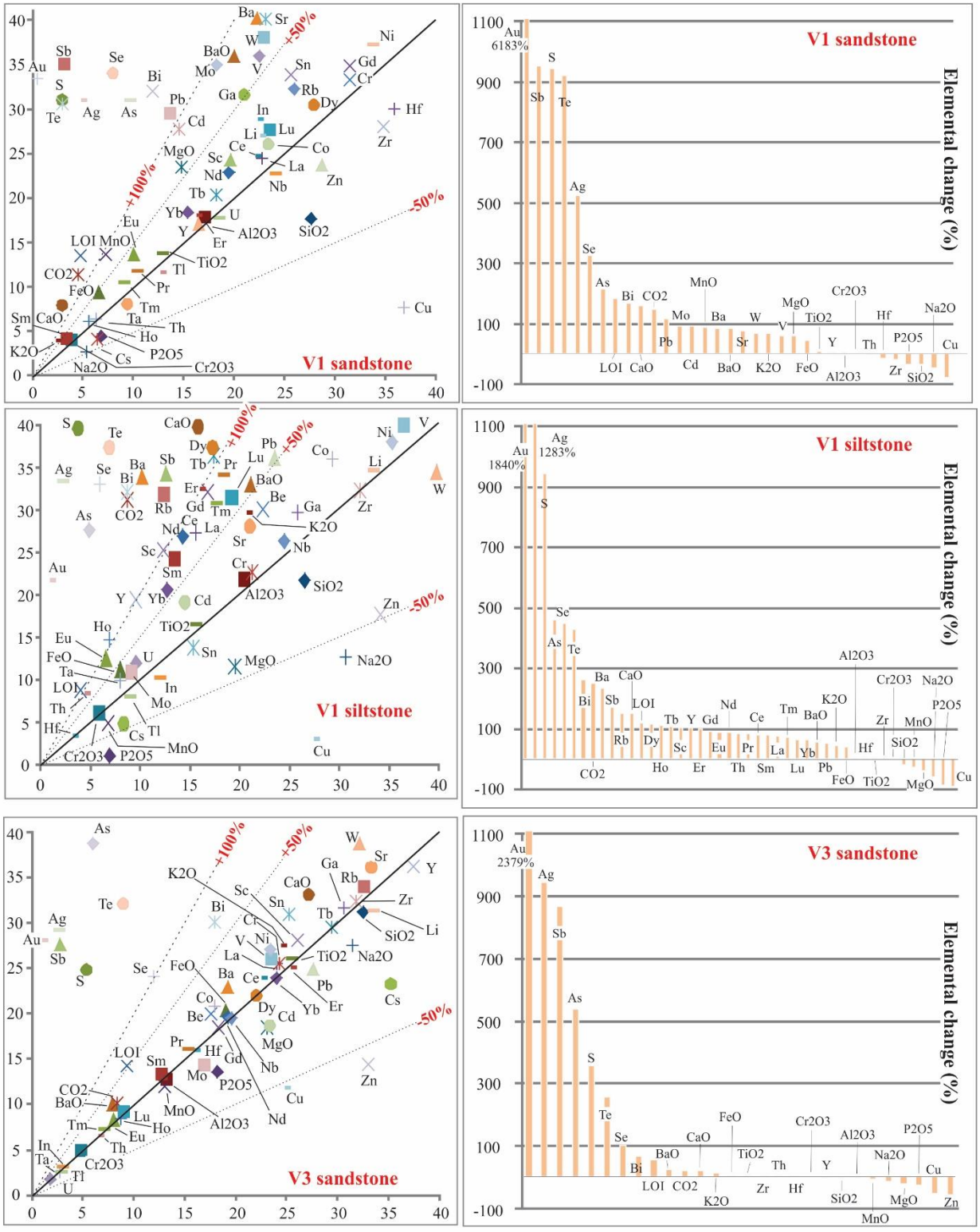

Figure 4-11. Isocon diagrams and % mass change histograms showing mass losses and gains in sandstone and siltstone wall rocks of V_1 and V_3 quartz-carbonate veins. All major oxides, Zr, Th, Hf, Y and elements with % mass change greater than 50% are included in the histograms.

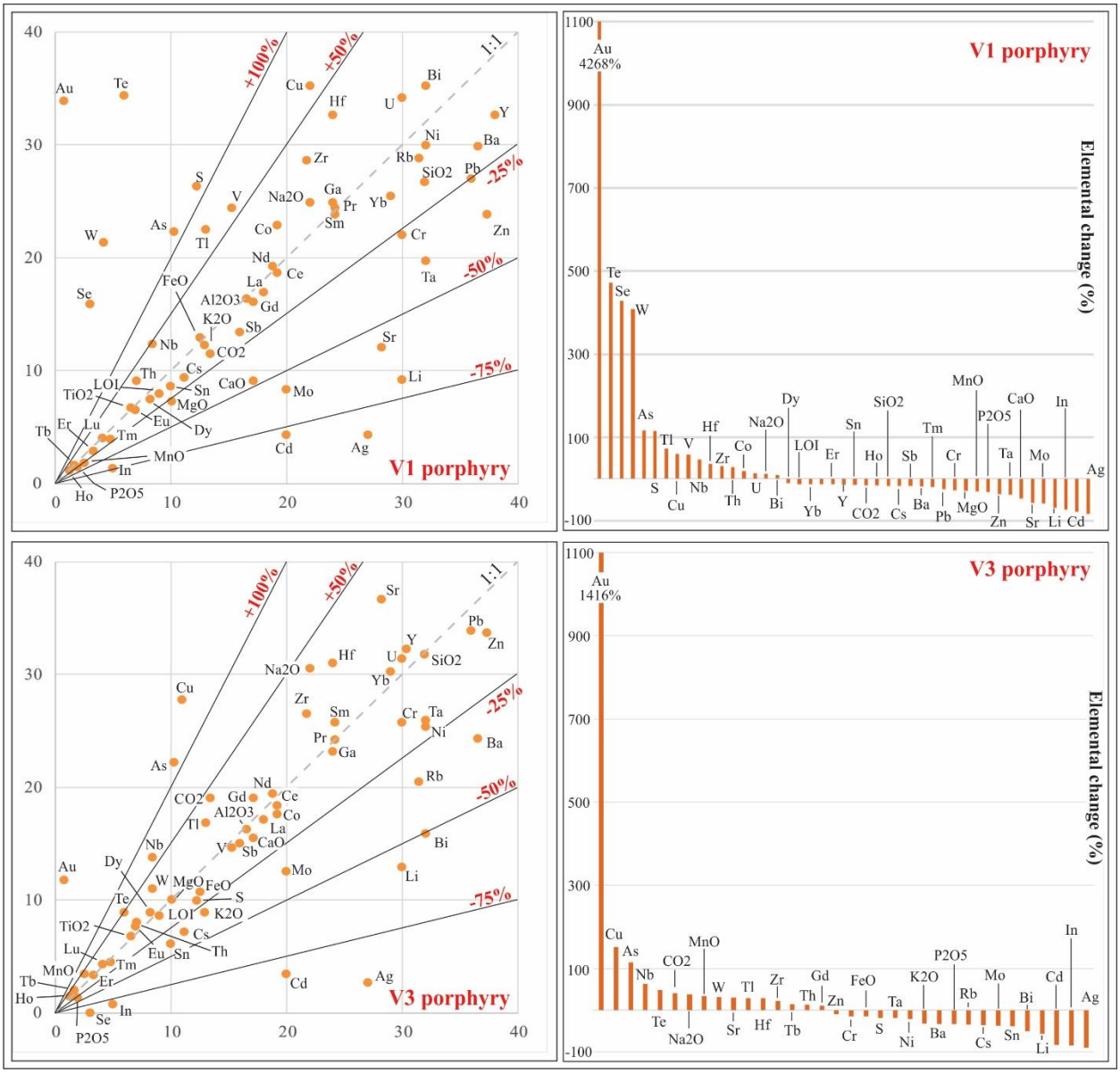

Figure 4-12. Isocon diagrams and % mass change histograms showing mass losses and gains in feldspar-quartz porphyry wall rocks of V_1 and V_3 quartz-carbonate veins. All major oxides, Zr, Th, Hf, Y and elements with % mass change greater than 50% are included in the histograms.

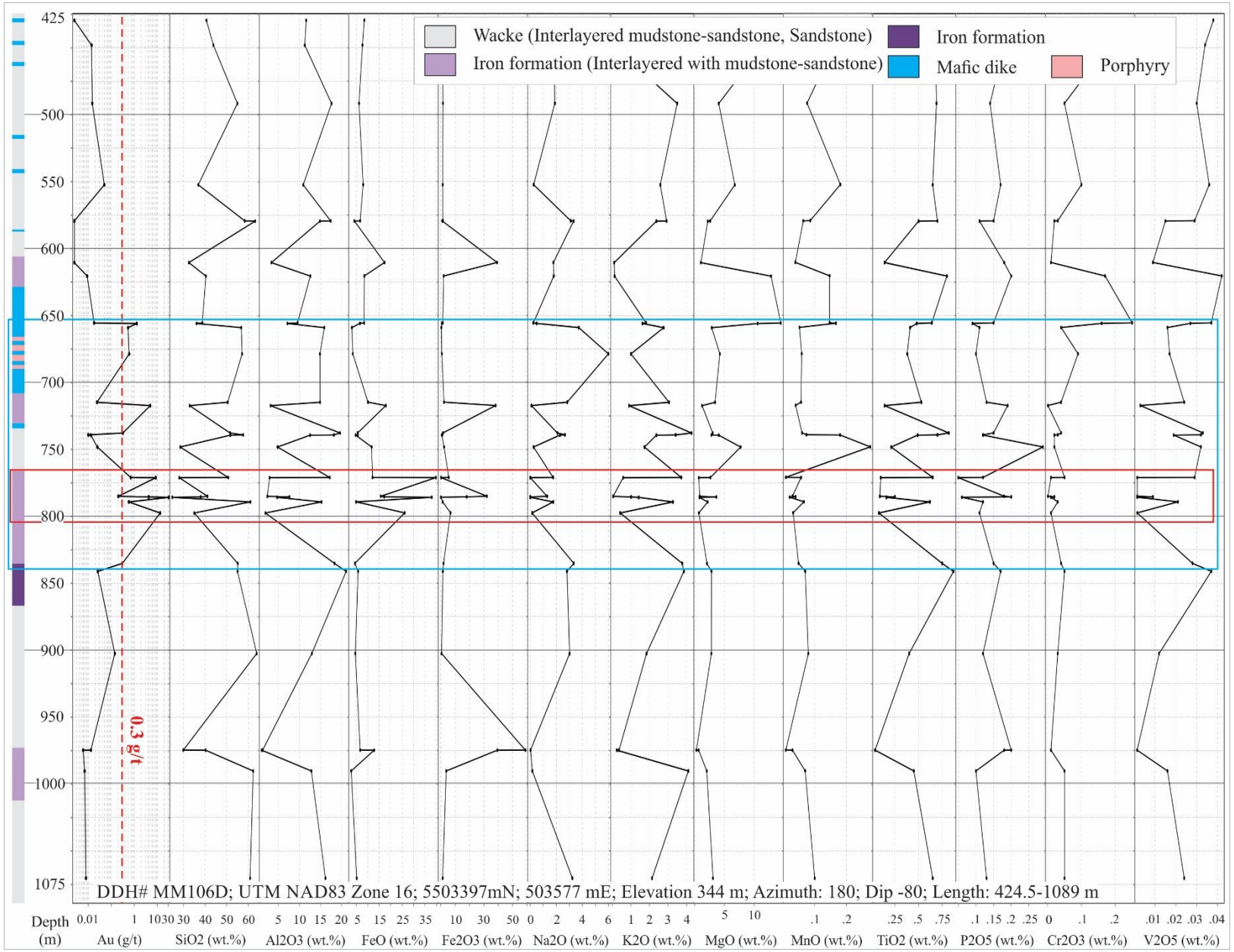
Wacke (Interlayered mudstone-sandstone, Sandstone)
Iron formation (Interlayered with mudstone-sandstone)
Iron formation
Mafic dike
Porphyry
DDH# MM106D; UTM NAD83 Zone 16; 5503397mN; 503577 mE; Elevation 344 m; Azimuth: 180; Dip -80; Length: 424.5-1089 m
0.3 g/t
Depth (m)
Au (g/t)
SiO2 (wt.%)
Al2O3 (wt.%)
FeO (wt.%)
Fe2O3 (wt.%)
Na2O (wt.%)
K2O (wt.%)
MgO (wt.%)
MnO (wt.%)
TiO2 (wt.%)
P2O5 (wt.%)
Cr2O3 (wt.%)
V2O5 (wt.%)

← Figure 4-13. Geochemical profile of major element oxides in drill hole # MM106D across section 503575E, UTM NAD 83, Zone 16. Figure 4-2 shows the location of the drill hole. The blue box outlines the interval where Au exceed 0.3 g/t, whereas the red box marks the highest gold values in the drill hole section. This plot is scaled to the length of the MM106D drill hole.

Figure 4-14. Geochemical profile of pathfinder elements and alteration indices in drill hole # MM106D across section 503575E, UTM NAD 83, Zone 16. Figure 4-2 shows the location of the drill hole. The blue box outlines the interval where Au exceed 0.3 g/t, whereas the red box marks the highest gold values in the drill hole section. This plot is scaled to the length of the MM106D drill hole. →

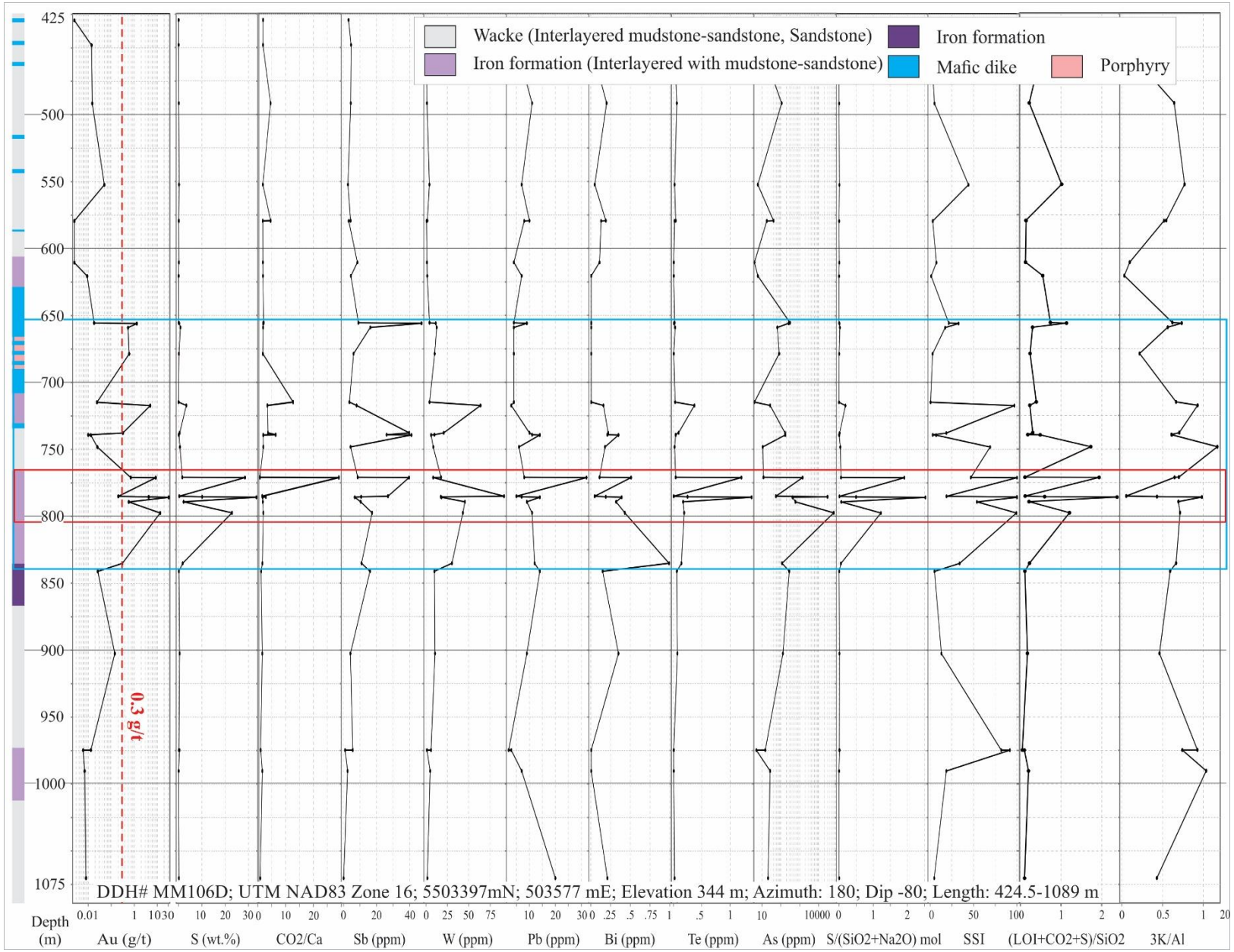
Wacke (Interlayered mudstone-sandstone, Sandstone)
Iron formation (Interlayered with mudstone-sandstone)
Iron formation
Mafic dike
Porphyry
0.3 g/t
DDH# MM106D; UTM NAD83 Zone 16; 5503397mN; 503577 mE; Elevation 344 m; Azimuth: 180; Dip -80; Length: 424.5-1089 m
Depth (m)
Au (g/t)
S (wt.%)
CO2/Ca
Sb (ppm)
W (ppm)
Pb (ppm)
Bi (ppm)
Te (ppm)
As (ppm)
S/(SiO2+Na2O) mol
SSI
(LOI+CO2+S)/SiO2
3K/Al

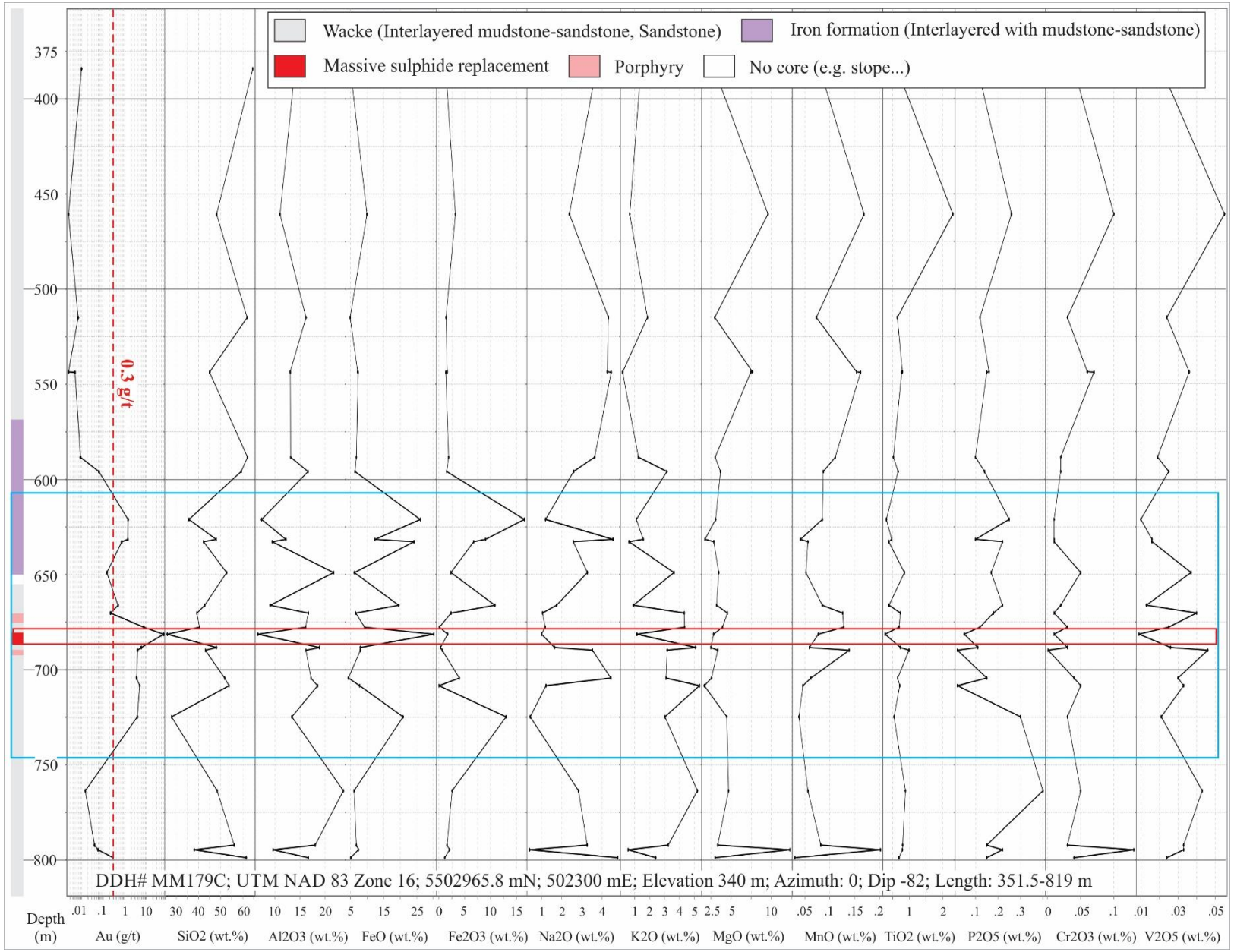
Wacke (Interlayered mudstone-sandstone, Sandstone)
Iron formation (Interlayered with mudstone-sandstone)
Massive sulphide replacement
Porphyry
No core (e.g. stope...)
0.3 g/t
DDH# MM179C; UTM NAD 83 Zone 16; 5502965.8 mN; 502300 mE; Elevation 340 m; Azimuth: 0; Dip -82; Length: 351.5-819 m
Depth (m)
Au (g/t)
SiO2 (wt.%)
Al2O3 (wt.%)
FeO (wt.%)
Fe2O3 (wt.%)
Na2O (wt.%)
K2O (wt.%)
MgO (wt.%)
MnO (wt.%)
TiO2 (wt.%)
P2O5 (wt.%)
Cr2O3 (wt.%)
V2O5 (wt.%)

← Figure 4-15. Geochemical profile of major element oxides in drill hole # MM179C across section 502300E, UTM NAD 83, Zone 16. Figure 4-2 shows the location of the drill hole. The blue box outlines the interval where Au exceed 0.3 g/t, whereas the red box marks the highest gold values in the drill hole section. This plot is scaled to the length of the MM179C drill hole.

Figure 4-16. Geochemical profile of pathfinder elements and alteration indices in drill hole # MM179C across section 502300E, UTM NAD 83, Zone 16. Figure 4-2 shows the location of the drill hole. The blue box outlines the interval where Au exceed 0.3 g/t, whereas the red box marks the highest gold values in the drill hole section. This plot is scaled to the length of the MM179C drill hole. →

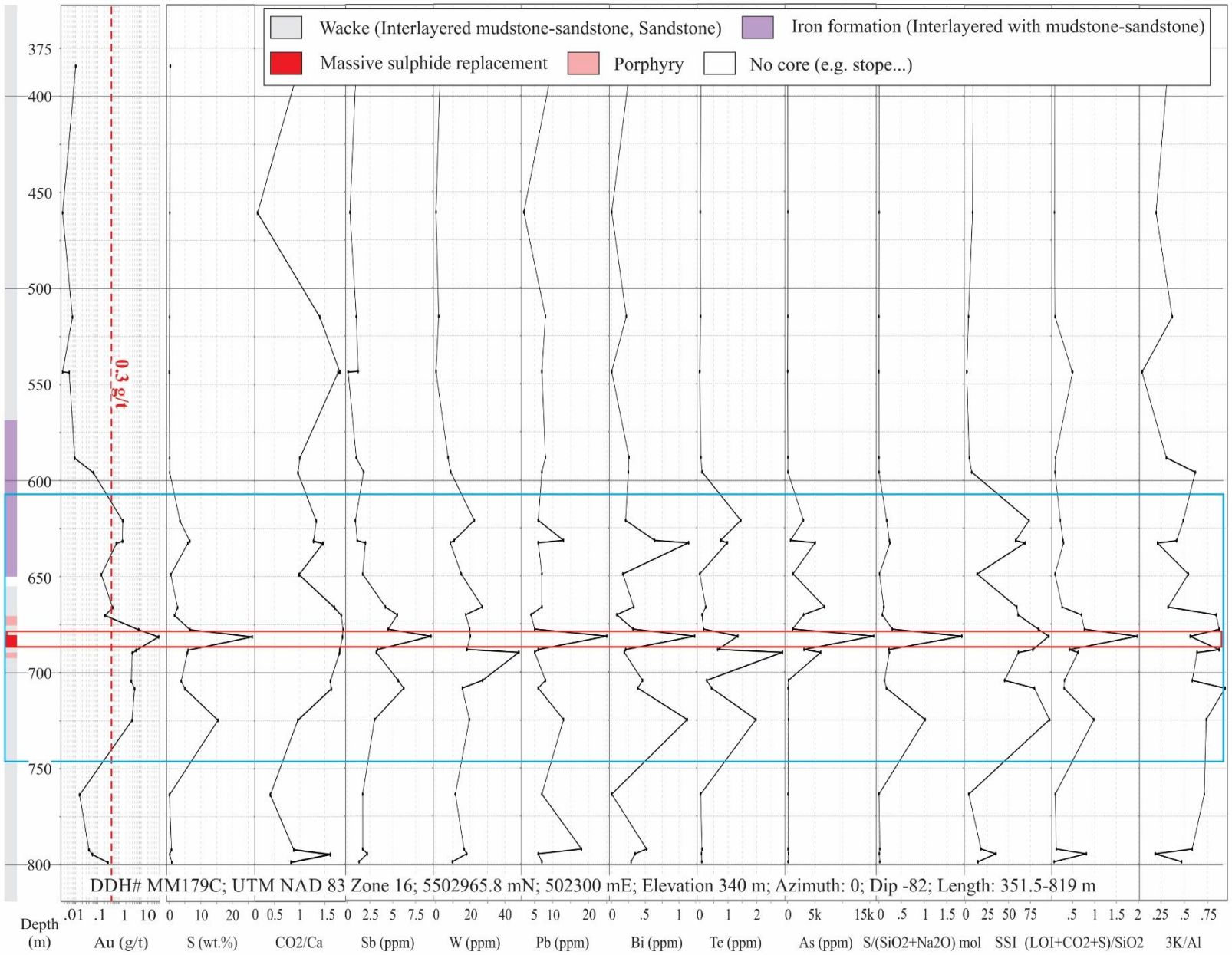
Wacke (Interlayered mudstone-sandstone, Sandstone)
Iron formation (Interlayered with mudstone-sandstone)
Massive sulphide replacement
Porphyry
No core (e.g. stope...)
0.3 g/t
DDH# MM179C; UTM NAD 83 Zone 16; 5502965.8 mN; 502300 mE; Elevation 340 m; Azimuth: 0; Dip -82; Length: 351.5-819 m
Depth (m)
Au (g/t)
S (wt.%)
CO2/Ca
Sb (ppm)
W (ppm)
Pb (ppm)
Bi (ppm)
Te (ppm)
As (ppm)
S/(SiO2+Na2O) mol
SSI
(LOI+CO2+S)/SiO2
3K/Al

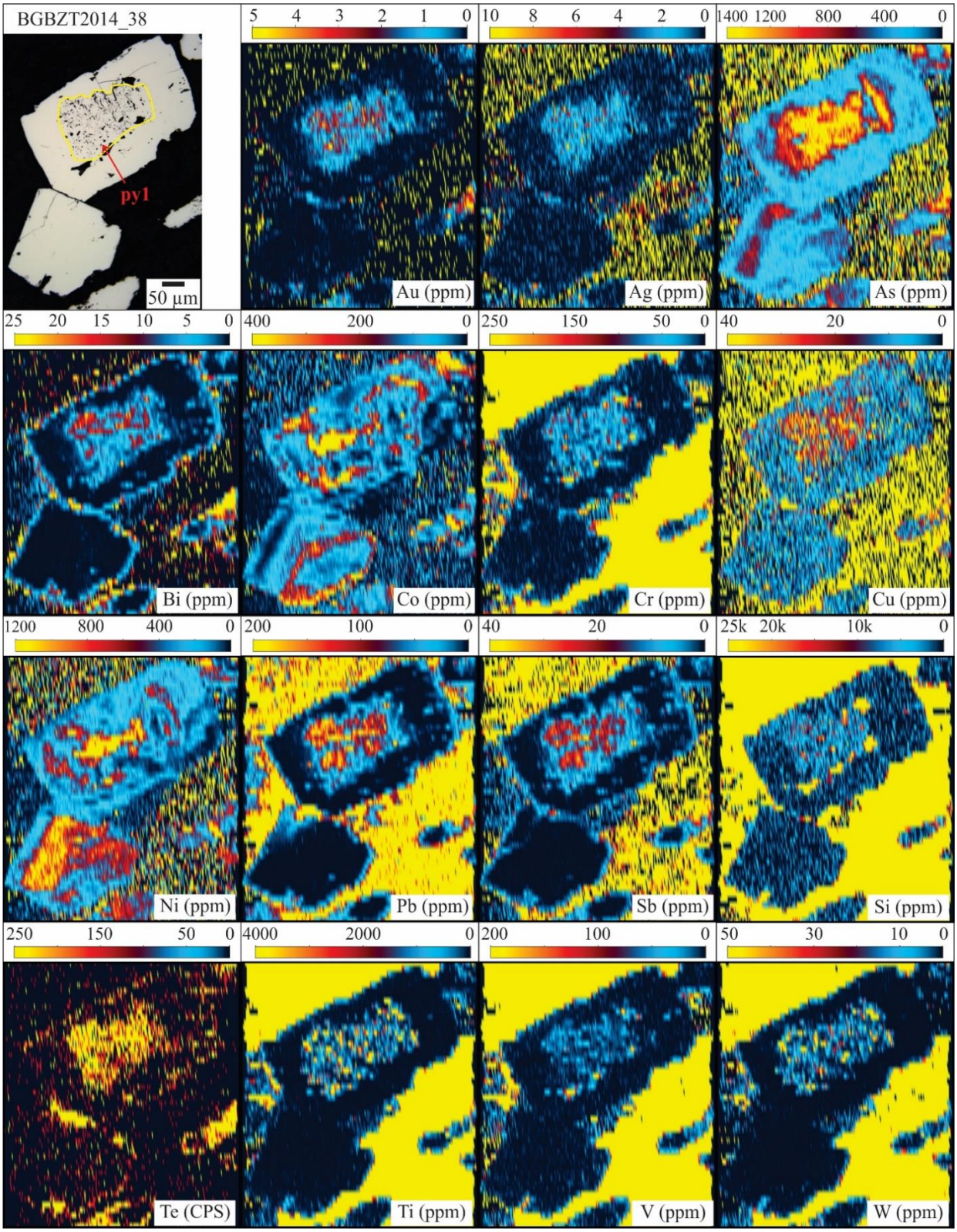

Figure 4-17. LA-ICP-MS elemental map of pyrite associated with quartz-carbonate V_1 vein in sandstone. Reflected light photomicrograph at upper left of diagram showing an inclusion-poor pyrite with an inclusion-rich core (py1) and a second lower inclusion-poor pyrite.

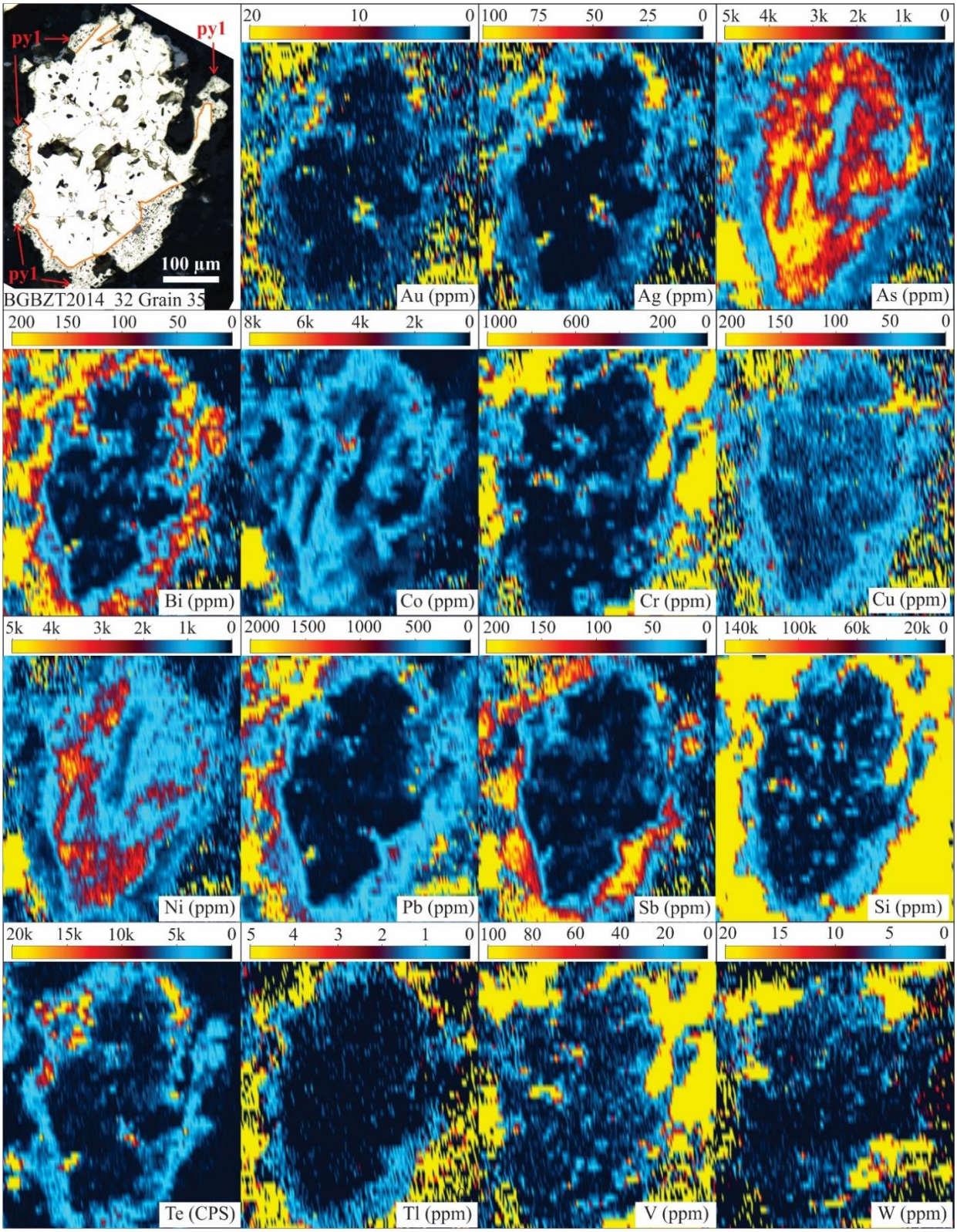

Figure 4-18. LA-ICP-MS elemental map of pyrite associated with quartz-tourmaline V_2 vein in sandstone. Reflected light photomicrograph at upper left of diagram showing inclusion-poor pyrite rimmed by inclusion-rich pyrite (py1).

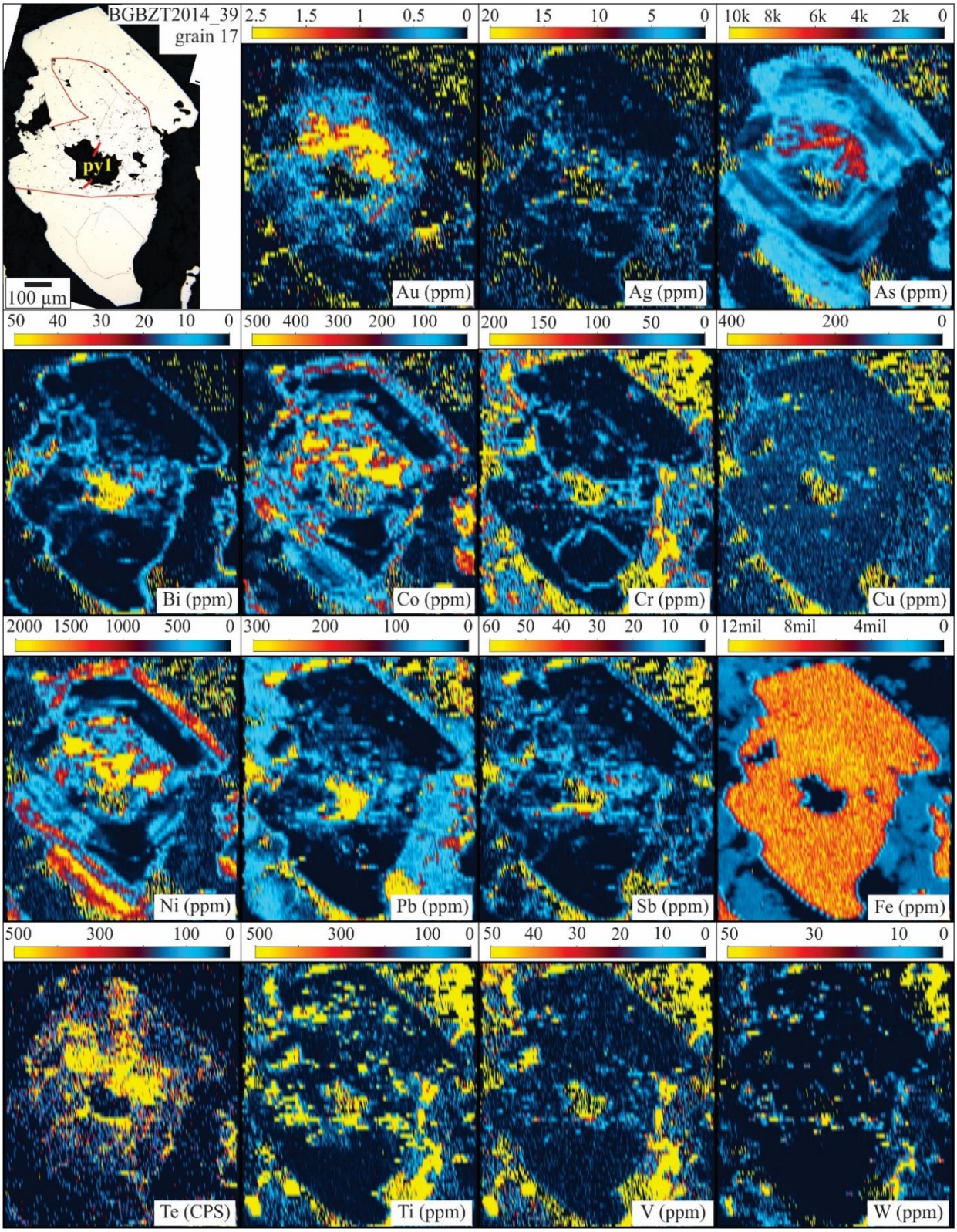

Figure 4-19. LA-ICP-MS elemental map of pyrite associated with quartz-carbonate V_3 vein-related gold mineralization in sandstone. Reflected light photomicrograph at upper left of diagram showing an inclusion-poor pyrite with an inclusion-rich core (py1).

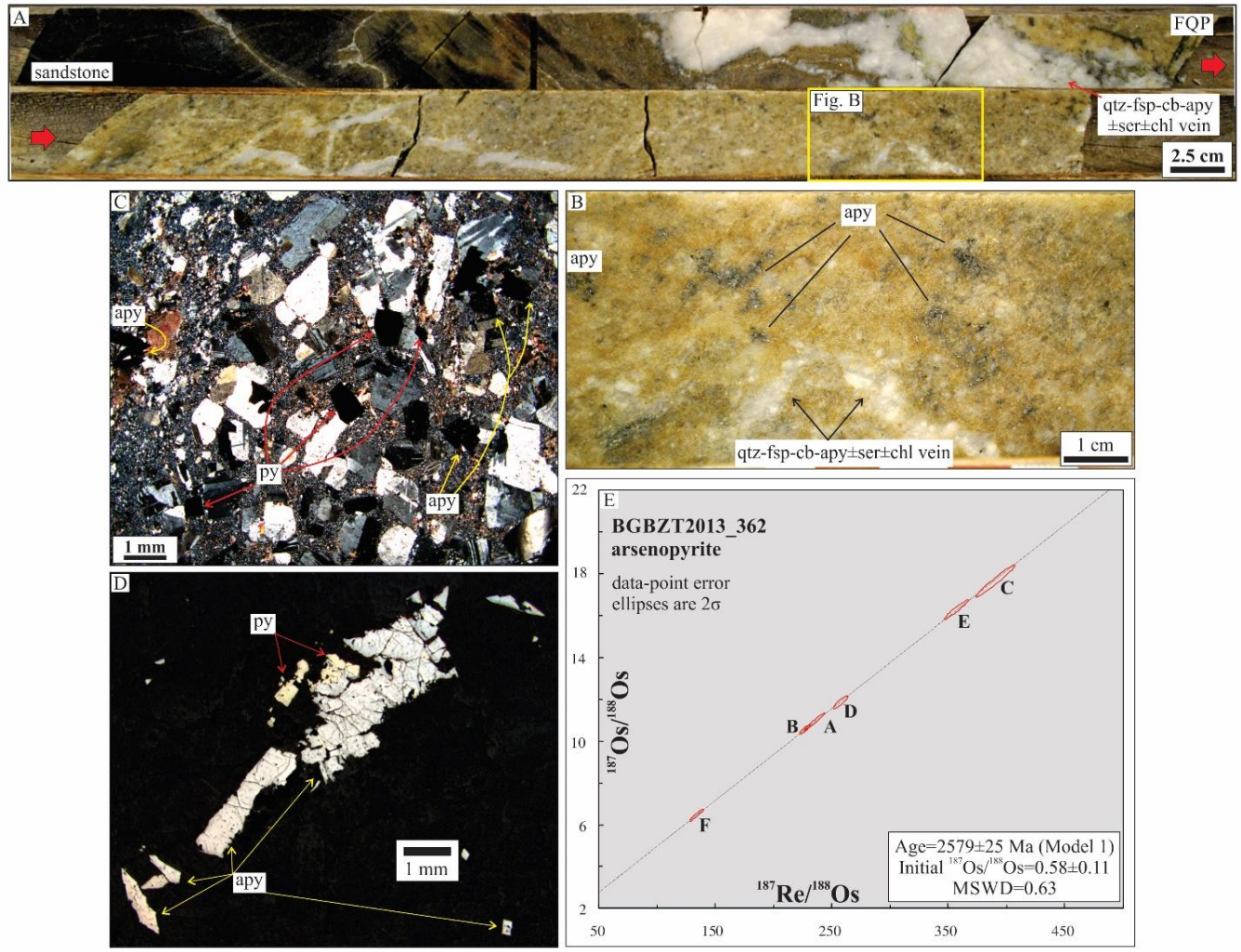

Figure 4-20. A-B) Drill core photograph of arsenopyrite-rich gold mineralization associated with quartz-carbonate veins adjacent to contact between feldspar-quartz porphyry and sandstone. The yellow box marks the location of Fig. 4-20B. C) Cross-polarized transmitted light photomicrograph of arsenopyrite (apy) and pyrite (py) in feldspar-quartz porphyry; D) Reflected light microphotograph of arsenopyrite and pyrite in the feldspar-quartz porphyry. E) Re-Os isochron diagram for arsenopyrite in feldspar-quartz porphyry.

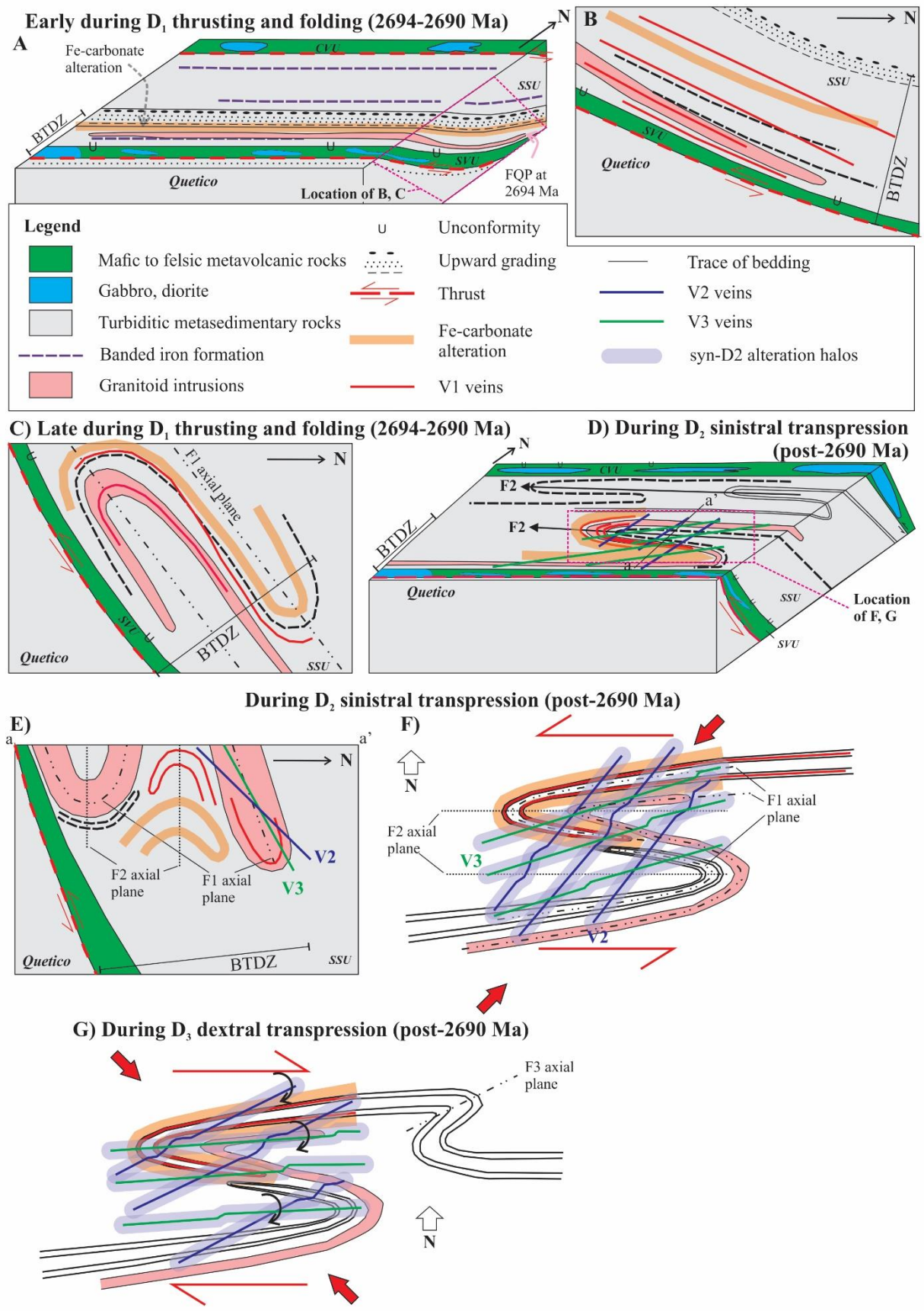
Early during D1 thrusting and folding (2694-2690 Ma)
A
Fe-carbonate alteration
CVU
SSU
BTDZ
SVU
Quetico
Location of B, C
FQP at 2694 Ma
N
B
N
SSU
SVU
Quetico
BTDZ
Legend
Mafic to felsic metavolcanic rocks
Gabbro, diorite
Turbiditic metasedimentary rocks
Banded iron formation
Granitoid intrusions
Unconformity
Upward grading
Thrust
Fe-carbonate alteration
V1 veins
Trace of bedding
V2 veins
V3 veins
syn-D2 alteration halos
C) Late during D1 thrusting and folding (2694-2690 Ma)
F1 axial plane
N
SVU
Quetico
BTDZ
SSU
D) During D2 sinistral transpression (post-2690 Ma)
N
CVU
F2
a'
F2
BTDZ
Quetico
SSU
SVU
Location of F, G
During D2 sinistral transpression (post-2690 Ma)
E)
a
a'
N
F2 axial plane
F1 axial plane
V2
V3
Quetico
BTDZ
SSU
F)
N
F2 axial plane
V3
F1 axial plane
V2
G) During D3 dextral transpression (post-2690 Ma)
F3 axial plane
N

← Figure 4-21. Schematic model for the emplacement of V_1 to V_3 veins: A) 3D block model and B) cross-section of the emplacement of early bedding-parallel Fe-carbonate alteration and quartz-carbonate V_1 veins during D_1 thrusting and folding event; C) Folding of the early bedding-parallel Fe-carbonate alteration and quartz-carbonate V_1 veins later during the D_1 event; D) Block diagram, E) cross-section F) map view of syn-D_2 events: Overprinting of F_1 folds by S-shaped F_2 folds during D_2 sinistral transpression; Emplacement of quartz-tourmaline V_2 veins, rotation of the veins, and emplacement of quartz-carbonate V_3 veins later during the D_2 event; G) Map view of syn-D_3 events: Rotation and stretching V_2 and V_3 veins and formation of F_3 flanking structures adjacent to the veins during D_3 dextral transpression.

Tables

Table 4-1. Summary of the gold production in the BGB (summarized from; Pye, 1952; Horwood and Pye, 1955; Ferguson, 1965; Mason et al., 1985; Mason and White, 1986 and references therein)

map #	Mine	Operation years	Au (oz)	Ag (oz)	Host unit	Host rock	Mineralization
Geraldton area							
1	Bankfield	1937-1947	66,416	7,590	SSU	clastic metasedimentary, BIF, felsic porphyry, diorite	East to NE-striking, steeply dipping quartz veins and altered wall rock; ore shoots plunge 65°W
2	Hard Rock	1938-1951	269,081	9,009	SSU	clastic metasedimentary, BIF, felsic porphyry, volcaniclastic rocks, peridotite, diorite	East to NE-striking, steeply dipping quartz veins and altered wall rock; ore shoots plunge 20-30°W
3	Little Longlac	1934-1956	605,449	52,750	SSU	clastic metasedimentary, BIF, diorite	Linear E- to-ENE-striking ore zones which are locally deformed by S-shaped fold-like structures
4	MacLeod-Cockshutt	1938-1966	1,366,404	90,864	SSU	clastic metasedimentary, BIF, felsic porphyry, volcaniclastic rocks, diorite, gabbro	Confined to porphyry-greywacke contact; East to ENE-striking steeply-dipping quartz veins and the adjacent altered wall rock; parallel to axial plane of Z-shaped drag folds; ore shoot plunges at ca. 25-30°W
5	MacLeod-Mosher	1967-1970	180,576	17,321		Note: This mine was created from the amalgamation of the MacLeod and Mosher mines in 1967.	
6	Magnet Consolidated	1938-1952	152,089	16,879	SSU	clastic metasedimentary, BIF, felsic porphyry, diorite	Subvertical ENE-striking quartz veins and at one location ca. 45° W-plunging saddle-reef type veins
7	Mosher Longlac	1962-1966	330,042	34,586	SSU	clastic metasedimentary, BIF, felsic porphyry, diorite	East- to ENE-striking, intermediately to subvertically N-dipping quartz veins
8	Tombill	1938-1942	68,739	8,595	SSU	clastic metasedimentary, BIF, felsic porphyry, diorite	quartz stringers along altered and sheared contact between the porphyry and greywacke or BIF; east-striking steeply S-dipping shear hosted quartz veins within conglomerate
Beardmore area							
9	Leitch	1937-1965	861,982	31,802	SSU	clastic metasedimentary	Shear zone-hosted NE-ENE-striking moderately to steeply N-dipping quartz vein; ore shoots plunge 50°-65°W
10	Sand River	1937-1942	50,065	3,628		clastic metasedimentary	
11	Northern Empire	1934-1941	149,492	19,803	SVU	mafic to intermediate metavolcanic rocks	shear zone-hosted quartz vein striking ENE and dipping subvertically S
	Total		**4,100,335**	**292,827**			

Table 4-2. Characteristics of the gold mineralization events by host rock

	Relative timing	Mudstone to sandstone-hosted	Banded iron formation-hosted	Porphyry-hosted
V_1 auriferous quartz-carbonate-pyrite-chalcopyrite+/-tourmaline vein	Early-D_1	pervasive sericite-pyrite-quartz-rutile alteration halo; inclusions of chalcopyrite, ilmenite, rutile, tetrahedrite, galena, monazite in pyrite	pyrite±arsenopyrite-sericite±chlorite± biotite-carbonate alteration; pyrrhotite, native gold, chalcopyrite and magnetite inclusions in pyrite and arsenopyrite	quartz-albite-Ca-Mg-Fe-carbonate-pyrite-rutile alteration halo; inclusions of chalcopyrite, native gold (Au:Ag=5-6:1), ilmenite, rutile, galena, sphalerite, and Ag-Bi-tellurides in pyrite
V_2 auriferous tourmaline-quartz ± pyrite ± pyrrhotite ± chalcopyrite ± molybdenite ± monazite vein	Syn-D_2	Ca-Mg-Fe-carbonate-tourmaline-pyrite-pyrrhotite-chalcopyrite, ilmenite, rutile and monazite alteration halo; Au-Ag-tellurides and galena inclusions and fracture-fillings in As-Pb-enriched pyrite;	no apparent alteration halo	albite-carbonate-pyrite-rutile alteration; rutile inclusions in pyrite
V_3 auriferous quartz-carbonate-tourmaline-pyrite-chalcopyrite ±xenotime ±monazite vein	Syn-D_2	strong sericite - carbonate - pyrite± arsenopyrite alteration; inclusions of native gold, pyrrhotite, chalcopyrite, ilmenite, rutile, galena in pyrite	pyrite(±pyrrhotite±arsenopyrite)-quartz-sericite-chlorite-biotite-carbonate-monazite alteration; magnetite, chalcopyrite, pyrrhotite, and rarely ilmenite, rutile inclusions in pyrite	Ca-Mg-Fe-carbonate-albite-pyrite-rutile-ilmenite alteration; rutile, ilmenite, pyrrhotite, chalcopyrite, native gold, fluor-apatite, galena, monazite, Au-Ag-, Ag- and Pb-Bi-tellurides and thorite inclusions in pyrite

Table 4-3. Whole rock geochemical composition of representative samples. Coordinates are provided in UTM NAD 83, Zone 16.

		Least altered siltstone	Altered siltstone (adjacent to V1 vein)	Least altered sandstone	Altered sandstone (adjacent to V1 vein)	Least altered sandstone	Altered sandstone (adjacent to V3 vein)
Sample ID	**Analytical Method**	BGBZT2014_38B	BGBZT2014_38A	BGBZT2014_34B	BGBZT2014_34A	BGBZT2014_36B	BGBZT2014_36A
		5502913.5mN,	504906.6mE	5502931.3mN,	504904.6mE	5502923.9mN,	504896.5mE
SiO2_pct	XRF-M01	53.04	43.31	55.12	35.46	64.9	62.38
Al2O3_pct	XRF-M01	20.38	21.56	17.19	17.84	13.34	12.77
Fe2O3_pct	XRF-M01						
FeO_pct	XRF-M01	7.98	11.19	6.56	9.45	4.77	5.07
MnO_pct	XRF-M01	0.068	0.05	0.073	0.137	0.087	0.08
MgO_pct	XRF-M01	3.89	2.31	2.97	4.67	2.3	1.84
CaO_pct	XRF-M01	0.794	1.98	3.091	7.897	2.725	3.296
Na2O_pct	XRF-M01	3.06	1.27	5.45	2.7	3.14	2.74
K2O_pct	XRF-M01	4.13	5.92	2.4	3.96	2.45	2.74
TiO2_pct	XRF-M01	0.79	0.83	0.65	0.69	0.51	0.52
P2O5_pct	XRF-M01	0.139	0.02	0.136	0.088	0.091	0.068
Cr2O3_pct	XRF-M01	0.03	0.03	0.02	0.02	0.01	0.01
V2O5_pct	n.a.	n.a.	n.a.	n.a.	n.a.	n.a.	n.a.
BaO_pct	XRF-M00	0.07	0.11	0.05	0.09	0.04	0.05
LOI_pct	XRF-M01	4.02	8.84	4.84	13.5	4.67	7.19
Total		98.39	97.42	98.55	96.50	99.03	98.76
CO2_pct	IRC-100	0.882	3.103	4.637	11.439	4.186	5.1
Total S_pct	IRC-100	0.754	7.861	0.298	3.099	0.541	2.472
La_ppm	IMC-100	15.59	27.16	22.74	24.32	23.93	25.41
Ce_ppm	IMC-100	30.79	55.23	44.34	49.37	45.22	47.74
Pr_ppm	IMC-100	3.693	6.792	5.301	5.936	5.178	5.397
Nd_ppm	IMC-100	14.34	26.75	19.49	22.8	19.15	19.66
Sm_ppm	IMC-100	2.706	4.822	3.572	4.18	3.207	3.318
Eu_ppm	IMC-100	0.663	1.2502	1.0109	1.3681	0.8105	0.837
Gd_ppm	IMC-100	2.107	4.004	3.146	3.474	2.621	2.639
Tb_ppm	IMC-100	0.29	0.6032	0.4577	0.5077	0.3667	0.368
Dy_ppm	IMC-100	1.727	3.721	2.8	3.037	2.208	2.181
Ho_ppm	IMC-100	0.3457	0.7371	0.5629	0.6086	0.4373	0.423
Er_ppm	IMC-100	1.072	2.153	1.643	1.806	1.274	1.252
Tm_ppm	IMC-100	0.1784	0.3075	0.2306	0.2637	0.1807	0.1823
Yb_ppm	IMC-100	1.268	2.059	1.54	1.833	1.198	1.193
Lu_ppm	IMC-100	0.1921	0.3128	0.2356	0.2748	0.1831	0.1828
Ba_ppm	IMC-100	253.9	844.5	444.7	805	384.5	456.7
Be_ppm	IMC-100	2.22	2.99	1.57	2.34	1.18	1.33
Cr_ppm	IMC-100	212	226	157	166	121	127
Cs_ppm	IMC-100	8.388	4.804	6.491	4.151	3.521	2.313
Ga_ppm	IMC-100	25.77	29.6	21.1	31.48	15.26	15.78
Ge_ppm		n.a.	n.a.	n.a.	n.a.	n.a.	n.a.
Hf_ppm	IMC-100	3.39	3.57	3.58	2.99	3.21	3.22
In_ppm	IMC-100	0.0607	0.0521	0.0447	0.0577	0.0311	0.0321
Nb_ppm	IMC-100	6.114	6.582	6.043	5.676	3.917	3.896
Rb_ppm	IMC-100	50.1	126.36	77.91	96.57	65.12	67.68
Sb_ppm	IMC-100	1.58	4.28	1.11	11.64	1.43	13.8
Sc_ppm	IMC-100	12.4	25.2	19.6	24.3	13	14
Sn_ppm	IMC-100	1.54	1.38	1.28	1.69	0.84	1.03
Sr_ppm	IMC-100	209.9	279.4	231.1	401	199.6	215.5
Ta_ppm	IMC-100	0.402	0.496	0.471	0.4	0.28	0.269
Th_ppm	IMC-100	4.566	8.468	6.397	6.396	6.636	6.704
Tl_ppm	IMC-100	0.605	0.54	0.429	0.391	0.31	0.273
U_ppm	IMC-100	1.91	2.417	1.866	1.781	1.828	1.814
V_ppm	IMC-100	182.2	199	134.9	215.6	93.9	103.3

Table 4-3. Whole rock geochemical composition of representative samples. Coordinates are provided in UTM NAD 83, Zone 16. (cont'd)

Sample ID	Analytical Method	Least altered siltstone	Altered siltstone (adjacent to V1 vein)	Least altered sandstone	Altered sandstone (adjacent to V1 vein)	Least altered sandstone	Altered sandstone (adjacent to V3 vein)
W_ppm	IMC-100	39.68	34.35	22.95	37.93	8.04	9.65
Y_ppm	IMC-100	9.62	19.39	16.5	17.16	12.47	12.02
Zr_ppm	IMC-100	128	129	139	112	127	129
Cd_ppm	IMC-100	0.073	0.095	0.073	0.138	0.078	0.062
Co_ppm	IMC-100	29.22	35.82	23.42	25.88	18.05	20.79
Cu_ppm	IMC-100	82.2	9.3	73.6	15.5	49.7	23.8
Li_ppm	IMC-100	33.4	34.6	22.6	26.9	16.8	15.6
Ni_ppm	IMC-100	105.6	113.5	67.5	74.4	46.8	54
Mn_ppm		n.a.	n.a.	n.a.	n.a.	n.a.	n.a.
Mo_ppm	IMC-100	1.86	2.16	1.83	3.5	1.71	1.43
Pb_ppm	IMC-100	7.8	12	6.9	14.7	9.2	8.3
Zn_ppm	IMC-100	102	53	86	71	66	29
Bi_ppm	IML-100	0.11	0.4	0.12	0.32	0.18	0.3
Te_ppm	IML-100	0.1	0.53	0.06	0.61	0.09	0.32
Se_ppm	IML-100	0.4	2.2	0.4	1.7	0.4	0.8
Au_ppb	IML-100	557	10807	53	3330	113	2802
Ag_ppm	IML-100	0.12	1.66	0.1	0.62	0.07	0.73
As_ppm	IML-100	73.9	413.2	39.5	123.9	12.1	77.4

Table 4-3. Whole rock geochemical composition of representative samples. Coordinates are provided in UTM NAD 83, Zone 16. (cont'd)

	Analytical Method	Altered feldspar-quartz porphyry (adjacent to V1 vein)	Altered feldspar-quartz porphyry (adjacent to V3 vein)		Analytical Method	Least altered feldspar-quartz porphyry		Analytical Method	Least altered BIF	Altered BIF (Sulphide-replaced rock)
		BGBZT2014_2	BGBZT2014_22			BGBST2013_421			BGBST2012_326	BGBST2012_300B
		5502820.6mN, 504787.7mE	5502852.6mN, 504797.7mE			5502845mN, 504801mE			MM106D; 974.6-974.67 m	MM106D; 785.67-786 m
SiO2_pct	XRF-M01	60.7	64.12	**SiO2_pct**	FUS-XRF	63.86	**SiO2 %**	FUS-XRF	29.9	24.8
Al2O3_pct	XRF-M01	18.59	16.44	**Al2O3_pct**	FUS-XRF	16.57	**Al2O3 %**	FUS-XRF	1.26	4.69
Fe2O3_pct	XRF-M01			**Fe2O3 %**	FUS-XRF	< 0.01	**Fe2O3 %**	FUS-XRF	58.92	0.04
FeO_pct	XRF-M01	2.92	2.16	**FeO_pct**	TITR	2.5	**FeO %**	TITR	6.7	37.92
MnO_pct	XRF-M01	0.02	0.034	**MnO_pct**	FUS-XRF	0.025	**MnO %**	FUS-XRF	0.009	0.021
MgO_pct	XRF-M01	0.82	1.01	**MgO_pct**	FUS-XRF	1.01	**MgO %**	FUS-XRF	0.28	0.8
CaO_pct	XRF-M01	2.061	3.129	**CaO_pct**	FUS-XRF	3.42	**CaO %**	FUS-XRF	1.15	1.57
Na2O_pct	XRF-M01	5.66	6.17	**Na2O_pct**	FUS-XRF	4.41	**Na2O %**	FUS-XRF	0.03	0.01
K2O_pct	XRF-M01	2.77	1.79	**K2O_pct**	FUS-XRF	2.58	**K2O %**	FUS-XRF	0.36	1.42
TiO2_pct	XRF-M01	0.38	0.34	**TiO2_pct**	FUS-XRF	0.33	**TiO2 %**	FUS-XRF	0.04	0.16
P2O5_pct	XRF-M01	0.156	0.134	**P2O5_pct**	FUS-XRF	0.2	**P2O5 %**	FUS-XRF	0.2	0.06
Cr2O3_pct	XRF-M01	<0.002	<0.002	**Cr2O3 %**	FUS-XRF	< 0.01	**Cr2O3 %**	FUS-XRF	0.01	0.01
V2O5_pct	n.a.	n.a.	n.a.	**V2O5 %**	FUS-XRF	0.007	**V2O5 %**	FUS-XRF	< 0.003	< 0.003
BaO_pct	XRF-M00	0.07	0.05	**LOI_pct**	FUS-XRF	4.49	**LOI %**	FUS-XRF	0.39	23.41
LOI_pct	XRF-M01	4.48	4.32	**Total**	FUS-XRF	99.40	**Total**		99.25	94.92
Total		98.63	99.70							
CO2_pct	IRC-100	2.595	3.838	**CO2_pct**	IR	2.69	**CO2 %**	IR	0.93	2.15
Total S_pct	IRC-100	1.496	0.502	**Total S_pct**	IR	0.61	**Total S %**	IR	0.14	33.4
La_ppm	IMC-100	19.2	17.33							
Ce_ppm	IMC-100	42.33	37.17	**La_ppm**	FUS-MS	18	**La (ppm)**	FUS-MS	3.85	7.29
Pr_ppm	IMC-100	5.538	4.898	**Ce_ppm**	FUS-MS	38.5	**Ce (ppm)**	FUS-MS	7.17	13.7
Nd_ppm	IMC-100	21.79	19.65	**Pr_ppm**	FUS-MS	4.85	**Pr (ppm)**	FUS-MS	0.89	1.68
Sm_ppm	IMC-100	3.381	3.253	**Nd_ppm**	FUS-MS	18.8	**Nd (ppm)**	FUS-MS	3.41	6.14
Eu_ppm	IMC-100	0.7304	0.7672	**Sm_ppm**	FUS-MS	3.03	**Sm (ppm)**	FUS-MS	0.66	1.03
Gd_ppm	IMC-100	1.823	1.918	**Eu_ppm**	FUS-MS	0.698	**Eu (ppm)**	FUS-MS	0.307	0.298
Tb_ppm	IMC-100	0.1847	0.1976	**Gd_ppm**	FUS-MS	1.71	**Gd (ppm)**	FUS-MS	0.63	1.02
Dy_ppm	IMC-100	0.839	0.897	**Tb_ppm**	FUS-MS	0.17	**Tb (ppm)**	FUS-MS	0.11	0.16
Ho_ppm	IMC-100	0.1249	0.14	**Dy_ppm**	FUS-MS	0.82	**Dy (ppm)**	FUS-MS	0.66	0.94
Er_ppm	IMC-100	0.325	0.339	**Ho_ppm**	FUS-MS	0.13	**Ho (ppm)**	FUS-MS	0.14	0.2
Tm_ppm	IMC-100	0.0442	0.0454	**Er_ppm**	FUS-MS	0.33	**Er (ppm)**	FUS-MS	0.41	0.58
Yb_ppm	IMC-100	0.289	0.305	**Tm_ppm**	FUS-MS	0.048	**Tm (ppm)**	FUS-MS	0.062	0.087
Lu_ppm	IMC-100	0.0455	0.0435	**Yb_ppm**	FUS-MS	0.29	**Yb (ppm)**	FUS-MS	0.37	0.59

Table 4-3. Whole rock geochemical composition of representative samples. Coordinates are provided in UTM NAD 83, Zone 16. (cont'd)

	Analytical Method	Altered feldspar-quartz porphyry (adjacent to V1 vein)	Altered feldspar-quartz porphyry (adjacent to V3 vein)		Analytical Method	Least altered feldspar-quartz porphyry		Analytical Method	Least altered BIF	Altered BIF (Sulphide-replaced rock)
Ba_ppm	IMC-100	677.2	491.7	**Lu_ppm**	FUS-MS	0.041	**Lu (ppm)**	FUS-MS	0.055	0.097
Be_ppm	IMC-100	2.03	1.7	**Ba_ppm**	FUS-MS	731	**Ba (ppm)**	FUS-MS	405	451
Cr_ppm	IMC-100	25	26	**Be (ppm)**	FUS-MS		**Be (ppm)**	FUS-MS	< 1	< 1
Cs_ppm	IMC-100	2.661	1.802	**Cr_ppm**	FUS-MS	30	**Cr (ppm)**	FUS-MS	< 20	30
Ga_ppm	IMC-100	28.26	23.37	**Cs_ppm**	FUS-MS	2.8	**Cs (ppm)**	FUS-MS	0.5	1.1
Ge_ppm		n.a.	n.a.	**Ga_ppm**	FUS-MS	24	**Ga (ppm)**	FUS-MS	2	7
Hf_ppm	IMC-100	3.71	3.13	**Ge (ppm)**	FUS-MS	1.6	**Ge (ppm)**	FUS-MS	3.2	1.2
In_ppm	IMC-100	0.0306	0.0156	**Hf_ppm**	FUS-MS	2.4	**Hf (ppm)**	FUS-MS	< 0.1	0.6
Nb_ppm	IMC-100	3.5	3.476	**In_ppm**	FUS-MS	< 0.1	**In (ppm)**	FUS-MS	< 0.1	< 0.1
Rb_ppm	IMC-100	65.52	41.31	**Nb_ppm**	FUS-MS	2.1	**Nb (ppm)**	FUS-MS	< 0.2	0.2
Sb_ppm	IMC-100	1.52	1.52	**Rb_ppm**	FUS-MS	63	**Rb (ppm)**	FUS-MS	17	41
Sc_ppm	IMC-100	4.1	3.7	**Sb_ppm**	FUS-MS	1.6	**Sb (ppm)**	FUS-MS	5.6	6.8
Sn_ppm	IMC-100	0.97	0.62	**Sc (ppm)**	FUS-MS	n.a.	**Sc (ppm)**	FUS-MS	2	6
Sr_ppm	IMC-100	205	555.5	**Sn_ppm**	FUS-MS	< 1	**Sn (ppm)**	FUS-MS	< 1	< 1
Ta_ppm	IMC-100	0.112	0.131	**Sr_ppm**	FUS-MS	423	**Sr (ppm)**	FUS-MS	54	69
Th_ppm	IMC-100	3.419	2.682	**Ta_ppm**	FUS-MS	0.16	**Ta (ppm)**	FUS-MS	< 0.01	0.09
Tl_ppm	IMC-100	0.255	0.17	**Th_ppm**	FUS-MS	2.35	**Th (ppm)**	FUS-MS	0.43	1.51
U_ppm	IMC-100	0.971	0.793	**Tl_ppm**	FUS-MS	0.13	**Tl (ppm)**	FUS-MS	< 0.05	< 0.05
V_ppm	IMC-100	83.2	44.2	**U_ppm**	FUS-MS	0.75	**U (ppm)**	FUS-MS	0.12	0.44
W_ppm	IMC-100	24.27	5.56	**V_ppm**	FUS-MS	46	**V (ppm)**	FUS-MS	22	42
Y_ppm	IMC-100	3.71	4.07	**W_ppm**	FUS-MS	4.2	**W (ppm)**	FUS-MS	5.9	18.1
				Y_ppm	FUS-MS	3.8	**Y (ppm)**	FUS-MS	4.9	6.7
Zr_ppm	IMC-100	130	107	**Zr_ppm**	FUS-MS	87	**Zr (ppm)**	FUS-MS	8	25
Cd_ppm	IMC-100	0.048	0.034	**Cd_ppm**	TD-MS	< 0.2	**Cd (ppm)**	TD-MS	< 0.2	< 0.2
Co_ppm	IMC-100	8.66	5.91	**Co_ppm**	TD-MS	6.4	**Co (ppm)**	TD-MS	1	6.8
Cu_ppm	IMC-100	2	2.8	**Cu_ppm**	TD-MS	1.1	**Cu (ppm)**	TD-MS	7.1	8.9
Li_ppm	IMC-100	5.2	6.5	**Li_ppm**	TD-MS	15	**Li (ppm)**	TD-MS	1	6
Ni_ppm	IMC-100	8.5	6.4	**Ni_ppm**	TD-MS	8	**Ni (ppm)**	TD-MS	5	21
Mn_ppm		n.a.	n.a.	**Mn (ppm)**	TD-MS	255	**Mn (ppm)**	TD-MS	132	205
Mo_ppm	IMC-100	0.47	0.63	**Mo_ppm**	TD-MS	< 1	**Mo (ppm)**	TD-MS	< 1	< 1
Pb_ppm	IMC-100	5.1	5.7	**Pb_ppm**	TD-MS	6	**Pb (ppm)**	TD-MS	2	14
Zn_ppm	IMC-100	27	34	**Zn_ppm**	TD-MS	37.3	**Zn (ppm)**	TD-MS	10.7	15.1
Bi_ppm	IML-100	0.05	0.02	**Bi_ppm**	AR-MS	0.04	**Bi (ppm)**	NP-MS	< 0.05	0.39
Te_ppm	IML-100	0.13	0.03	**Te_ppm**	AR-MS	< 0.02	**Te (ppm)**	NP-MS	< 0.01	1.38

Table 4-3. Whole rock geochemical composition of representative samples. Coordinates are provided in UTM NAD 83, Zone 16. (cont'd)

	Analytical Method	Altered feldspar-quartz porphyry (adjacent to V1 vein)	Altered feldspar-quartz porphyry (adjacent to V3 vein)		Analytical Method	Least altered feldspar-quartz porphyry		Analytical Method	Least altered BIF	Altered BIF (Sulphide-replaced rock)
Se_ppm	IML-100	0.6	<0.4	**Se_ppm**	AR-MS	< 0.1	**Se (ppm)**	NP-MS	< 1	3
Au_ppb	IML-100	1539	475	**Au_ppb**	FA-AA+ FA-GRA	31	**Au (ppb)**	FA-AA+ FA-GRA	13	31400
Ag_ppm	IML-100	0.16	0.09	**Ag_ppm**	FA-GRA + FUS-MS	0.9	**Ag (ppm)**	FA-GRA + FUS-MS	< 0.5	0.7
As_ppm	IML-100	25.3	22.4	**As_ppm**	NP-MS + FUS-Na2O2	10.3	**As (ppm)**	NP-MS + FUS-Na2O2	15	415

Methods abbreviations

FUS	fusion
FUS-XRF	XRF
FUS-MS	ICP MS analyses with Li meta/tetraborate fusion
TITR	Titration
IR	Infrared
TD-MS	ICP MS analyses with 4-acid digestion
NP-MS	Aqua-regia and ICP-MS
FA-AA	Fire Assay - Atomic absorption
FA-GRA	Fire Assay - Gravimetric

Table 4-4. Elemental changes from less mineralized to more mineralized samples in sandstone, siltstone and porphyry during the early D_1 and syn-D_2 gold mineralization events based on Grant's isocon method (Grant, 1986). This list includes major oxides with at least 20% and trace elements with at least 50 % elemental changes.

	Enrichment in:	**Depletion in:**
V1 in siltstone	Au, Ag, S, As, Se, Te, Bi, CO2, Ba, Sb, Rb, CaO, LOI, Dy, Ho, Tb, Sc, Y, Er, Gd, Eu, Nd, Th, Pr, Ce, Sm, La, Tm, Le, Yb, BaO, Pb, K2O, FeO	Na2O, P2O5, Cu, MgO, MnO
V1 in sandstone	Au, Sb, S, Te, Ag, Se, As, LOI, Bi, CaO, CO2, Pb, Mo, Cd, MnO, Ba, BaO, Sr, W, K2O, V, MgO, FeO	Na2O, Cu, SiO2, P2O5
V3 in sandstone	Au, S, Sb, As, S, Te, Se, Bi, LOI, BaO, CO2, CaO	Cu, Zn, P2O5, MgO
V1 in porphyry	Au, Te, Se, W, As, S, Tl, Cu, V	Ag, Cd, In, Li, Mo, Sr, CaO, P2O5, MnO, MgO
V3 in porphyry	Au, Cu, As, Nb, CO2, Na2O, MnO	Bi, Li, Cd, In, Ag, K2O, P2O5

Table 4-5. Spearman correlation coefficients between Au and various pathfinder elements and alteration indices in all samples combined and for each lithology

Spearman correlation with Au	All samples (n=207)	Siltstone (n=41)	Sandstone (n=78)	BIF (n=13)	Sulphide-replaced rock (n=20)	BIF+sulfide replaced rock combined (n=33)	Porphyry (n=33)	Mafic dike (n=22)
FeO_pct	0.29	0.33	-0.003	0.56	0.2	0.71	0.26	-0.35
CaO_pct	-0.12	0.2	0.23	-0.54	0.14	-0.16	-0.029	0.8
K2O_pct	0.09	0.12	0.37	0.36	-0.072	0.076	0.017	0.56
LOI_pct	0.35	0.24	0.33	0.3	-0.053	0.66	0.24	0.47
CO2_pct	-0.05	0.22	0.2	-0.42	-0.051	-0.13	0.28	0.55
S_pct	0.89	0.9	0.9	0.81	0.15	0.75	0.47	0.66
Ba_ppm	-0.018	0.028	0.17	0.23	0.024	-0.2	-0.27	0.6
Be_ppm	0.11	0.12	0.5	-0.13	-0.31	-0.57	-0.16	0.63
Sb_ppm	0.36	0.2	0.41	-0.025	-0.37	0.26	0.22	0.17
W_ppm	0.73	0.71	0.74	0.6	-0.03	0.035	0.64	0.75
Cd_ppm	0.15	0.092	0.24	NaN	0.46	0.39	0.29	0.45
Mo_ppm	0.29	0.52	0.46	0.1	-0.065	-0.012	0.02	0.075
Pb_ppm	0.38	0.065	0.24	0.49	0.44	0.79	-0.16	0.4
Bi_ppm	0.6	0.49	0.62	0.66	-0.017	0.65	0.044	0.49
Te_ppm	0.59	0.55	0.57	0.71	0.13	0.6	0.53	0.38
Se_ppm	0.26	0.36	0.27	0.79	-0.068	0.15	0.089	0.41
Ag_ppm	0.14	-0.18	0.053	0.27	0.39	0.63	0.032	-0.095
As_ppm	0.61	0.33	0.66	0.56	-0.11	0.62	0.54	0.65
Zn_ppm	-0.43	-0.39	-0.38	0.35	-0.26	-0.44	-0.15	0.072
Cu_ppm	-0.17	-0.16	-0.22	0.25	-0.062	0.37	-0.062	-0.15
CO2/Ca	0.24	0.33	0.27	0.03	-0.16	0.18	0.41	-0.0074
SSI: sodium-sulphide index	0.81	0.83	0.84	0.71	-0.13	0.67	0.4	0.75
MSI=3K/Al: muscovite saturation i.	0.43	0.36	0.38	0.32	0.026	0.11	0.0071	0.66
EPAI: potassic alteration i.	0.41	0.36	0.64	0.49	0.077	0.032	0.027	0.56
KSI: potassium sulphide i.	0.76	0.81	0.74	0.64	0.15	0.75	0.49	0.55
KVI: potassic volatile index:	0.13	0.086	-0.038	-0.17	0.11	0.52	0.22	-0.49
S/(SIO2+Na2O) mol	0.88	0.89	0.88	0.82	0.17	0.76	0.47	0.69
(LOI+CO2+S)/SiO 2	0.46	0.5	0.42	0.45	0.17	0.73	0.33	0.64

Table 4-5. Spearman correlation coefficients between Au and various pathfinder elements and alteration indices in all samples combined and for each lithology (cont'd)

SSI: sodium-sulfide index: S/S+Na2O molar ratio: 100*[S/32.066]/[(S/32.066)+ 2*Na2O/(61.978)]; Gemmell et al., 2006, 2007

MSI: muscovite saturation index: 3K/Al molar ratio: [3*2*K_2O/(94.196)]/[2*Al_2O_3/ (101.961276)]; Kishida and Kerrich et al., 1987

EPAI: potassic alteration index: K/Al+Na molar ratio: [2*K_2O/(94.196)]/[2*Al_2O_3/(101.961276)-2*Na_2O/ (61.978)]; Whitbread and Moore, 2004

KSI: potassium sulfide index: S/S+K Molar Ratio: 100* [S/32.066]/[(S/32.066)+2*K2O/(94.196)]; Gemmell et al., 2006, 2007

KVI: potassic volatile index: 100*LOI/(LOI+K2O) molar ratio: 100*[LOI/18.01528]/[(LOI/18.01528)+2*K2O/ (94.196)]; Gemmell et al., 2006, 2007

Table 4-6. Re-Os isotope data of arsenopyrite in mineralized zone

Sample ID	Re (ppb)	± 2σ	Os (ppt)	± 2σ	$^{187}Re/^{188}Os$	± 2σ	$^{187}Os/^{188}Os$	± 2σ	Model age (Ma)	± 2σ
BGBZT-2013-362-A	0.94	0	46.3	1.2	235.5	7.1	10.94	0.33	2603	19
BGBZT-2013-362-B	0.938	0	47	0.6	227.1	3.6	10.55	0.18	2600	22
BGBZT-2013-362-C	0.693	0	28.1	1	390.4	13.9	17.65	0.63	2580	21
BGBZT-2013-362-D	0.852	0	40.3	0.7	257.5	5.2	11.85	0.26	2588	26
BGBZT-2013-362-E	0.93	0	39	0.9	356.9	8.6	16.28	0.39	2597	16
BGBZT-2013-362-F	1.121	0.01	73.5	1.9	134.1	5	6.46	0.24	2608	29

Appendices

Appendix 4-A. Analytical methods

Petrography

Over 200 polished thin sections were prepared of least altered to strongly altered mineralized samples. Semi-quantitative mineral chemical analyses were collected using an Oxford energy-dispersive spectrometer mounted on the JEOL JSM-6400 scanning electron microscope (SEM) at the Central Analytical Facilities of Laurentian University, using 20 kV acceleration voltage and a 1.005 nA beam current at 15 mm working distance.

Mineral-chemical mapping of sulfides

The mineral chemistry of gold-prospective pyrite and arsenopyrite grains were analyzed in situ on polished thin sections using the Thermo X Series II inductively coupled plasma mass spectrometer (ICP-MS) interfaced with a Resonetics RESOlution M-50 193 nm ArF excimer laser at the Chemical Fingerprinting Laboratory, Laurentian University, Sudbury, ON. The beam diameters were chosen based on the size of the grain of interest and the type of analyses to be carried out. For line analyses, beam size was consistently 36 μm whereas for elemental mapping the beam diameter varied between 14 and 26 μm. The scan rates ranged between 7 and 18 μm/s, i.e., 1/3 to ½ of the beam diameter per second. The laser pulse rate, the fluence and the resulting energy density was 8 Hz, 60 mJ and 5 J/cm2, respectively. Ultra-pure He flowing at a constant rate of 650 ml/min was used as transport gas and 6 ml/min N2 was added to the cell flow to increase sensitivity (Durrant, 1994).

For the quantification of the trace element concentrations of the analyzed sulfides, the stoichiometric Fe composition was used as the internal standard and calibrations were done using certified reference materials Po725 (Au, Pd), GSD or NIST610 (Ag, As, Bi, Co, Cr, Cu, In, Mn, Mo, Ni, Pb, Sb, Se, Si,

Sn, Ti, Tl, V, W, Zn and Te). The data reduction was carried out using Iolite software package (Paton et al., 2011) and the laser mapping add-on packages developed by Petrus et al. (2017).

Whole rock geochemistry

Samples collected in 2012, 2013 and 2016 were analyzed at Activation Laboratories Ltd. in Ancaster, Ontario (year of collection indicated in the sample ID). The samples were crushed in a Cr-free steel mill and dissolved by metaborate/tetraborate, 4-acid, Aqua Regia or sodium peroxide digestion prior to whole rock geochemical analyses using fusion X-ray fluorescence spectrometry (XRF) and inductively coupled plasma mass spectrometry (ICP-MS) to obtain major oxide and trace element compositions, respectively. The analytical methods are presented along with the composition of representative samples in Table 3. Gold values were determined by atomic absorption or gravimetric fire assay methods when Au<3000 ppb and Au>3000 ppb, respectively. The latter method was also used for ore grade Ag analyses. Total S, CO_2 and FeO concentrations were determined by infrared absorption and titration, respectively. Arsenic values were analyzed by ICP-MS following peroxide fusion if their concentration exceeded 10,000 ppm.

The samples collected in 2014 were crushed by agate mill and dissolved using closed vessel multi-acid or Aqua Regia digestion at the Geoscience Laboratories of the Ministry of Northern Developments and Mines in Sudbury, Ontario. Major oxide and trace elements were analyzed using fusion X-ray fluorescent spectrometry (XRF) and inductively coupled plasma mass spectrometry (ICP-MS), respectively. Accuracy and precision are summarized in Appendix 4-B.

Re-Os geochronology

Re-Os isotope dating of arsenopyrite was carried out at the Canadian Centre of Isotopic Microanalysis (CCIM) at the University of Alberta, Canada. The arsenopyrite concentrate derived from the selected

sample (BGBZT2013_362C) was first analyzed using isotope dilution negative thermal ionization mass spectrometry (ID-NTIMS) to determine if it had sufficient Re to proceed with the datation. The mineral concentrate was prepared by crushing using metal-free mortar and arsenopyrite fragments were separated using gravity and magnetic methods. An aliquot of the concentrate was placed in a borosilicate glass Carius tube and a mixed ^{185}Re + ^{188}Os + ^{190}Os spike was added to samples devoid of common Os (Markey et al., 2007). This mixture was subsequently dissolved, chemically separated and purified as described in Shirey and Walker (2005), Cohen and Waters (1996), Birck and others (1997). The Re and Os isotopic compositions were analyzed by ID-NTIMS as described in Morelli and others (2005). The model age was calculated using the decay constant of ^{187}Re isotope from Smoliar and others (1996). The Re-Os ages were calculated and plotted using Isoplot v. 3.0 (Ludwig, 2003) with errors at the 2σ level.

Appendix 4-B. Calculated precision and accuracy of whole rock geochemical data

	Method 2012	LOD 2012	LOQ 2012 [1]	Accuracy 2012 (%RD)	Precision 2012 (%RSD)
SiO2 (wt.%)	FUS-XRF	0.01	0.033	0.02-1.13	≤1
Al2O3 (wt.%)	FUS-XRF	0.01	0.033	≤ 11.76*	0.15-7.43
Fe2O3(t) (wt.%)	FUS-XRF	0.01	0.033	≤ 3.07	≤2.82
FeO (wt.%)	TITR	0.1	0.33	0.48-30*	≤7.86
MnO (wt.%)	FUS-XRF	0.001	0.0033	≤ 6.97	≤5.44
MgO (wt.%)	FUS-XRF	0.01	0.033	0.24-25*	≤3.93
CaO (wt.%)	FUS-XRF	0.01	0.033	≤ 300*	≤12.69
Na2O (wt.%)	FUS-XRF	0.01	0.033	≤ 56.57*	≤6.15
K2O (wt.%)	FUS-XRF	0.01	0.033	0.11-40*	≤9.42
TiO2 (wt.%)	FUS-XRF	0.01	0.033	≤ 40*	≤5.51
P2O5 (wt.%)	FUS-XRF	0.01	0.033	≤ 66.67*	≤28.28*
Cr2O3 (wt.%)	FUS-XRF	0.01	0.033	≤ 50*	≤47.14*
V2O5 (wt.%)	FUS-XRF	0.003	0.0099	2.32-14.29*	≤6.33
LOI (wt.%)	FUS-XRF			n.d.	≤9.47
CO2 (wt.%)	IR	0.01	0.033	0.11-6.71	≤ 10.86
Total S (wt.%)	IR	0.01	0.033	≤ 8.33	≤ 15.33
			0		
La (ppm)	FUS-MS	0.05	0.165	0.22-9.94	≤6.32
Ce (ppm)	FUS-MS	0.05	0.165	0.33-9.92	≤6.06
Pr (ppm)	FUS-MS	0.01	0.033	0.36-8.65	≤4.82
Nd (ppm)	FUS-MS	0.05	0.165	1.27-9.51	0.82-5.43
Sm (ppm)	FUS-MS	0.01	0.033	≤ 9.64	0.95-7.71
Eu (ppm)	FUS-MS	0.005	0.0165	0.51-10.22	0.21-6.6
Gd (ppm)	FUS-MS	0.01	0.033	≤ 4.17	≤2.53
Tb (ppm)	FUS-MS	0.01	0.033	≤ 7.56	≤4.42
Dy (ppm)	FUS-MS	0.01	0.033	0.54-10.63	1.27-4.33
Ho (ppm)	FUS-MS	0.01	0.033	0.84-7.14	≤6.15
Er (ppm)	FUS-MS	0.01	0.033	0.1-7.14	0.52-7.32
Tm (ppm)	FUS-MS	0.005	0.0165	2.12-5.95	≤6.24
Yb (ppm)	FUS-MS	0.01	0.033	≤ 8.97	0.5-6.73
Lu (ppm)	FUS-MS	0.002	0.0066	0.33-10.83	0.31-5.8
Ba (ppm)	FUS-ICP	3	9.9	2-14.56	≤3.68
Be (ppm)	FUS-ICP	1	3.3	≤15.39*	0
Cr (ppm)	FUS-MS	20	66	± ≤4.58	± ≤ 15.71*
Cs (ppm)	FUS-MS	0.1	0.33	≤5.75	≤4.56
Ga (ppm)	FUS-MS	1	3.3	≤4.8	≤20.2*
Ge (ppm)	FUS-MS	0.5	1.65	0.9-44.44*	≤16.64*

Appendix 4-B. Calculated precision and accuracy of whole rock geochemical data (cont'd)

	Method 2012	LOD 2012	LOQ 2012 [1]	Accuracy 2012 (%RD)	Precision 2012 (%RSD)
Hf (ppm)	FUS-MS	0.1	0.33	≤ 19.29	≤10.88
In (ppm)	FUS-MS	0.1	0.33	3.75-8	BDL
Nb (ppm)	FUS-MS	0.2	0.66	0.1-4.83	≤12.86*
Rb (ppm)	FUS-MS	1	3.3	0.4-10.53	≤4.04
Sb (ppm)	FUS-MS	0.2	0.66	≤ 9.24	≤20.74
Sc (ppm)	FUS-ICP	1	3.3	≤ 45*	≤3.63
Sn (ppm)	FUS-MS	1	3.3	4.9-33.33*	0
Sr (ppm)	FUS-ICP	2	6.6	1.97-7.5	≤2.62
Ta (ppm)	FUS-MS	0.01	0.033	0.38-12.9	1.1-31.43
Th (ppm)	FUS-MS	0.05	0.165	0.7-7.81	≤7.44
Tl (ppm)	FUS-MS	0.05	0.165	~0.6	2.67-33.1
U (ppm)	FUS-MS	0.01	0.033	≤ 4.93	BDL
V (ppm)	FUS-ICP	5	16.5	5-28.57*	≤1.41
W (ppm)	FUS-MS	0.5	1.65	≤ 2.19	≤13.7
Y (ppm)	FUS-MS	0.5	1.65	0.51-10.24	≤5.81
Zr (ppm)	FUS-MS	1	3.3	≤ 7.42	≤4.88
Cd (ppm)	TD-MS	0.2	0.66	≤ 30.30	n.d.
Co (ppm)	TD-MS	0.5	1.65	≤ 4.88	0.43-5.64
Cu (ppm)	TD-MS	0.5	1.65	4.52-195.67	1.31-7.71
Li (ppm)	TD-MS	1	3.3	2.94-26.13	≤12.86
Ni (ppm)	TD-MS	1	3.3	1.43-15.15	≤6.37
Mn (ppm)	TD-MS	2	6.6	2.58-11.93	1.02-10.52
Mo (ppm)	TD-MS	1	3.3	5.55-233.33*	≤47.14*
Pb (ppm)	TD-MS	2	6.6	2.85-13.03	≤20.20*
Zn (ppm)	TD-MS	0.5	1.65	2.76-28.16	0.9-7.24
Bi (ppm)	NP-MS	0.05	0.165	25*	≤7.44*
Te (ppm)	NP-MS	0.01	0.033	n.d.	2.89-47.14*
Se (ppm)	NP-MS	1	3.3	n.d.	≤47.14*
Au (ppb)	FA-AA	5	16.5	1.38-6.13	0.49-47.14
Au (g/t)	FA-GRA	0.03	0.099	1.04-3.65	n.d.
Ag (ppm)	FUS-MS	0.5	1.65	2.4-2480.65*	≤28.28*
Ag (g/t)	FA-GRA	3	9.9	2.77-8.73	n.d.
As (ppm)	NP-MS	1	3.3	n.d.	≤100.21
As (wt.%)	FUS-Na2O	0.01	0.033	≤ 12.36*	~0

Appendix 4-B. Calculated precision and accuracy of whole rock geochemical data (cont'd)

	Method 2013	LOD 2013	LOQ 2013 [1]	Accuracy 2013 (%RD)	Precision 2013 (%RSD)
SiO2 (wt.%)	FUS-XRF	0.01	0.033	0.75-1.63	0.24-0.41
Al2O3 (wt.%)	FUS-XRF	0.01	0.033	≤ 3.4	0.27-2.93
Fe2O3(t) (wt.%)	FUS-XRF	0.01	0.033	0.39-2.65	≤ 1.34
FeO (wt.%)	TITR	0.1	0.33	0.19-25.87	≤ 5.89
MnO (wt.%)	FUS-XRF	0.001	0.0033	≤ 16.67*	≤ 2.32
MgO (wt.%)	FUS-XRF	0.01	0.033	≤ 4.84	≤ 1.55
CaO (wt.%)	FUS-XRF	0.01	0.033	0.75-10	0.22-3.16
Na2O (wt.%)	FUS-XRF	0.01	0.033	1.1-56.25*	0.45-3.16
K2O (wt.%)	FUS-XRF	0.01	0.033	≤ 33.33*	≤ 1.63
TiO2 (wt.%)	FUS-XRF	0.01	0.033	≤ 28.57*	≤ 1.08
P2O5 (wt.%)	FUS-XRF	0.01	0.033	0.9-42.86*	≤ 17.68 *
Cr2O3 (wt.%)	FUS-XRF	0.01	0.033	n.d.	≤ 28.28 *
V2O5 (wt.%)	FUS-XRF	0.003	0.0099	~ 4.17	1.75-6.43
LOI (wt.%)	FUS-XRF				
CO2 (wt.%)	IR	0.01	0.033	≤ 8.29	≤ 12.48
Total S (wt.%)	IR	0.01	0.033	≤ 8.82	≤ 3.63
La (ppm)	FUS-MS	0.05	0.165	0.28-10	0.26-6.39
Ce (ppm)	FUS-MS	0.05	0.165	2.07-7.37	≤ 7.59
Pr (ppm)	FUS-MS	0.01	0.033	4.56-8.06	0.24-10.35*
Nd (ppm)	FUS-MS	0.05	0.165	2.31-9.81	0.84-7.73
Sm (ppm)	FUS-MS	0.01	0.033	1.21-7	0.2-8.32
Eu (ppm)	FUS-MS	0.005	0.0165	4.91-8.67	≤ 12.86
Gd (ppm)	FUS-MS	0.01	0.033	1.33-7.5	0.52-6.73
Tb (ppm)	FUS-MS	0.01	0.033	0.3-16	≤ 4.88
Dy (ppm)	FUS-MS	0.01	0.033	0.55-7.33	0.5-12.12
Ho (ppm)	FUS-MS	0.01	0.033	0.83-6.67	≤ 20.20*
Er (ppm)	FUS-MS	0.01	0.033	0.1-7.38	≤ 14.14
Tm (ppm)	FUS-MS	0.005	0.0165	2.6-7.19	≤ 10.10*
Yb (ppm)	FUS-MS	0.01	0.033	0.22-5.37	0.88-8.32*
Lu (ppm)	FUS-MS	0.002	0.0066	1.17-8.85	≤ 8.25
Ba (ppm)	FUS-ICP	3	9.9	7.5-8.79	≤ 2.23
Be (ppm)	FUS-ICP	1	3.3	n.a.	n.a.
Cr (ppm)	FUS-MS	20	66	≤ 2.7	≤ 3.82
Cs (ppm)	FUS-MS	0.1	0.33	≤ 9.09	≤ 5.66
Ga (ppm)	FUS-MS	1	3.3	≤ 6.25	≤ 4.88
Ge (ppm)	FUS-MS	0.5	1.65	≤ 90*	≤ 9.87
Hf (ppm)	FUS-MS	0.1	0.33	≤ 7.69	≤ 9.43
In (ppm)	FUS-MS	0.1	0.33	0	BDL

Appendix 4-B. Calculated precision and accuracy of whole rock geochemical data (cont'd)

	Method 2013	LOD 2013	LOQ 2013 [1]	Accuracy 2013 (%RD)	Precision 2013 (%RSD)
Nb (ppm)	FUS-MS	0.2	0.66	0	1.32-23.57*
Rb (ppm)	FUS-MS	1	3.3	0.8-8.97	≤ 2.57
Sb (ppm)	FUS-MS	0.2	0.66	≤ 4.17	≤ 8.11
Sc (ppm)	FUS-ICP	1	3.3	n.a.	n.a.
Sn (ppm)	FUS-MS	1	3.3	33.33*	BDL
Sr (ppm)	FUS-ICP	2	6.6	1.82-6.32	0.39-4.29
Ta (ppm)	FUS-MS	0.01	0.033	4.15-6	≤ 6.43
Th (ppm)	FUS-MS	0.05	0.165	0.78-11.67	≤ 10.57
Tl (ppm)	FUS-MS	0.05	0.165	≤ 60	1.59-21.43*
U (ppm)	FUS-MS	0.01	0.033	≤ 6.96	≤ 20.20*
V (ppm)	FUS-ICP	5	16.5	0.68-3.87	0.56-3.75
W (ppm)	FUS-MS	0.5	1.65	≤ 3.44	≤ 38.16
Y (ppm)	FUS-MS	0.5	1.65	0.63-8.33	≤ 1.18
Zr (ppm)	FUS-MS	1	3.3	2.13-9.55	≤ 10.52
Cd (ppm)	TD-MS	0.2	0.66	≤ 24.24	≤ 20.20*
Co (ppm)	TD-MS	0.5	1.65	≤ 2.8	≤ 5.66
Cu (ppm)	TD-MS	0.5	1.65	1.81-20.15	0.73-12.86
Li (ppm)	TD-MS	1	3.3	5.88-27.74	≤ 7.07
Ni (ppm)	TD-MS	1	3.3	2.38-13.36	≤ 2.67
Mn (ppm)	TD-MS	2	6.6	1.94-17.24	0.39-3.4
Mo (ppm)	TD-MS	1	3.3	≤ 54.2	≤ 47.14*
Pb (ppm)	TD-MS	2	6.6	3.85-16.19	0
Zn (ppm)	TD-MS	0.5	1.65	0.29-11.86	1.11-14.14
Bi (ppm)	AR-MS	0.02	0.066	0.53-44.83	≤ 28.28*
Te (ppm)	AR-MS	0.02	0.066	0.77-46.88	BDL
Se (ppm)	AR-MS	0.1	0.33	10.84-207.69*	≤ 60.61*
Au (ppb)	FA-AA	5	16.5	≤ 10.34	≤ 17.68*
Au (g/t)	FA-GRA	0.03	0.099	≤ 16.67	11.54
Ag (ppm)	FUS-MS	0.5	1.65	1.8-3.7	6.73-28.28*
Ag (g/t)	FA-GRA	3	9.9	0.79-8.73	0
As (ppm)	AR-MS	0.1	0.33	0.23-37.76	≤ 18.61
As (wt.%)	FUS-Na2O	0.01	0.033	0.87-6.32	n.d.

Appendix 4-B. Calculated precision and accuracy of whole rock geochemical data (cont'd)

	Method 2014	LOD 2014	LOQ 2014	Accuracy 2014 (%RD)	Precision 2014 (%RSD)
SiO2 (wt. %)	XRF-M01	0.04	0.132	0.18-0.48	0.31
Al2O3 (wt. %)	XRF-M01	0.02	0.066	0.29-1.38	0.37
Fe2O3(t) (wt. %)	XRF-M01	0.01	0.033	0.6-1.43	0.3
MnO (wt. %)	XRF-M01	0.002	0.0066	1.59-3.33	1.89
MgO (wt. %)	XRF-M01	0.01	0.033	0.88-1.68	0.21
CaO (wt. %)	XRF-M01	0.006	0.0198	0.08-0.11	0.15
Na2O (wt. %)	XRF-M01	0.02	0.066	1.13-50*	0.24
K2O (wt. %)	XRF-M01	0.01	0.033	0-0.74	0.78
TiO2 (wt. %)	XRF-M01	0.01	0.033	0	0
P2O5 (wt. %)	XRF-M01	0.002	0.0066	1.56-87.5*	1.33
Cr2O3 (wt. %)	XRF-M01	0.002	0.0066	1.14-60.68*	0
V2O5 (wt.%)		n.a.	-	n.a.	n.a.
LOI (wt.%)	XRF-M01	0.05	0.165	0.08-2.24	1.78
CO2 (wt.%)	IRC-100	0.023	0.0759	n.d.	4.56-5.79
Total S (wt.%)	IRC-100	0.003	0.0099	n.d.	≤ 0.92
La (ppm)	IMC-100	0.1	0.33	1.11-3	3.03
Ce (ppm)	IMC-100	0.12	0.396	0.46-6.44	3.04
Pr (ppm)	IMC-100	0.014	0.0462	1.16-2.93	2.87
Nd (ppm)	IMC-100	0.06	0.198	2.70-4.23	3.52
Sm (ppm)	IMC-100	0.026	0.0858	1.39-3.63	2.08
Eu (ppm)	IMC-100	0.0031	0.01023	0.11-2.71	2.89
Gd (ppm)	IMC-100	0.009	0.0297	0.61-0.64	2.76
Tb (ppm)	IMC-100	0.0023	0.00759	2.22-4.4	1.69
Dy (ppm)	IMC-100	0.009	0.0297	0.17-0.56	1.4
Ho (ppm)	IMC-100	0.0025	0.00825	5.34-5.39	0.29
Er (ppm)	IMC-100	0.007	0.0231	2.9-5.87	1.94
Tm (ppm)	IMC-100	0.0019	0.00627	2.81-4.88	1.59
Yb (ppm)	IMC-100	0.009	0.0297	2.92-6.12	3.34
Lu (ppm)	IMC-100	0.002	0.0066	3.48-3.81	3.7
Ba (ppm)	IMC-100	0.8	2.64	0.82-3.66	13.37
Be (ppm)	IMC-100	0.04	0.132	14.35-17.54	4.17
Cr (ppm)	IMC-100	3	9.9	≤ 6.19	0.69
Cs (ppm)	IMC-100	0.013	0.0429	4.57-9.77	2.47
Ga (ppm)	IMC-100	0.04	0.132	1.9-3.91	0.59
Ge (ppm)	FUS-MS	n.a.	n.a.	n.d.	n.d.
Hf (ppm)	IMC-100	0.14	0.462	0-6.1	1.93
In (ppm)	IMC-100	0.0018	0.00594	n.d.	n.d.

Appendix 4-B. Calculated precision and accuracy of whole rock geochemical data (cont'd)

	Method 2014	LOD 2014	LOQ 2014	Accuracy 2014 (%RD)	Precision 2014 (%RSD)
Nb (ppm)	IMC-100	0.028	0.0924	10.53-21.87	0.31
Rb (ppm)	IMC-100	0.11	0.363	6.34-8.04	23.21
Sb (ppm)	IMC-100	0.04	0.132	6.34-8.04	1.29
Sc (ppm)	IMC-100	1.1	3.63	5.38-5.72	4.08
Sn (ppm)	IMC-100	0.16	0.528	10.87-15.07	5.32
Sr (ppm)	IMC-100	0.6	1.98	3.8-6.5	0.28
Ta (ppm)	IMC-100	0.007	0.0231	21.93-26.74	1.11
Th (ppm)	IMC-100	0.018	0.0594	0.8-4.44	3.85
Tl (ppm)	IMC-100	0.002	0.0066	1.11-23.53	0.22
U (ppm)	IMC-100	0.011	0.0363	1.72-3.94	2.81
V (ppm)	IMC-100	0.8	2.64	5.43-6.92	0.48
W (ppm)	IMC-100	0.05	0.165	12.5	1.62
Y (ppm)	IMC-100	0.05	0.165	3.75-9.25	3.05
Zr (ppm)	IMC-100	6	19.8	1.7-2.17	1.13
Cd (ppm)	IMC-100	0.013	0.0429	46.99	1.79
Co (ppm)	IMC-100	0.13	0.429	3.5-3.73	0.55
Cu (ppm)	IMC-100	1.4	4.62	2.75-3.21	0
Li (ppm)	IMC-100	0.4	1.32	19.09-22.13	3.74
Ni (ppm)	IMC-100	0.7	2.31	2.63-5.73	1.7
Mn (ppm)	n.a.	n.a.	n.a.	n.a.	n.a.
Mo (ppm)	IMC-100	0.08	0.264	18.81	1.04
Pb (ppm)	IMC-100	0.18	0.594	≤6.75	1.4
Zn (ppm)	IMC-100	1.8	5.94	1.89-3.49	0
Bi (ppm)	IML-100	0.01	0.033	1.03	0
Te (ppm)	IML-100	0.01	0.033	4.72	0
Se (ppm)	IML-100	0.4	1.32	2.95	BDL
Au (ppm)	IML-100	0.002	0.0066	26.09*	15.71
Ag (ppm)	IML-100	0.01	0.033	3.26	20.2
As (ppm)	IML-100	0.8	2.64	0.13	3.2

Appendix 4-B. Calculated precision and accuracy of whole rock geochemical data (cont'd)

	Method 2016	LOD 2016	LOQ 2016 [1]	Accuracy 2016 (%RD)	Precision 2016 (%RSD)
SiO2 (wt.%)	FUS-XRF	0.01	0.033	0.78-1.18	0.23
Al2O3 (wt.%)	FUS-XRF	0.01	0.033	0.15-1.22	0.41
Fe2O3(t) (wt.%)	FUS-XRF	0.01	0.033	0.39-3.1	0.39
FeO (wt.%)	TITR	0.1	0.33	~3.88	0.00
MnO (wt.%)	FUS-XRF	0.001	0.0033	1-1.72	0.00
MgO (wt.%)	FUS-XRF	0.01	0.033	≤ 1.1	0.33
CaO (wt.%)	FUS-XRF	0.01	0.033	1.35-5.88	0.73
Na2O (wt.%)	FUS-XRF	0.01	0.033	0.94-10	0.50
K2O (wt.%)	FUS-XRF	0.01	0.033	0.34-33.33*	0.87
TiO2 (wt.%)	FUS-XRF	0.01	0.033	≤ 3.45	2.18
P2O5 (wt.%)	FUS-XRF	0.01	0.033	≤ 42.86*	4.29
Cr2O3 (wt.%)	FUS-XRF	0.01	0.033	≤ 20	0.00
V2O5 (wt.%)	FUS-XRF	0.003	0.0099	≤ 16.67	38.57*
LOI (wt.%)	FUS-XRF			n.d.	0.91
CO2 (wt.%)	IR	0.01	0.033	≤ 4.81	2.44
Total S (wt.%)	n.a.	n.a.	n.a.	n.a.	n.a.
La (ppm)	FUS-MS	0.05	0.165	≤ 11.11	1.00
Ce (ppm)	FUS-MS	0.05	0.165	0.17-7.83	0.84
Pr (ppm)	FUS-MS	0.01	0.033	1.27-4.72	1.46
Nd (ppm)	FUS-MS	0.05	0.165	0.3-9.57	0.25
Sm (ppm)	FUS-MS	0.01	0.033	1.16-9.09	3.18
Eu (ppm)	FUS-MS	0.005	0.0165	2.16-6.95	0.00
Gd (ppm)	FUS-MS	0.01	0.033	5.33-5.41	0.77
Tb (ppm)	FUS-MS	0.01	0.033	≤ 7.51	2.18
Dy (ppm)	FUS-MS	0.01	0.033	2.16-6.56	1.37
Ho (ppm)	FUS-MS	0.01	0.033	0.83-6.58	0.00
Er (ppm)	FUS-MS	0.01	0.033	3.73-8.11	0.95
Tm (ppm)	FUS-MS	0.005	0.0165	0.43-7.52	1.37
Yb (ppm)	FUS-MS	0.01	0.033	≤ 9.4	0.00
Lu (ppm)	FUS-MS	0.002	0.0066	≤ 7.75	0.61
Ba (ppm)	FUS-MS	3	9.9	≤ 8.47	0.27
Be (ppm)	TD-MS	0.1	0.33	≤ 28.57	n.a.
Cr (ppm)	FUS-MS	20	66	3.45-11.11	0
Cs (ppm)	FUS-MS	0.1	0.33	1.44-4.35	1.05
Ga (ppm)	FUS-MS	1	3.3	≤ 6.67	4.29
Ge (ppm)	FUS-MS	0.5	1.65	4.46-50*	0.00
Hf (ppm)	FUS-MS	0.1	0.33	7.69-9.09	0.00
In (ppm)	FUS-MS	0.1	0.33	~ 15.38	BDL

Appendix 4-B. Calculated precision and accuracy of whole rock geochemical data (cont'd)

	Method 2016	LOD 2016	LOQ 2016 [1]	Accuracy 2016 (%RD)	Precision 2016 (%RSD)
Nb (ppm)	FUS-MS	0.2	0.66	≤ 3.29	3.39
Rb (ppm)	FUS-MS	1	3.3	≤ 4.35	1.40
Sb (ppm)	FUS-MS	0.2	0.66	3.23-6.25	~28.28*
Sc (ppm)	FUS-MS	n.a.	n.a.	n.a.	n.a.
Sn (ppm)	FUS-MS	1	3.3	~4.9	BDL
Sr (ppm)	FUS-MS	2	6.6	0.69-6.67	1.62
Ta (ppm)	FUS-MS	0.01	0.033	1.61-10	1.70
Th (ppm)	FUS-MS	0.05	0.165	≤ 9.7	0.55
Tl (ppm)	FUS-MS	0.05	0.165	8.33-65*	6.15
U (ppm)	FUS-MS	0.01	0.033	4.35-5.19	0.39
V (ppm)	FUS-MS	5	16.5	0.32-8.28	5.44
W (ppm)	FUS-MS	0.5	1.65	4.55-13.2*	BDL
Y (ppm)	FUS-MS	0.5	1.65	0.92-9.44	1.77
Zr (ppm)	FUS-MS	1	3.3	≤ 5.77	0.53
Cd (ppm)	TD-MS	0.1	0.33	≤ 53.49*	n.d.
Co (ppm)	TD-MS	0.1	0.33	5.48-13.77	n.d.
Cu (ppm)	TD-MS	0.2	0.66	0.9-14.83	n.d.
Li (ppm)	TD-MS	0.5	1.65	1.12-17.3	n.d.
Ni (ppm)	TD-MS	0.5	1.65	0.81-23.33	n.d.
Mn (ppm)	TD-MS	1	3.3	5.8-20.99	n.d.
Mo (ppm)	TD-MS	0.05	0.165	≤ 75.42	n.d.
Pb (ppm)	TD-MS	0.5	1.65	0.19-17.46	n.d.
Zn (ppm)	TD-MS	0.2	0.66	0.97-24.74	n.d.
Bi (ppm)	TD-MS	0.02	0.066	1.58-44.98	n.d.
Te (ppm)	TD-MS	0.1	0.33	~3.09	n.d.
Se (ppm)	TD-MS	0.1	0.33	19.64-68.09*	n.d.
Au (ppb)	n.a.	n.a.	n.a.	n.a.	n.a.
Au (g/t)	n.a.	n.a.	n.a.	n.a.	n.a.
Ag (ppm)	FUS-MS	0.5	1.65	~11.11	9.43*
Ag (g/t)	n.a.	n.a.	n.a.	n.a.	n.a.
As (ppm)	TD-MS	0.1	0.33	3.06-39.7	n.d.
As (wt.%)	n.a.	n.a.	n.a.	n.a.	n.a.

Limit of detection (LOD)
(1) Limit of quantification (LOQ)~3.3*LOD (after Piercey,2014 and references therein)

%RD: percent relative difference

%RSD: percent relative standard deviation

* the poor precision at concentrations below or near LOQ

BDL: below detection limit in each analyses

5. CHAPTER 5 - SUMMARY AND CONCLUDING REMARKS

The Beardmore-Geraldton greenstone belt is a Neoarchean, polydeformed, transitional zone along the boundary between the granite-greenstone eastern Wabigoon and the metasedimentary Quetico subprovinces of the Superior Province. The BGB produced over 4.1 Moz Au over the last century (Mason and McConnell, 1983; Mason and White, 1986). Renewed successful exploration in the Geraldton area outlined new resources of 6.4 Moz Au (G Mining Services, 2016), and highlighted the need for a better understanding of the geology of the BGB.

The three panels of metasedimentary rocks in the belt were sampled for detrital zircon geochronology. Analyses of over 300 detrital zircons indicate that the metasedimentary rocks of the BGB and the northern Quetico were derived from similar source rocks aged predominantly between 2690 Ma and 2900 Ma with a few older ages >3200 Ma. The detritus feeding this sedimentary succession was eroded predominantly from the eastern Wabigoon subprovince. The age of the sedimentation is bracketed between 2700 Ma, the age of the youngest detrital zircon population and 2694±1 Ma, the crystallization age of a feldspar-quartz porphyry (FQP) intrusion that intrudes the metasedimentary units. Granitoid intrusions in the belt vary in age from ca. 2694 Ma to ca. 2690 Ma and their geochemistry suggests that they formed at depths >50 km and evolved (transitioned?) from tonalite-trondhjemite-granodiorite suite to sanukitoid suite intrusions over a period of 4 Ma. This change in geochemical signature indicates an increasing mantle contribution to the melts which is consistent with a shift from subduction/subcretion to slab break-off/delamination.

The ductile deformation history of the BGB began with the formation of F_1 folds and S_1 cleavage during D_1 thrusting. The latter occurred after the emplacement of ca. 2694 Ma FQP dikes and before the emplacement of the stitching ca. 2690 Ma Croll Lake stock (Corfu, 2000). Auriferous quartz-carbonate veins surrounded by sericite-carbonate-pyrite alteration halos were emplaced during D_1 and

thus represent a hitherto unrecognized mineralization event in the belt. Following thrusting, bulk shortening oblique to the belt during a regional, sinistral, D_2 transpression event produced map-scale, east-striking, F_2 folds, the regional S_2 cleavage and L_2 stretching lineation, and sinistral high strain zones. Previously emplaced auriferous quartz-carbonate veins were strongly folded along one of these high strain zones, the Bankfield-Tombill deformation zone, which hosts several gold deposits including the Hardrock deposit. New auriferous quartz-carbonate and tourmaline-quartz veins were emplaced during this event and contributed to the enrichment in gold along the Bankfield-Tombill deformation zone. Renewed oblique bulk shortening during regional D_3 dextral transpression reactivated the D_2 high strain zones as dextral transcurrent shear zones and remobilized the mineralization along dextral shear bands. Pre-existing linear fabric elements, such as F_1, F_2, F_3 fold axes and the L_2 stretching lineation, were rotated towards the fabric attractor defined by the maximum principal pure shear strain rate of the transpression, resulting in the coaxial orientation of all linear structures in the belt. The orientation of the fabric attractor is oblique (~20°) to the shear direction indicating that D_3 dextral transpression has triclinic symmetry.

The Hardrock deposit is a world-class orogenic gold deposit with significant newly discovered resources that drove the need and interest to better understand the geology of the deposit. The gold is associated with several generations of strongly folded, and E- to NE-striking quartz-carbonate and tourmaline-rich veins suggesting that gold deposition spanned multiple deformation events. Gold mineralization was emplaced early during D_1 thrusting and D_2 sinistral transpression, and was remobilized during D_3 along fractures filled with sulfides. Thus, these results dispute previous studies which attributed the formation of the gold deposits to D_3 dextral transpression. Fluid-rock sulfidation reactions triggered gold deposition and the precipitation of inclusion-rich pyrite with elevated Ag, As, Bi, Co, Ni, Pb, Sb, Te concentrations. Beyond the narrow alteration halos surrounding the mineralized veins, a broader, up to 250 m wide, carbonate-sericite alteration envelope with elevated S, Te, As, W

and Bi pathfinder element concentrations encompasses the deposit. These elements can be used as vectors towards gold mineralization and as tools for the discovery of additional gold resources in the belt.

The geological assembly and evolution of the Beardmore-Geraldton belt are similar to other Archean greenstone belts that host major orogenic gold camps in the Superior and Yilgarn cratons. Similar to world-class orogenic gold camps, the BGB has: 1) metasedimentary rocks dominated by syn-tectonic fluvial and turbiditic sandstones that were deposited in a fault-bounded successor basin unconformably overlying an older mafic volcanic substrate; 2) TTG and sanukitoid intrusions that were emplaced shortly after sedimentation; 3) a polyphase deformation history characterized by early thrusting and folding (D_1) followed by D_2 sinistral transpression and D_3 dextral transpression; 4) the Hardrock gold deposit is localized along the multitude of secondary structures within the belt-bounding, crustal-scale Bankfield-Tombill deformation zone.

Future work and outstanding problems

The goal of this thesis was to better understand the evolution of the BGB, characterize its gold endowment, and determine the controls on gold mineralization at the Hardrock deposit. In Chapter 2, the results of a detrital zircon geochronological study are presented. Because of the large 2σ errors of the analyses, the maximum depositional ages of all units are similar. Better resolution of their maximum depositional age could be obtained by dating the youngest detrital zircons in each unit using a TIMS instrument. Chapter 4 revealed complex structural controls and relative timings on the emplacement of the gold mineralized veins. Monazite and rutile are present in the mineralized veins and should be dated to determine the absolute timing of the gold mineralizing events. Fluid inclusion studies combined with evaporate mound analyses would help to define the composition and P-T conditions of the gold-mineralizing hydrothermal fluids during each mineralizing event. Stable

oxygen, hydrogen and sulphur isotopic studies on the gold mineralized veins would better define the physico-chemical properties of the gold-mineralizing hydrothermal fluids, their source, and that of sulphur in associated gold-bearing sulfide minerals. Due to the small size of molybdenite grains in the gold mineralized veins, Re-Os dating of these grains was impossible. This has become possible due to improved analytical techniques (Lawley and Selby, 2012), and these techniques should be used to determine the absolute timing of the gold mineralizing events at the Hardrock deposit and other deposits in the BGB.

References

Corfu, F., 2000. Extraction of Pb with artificially too-old ages during stepwise dissolution experiments on Archean zircon. Lithos 53, 279–291.

G Mining Services, 2016. NI 43-101 Technical Report - Hardrock Project, Ontario, Canada. 509 p.

Lawley, C. J. M., & Selby, D. (2012). Re-os geochronology of quartz-enclosed ultrafine molybdenite: Implications for ore geochronology. Economic Geology, 107(7), 1499–1505. https://doi.org/10.2113/econgeo.107.7.1499

Mason, J.K., McConnell, C.D., 1983. Gold mineralization in the Beardmore-Geraldton area, In: Colvine, A.C. (Ed.), The Geology of Gold in Ontario, Ontario Geological Survey, Misc. Paper 110. pp. 84–97.

Mason, J.K., White, G., 1986. Gold occurrences, prospects and deposits of the Beardmore-Geraldton area, District of Thunder Bay and Cochrane. Ontario Geological Survey, Open File Report 5630. 680 p.

6. APPENDICES

Appendix 6-A. Lafrance, B., Tóth, Z., Dubé, B., and Mercier-Langevin, P., 2012. Targeted Geoscience Initiative 4. Lode Gold Deposits in Ancient Deformed and Metamorphosed Terranes: Geological Setting of Banded Iron Formation–Hosted Gold Mineralization in the Geraldton Area, Northern Ontario. Summary of Field Work and Other Activities 2012, Ontario Geological Survey, Open File Report 6280, p.48-1 to 48-10.

48. Targeted Geoscience Initiative 4. Lode Gold Deposits in Ancient Deformed and Metamorphosed Terranes: Geological Setting of Banded Iron Formation–Hosted Gold Mineralization in the Geraldton Area, Northern Ontario

B. Lafrance[1], Z. Tóth[1], B. Dubé[2] and P. Mercier-Langevin[2]

[1]Mineral Exploration Research Centre, Laurentian University, Sudbury, Ontario P3E 2C6
[2]Geological Survey of Canada, Québec, Québec G1K 9A9

INTRODUCTION

The characterization of banded iron formation (BIF)-hosted gold ore systems is one of the main themes of the Targeted Geoscience Initiative 4 (TGI-4) Lode Gold project of the Geological Survey of Canada (Dubé et al. 2011). The main goals of the project are to 1) improve knowledge of the geological settings and footprints of selected gold deposits or districts in mature and emerging camps; 2) provide key descriptive and genetic parameters and improved geological and exploration models; 3) develop more robust exploration vectors and means to help identify fertile mineral systems; and 4) train and mentor students in order to increase the number of highly qualified personnel. The Geraldton area was selected as 1 of 4 areas to study BIF-hosted ore systems because of excellent descriptions of its deposits by Pye (1952), Horwood and Pye (1955) and Macdonald (1988), easy accessibility to large stripped outcrops exposing the ore-hosting structures and iron formation, and availability of new exploration data and drill cores across the main deposits and ore zones in the area. This project is carried out in collaboration with the Ontario Geological Survey and Premier Gold Mines Limited.

The project began this past summer with detailed mapping of 2 large stripped outcrops and sampling of drill cores along 2 sections across the 2 main ore zones (F zone and North zone) of the Hardrock–MacLeod–Cockshutt deposit. The preliminary results of the mapping are presented in this report.

BACKGROUND

The Geraldton area is located east of Lake Nipigon in the eastern part of the Beardmore–Geraldton belt along the southern margin of the Wabigoon Subprovince of the Archean Superior Province (Figure 48.1). The Beardmore–Geraldton belt comprises 3 metasedimentary rock panels (southern, central and northern sedimentary units) that are fault bounded and interleaved with 3 volcanic rock panels (southern, central and northern volcanic units). The southern volcanic unit has mid-ocean ridge basalt geochemical affinity and it represents ocean floor crust that formed south of an oceanic island arc (central volcanic unit) and back-arc basin (northern volcanic unit) (Tomlinson et al. 1996). A felsic flow and a synvolcanic dike in the central and northern volcanic units, respectively, have U/Pb zircon crystallization ages of 2724.9±1.2 Ma (Hart, ter Meer and Jolette 2002). Thus, at 2725 Ma, these 2 volcanic units stood as an island-arc and back-arc system outboard and south of the Wabigoon Subprovince. The 3 volcanic units collided and were accreted to the southern margin of the Wabigoon Subprovince prior to the deposition of the sedimentary units at *circa* 2696 Ma to *circa* 2691 Ma (Lafrance, DeWolfe and Stott 2004). From

Summary of Field Work and Other Activities 2012,
Ontario Geological Survey, Open File Report 6280, p.48-1 to 48-10.

north to south, the sedimentary units record progressively deeper depositional environments. They were emplaced unconformably above the volcanic units as fluvial to alluvial fan deposits (northern sedimentary unit), deltaic to subaqueous fan deposits (central sedimentary unit), and deeper water turbidite deposits (southern sedimentary unit) (Devaney and Williams 1989). They represent a southward-prograding clastic wedge that was fed by the erosion of the uplifted Wabigoon Subprovince (Devaney and Williams 1989).

Thrust imbrications of the volcanic and sedimentary units began shortly after deposition of the sedimentary units during an early D_1 deformation event (Devaney and Williams 1989; Lafrance, DeWolfe and Stott 2004). Rare isoclinal F_1 folds are the only manifestation of the D_1 event as structural contacts and possible thrust faults between volcanic and sedimentary units were later reactivated as transcurrent shear zones. During D_2 north-south compression, the southern sedimentary unit was regionally folded into tight to isoclinal, east-striking, F_2 folds with an axial planar S_2 cleavage (Lafrance, DeWolfe and Stott 2004). The S_2 cleavage is oriented at high angle to bedding in F_2 fold hinges and is generally parallel to bedding along the limbs of the folds. The S_2 foliation is expressed by the flattening of clasts and pillows in the volcanic units and by a bedding-parallel cleavage in the central and northern sedimentary units. Late, regional, D_3 dextral transpression produced most penetrative structures in the belt. During the D_3 event, F_2 and S_2 were folded by outcrop- to map-scale, west-plunging, Z-shaped F_3 folds. The D_2 structures were overprinted by a regional S_3 cleavage oriented anticlockwise to bedding, and they were transected by east-trending, dextral, transcurrent D_3 shear zones (Lafrance, DeWolfe and Stott 2004). The

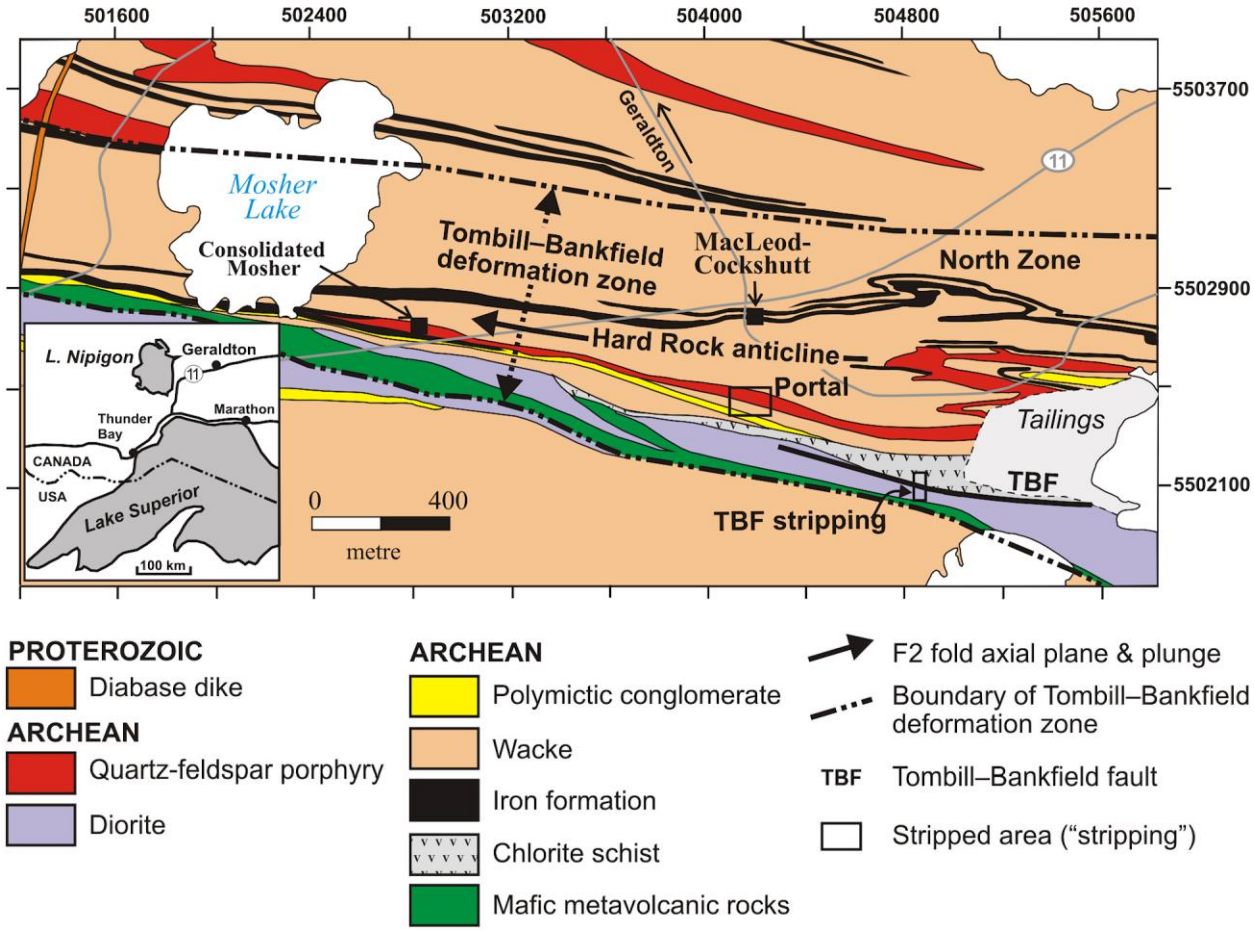

Figure 48.1. Simplified geological map of the Geraldton area (*after* Horwood and Pye (1955) and Pye (1952) with modifications by authors). "Portal" indicates area named Portal stripping. UTM co-ordinates are based on North American Datum 1927 (NAD27), Zone 16. Inset map shows the location of Geraldton.

F_3 folds and S_3 cleavage are, in turn, overprinted by Z-shaped F_3' folds and associated S_3' cleavage, which formed during the same progressive D_3 deformation event (Lafrance, DeWolfe and Stott 2004). Felsic porphyry dikes and sills with a U/Pb crystallization age of 2691 $^{+3}/_{-2}$ Ma (Anglin 1987; Anglin et al. 1987) are folded by F_2 and overprinted by S_3, providing a maximum deformation age of *circa* 2691 Ma for both the D_2 and D_3 events.

All past-producing gold mines in the Geraldton area (e.g., Little Long Lac, Hardrock, MacLeod–Cockshutt, Consolidated Mosher, Magnet, Bankfield) are in the southern sedimentary unit. Most ore zones are hosted in a 1 km wide high-strain zone, called the Tombill–Bankfield deformation zone (*see* Figure 48.1), located close to the contact between the southern sedimentary unit and the Quetico Subprovince sedimentary rocks to the south (Lafrance, DeWolfe and Stott 2004). A discrete brecciated fault zone known as the Tombill–Bankfield fault, occurs within the wider, more ductile, deformation zone. The deposits hosted by the deformation zone collectively produced 2.36 million ounces of gold (Mason and White 1986). Gold occurs in sulphide-rich replacement lenses and quartz-carbonate veins in the hinge of F_2 and F_3 folded iron formation (e.g., North zone). It also occurs in quartz veins and associated sericitic selvages in folded porphyry bodies and in wacke near or at the contact with porphyry (e.g., F zone) (Horwood and Pye 1955). It is further found in quartz stringer zones within wacke and diorite (Horwood and Pye 1955). Gold mineralization is interpreted to be syn-D_3 and to have been emplaced in faults, shear zones and fractures that formed along sheared contacts and across the hinge of F_2 and F_3 folds (Anglin 1987; Macdonald 1988; Lafrance, DeWolfe and Stott 2004). A stripped outcrop exposing the Tombill–Bankfield fault, and a second larger stripped outcrop, informally named the Portal stripping, showing excellent overprinting relationships between structures and mineralization along the Tombill–Bankfield deformation zone, provide new key information and were mapped in detail. They are described below.

PORTAL STRIPPING

The Portal stripping is a 60 by 90 m stripped outcrop located along the south limb of the Hard Rock anticline, 300 m south of the MacLeod–Cockshutt headframe (*see* Figure 48.1). A feldspar porphyry body takes up more than half of the outcrop (Figure 48.2). It is pinkish white on outcrop surface, pinkish grey on fresh surface, and it consists of 40 volume % feldspar phenocryst (1 to 4 mm in size) and 10 volume % quartz phenocryst (1 to 1.5 mm in size) within a fine-grained homogeneous matrix. It contains rare xenoliths of iron formation and altered mafic rock, and it is in intrusive contact with surrounding wacke, iron formation and green mudstone. The wacke is greenish grey on outcrop and fresh surfaces, and it consists of sandstone beds (≤15 cm thick) interlayered with mudstone beds (<1 to 3 cm thick). Excellent, normal grading, top indicators are observed in the sandstone beds. Iron formation consists of up to 20 cm thick, finely laminated, black cherty magnetite beds, interspersed within thickly bedded (≤25 cm) wacke similar to that described above. Iron formation beds, millimetres to 2.5 cm thick, are further associated with laminated to thinly bedded (0.5 to 2.5 cm) mudstone, varying in colour from dark greenish grey on fresh and outcrop surfaces to dark green on outcrop surface. A polymictic pebbly sandstone or conglomerate occupies the southern part of the outcrop. It is brownish light grey to dark grey on outcrop and fresh surfaces, respectively, and it contains strongly deformed, elongate clasts of mafic to intermediate volcanic rocks and sandstone, as well as more spherical clasts of granitic composition. The percentage of clasts is difficult to estimate due to the strong deformation and gradational contacts between clasts and the sandy matrix. Another porphyry, which contains more quartz (10 to 15 volume %) and less feldspar (30 volume %) phenocrysts than the main feldspar porphyry, was emplaced into the green mudstone and wacke with iron formation beds. Numerous, greenish grey to dark brown, gabbroic to ultramafic dikes are roughly parallel to bedding in all rock types. The dikes vary in thickness from a few centimetres up to 2 m. They are strongly chloritic, commonly iron carbonatized and they contain elongate white streaks of carbonatized feldspar(?).

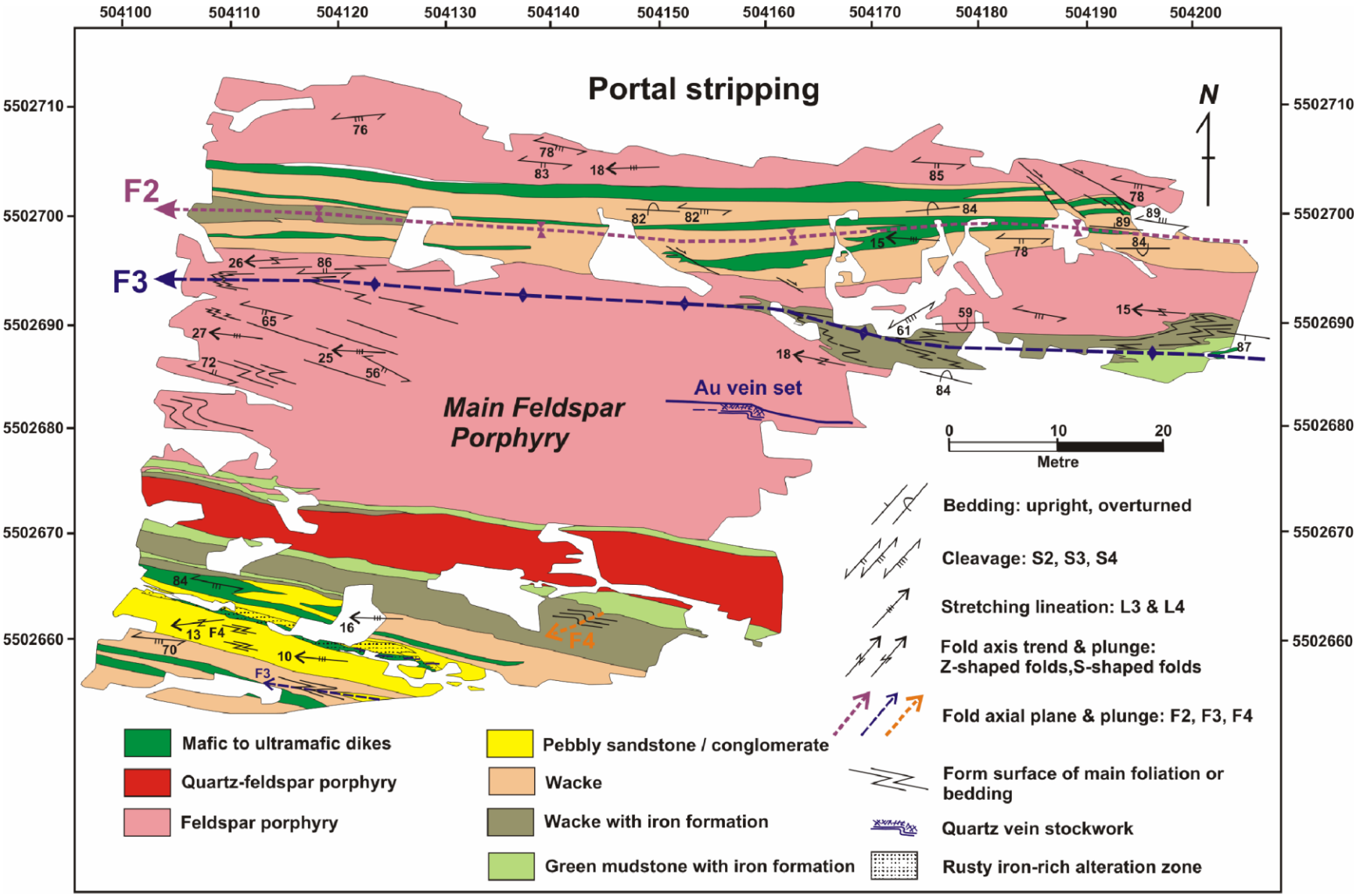

Figure 48.2. Geological map of the Portal stripping. Location of the map is shown in Figure 48.1. UTM co-ordinates provided using North American Datum 1983 (NAD83), Zone 16.

The Portal stripping displays excellent structural overprinting relationships: ductile structures observed on outcrop can be ascribed to 3 generations of structures. The oldest generation of structures is represented by an isoclinal synform that occupies the entire width of the wacke panel north of the main feldspar porphyry body (*see* Figure 48.2). The synform is defined by folded bedding-parallel mafic dikes and by folded sandstone beds that young away from the core of the fold (Photo 48.1A). The synform youngs downward; thus, it has the younging characteristic of a downward-facing synform or synformal anticline. It has a subvertical, west-striking, penetrative axial plane cleavage, and a shallowly (15 to 20°), west-plunging, fold axis. The latter is parallel to a strong mineral stretching lineation defined by stretched amygdules and discontinuous dark green chlorite and white carbonatized feldspar in mafic dikes. The cleavage is parallel to the contact between the wacke and the main feldspar porphyry, where it is expressed as a strong sericitic foliation that is penetrative throughout the porphyry. Because early F_1 folds in Geraldton typically lack an axial plane cleavage and because S_2 is the oldest cleavage observed in folded porphyry in the hinge of the F_2 Hard Rock anticline (Lafrance, DeWolfe and Stott 2004), the downward-facing synform and its axial plane cleavage are interpreted as F_2 and S_2 structures that formed during D_2 north-south shortening across the belt. The synform is overprinted by a cleavage (S_3) oriented clockwise to bedding on both limbs of the fold (*see* Figure 48.2). The S_3 cleavage is a differentiated cleavage defined by chloritic and sericitic foliation planes alternating with 1 to 2 mm wide white felsic microlithons. It is axial planar to S-shaped F_3 folds in the wacke north of the main porphyry (Photo 48.1B and 48.1C). In the porphyry, where the penetrative sericitic S_2 cleavage is folded by F_3 folds, the S_3 cleavage forms a composite S_2–S_3 fabric expressed by the intensification and decreased spacing of the S_2 cleavage planes along the long limbs of asymmetrical F_3 folds (Photo 48.1D). From north to south across the main porphyry body, the asymmetry of the F_3 folds changes from S-shaped to M-shaped to Z-shaped and, thus, the porphyry is folded by a large F_3 fold that has a thin north limb and a thick south limb (*see* Figure 48.2). The attitude of F_3 folds is similar to that of F_2 folds. Their axial plane is steep and west striking, and they plunge shallowly to the west (~20°) parallel to a strong stretching lineation represented by rods of presumably recrystallized quartz and feldspar aggregates in the porphyry.

A small, parasitic, F_3 fold on the north limb of the folded porphyry is overprinted by a cleavage (S_4), striking 240 to 250° and dipping 80° to the north. The S_4 cleavage is oriented anticlockwise to bedding and is axial planar to local asymmetrical Z-shaped F_4 folds overprinting the S_3 cleavage. The folds are, in turn, overprinted by steeply dipping dextral shear bands striking approximately 115° to 125°. The orientation of the shear bands is similar to that of dextral shear fractures shown in Figure 48.2. Shear bands are observed across the main porphyry and wacke, but they become more abundant south of the main porphyry where they form a penetrative dextral slip cleavage (Photo 48.1E). A bedding- and contact-parallel, composite S_2–S_3 foliation is present in all rock types south of the main porphyry. A shallowly west-plunging stretching lineation, which is defined by rod-like elongate pebbles in conglomerate, lies along the composite foliation plane. The intersection lineation between the dextral shear bands and composite S_2–S_3 foliation is roughly perpendicular to the shallowly plunging stretching lineation, which is consistent with the formation of these structures during dextral transcurrent shear. On horizontal surface, strong granitic pebbles are surrounded by dextral asymmetrical strain shadows. The clasts locally contain northwest-southeast oriented, steeply dipping, extensional quartz veinlets and weak elongate volcanic clasts are folded by Z-shaped F_4 folds, further suggesting dextral transcurrent shear (Photo 48.1F). Although these structures occur throughout the Portal stripping, they are more abundant or pronounced in the southern part of the stripping where dextral transcurrent shear was more intense. The F_4 folds and S_4 cleavage correspond to the F_3' folds and S_3' cleavage of Lafrance, DeWolfe and Stott (2004), which are interpreted as late structures that formed during a progressive D_3 dextral transpressional event that began with the formation of F_3 folds, a regional S_3cleavage, and dextral transcurrent shear zones.

A set of milky fault-fill white quartz veins with minor ankerite yielded high gold values (Premier Gold Mines Ltd. staff, personal communication, 2012). The veins were emplaced in the main porphyry body on the south limb of the large F_3 fold (*see* Figure 48.2). The veins strike east (100°), dip south (60°)

Photo 48.1. Field photographs of the Portal stripping. A) Downward-facing synformal F_2 fold. A mafic dike occupies the hinge of the fold. Blue arrows indicate younging direction in wacke. Camera casing, 15 cm in length, for scale. B) S-shaped F_3 fold defined by folded wacke and mafic dikes, north of the main feldspar porphyry body. Photo scale is 9 cm in length. C) Close-up of F_3 fold hinge shown in Photo 48.1B. S_2 cleavage in wacke is folded by F_3. Coin (18 mm diameter) for scale. D) S_2 cleavage folded by S-shaped F_3 folds along the northern margin of the main feldspar porphyry body. S_3 cleavage is defined by the intensification of S_2 along the long limb of the folds. Coin (20 mm diameter) for scale. E) Penetrative dextral shear bands indicating dextral transcurrent movement, south of the main feldspar porphyry body. Coin (19 mm diameter) for scale. F) Dextral shear bands and dextral asymmetrical strain shadow around granitic clast in conglomerate. Coin (19 mm diameter) for scale. G) Mineralized quartz vein stockwork in the main feldspar porphyry body. Photo scale is 9 cm in length.

and are up to 10 cm thick. They are associated with a stockwork of smaller quartz veins and surrounded by silicified porphyry containing minor pyrite (Photo 48.1G). The quartz veins are folded by a Z-shaped F_3 fold that is parasitic to the large F_3 fold, and they are transposed and locally boudinaged suggesting either early- or pre-D_3 emplacement of the gold-bearing veins.

TOMBILL–BANKFIELD FAULT STRIPPING

The Tombill–Bankfield fault is described as a zone of intense shearing, brecciation, silicification and carbonatization (Pye 1952; Horwood and Pye 1955). It was thought to be a major break that influenced the location of most deposits in Geraldton (Pye 1952). This recently led Premier Gold Mines Ltd. to excavate 3 to 4 m of overburden to expose bedrock where a drill hole intersected black smoky quartz veins along the trace of the fault. This new stripping is the best known exposure of the fault at surface, but it will be reburied during the coming year.

The fault occurs at the contact between diorite to the south and sandstone to the north (Figure 48.3). The sandstone is interleaved with diorite, mafic pillowed flows and a fine-grained, synvolcanic, mafic dike. Diorite is greenish dark grey on outcrop and fresh surfaces. It consists of approximately 45% chloritized green amphibole, up to 1 cm in size, surrounded by greenish white feldspar. Epidote-quartz-amphibole patches and veins occur throughout the rock and are cut by late quartz-iron carbonate veins. Local tourmaline-rich quartz veins and breccias are present. Sandstone varies in colour and composition from a more sericitic, greenish light grey rock with bed thicknesses of 2 to 10 cm and grain size of 1 to 2 mm, to a more chloritic, brownish dark grey, interlayered sandstone–mudstone with bed thicknesses of 2 to 5 cm. Mafic pillowed flow consists of dark green, aphyric pillows with thin (~1 cm thick) selvages (Photo 48.2A). The synvolcanic dike is dark green, aphyric and massive. It is in sharp contact with the diorite and mafic pillowed flow. The mafic pillowed flow and synvolcanic dike are cut by multiple epidote-quartz veins that are, in turn, transected by quartz-iron carbonate-tourmaline veins.

The diorite has a strong differentiated foliation (S_2) defined by feldspar-rich felsic bands, alternating with amphibole-rich mafic bands (average thickness of 3 to 5 mm). The S_2 foliation strikes east (~100°) and dips steeply (70 to 85°) to the south. It is folded by Z-shaped F_3 folds associated with an axial plane S_3 cleavage defined by chlorite. The S_3 cleavage is oriented anticlockwise to the S_2 foliation; it strikes east-northeast (70 to 85°) and dips steeply (70 to 85°) to the south. The S_3cleavage becomes more intense and closely spaced in narrow shear zones (<50 cm thick) surrounding less deformed, metre wide, lozenges of diorite. The shear zones contain a shallowly west-plunging (~15°), chloritic, mineral lineation, similar in orientation to F_3 fold axes. Dextral shear bands, striking approximately 120° or approximately 300° and dipping steeply (80 to 85°) to the south or north, and Z-shaped drag folds defined by folded quartz-iron carbonate veins, are present along most shear zones, suggesting dextral transcurrent shear. Pillows in the mafic pillowed flow are flattened parallel to the S_2 foliation. The strain appears to increase in intensity within sandstone and mudstone where the S_2 foliation is oriented parallel to bedding and the S_3 cleavage is oriented anticlockwise to the S_2 foliation as observed in the diorite. Similar dextral shear sense indicators, that is, shear bands and drag folds, are developed in sheared sandstone–mudstone and mafic pillowed flows, but, in addition, spectacular dextral asymmetrical strain shadows are present around pillow fragments (Photo 48.2B).

Black smoky fault-fill quartz veins occur along the fault. The fault is parallel to S_2 and so it formed either during or after the D_2 deformation event. The veins are individually 1 to 15 cm thick and collectively approximately 1 m thick, and they strike 90 to 105° and dip 75 to 85°S parallel to the fault. They are cut by multiple, millimetre-thick, milky white, quartz veins, filling fractures that are perpendicular to the margins of the black smoky quartz veins and that span the width of those veins. A 1.5 m thick, bleached (light grey), alteration halo surrounds the black smoky quartz veins. The veins were broken up and brecciated (Photo 48.2C), and an anticlockwise S_3 cleavage formed in the alteration halo,

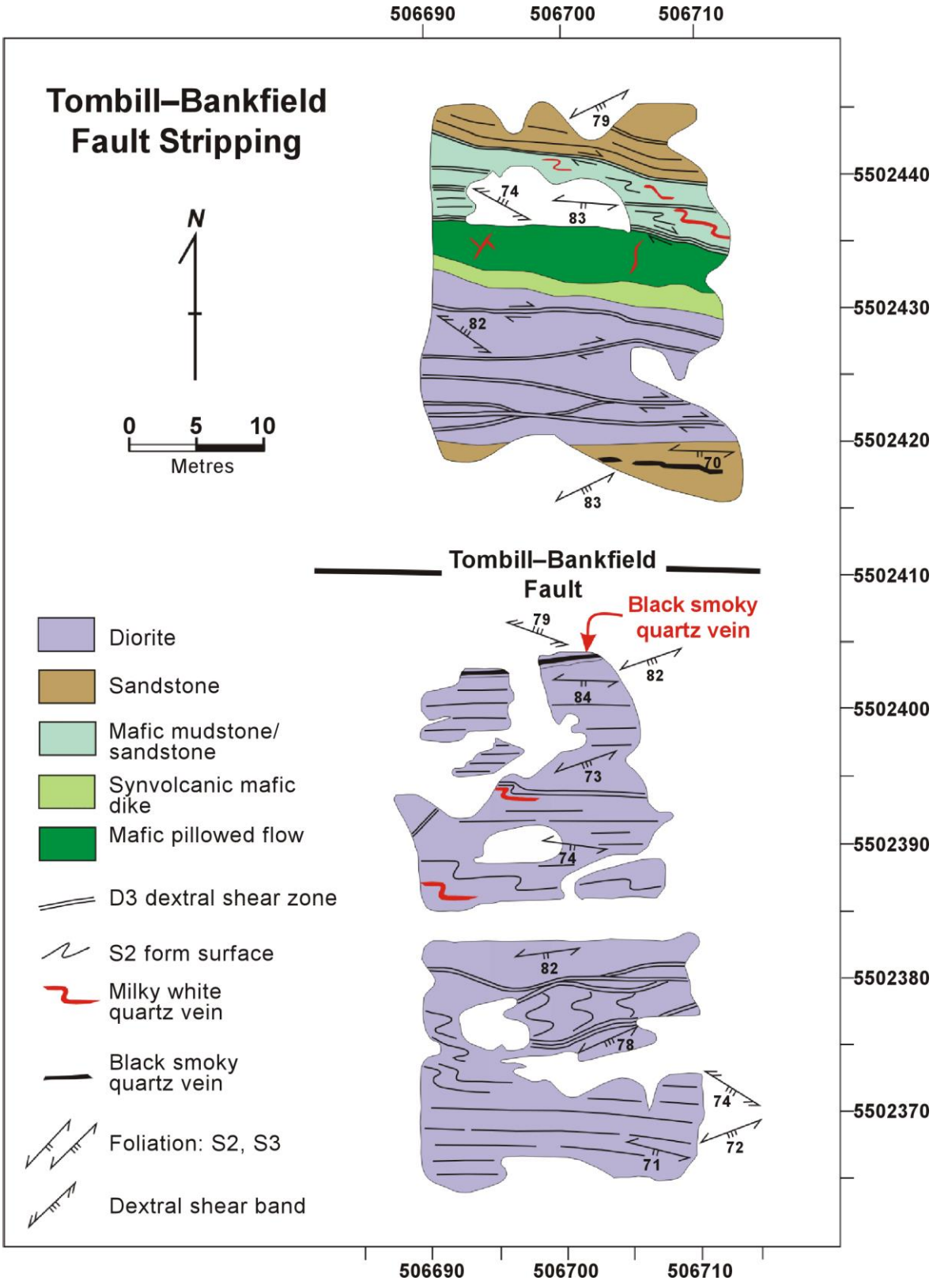

Figure 48.3. Geological map of the Tombill–Bankfield fault stripping. Location of the map is shown in Figure 48.1. UTM co-ordinates provided using NAD83, Zone 16.

during D_3 dextral shear reactivation of the fault. Pyrite and chalcopyrite(?) occupy dextral shear bands that have a strike of 125 to 140° and a dip of approximately 70° to the south (Photo 48.2D), similar to the orientation of shear bands associated with narrow dextral shear zones north and south of the fault. Thus, the smoky quartz veins were emplaced either during D_2 deformation or early during D_3 dextral shear, and sulphide mineralization was remobilized into shear bands during D_3 dextral shear. Grab samples of the veins yielded low gold values, so no further work is planned for this stripping and fault (Premier Gold Mines Ltd. staff, personal communication, 2012).

CONCLUSIONS

The Portal and Tombill–Bankfield strippings occur in a high-strain corridor that encompasses the south limb of the Hard Rock anticline. Rocks at both stripped outcrops underwent intense deformation during the D_2 event, which resulted in the development of a penetrative S_2 foliation, and were further folded and deformed during D_3 dextral transcurrent shear. The timing of mineralization differs between the 2 stripped outcrops. At the Portal stripping, the auriferous quartz veins are pre- or early D_3 dextral shear, whereas at the Tombill–Bankfield fault stripping, fault-fill veins are either syn-D_2 event or early D_3 shear and sulphide mineralization is syn-D_3 dextral shear. This suggests that at least 2 mineralizing events occurred in the Geraldton area. Thus, the ore zones may have formed, and were possibly upgraded, during more than one mineralization event. As the earliest mineralization event predates F_4 and F_3 folding, polyphase folding is likely an important control on the actual geometry and distribution of the ore zones.

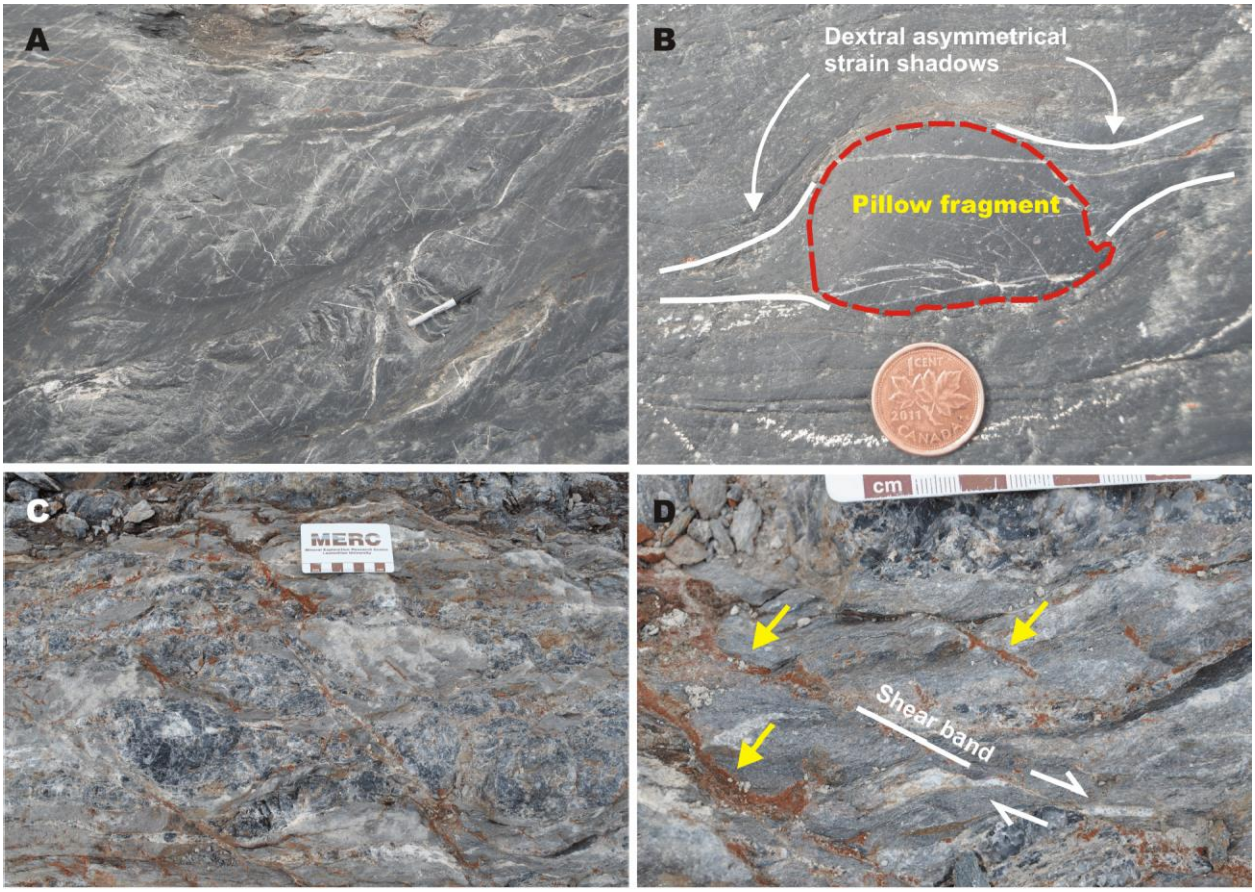

Photo 48.2. Field photographs of the Tombill–Bankfield stripping. A) Pillow in mafic pillowed flow. Pencil is 10 cm in length. B) Dextral asymmetrical strain shadows around pillow fragment. Coin (19 mm diameter) for scale. C) Fractured and broken-up black smoky quartz vein along the Tombill–Bankfield fault. Photo scale is 9 cm in length. D) Sulphide mineralization (indicated by yellow arrows) was emplaced along dextral shear bands during D_3.

ACKNOWLEDGMENTS

This project is part of a PhD thesis undertaken by Z. Tóth at Laurentian University, Sudbury, supervised by B. Lafrance. We gratefully acknowledge the support of the Ontario Geological Survey and funding of the project through the TGI-4 program of Natural Resources Canada. We thank Nicholas Whynot, Andrew Hackner, Tammy Lehtinen and Tim Twomey for discussions on gold mineralization in the Geraldton area and access to drill cores, outcrops and historical data. Phil Thurston (Laurentian) and Vicki McNicoll (GSC) contributed to discussions on the geology of the Beardmore–Geraldton belt.
Williams Oswald (Institut national de la recherche scientifique (INRS)) provided essential training on the use of the differential global positioning system (GPS) for mapping.

REFERENCES

Anglin, C.D. 1987. Geology, structure and geochemistry of gold mineralization in the Geraldton area, northwestern Ontario; unpublished MSc thesis, Memorial University of Newfoundland, St. John's, Newfoundland, 283p.

Anglin, C.D., Franklin, J.M., Loveridge, W.D., Hunt, P.A. and Osterberg, S.A. 1988. Use of zircon U-Pb ages of felsic intrusive and extrusive rocks in eastern Wabigoon Subprovince, Ontario, to place constraints on base metal and gold mineralization; *in* Radiogenic Age and Isotopic Studies: Report 2, Geological Survey of Canada, Paper 88-2, p.109-115.

Devaney, J.R. and Williams, H.R. 1989. Evolution of an Archean subprovince boundary: a sedimentological and structural study of part of the Wabigoon–Quetico boundary in northern Ontario; Canadian Journal of Earth Sciences, v.26, p.1013-1026.

Dubé, B., Mercier-Langevin, P., Castonguay, S., McNicoll, V.J., Pehrsson, S.J., Bleeker, W., Schetselaar, E.M. and Jackson, S. 2011. Targeted Geoscience Initiative 4. Lode gold deposits in ancient, deformed and metamorphosed terranes—footprints and exploration implications: a preliminary overview of themes, objectives and targeted areas; *in* Summary of Field Work and Other Activities 2011, Ontario Geological Survey, Open File Report 6270, p.38-1 to 38-10.

Hart, T.R., ter Meer, M. and Jolette, C. 2002. Precambrian geology of Kitto, Eva, Summers, Dorothea, and Sandra townships, northwestern Ontario: Phoenix bedrock mapping project; Ontario Geological Survey, Open File Report 6095, 206p.

Horwood, H.C. and Pye, E.G. 1955. Geology of Ashmore Township; Ontario Department of Mines, Annual Report, 1951, v.60, pt.5, 105p.

Lafrance, B., DeWolfe, J.C. and Stott, G.M. 2004. A structural reappraisal of the Beardmore–Geraldton belt at the southern boundary of the Wabigoon Subprovince, Ontario, and implications for gold mineralization; Canadian Journal of Earth Sciences, v.41, p.217-235.

Macdonald, A.J. 1988. The Geraldton gold camp: the role of banded iron formation; Ontario Geological Survey, Open File Report 5694, 176p.

Mason, J. and White, G. 1986. Gold occurrences, prospects, and deposits of the Beardmore–Geraldton area, districts of Thunder Bay and Cochrane; Ontario Geological Survey, Open File Report 5630, 680p.

Pye, E.G. 1952. Geology of Errington Township, Little Long Lac area; Ontario Department of Mines, Annual Report, 1951, v.60, pt.6, 140p.

Tomlinson, K.Y., Hall, R.P., Hughes, D.J. and Thurston, P.C. 1996. Geochemistry and assemblage accretion of metavolcanic rocks in the Beardmore–Geraldton greenstone belt, Superior Province; Canadian Journal of

Earth Sciences, v.33, p.1520-1533.

Appendix 6-B. Tóth, Z., Lafrance, B., Dubé, B., Mercier-Langevin, P., and McNicoll, V. J. 2013. Targeted Geoscience Initiative 4. Lode Gold Deposits in Ancient Deformed and Metamorphosed Terranes: Geological Mapping and Structural Re-Appraisal of the Banded Iron Formation–Hosted Gold Mineralization in the Geraldton Area, Ontario; in Summary of Field Work and Other Activities 2013, Ontario Geological Survey, Open File Report 6290, p.58-1 to 58-14.

58. Targeted Geoscience Initiative 4. Lode Gold Deposits in Ancient Deformed and Metamorphosed Terranes: Geological Mapping and Structural Re-Appraisal of the Banded Iron Formation–Hosted Gold Mineralization in the Geraldton Area, Ontario

Z. Tóth[1], B. Lafrance[1], B. Dubé[2], P. Mercier-Langevin[2] and V.J. McNicoll[3]

[1]Mineral Exploration Research Centre, Department of Earth Sciences, Goodman School of Mines, Laurentian University, Sudbury, Ontario P3E 2C6
[2]Geological Survey of Canada, Earth Sciences Sector, Natural Resources Canada, Québec City, Québec G1K 9A9
[3]Geological Survey of Canada, Earth Sciences Sector, Natural Resources Canada, Ottawa, Ontario K1A 0E8

INTRODUCTION

As part of the Targeted Geoscience Initiative 4 Lode Gold project of Natural Resources Canada, the goal of the project is to characterize the structural controls on gold mineralization and their mineralogical and geochemical footprints in the Geraldton area, Ontario (Dubé et al. 2011). This area was chosen because of the ongoing advanced exploration being carried out in the area by Premier Gold Mines Ltd. This exploration work provides access to large areas of stripped outcrops that show the relationships between gold mineralization and structures. The company's recent drill holes also provide access to new information on the nature, distribution and chronology of the gold-bearing hydrothermal alteration (Lafrance et al. 2012), helping to improve our understanding of mineralization processes in banded iron formation-bearing successions within the Precambrian.

During the summer of 2013, 3 stripped outcrops were mapped in detail and drill core that intersected mineralized zones in different host rocks were logged and sampled for petrographic and lithogeochemical analysis. This report presents some of the key new data resulting from the detailed mapping carried out during the 2013 field season.

BACKGROUND

The study area—the Beardmore–Geraldton belt—is located along the boundary between the Wabigoon (granite-greenstone) and Quetico (sedimentary) subprovinces. The study area extends from the east shore of Lake Nipigon to Longlac in the east. The Beardmore–Geraldton belt is composed of 3 metavolcanic and 3 metasedimentary units (Lafrance, DeWolfe and Stott 2004, and references therein). The volcanic units formed in different, but originally adjoining, parts of an ancient arc system. The volcanic units represent (from north to south) back-arc basin, oceanic island arc and mid-ocean ridge basalt-type oceanic crust (Tomlinson et al. 1996). The 3 sedimentary units formed a southward-prograding clastic wedge (Barrett and Fralick 1985; Williams 1987; Devaney and Williams 1989). They were deposited, from north to south, in alluvial fan/braid-plain, fluvial to deltaic, and submarine fan and/or basin-plain environments (Barrett and Fralick 1985; Williams 1987; Devaney and Williams 1989). The rocks in the study area are typically metamorphosed to greenschist facies, but the metamorphic grade increases to lower amphibolite facies along the eastern, southern and northern margins of the belt (Macdonald 1944; Pirie and Mackasey 1978; Lavigne 1983; Beakhouse 1984; Macdonald 1983; Williams 1987).

Lafrance, DeWolfe and Stott (2004) suggested that the Beardmore–Geraldton belt went through 3 major phases of deformation. The D_1 thrusting resulted in the formation of rare, small amplitude isoclinal F_1 folds (Devaney and Williams 1989; Lafrance, DeWolfe and Stott 2004). These F_1 folds were refolded by tight, upright, west-plunging F_2 folds, with an axial planar S_2 cleavage, during the north-south compression of the second deformation event (Devaney and Williams 1989; Lafrance, DeWolfe and Stott 2004). The third deformation event was expressed as dextral transpression and resulted in the formation of Z-shaped, west-plunging F_3 folds and a regional S_3 cleavage (Lafrance, DeWolfe and Stott 2004). Late, north-northwest-trending faults with sinistral movement cut all the older structural elements (Pye 1952; Horwood and Pye 1955; Kresz and Zayachivsky 1991).

Ore recovered from past-producing mines in the Beardmore–Geraldton belt yielded more than 4.1 million ounces of gold (Mason and McConnell 1982). The past-producing gold mines in the Geraldton area of the Beardmore–Geraldton belt were all located in the southern sedimentary assemblage and mostly within the kilometre-wide Tombill–Bankfield deformation zone (Pye 1952; Lafrance, DeWolfe and Stott 2004). Previous studies suggested that the gold mineralization was deposited during D_3 dextral shear (Pye 1952; Horwood and Pye 1955; Anglin 1987; Macdonald 1988; Lafrance, DeWolfe and Stott 2004; DeWolfe, Lafrance and Stott 2007; Lavigne 2009).

"HEADFRAME" EXPOSURE

The "Headframe" exposure is a 30 by 20 m stripped outcrop located along the northern limb of the Hard Rock anticline, approximately 30 m southeast of the No. 1 headframe of the past-producing Macleod–Cockshutt Mine (Figure 58.1).

This stripped outcrop exposes banded iron formation interlayered with mudstone to sandstone intruded by minor mafic dikes (Figure 58.2). Massive iron formation layers with thicknesses on the order of centimetres to several tens of centimetres are interbedded with mudstone to sandstone. The layers of banded iron formation are dark greyish black with locally a reddish tint on fresh surfaces, whereas their weathered surface is reddish dark grey. The thick, massive iron formation beds contain magnetite-rich beds and lesser amounts (10 to 20%) of jasper-rich beds. The beds are finely laminated on a scale of millimetres. The original thickness of the beds is difficult to estimate due to the strong deformation. The often slightly magnetic mudstone to sandstone layers are generally (greenish) light to medium grey in colour and greenish dark grey with brown colourization where altered by iron carbonate. The sandstone beds are medium grained and approximately 10 to 15 cm thick. The mafic dikes are (brownish) light green on outcrop surfaces and medium grey on fresh surfaces. They are very fine grained and composed of felsic and mafic minerals, presumably feldspar and chlorite. They have recorded a penetrative chlorite and iron-carbonate alteration on the margins of quartz–iron-carbonate veins. They were interpreted as mafic dikes because they cut across beds of sedimentary rocks.

Numerous tight to isoclinal F_1 folds, with amplitudes on the order of tens of centimetres to metres, are refolded by S-shaped F_2 folds, with amplitudes on the order of centimetres to metres (Photo 58.1A). A continuous chloritic S_1 foliation is axial planar to F_1 folds in mafic dikes (Photos 58.1B and 58.1C). A spaced (~0.5 mm) chloritic S_1 foliation is present in the interlayered sandstone to mudstone (Photo 58.1D), but is difficult to distinguish from bedding. The F_2 folds are open and have a strong axial planar S_2 cleavage (Photo 58.1E) defined by mafic minerals, presumably chlorite in the sedimentary rocks as well as in the mafic dikes. The S_2 cleavage is a spaced cleavage (0.5 to 1 mm), oriented approximately 15 to 20° clockwise to bedding. Beds and laminae in the banded iron formation are commonly transposed parallel to S_2 along the limbs of F_2 folds. Locally, S_2 foliation—that is, the first, strong foliation that can apparently be observed in the sedimentary rocks—is folded by open to gentle, S-shaped F_3 folds with amplitudes on the order of millimetres to tens of centimetres. These F_3 folds have a weak axial planar crenulation foliation that is visible only in the mudstone (Photo 58.1F). The S_3 foliation has a spacing of

0.2 to 0.3 mm and is roughly parallel to S_2. The S_2 foliation and the long limbs of the F_2 folds are folded by open to tight, Z-shaped F_4 folds, with amplitudes on the order of centimetres to tens of centimetres, which have a strong axial planar S_4 cleavage (Photo 58.1G). The S_4 foliation is a spaced cleavage (spacing varies from 0.1 to 5 mm, depending on the host rock) that is oriented 8 to 10° anticlockwise to bedding. The S_4 foliation is not folded by S-shaped folds and overprints F_3 folds (Photos 58.1H and 58.1I).

Gold mineralization is not exposed in this outcrop. Quartz-iron-carbonate veins and their iron-carbonatized wall rocks are folded by F_1 folds, suggesting that they were emplaced either before or during the early stages of D_1 (Photos 58.1J and 58.1K). A second generation of quartz-carbonate veins cuts across F_1 folds and is folded by F_2 folds, suggesting that they were emplaced after the D_1 event and prior to or early in the D_2 event. Although auriferous semi-massive sulphide replacement or auriferous veins were not observed, sulphides are emplaced in the neck of boudins that formed late during dextral shear.

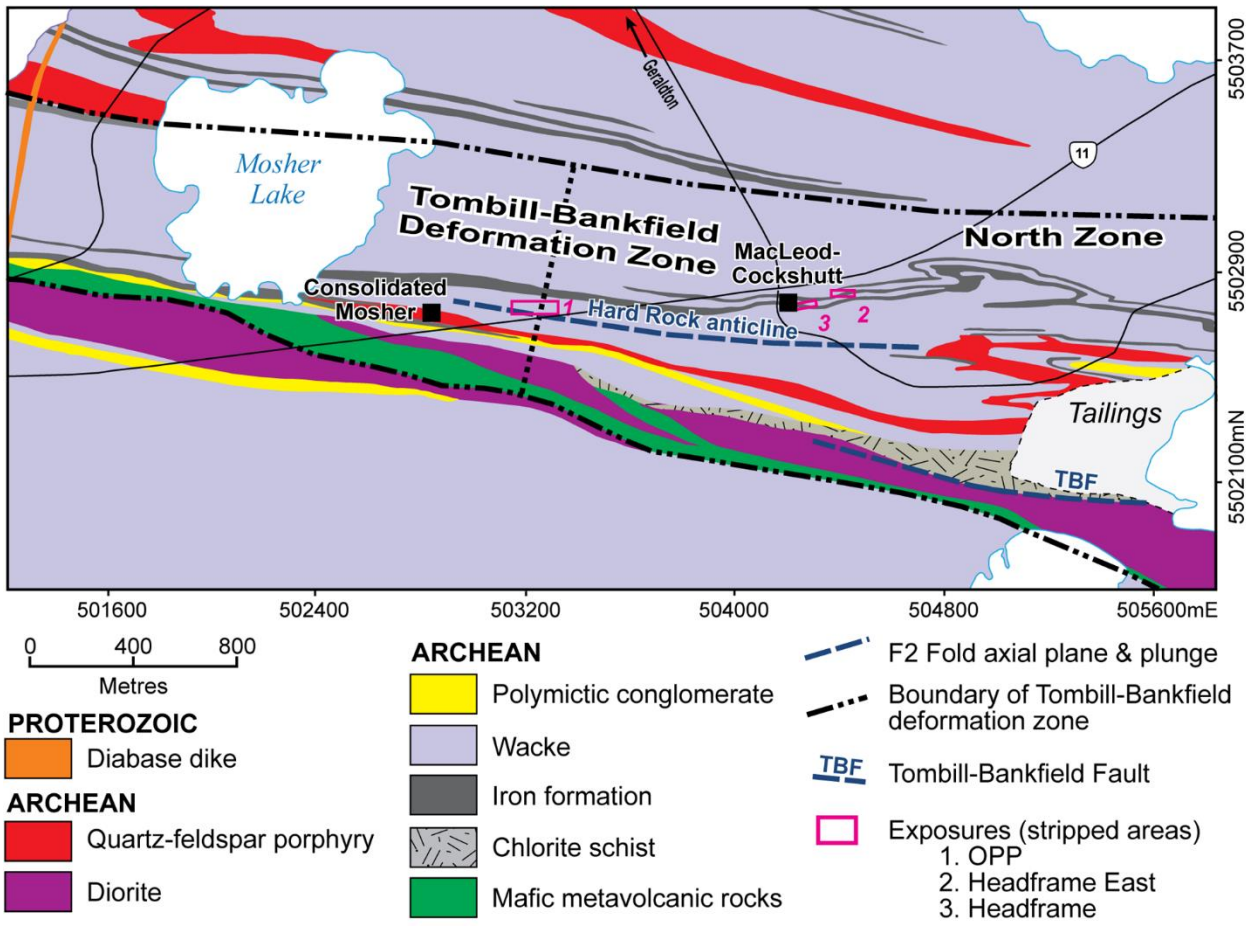

Figure 58.1. Simplified geological map of the Geraldton area showing the location of the stripped outcrops or exposures mapped in 2013. (Geology *after* Horwood and Pye (1955) and Pye (1952), with modifications by authors.) Universal Transverse Mercator (UTM) co-ordinates are based on North American Datum 1927 (NAD27), Zone 16.

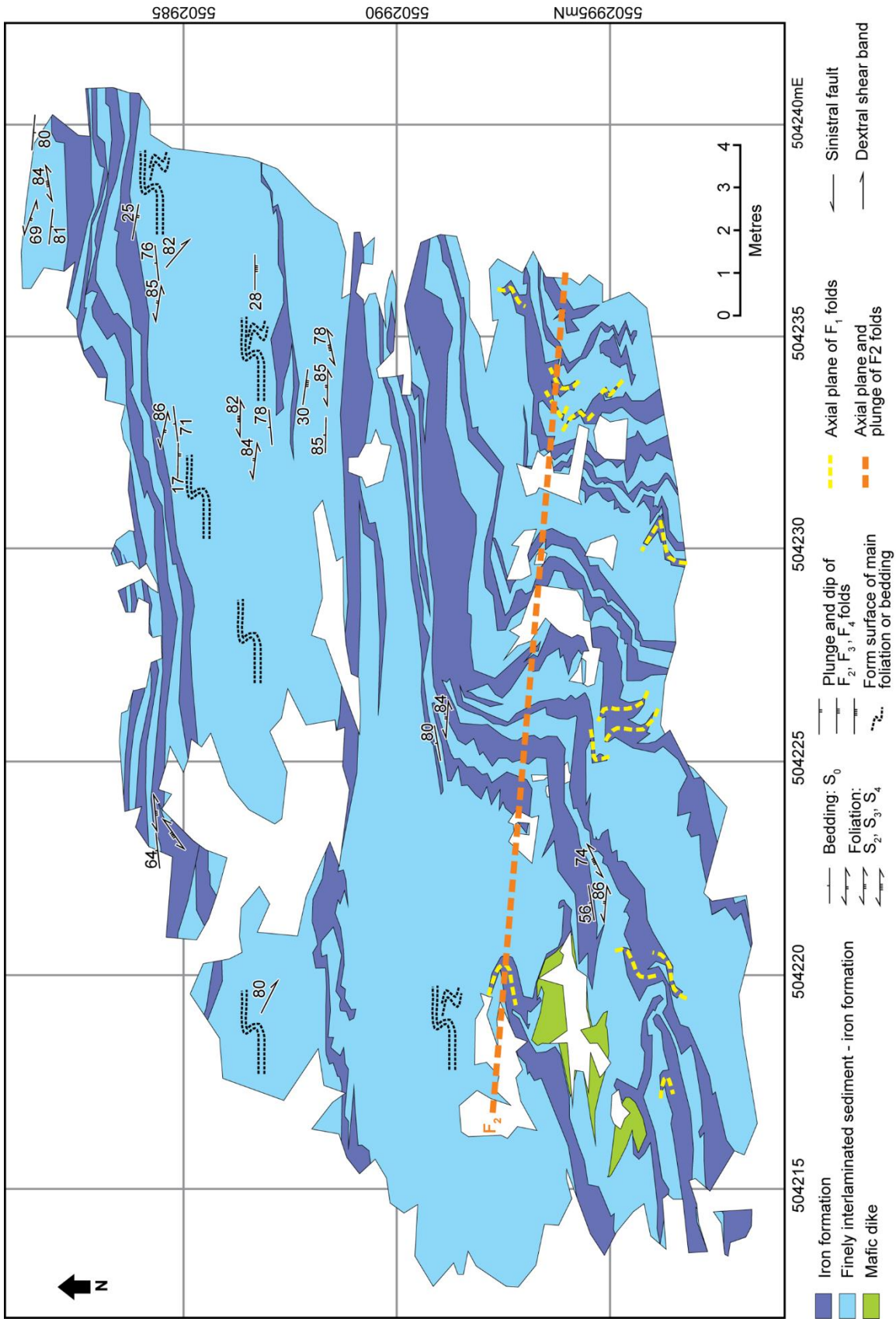

Figure 58.2. Detailed geological map of the "Headframe" exposure (area 3 on Figure 58.1). All UTM co-ordinates are based on North American Datum 1983 (NAD83), Zone 16.

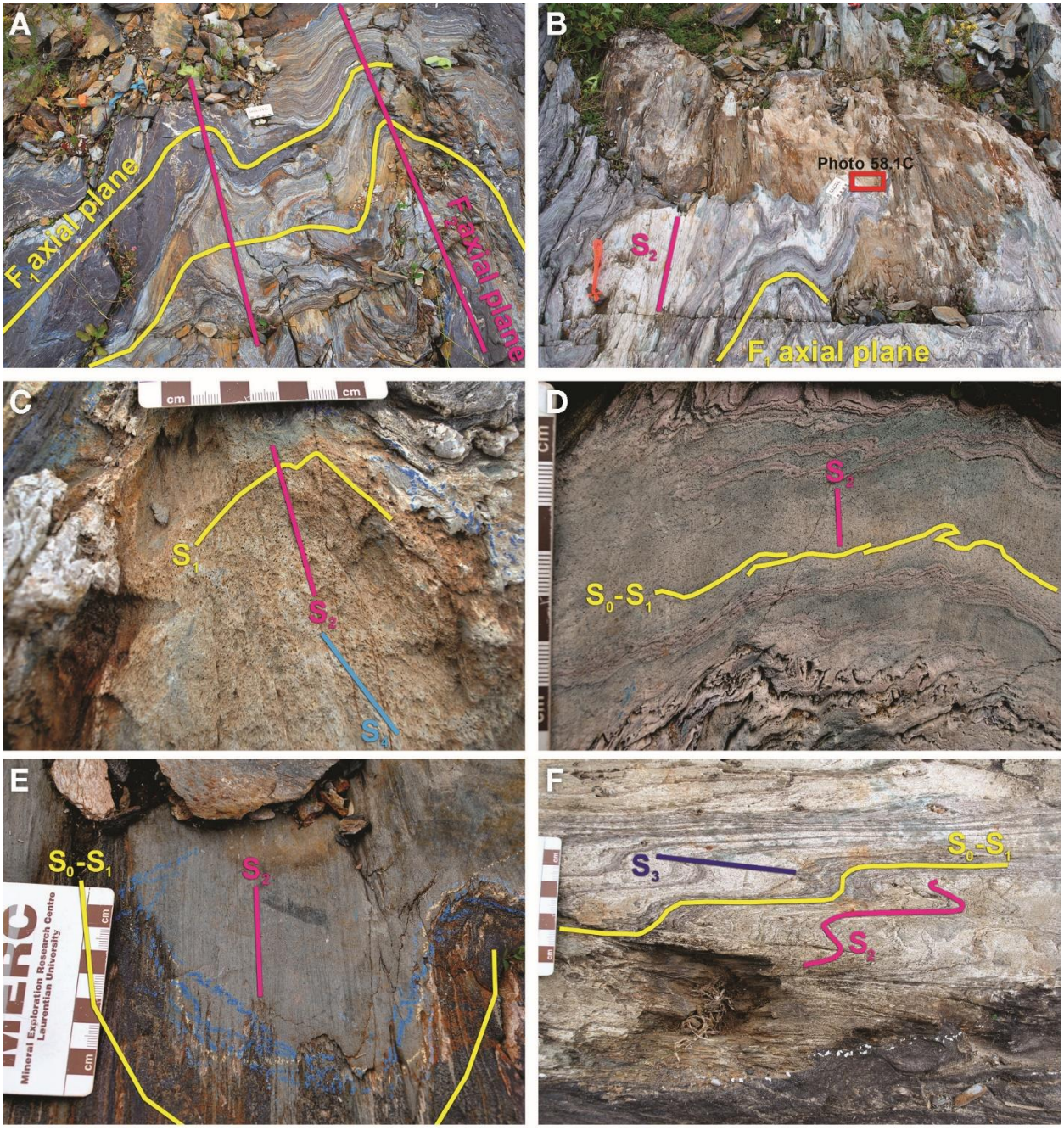

Photo 58.1. Field photographs of the "Headframe" exposure (area 3 on Figure 58.1). **A)** Tight F_1 folds refolded by S-shaped F_2 folds in iron formation. **B)** F_1 fold refolded by S-shaped F_2 fold and overprinted by axial planar S_2 foliation in iron formation, sedimentary rocks and mafic dike. Red rectangle shows the location of the Photo 58.1C photograph. **C)** S_1 foliation axial planar to F_1 fold, folded by F_2 folds and overprinted by axial planar S_2 foliation that is parallel to S_3 and oblique to S_4 foliation in mafic dike. **D)** Bedding-parallel S_1 foliation folded by F_2 and overprinted by S_2 foliation in siltstone. **E)** F_2 fold with only one strong, axial planar foliation (S_2). **F)** Well-developed S_2 foliation folded by S-shaped F_3 fold, overprinted by axial planar S_3 foliation that is typically subparallel to S_2.

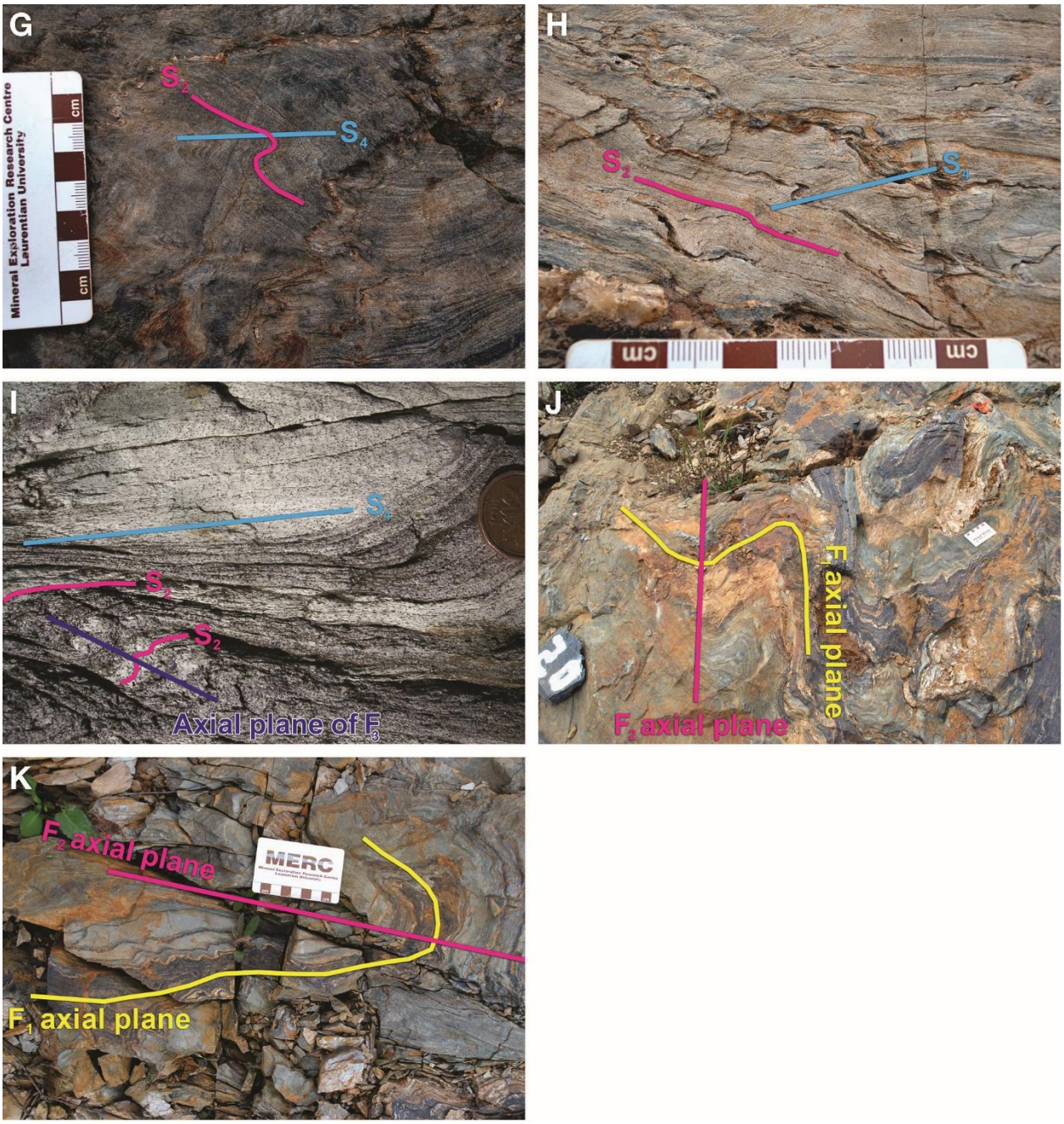

Photo 58.1, continued. Field photographs of the "Headframe" exposure (area 3 on Figure 58.1). **G)** S_2 or composite foliation folded by Z-shaped F_4 folds and overprinted by S_4 foliation axial planar to F_4 folds. **H)** S_4 foliation axial planar to Z-shaped F_4 folds does not display S-shaped folding. **I)** S_4 foliation overprints S-shaped F_3 folds. The diameter of the coin is 19 mm. **J)** Strongly iron-carbonate–altered rock folded by F_1 and refolded by S-shaped F_2 fold assumed to partially surround and partially overprint banded iron formation. **K)** Quartz-iron-carbonate vein folded by F_1 and refolded by F_2 folds in banded iron formation.

“OPP” EXPOSURE

The “OPP” exposure is a 130 by 50 m stripped outcrop that lies along the northern limb of the Hard Rock anticline, 250 m west of the Ontario Provincial Police station and 100 m north of Highway 11 (*see* Figure 58.1).

Interlayered mudstone–siltstone–minor sandstone and iron formation is exposed over two-thirds of the outcrop (Figure 58.3). The mudstone, siltstone and sandstone are light to dark grey and green on outcrop surfaces and brownish dark grey on fresh surfaces. Beds are up to several centimetres thick and normal grading is visible in coarse-grained sandstone beds, indicating younging direction to the north. Laminae of banded iron formation are present in the sandstone beds. The banded iron formation is dark blue to reddish brown on outcrop surfaces and dark grey on fresh surfaces. Beds vary in thickness from several centimetres to tens of centimetres. Transposed clastic sandstone dikes are associated with the iron formation. Interlayered sandstone to mudstone constitute the northern part of the outcrop. This part of the exposure lacks the iron formation layers present in the rest of the outcrop described above, and it is more thickly bedded with beds varying in thickness from a few centimetres to several tens of centimetres. Normal grading with younging to the north is locally observed.

Quartz-feldspar porphyry dike(s) cut across bedding in the sedimentary sequence. The dikes are strongly folded and transposed parallel to bedding. Their colour varies from green to pinkish brown due to iron-carbonate alteration. The rock contains approximately 27% feldspar (up to 7 mm) and about 3% quartz phenocrysts within a matrix composed of approximately 45% feldspar, approximately 20% chlorite and approximately 5% quartz. Brownish green amygdaloidal mafic dikes are also transposed parallel to bedding. They have a strong foliation defined by chlorite and presumably iron carbonate.

Three generations of ductile structures are present. Rare, tightly folded F_1 folds (Photo 58.2B) are refolded by open to tight, centimetre-scale, typically S-shaped, F_2 folds. The folds, where present in iron formation, have no axial planar cleavage, but a strong folded S_1 foliation is observed in the quartz-feldspar porphyry dike in the hinge of F_2 folds (Photo 58.2A). The F_2 folds occur in all rock types and they have a penetrative axial planar S_2 cleavage that is oriented either parallel or slightly clockwise to bedding along the long limbs of F_2 folds (Photo 58.2C). These structural relationships are consistent with this outcrop being located in an area that represents the shared north limb of the Hard Rock anticline and south limb of the Ellis syncline. The S_2 foliation is itself folded by Z-shaped, small-scale F_4 folds with a strong axial planar S_4 foliation (Photo 58.2D). The S_4 foliation is oriented 10 to 20° anticlockwise both to bedding and to the S_2 foliation. Centimetre to metre-scale dextral shear bands cut across all generations of the structures observed in this outcrop, and they form a penetrative foliation within the porphyry and the mafic dikes (Photo 58.2E). A local S-C fabric also provides evidence of dextral shear, in which bedding or S_2 played the role of a pre-existing foliation into which S_4 was dragged. Quartz-carbonate veins are boudinaged and the boudins are rotated in an anticlockwise manner. The asymmetry of the F_4 folds and dextral shear bands are compatible with D_4 transcurrent dextral shearing. It is important to note that S_2 foliation is locally folded by local, small amplitude, S-shaped folds.

Multiple generations of veins were observed at this exposure. Early iron-carbonate veins and/or alteration are parallel to bedding, often confined within iron formation beds, and they are folded by F_2 and transposed parallel to S_2. The hydrothermal alteration is characterized by quartz-carbonate veins and associated strong iron-carbonate alteration and silicification in the porphyry dike. Such alteration is characteristic of most syndeformational gold deposits hosted in greenstone rocks metamorphosed to greenschist facies (orogenic type deposits, Dubé and Gosselin 2007). The iron-carbonate alteration is commonly distributed parallel to bedding, potentially due to selective replacement, and is folded by F_2 folds (Photo 58.2G) implying that the carbonatization occurred early in, or prior to, the D_2 deformation event. The timing of the iron-carbonate replacement relative to F_1 folds cannot be established on this exposure because of the scarcity of F_1 folds.

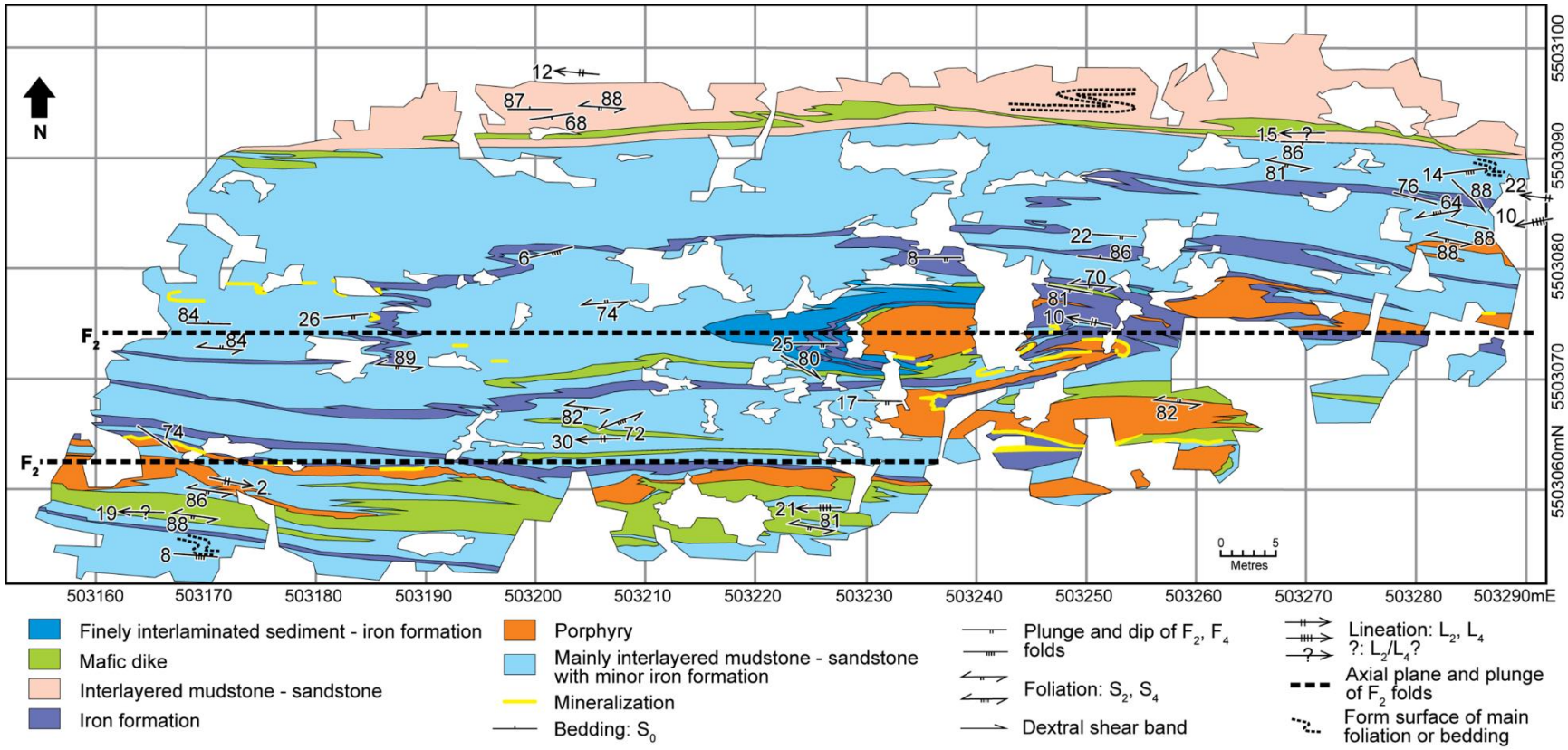

Figure 58.3. Detailed geological map of the "OPP" exposure (area 1 in Figure 58.1). All UTM co-ordinates provided in NAD83, Zone 16.

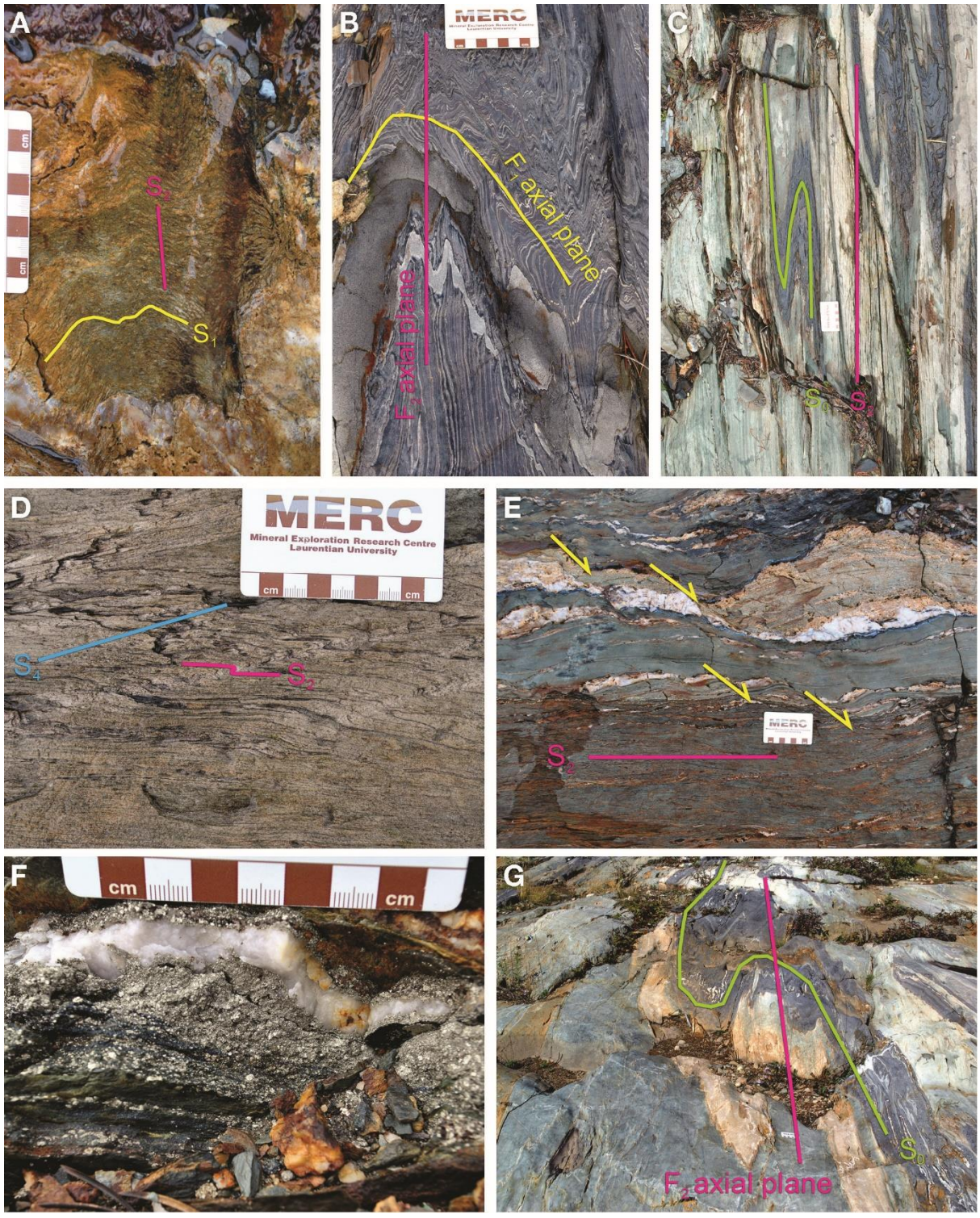

Photo 58.2. Field photographs of the "OPP" exposure (area 1 on Figure 58.1). **A)** S_1 foliation folded by S-shaped F_2 folds and overprinted by S_2 foliation axial planar to F_2 fold in porphyry dike. **B)** Tight to isoclinal F_1 fold refolded by S-shaped, open to tight F_2 fold in iron formation. **C)** Iron formation tightly folded by S-shaped F_2 fold and overprinted by axial planar S_2 foliation. **D)** S_2 foliation folded by Z-shaped F_4 folds and overprinted by axial planar S_4 foliation. **E)** Dextral shear bands cutting porphyry dike, sedimentary rocks and mafic dike. **F)** Semi-massive pyrite replacement representing the gold mineralization is associated with quartz-carbonate veins in iron formation. **G)** Iron-carbonate alteration emplaced parallel to bedding and folded by S-shaped F_2 folds.

Veins of quartz-carbonate ± sulphide are typically surrounded by chlorite-sericite wall rocks in the sedimentary rocks and by hematite in the iron formation. The veins are either parallel or oblique to bedding and were boudinaged prior to F_2 folding, suggesting that they were emplaced prior to D_2 deformation. Boudinaged quartz-carbonate ± minor sulphide veins cut across other quartz-carbonate ± minor sulphide veins that are folded by F_2 folds and, thus, were emplaced even later during F_2 folding or after the F_2 folding.

Gold mineralization (based on channel sampling done by Premier Gold Mines Ltd.) occurs as semi-massive sulphide replacement of banded iron formation associated with quartz-iron carbonate-sulphide veins (Photo 58.2F). The sulphide replacement assemblage is composed of pyrite, arsenopyrite and chalcopyrite. The veins are surrounded by a centimetre-wide chlorite-sericite alteration halo. Gold mineralization is typically localized along contacts between the banded iron formation and the porphyry dike, emphasizing the role of competency contrast in the formation of pathways for gold-bearing hydrothermal fluid. The gold mineralization in the "OPP" exposure is folded by F_2 folds, suggesting that it was emplaced prior to or early in the D_2 deformation event.

"HEADFRAME EAST" EXPOSURE

The "Headframe East" exposure is a 20 by 45 m stripped outcrop that lies along the northern limb of the Hard Rock anticline, 150 m east of the No. 1 headframe of the past-producing MacLeod–Cockshutt Mine, and 70 m south of Highway 11 (*see* Figure 58.1). The stripped outcrop consists of massive, sediment-devoid iron formation in the south, to interlayered mudstone to sandstone in the centre, to pebbly sandstone in the northern part of the outcrop (Figure 58.4).

The massive iron formation consists of millimetre-thick magnetite-rich laminae interlayered with minor jasper-rich and mudstone laminae. It is reddish dark grey on outcrop and fresh surfaces. Interlayered mudstone to sandstone in the central part of the exposure contains iron formation layers similar to those described above. The sandstone and mudstone beds vary in thickness from 1 cm to less than 50 cm. They are (brownish) light grey on outcrop surfaces and darker grey on fresh surfaces.

The northern half of this exposure is composed dominantly of interlayered mudstone to sandstone locally interlayered with banded iron formation, the layers of which do not exceed 20 cm in thickness. This well-bedded sequence gradually changes into massive, coarse-grained, strongly iron-carbonate–altered sandstone that contains variably elongated, but rounded, clasts ranging from 3–4 cm to 30–40 cm in diameter. The clasts are assumed to have mainly granitic compositions as they are rigid even if elongated, folded and fractured, and are locally surrounded by an asymmetrical strain shadow.

Numerous tight F_1 folds are refolded by gentle to tight, S-shaped, shallowly west-plunging F_2 folds with amplitudes on the order of centimetres to metres and are overprinted by an axial planar S_2 foliation. The S_2 foliation is oriented 20 to 30° clockwise to the east-trending bedding. Gentle to open F_2 folds are often tightly folded as the result of later dextral shear located along their long limb. F_3 folds were not observed in this outcrop. Shallow to intermediate west-plunging, centimetre-scale, open to gentle Z-shaped F_4 folds fold the S_2 foliation. The S_4 foliation is axial planar to F_4 folds and is oriented 20 to 40° anticlockwise to the S_2 foliation. Dextral shear bands cut all the previously described structures. Two co-linear L_2 and/or L_4 lineations (mineral or rib-and-groove lineations) are present either on bedding or S_2 planes and may have formed during the same or during 2 separate deformation events. Another shallowly east- or west-plunging, small, approximately 1 mm slip lineation of unknown origin is observed along bedding and S_2 foliation planes.

Quartz-iron-carbonate or locally pinkish iron-carbonate veins in banded iron formation are folded by F_1 and F_2 folds and transposed parallel to S_2 foliation in F_2 fold hinges, suggesting that they were emplaced either prior to or early in the D_2 deformation. Quartz-iron-carbonate veins that are folded by

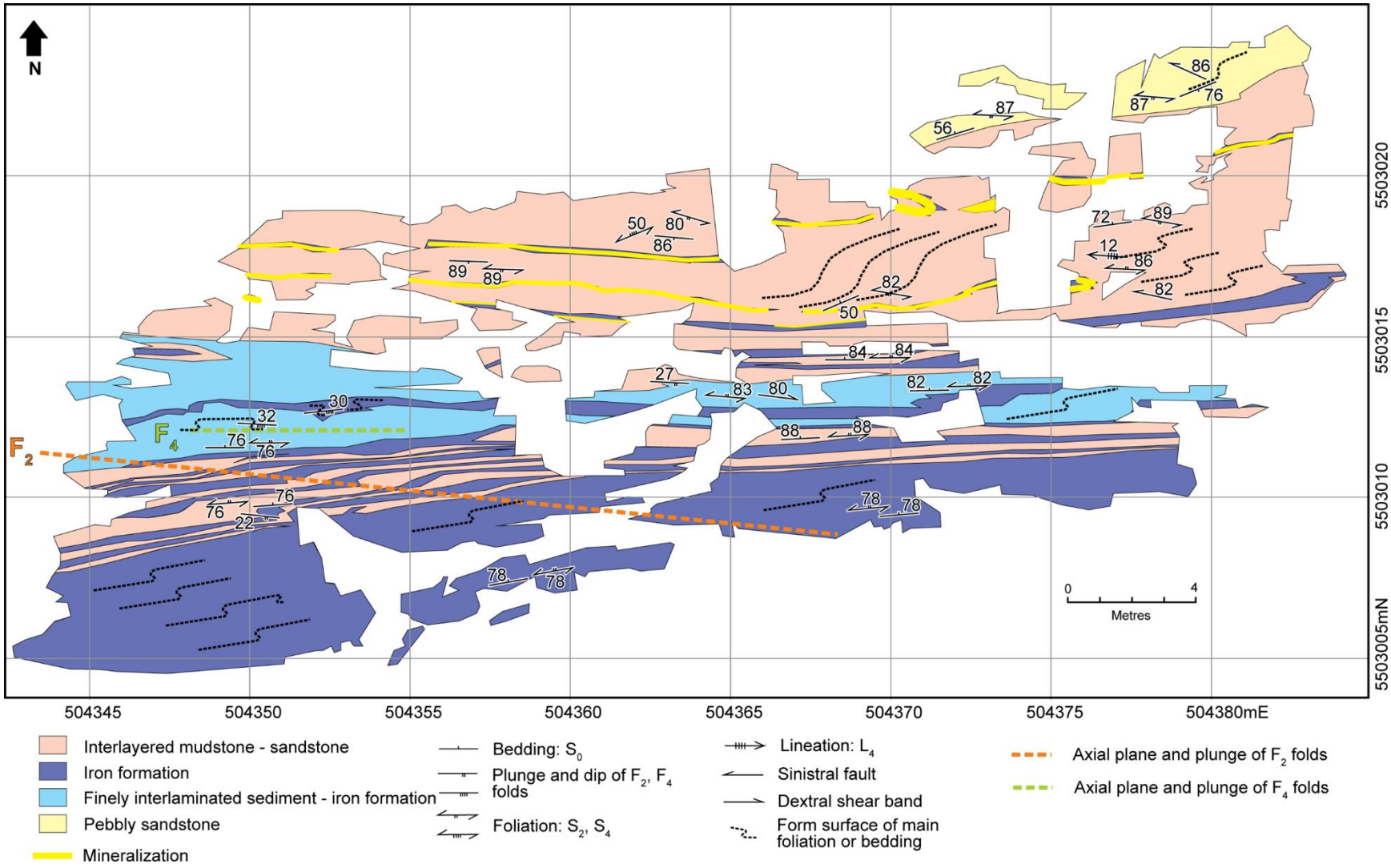

Figure 58.4. Geological map of the "Headframe East" exposure (area 2 on Figure 58.1). All UTM co-ordinates provided in NAD83, Zone 16.

F_2 folds, and boudinaged only after folding, cut the iron-carbonate veins and alteration. The relationship between the veins described above is uncertain; their relative timing of emplacement can only be assumed based on their deformation. Quartz-iron-carbonate ± sulphide and calcite veins are folded by F_2 folds, suggesting their emplacement was prior to or early in the D_2 deformation event. These veins are often laminated and cut across bedding-parallel quartz-carbonate veins. They are sometimes surrounded by millimetre- to centimetre-wide chlorite-sericite alteration halos without associated sulphide.

The gold mineralization in this exposure (based on grab samples taken by Premier Gold Mines Ltd.) is characterized by sulphide replacement of the oxide-facies banded iron formation. It consists of semi-massive pyrite-chalcopyrite ± arsenopyrite ± molybdenite(?) as alteration halos of quartz-carbonate veins. It appears only in banded iron formation layers in the northern part of the stripped outcrop, as opposed to the massive iron formation in the southern part of the outcrop. The gold mineralization is folded by S-shaped F_2 and Z-shaped F_4 folds and is overprinted by dextral shear bands; therefore, the gold mineralization was emplaced either prior to, or very early in, the D_2 deformation event.

CONCLUSION

All 3 mapped outcrops are located along the north limb of the regional F_2 Hard Rock anticline. Tight F_1 folds are refolded by gentle to tight, S-shaped F_2 folds that are parasitic folds to the Hard Rock anticline. The S-shaped F_3 folding of S_2 at the "Headframe" and "OPP" exposures suggests local sinistral shearing prior to dextral shearing during D_4. The D_4 event is a late, dextral transcurrent shearing event that produced multiple Z-shaped drag folds with a strong axial planar foliation and dextral shear bands.

Gold mineralization occurs as semi-massive sulphide replacement associated with quartz-iron-carbonate veins at the "OPP" and "Headframe East" exposures. It is folded by S-shaped F_2 folds, suggesting that gold mineralization was emplaced either prior to, or early in, the D_2 deformation. Iron-carbonate alteration, which is typically associated with gold mineralization in other similar world-class gold camps (Dubé and Gosselin 2007), is folded by F_1 folds. However, the gold mineralization exposed in the stripped outcrops does not show evidence of deformation by F_1 folds. If this iron-carbonate alteration is associated with gold mineralization, this would suggest the possibility of a mineralizing event that predated D_2 deformation and was presumably synchronous with the D_1 deformation event. Alternatively, this may suggest that there are several stages of iron-carbonate alteration in this area, as documented in Timmins and Red Lake (Dubé et al. 2004; Dubé and Gosselin 2007). The stripped outcrops clearly expose the complexity of the structural setting of the gold deposits in the Geraldton area, with several generations of foliations and folds. Better defining the chronology of deformation in relation to the emplacement of the bulk of the gold mineralization could impact the understanding of the distribution and geometry of the auriferous lodes and also help better define the key parameters responsible for their formation.

ACKNOWLEDGMENTS

This project is part of a PhD thesis undertaken by the lead author at Laurentian University, Sudbury, Ontario, with supervision by Bruno Lafrance and Benoit Dubé (Geological Survey of Canada). We gratefully acknowledge the funding of the Targeted Geoscience Initiative 4 Lode Gold project of Natural Resources Canada, as well as the support of the Ontario Geological Survey. We thank Premier Gold Mines Ltd. for access to its properties, drill core and database, particularly Nick Whynot, Andrew Hackner, Daniel Grabiec, Tom Salmi and the crew located in Geraldton.

REFERENCES

Anglin, C.D. 1987. Geology, structure and geochemistry of gold mineralization in the Geraldton area, northwestern Ontario; unpublished MSc thesis, Memorial University of Newfoundland, St. John's, Newfoundland, 283p.

Barrett, T.J. and Fralick, P.W. 1985. Sediment redeposition in Archean iron formation: Examples from the Beardmore–Geraldton belt, Ontario; Journal of Sedimentary Petrology, v.55, p.205-212.

Beakhouse, G.P. 1984. Geology of the Grenville Lake area, Thunder Bay District; Ontario Geological Survey, Open File Report 5513, 146p.

Devaney, J.R. and Williams, H.R. 1989. Evolution of an Archean subprovince boundary: A sedimentological and structural study of part of the Wabigoon–Quetico boundary in northern Ontario; Canadian Journal of Earth Sciences, v.26, p.1013-1026.

DeWolfe, J.C., Lafrance, B. and Stott, G.M. 2004. Geology of the shear-hosted Brookbank gold prospect in the Beardmore–Geraldton belt, Wabigoon Subprovince, Ontario; Canadian Journal of Earth Sciences, v.44, p.925-946.

Dubé, B. and Gosselin, P. 2007. Greenstone-hosted quartz-carbonate vein deposits, *in* Mineral deposits of Canada: A synthesis of major deposit-types, district metallogeny, the evolution of geological provinces, and exploration methods, Geological Association of Canada, Mineral Deposits Division, Special Publication No. 5, p.49-73.

Dubé, B., Mercier-Langevin, P., Castonguay, S., McNicoll, V.J., Pehrsson, S.J., Bleeker, W., Schetselaar, E.M. and Jackson, S. 2011. Targeted Geoscience Initiative 4. Lode gold deposits in ancient, deformed and metamorphosed terranes—footprints and exploration implications: A preliminary overview of themes, objectives and targeted areas; *in* Summary of Field Work and Other Activities 2011, Ontario Geological Survey, Open File Report 6270, p.38-1 to 38-10.

Dubé, B., Williamson, K., McNicoll, V., Malo, M., Skulski, T., Twomey, T. and Sanborn-Barrie, M.J. 2004. Timing of gold mineralization in the Red Lake gold camp, northwestern Ontario, Canada: New constraints from U-Pb geochronology at the Goldcorp high-grade zone, Red Lake mine and at the Madsen mine; Economic Geology, v.99, p.1611-1642.

Horwood, H.C. and Pye, E.G. 1955. Geology of Ashmore Township; Ontario Department of Mines, Annual Report, 1951, v.60, pt.5, 105p.

Kresz, D.U. and Zayachivsky, B. 1991. Precambrian geology, northern Long Lake area; Ontario Geological Survey, Report 273, 77p.

Lafrance, B., DeWolfe, J.C. and Stott, G.M. 2004. A structural reappraisal of the Beardmore–Geraldton Belt at the southern boundary of the Wabigoon Subprovince, Ontario, and implication for gold mineralization; Canadian Journal of Earth Sciences, v.41, p.217-235.

Lafrance, B., Tóth, Z., Dubé, B. and Mercier-Langevin, P. 2012. Targeted Geoscience Initiative 4. Lode gold deposits in ancient deformed and metamorphosed terranes: Geological setting of banded iron formation–hosted gold mineralization in the Geraldton area, northern Ontario; *in* Summary of Field Work and Other Activities 2012, Ontario Geological Survey, Open File Report 6280, p.48-1 to 48-10.

Lavigne, M.J. 1983. Gold deposits of the Geraldton area; *in* Summary of Field Work 1983, Ontario Geological Survey, Miscellaneous Paper 116, p.198-200.

——— 2009. Distribution of gold with respect to lithologies, metamorphic facies and strain state in the Beardmore–Geraldton greenstone belt; Ontario Geological Survey, Open File Report 6241, 88p.

Macdonald, A.J. 1983. A re-appraisal of the Geraldton gold camp; *in* Summary of Field Work 1983, Ontario Geological Survey, Miscellaneous Paper 116, p.194-197.

——— 1988. The Geraldton gold camp: The role of banded iron formation; Ontario Geological Survey, Open File Report 5694, 176p.

Macdonald, R.D. 1944. Regional metamorphism in the Kenogamisis River area; Journal of Geology, v.52, p.414-423.

Mason, J.K. and McConnell, C.D. 1982. Gold mineralization in the Beardmore–Geraldton area; *in* The geology of gold in Ontario, Ontario Geological Survey, Miscellaneous Paper 100, p.84-97.

Pirie, J. and Mackasey, W.O. 1978. Preliminary explanation of regional metamorphism in parts of the Quetico metasedimentary belt, Superior Province, Ontario; *in* Metamorphism in the Canadian Shield, Geological Survey of Canada, Paper 78-10, p.37-48.

Pye, E.G. 1952. Geology of Errington Township, Little Long Lac area; Ontario Department of Mines, Annual Report, 1951, v.60, pt.6, 140p.

Tomlinson, K.Y., Hall, R.P., Hughes, D.J. and Thurston, P.C. 1996. Geochemistry and assemblage accretion of metavolcanic rocks in the Beardmore–Geraldton greenstone belt, Superior Province; Canadian Journal of Earth Sciences, v.33, p.1520-1533.

Williams, H.R. 1987. Structural studies in the Wabigoon and Quetico subprovinces; Ontario Geological Survey, Open File Report 5668, 163p.

Appendix 6-C. Tóth, Z., Lafrance, B., Dubé, B., Mercier-Langevin, P., and McNicoll, V. J, 2014. Targeted Geoscience Initiative 4. Lode Gold Deposits in Ancient Deformed and Metamorphosed Terranes: Relative chronology between hydrothermal activity, gold mineralization and deformation events in the Geraldton area, NW Ontario; in Summary of Field Work and Other Activities 2014, Ontario Geological Survey, Open File Report 6300, p.40-1 to 40-10.

40. Targeted Geoscience Initiative 4. Lode Gold Deposits in Ancient Deformed and Metamorphosed Terranes: Relative Chronology Between Hydrothermal Activity, Gold Mineralization and Deformation Events in the Geraldton Area, Northwestern Ontario

Z. Tóth[1], B. Lafrance[1], B. Dubé[2], P. Mercier-Langevin[2] and V.J. McNicoll[3]

[1]Mineral Exploration Research Centre, Department of Earth Sciences, Goodman School of Mines, Laurentian University, Sudbury, Ontario P3E 2C6
[2]Geological Survey of Canada, Earth Sciences Sector, Natural Resources Canada, Québec City, Québec G1K 9A9
[3]Geological Survey of Canada, Earth Sciences Sector, Natural Resources Canada, Ottawa, Ontario K1A 0E8

INTRODUCTION

As part of the Targeted Geoscience Initiative 4 Lode Gold program of National Resources Canada, this project aims to improve knowledge of the structural and stratigraphic settings and the geochemical footprint of gold mineralization and associated hydrothermal alteration in the Geraldton area, Ontario (Dubé et al. 2011). Gold deposits in the Geraldton area were in production until 1970; interest has been renewed because planning is underway by Premier Gold Mines Ltd to mine some of these deposits as an open pit operation. The total indicated resource is 4.870 million ounces gold and the total inferred resource is 2.74 million ounces gold for the Hardrock property in Geraldton (www.premiergoldmines.com, news release, July 8, 2014). Premier Gold Mines Ltd. provided access to their extensive drill-core collection and to newly exposed ("stripped") mineralized outcrops. These outcrops were very helpful in establishing the timing of the gold mineralization events in the Geraldton area and in refining the structural interpretation of the Beardmore–Geraldton greenstone belt.

A total of 8 stripped outcrops have been mapped during the past 3 field seasons (Figure 40.1) (Lafrance et al. 2012; Tóth et al. 2013a). Samples were taken from drill holes, as well as from the mapped exposures, to define the geochemical footprint of the gold mineralization and the associated hydrothermal alteration. The past field season focussed on defining the relative timing of the gold mineralization and associated hydrothermal alteration in relationship with the various deformation events using key field relationships from previously mapped outcrops as well as newly stripped outcrops. The latter exposes the hinge of the Hard Rock anticline at Porphyry Hill and the mineralized F Zone on the north limb of the Hard Rock anticline. These 2 new exposures are described in this report.

BACKGROUND

The Beardmore–Geraldton greenstone belt is located east of Lake Nipigon along the margin between the granite-greenstone Wabigoon Subprovince and the metasedimentary Quetico Subprovince. This 90 km long greenstone belt is composed of 3 metavolcanic and 3 metasedimentary units that are bounded by shear zones. From north to south, the metavolcanic units formed in back-arc, island arc and oceanic crust environments (Tomlinson et al. 1996). The metasedimentary units were deposited as part of a southward-prograding clastic wedge representing, from north to south, alluvial fan or braid-plain, subaqueous fan and/or prodelta, submarine fan and/or basin-plain environments (Williams 1987; Devaney and Williams 1989).

The Beardmore–Geraldton greenstone belt underwent 4 deformation events that are summarized in Table 40.1 (Tóth et al. 2013a, 2014). The deformation of the belt started with D_1 thrusting and the formation of isoclinal, recumbent F_1 folds and strong, axial-planar S_1 foliation. During D_2 north-to-south compression, F_1 folds were refolded by tight, upright, west-plunging, regional F_2 folds, which have an east-trending, steeply dipping, axial planar S_2 foliation (Lafrance, DeWolfe and Stott 2004). During D_3 sinistral transcurrent faulting, F_2 folds were refolded by centimetre-scale S-shaped F_3 drag folds with an axial planar S_3 crenulation cleavage (Tóth et al. 2013a, 2014). The last ductile deformation event recorded by these rocks was D_4 dextral transcurrent faulting. It resulted in the formation of regional, Z-shaped, west-plunging F_4 folds with an axial-planar east-northeast-trending, steeply dipping S_4 cleavage, and regional dextral strike-slip shear zones characterized by well-developed dextral shear bands and Z-shaped

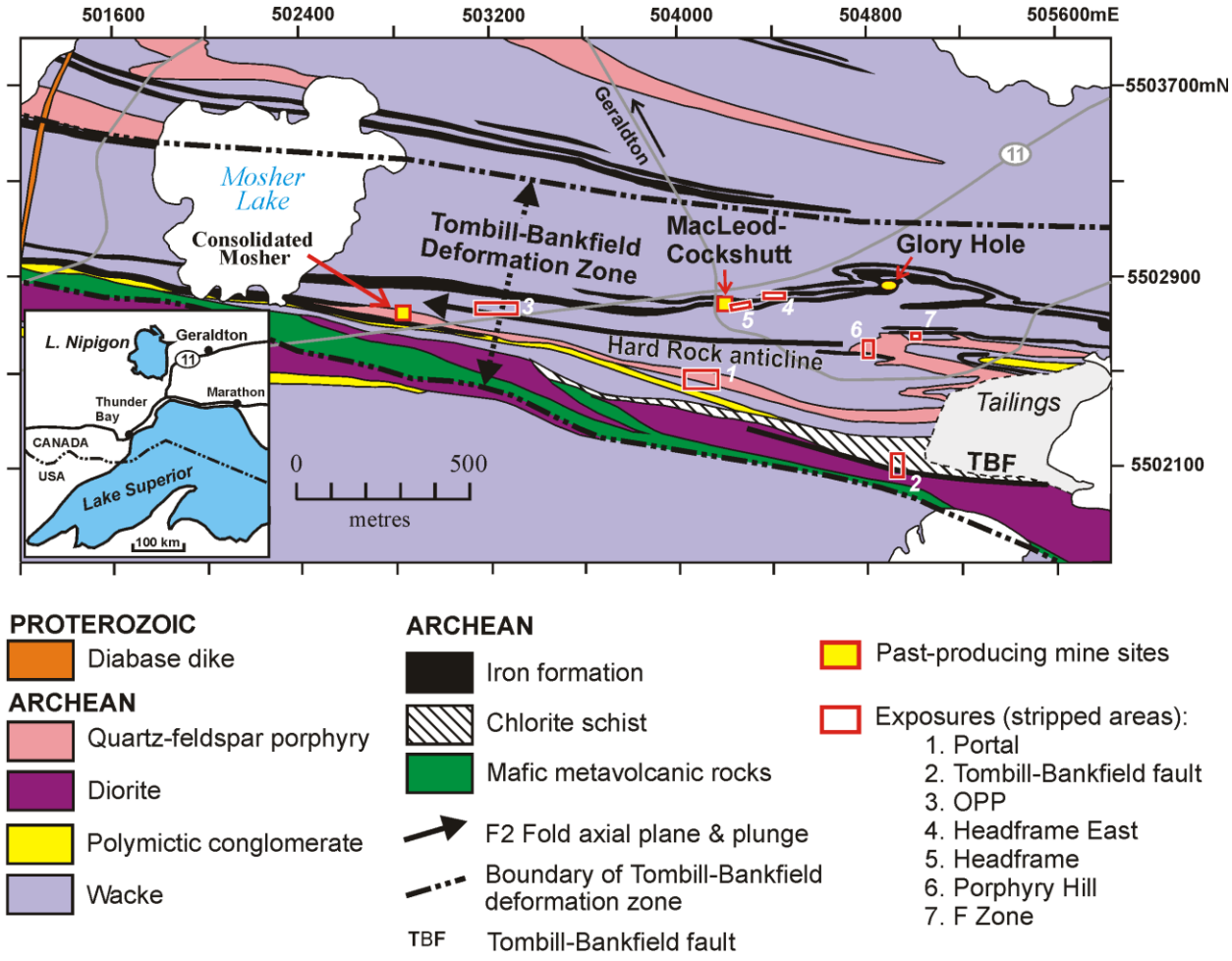

Figure 40.1. Simplified geological map of the Geraldton area showing the location of the exposures mapped during the past 3 field seasons (geology *after* Horwood and Pye (1955) and Pye (1952), with modifications by authors). Universal Transverse Mercator (UTM) co-ordinates are based on North American Datum 1927 (NAD27), Zone 16.

Table 40.1. Summary of deformation and gold mineralization events in the Beardmore–Geraldton greenstone belt (Lafrance, DeWolfe and Stott 2004; Tóth et al. 2013a, 2014, this paper).

Regional Deformation Style	Description of Structures	
	Fold	Foliation
Gold mineralization ▶		
D_1 thrusting	Isoclinal, recumbent F_1 folds; up to 1 m in amplitude	Strong S_1; appears in some mafic dikes and quartz-feldspar porphyry; typically bedding-parallel in sedimentary rocks
D_2 north-south compression	Tight upright regional F_2 folds; plunge: 20°W to 70°W; amplitude up to several kilometres	East-trending, steeply dipping S_2; axial planar to F_2 folds; parallel or slightly clockwise or anticlockwise of bedding
Gold mineralization ▶		
D_3 sinistral transcurrent shear	Tight to open S-shaped F_3 folds; amplitude up to tens of centimetres	East-trending, steeply dipping S_3 crenulation cleavage; axial planar to F_3 folds
Gold mineralization? ▶	Z-shaped F_4 folds; plunge: 20°W to 60°W; amplitude up to several kilometres	East-northeast-trending, steeply dipping regional S_4; axial planar to F_4; regionally oriented anticlockwise to bedding
D_4 dextral transpression	Dextral east-trending shear zones localized along S_2 and lithological contacts	
	Z-shaped F_4' drag folds overprinting S_4 foliation in shear zones	Sinistral slip S_4' crenulation cleavage; axial planar to F_4'

F_4' drag folds with an axial-planar S_4' crenulation cleavage (*after* Lafrance et al. 2004). Previous studies suggest that gold was emplaced during D_4 dextral shear (Pye 1952; Horwood and Pye 1955; Anglin 1987; Macdonald 1988; Lafrance, DeWolfe and Stott 2004; DeWolfe, Lafrance and Stott 2007; Lavigne 2009). This was disputed by Tóth et al. (2013a) who suggested that gold was emplaced either prior to or early during D_2. This paper expands on the results and interpretation by Tóth et al. (2013a) by presenting new data from the previously unmapped F Zone and Porphyry Hill exposures.

PORPHYRY HILL EXPOSURE

The Porphyry Hill stripped outcrop (*see* Figure 40.1, area 6) is located 600 m east-southeast of the No. 1 headframe of the past-producing MacLeod–Cockshutt Mine and 400 m south of Highway 11. It exposes the hinge of the kilometre-scale F_2 Hard Rock anticline.

From north to south, the outcrop consists of quartz-feldspar porphyry, interlayered mudstone and sandstone with thin banded iron formation layers, banded iron formation, and interlayered mudstone and sandstone intruded by numerous mafic dikes (Figure 40.2).

All deformation events are represented on this outcrop. The D_1 event is represented by an F_1 fold defined by a folded quartz vein and overprinted by a parasitic M-shaped F_2 fold (Photo 40.1A). The latter is in the hinge of the regional Hard Rock anticline, the axial plane of which passes through the middle of the porphyry. The F_2 folds in the porphyry have a strong axial planar S_2 cleavage, which is expressed as a bedding-parallel transposition foliation in banded iron formation, mudstone and sandstone on the south limb of the Hard Rock anticline, south of the porphyry. The transposition S_2 foliation is axial planar to Z-shaped F_2 folds (Photo 40.1B), which are transected by slightly bedding-transgressive sinistral faults that formed during the D_3 event (Photo 40.1C). Evidence for D_3 sinistral component of shearing is also present in the porphyry as sinistral shear bands dragging S_2 foliation. Transposed bedding and S_2 foliation are folded by centimetre-scale, open to tight, Z-shaped F_4 folds with axial planar S_4 crenulation cleavage (Photo 40.1D). Dextral shear bands formed during the same D_4 event and cut across all other structures.

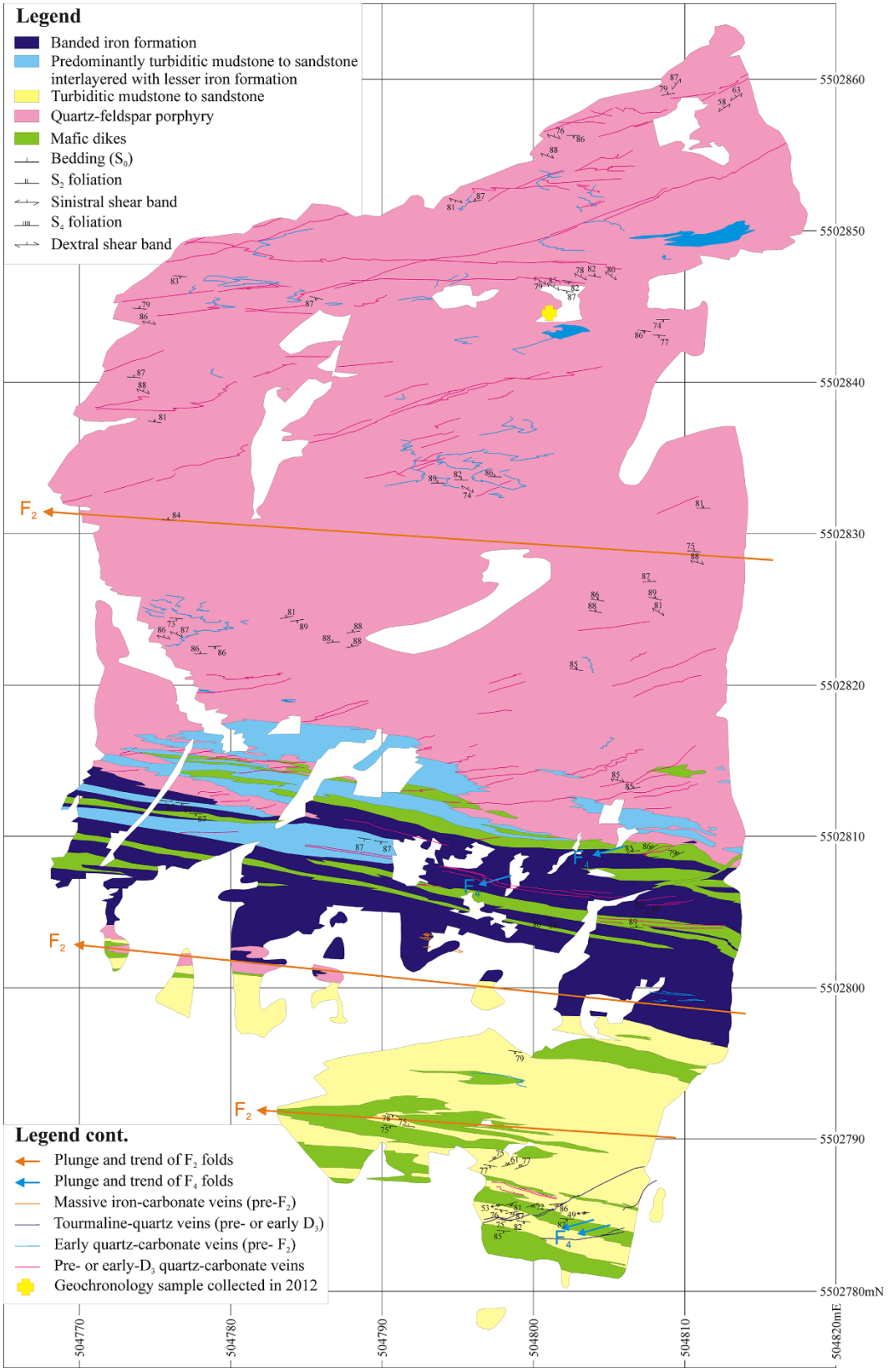

Figure 40.2. Detailed geological map of the "Porphyry Hill" exposure (*see* Figure 40.1, area 6). All UTM co-ordinates provided in NAD83, Zone 16.

Several generations of veins are present at Porphyry Hill. The first generation consists of quartz-carbonate-tourmaline veins and is folded by F_1 folds, suggesting that it was emplaced before or early during D_1 deformation (*see* Photo 40.1A). Other quartz-tourmaline ± carbonate veins containing visible gold are folded by isoclinal F_2 and tight, S-shaped F_3 folds, suggesting that it was emplaced no later than the beginning of D_2 deformation. The veins are surrounded by strong silicification, sericitization, sulphidation and likely carbonate alteration.

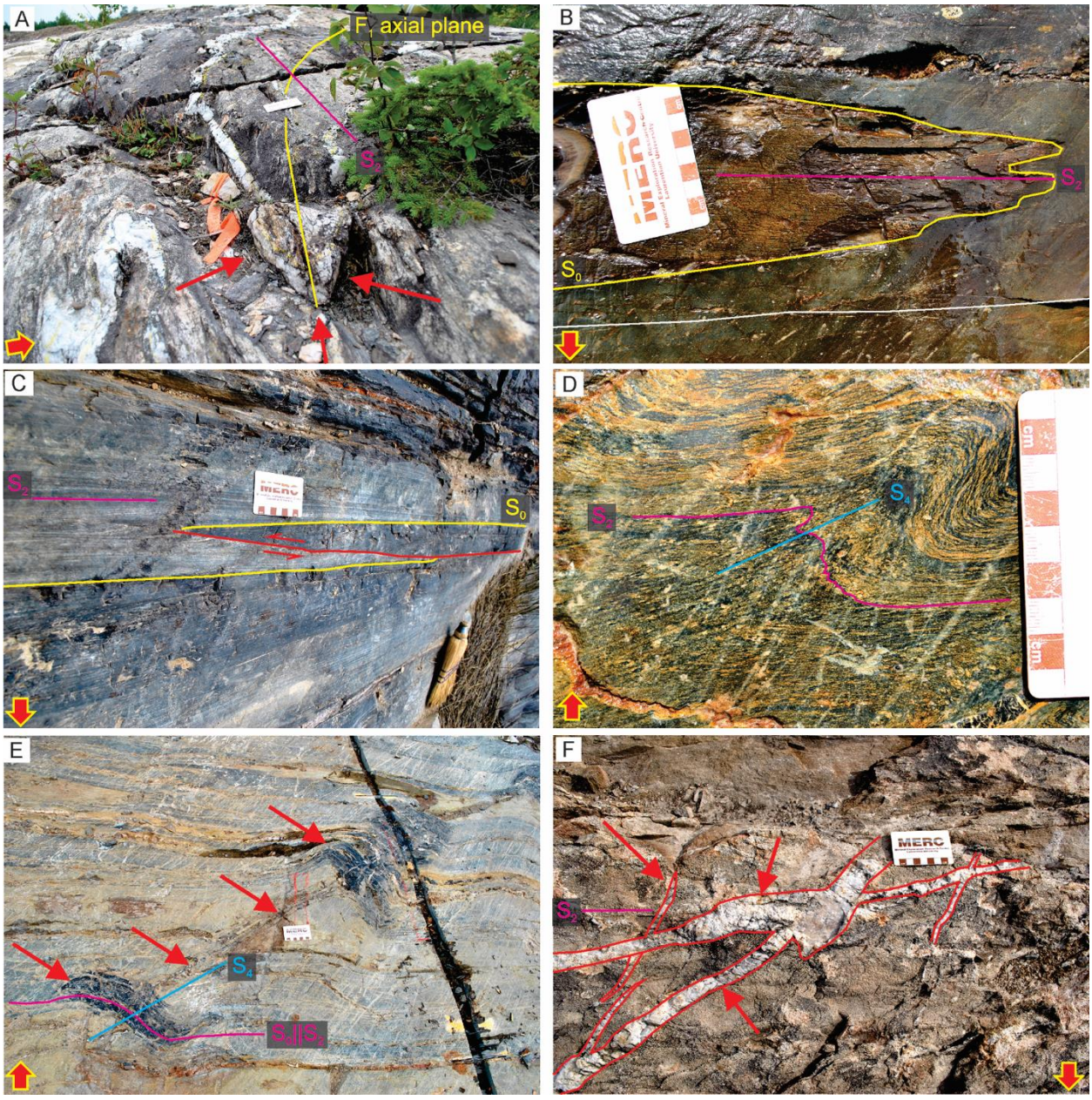

Photo 40.1. Field photographs of the "Porphyry Hill" exposure (*see* Figure 40.1, area 6). The yellow-outlined red arrows indicate north on each photograph. Red arrows indicate veins described in caption. **A)** Quartz–iron-carbonate–tourmaline veins are folded by F_1 and refolded by F_2 folds. **B)** The S_2 cleavage formed axial planar to metre-scale F_2 folds in mudstone to sandstone and mafic dikes. **C)** Sinistral displacement along oblique D_3 shear fracture. **D)** S_2 foliation folded by centimetre-scale Z-shaped F_4 fold and overprinted by axial-planar S_4 cleavage. **E)** East-northeast-trending tourmaline-quartz-carbonate veins and associated tourmaline alteration penetrating metasedimentary rocks along S_2 foliation and trigger the formation of Z-shaped F_4 asymmetrical drag folds during D_4 dextral shear. **F)** East- to northeast-trending quartz ± carbonate ± tourmaline veins emplaced before or early during D_3 deformation in quartz-feldspar porphyry, some of which were found to be auriferous.

Several vein types were emplaced prior to, or more likely during, D_3 deformation. The veins typically strike east-northeast to northeast, cut across S_2 foliation, and are oriented anticlockwise, suggesting that they were emplaced as extensional tension gashes during D_3 sinistral shear. The veins may be up to tens of metres in length and cut across the porphyry (*see* Figure 40.2). Some of the veins consist of tourmaline, quartz and carbonate. They are associated with a strong tourmaline alteration that penetrated metasedimentary wall rocks along S_2 foliation (Photo 40.1E) and triggered the formation of Z-shaped F_4 folds as fringe structures during D_4 dextral shear. These D_4 dextral shear bands cut across tourmaline veins and sulphides are present along them, suggesting that the sulphides and possibly gold were emplaced during D_4 deformation.

Other veins, created prior to or during D_3 deformation, consist of quartz ± carbonate ± tourmaline, surrounded by strong carbonate ± sericite ± pyrite alteration halos. Visible gold was found in some of the veins. The veins are more abundant within the quartz-feldspar porphyry; the veins trend 10 to 70° anticlockwise to S_2 foliation (Photo 40.1F). The veins cut across F_2 folds, are folded by S-shaped F_3 and Z-shaped F_4 folds, and are overprinted by D_4 dextral shear bands, suggesting that they were emplaced prior to or during D_3 sinistral shear.

Narrow, millimetre-thick quartz veinlets were locally emplaced in dextral shear bands and, in turn, were also cut by them suggesting emplacement during D_4 deformation. Another set of dextral shear veins, composed of quartz-carbonate, is oriented at approximately 5° clockwise to S_2 foliation and is folded by small, Z-shaped F_4 folds.

Gold mineralization was observed in various forms. Local semi-massive sulphide replacement of banded iron formation consists of pyrite and arsenopyrite surrounding quartz-carbonate veins, a few millimetres to 1 to 2 cm thick, and yielded high gold values (B. Cleland, Premier Gold Mines Ltd., personal communication, 2014). The structural setting of these veins is uncertain because of the high strain recorded by the host rocks and later weathering of the sulphides.

F ZONE EXPOSURE

The F Zone stripping is located 350 m south of Highway 11 and 750 m east-southeast of the No. 1 headframe of the past-producing MacLeod–Cockshutt Mine in Geraldton (Figure 40.3; *see also* Figure 40.1, area 7). This exposure was cleaned to expose the F Zone mineralization that lies along the northern contact between the quartz-feldspar porphyry and metasedimentary rocks. Historical diamond-drill holes across the zone yielded gold grades averaging between 3.5 and 13 g/t gold over a width of approximately 21 to 23 feet (Horwood and Pye 1955, p.67-68). The zone has been described as consisting "of a multitude of narrow quartz stringers mostly of east-west strike and vertical or nearly vertical dip" locally with "spectacular concentrations of visible gold" (Horwood and Pye 1955, p.67-68).

The stripped outcrop consists of interbedded mudstone to coarse-grained sandstone with an average bed thickness of 15 cm. One layer of banded iron formation is exposed in the northeastern corner of the stripped outcrop. Beds are folded by metre-scale isoclinal F_1 folds that are refolded by open to tight S-shaped centimetre- to metre-scale F_2 folds (Photo 40.2A). The S-shaped asymmetry of the F_2 folds is consistent with the location of the outcrop on the north limb of the kilometre-scale F_2 Hard Rock anticline. A continuous S_2 cleavage (spacing of 0.5 to 1 mm) is axial planar to the folds and is defined by alternating chlorite-rich and iron-carbonate–rich microlithons. The S_2 foliation is folded by rare, millimetre- to centimetre-scale Z-shaped asymmetrical F_4 folds and overprinted by S_4 foliation (Photo 40.2B). The S_4 foliation is a continuous crenulation cleavage (spacing of 0.2 to 0.7 mm) defined by alternating iron-carbonate-rich and chlorite-rich microlithons.

Selective iron-carbonate replacement of bedding (*see* Photo 40.2A) and bedding-parallel quartz-carbonate veins are folded by F_1 and refolded by F_2 folds, suggesting that they were emplaced either prior to or early in D_1 deformation. Iron-carbonate altered beds are typically transposed parallel to S_2 foliation. The F_1 folding of bedding-parallel quartz-carbonate veins cannot always be documented; however, they were boudinaged prior to F_2 folding (Photo 40.2C), implying that they were already present during D_1 deformation, so they were emplaced prior to, or at the beginning of, D_1 deformation. Some early quartz-carbonate veins (few millimetres to 10 cm in thickness) are surrounded by moderate to strong sericite-carbonate-pyrite alteration halos (typically few centimetres thick) (Photo 40.2D). Channel samples intersecting these veins and their alteration halo yielded gold values between 2 and 15 g/t gold (B. Cleland, Premier Gold Mines Ltd., personal communication, 2014).

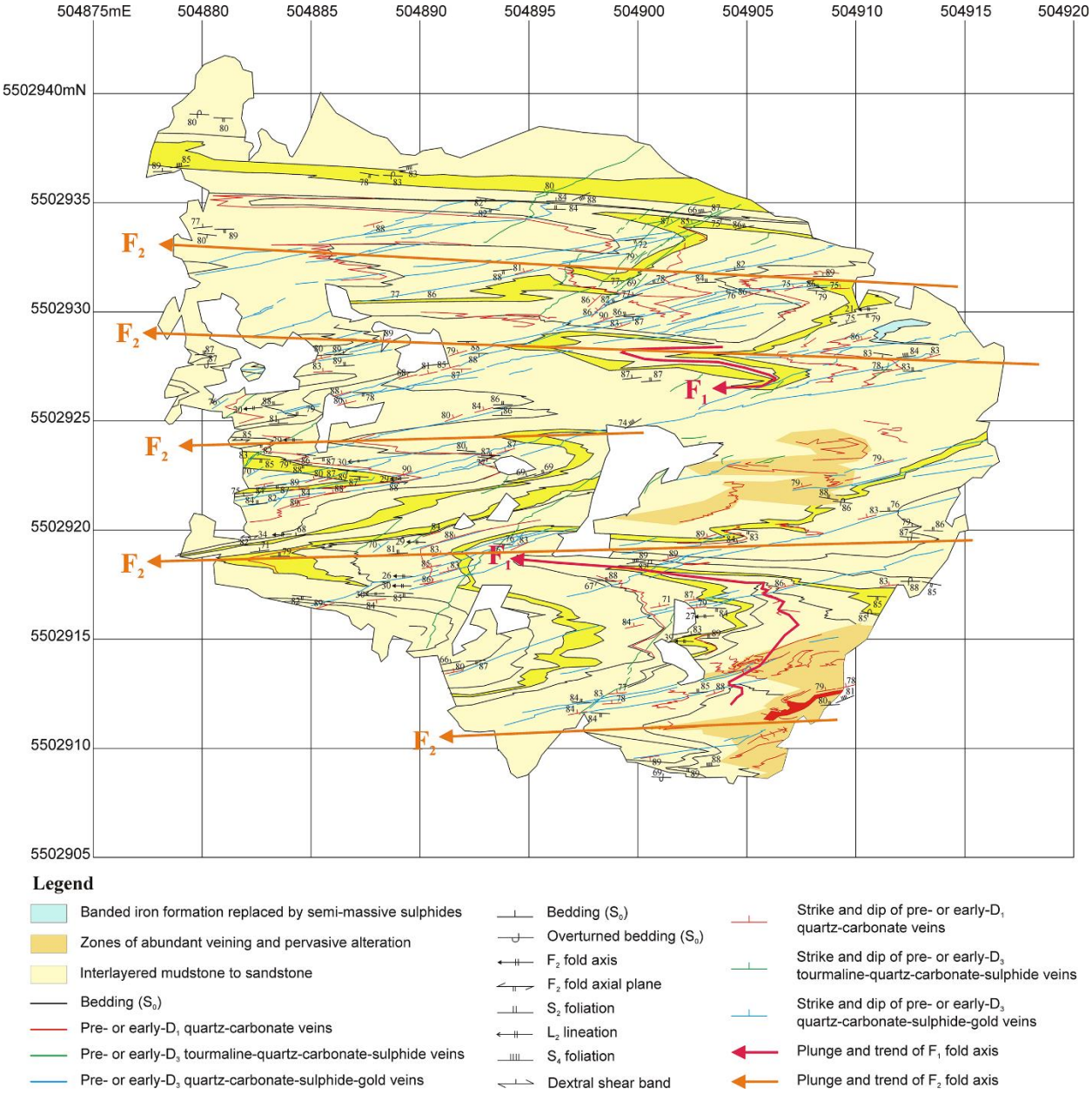

Figure 40.3. Detailed geological map of the "F Zone" exposure (*see* Figure 40.1, area 7). All UTM co-ordinates provided in NAD83, Zone 16. Some mudstone to sandstone beds have been highlighted by yellow to better show the overall structural pattern of the outcrop.

Northeast- to east-northeast-trending tourmaline ± quartz ± carbonate ± sulphide veins are surrounded by 1 to 2 cm thick carbonate-sericite-pyrite alteration halos. The veins are zoned with tourmaline along the margins and quartz ± carbonate ± sulphide within the centre of the veins. The veins cut across F_2 fold hinges (Photo 40.2E) and are folded by gentle S-shaped F_3 folds, suggesting that they were emplaced prior to or early during D_3 sinistral shear deformation. The tourmaline veins are cut, but by east-northeast-

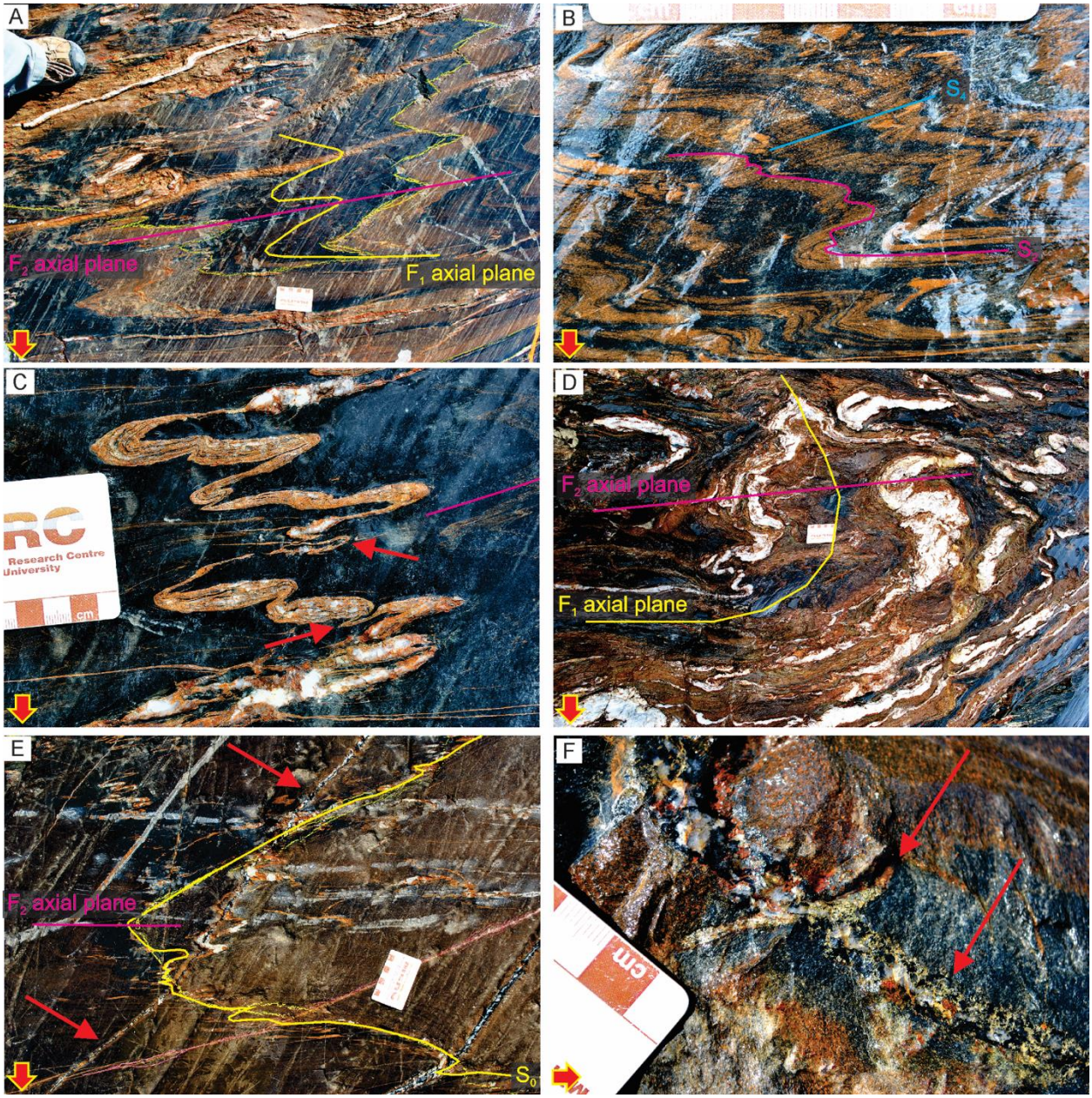

Photo 40.2. Field photographs of the "F Zone" exposure (*see* Figure 40.1, area 7). The yellow-outlined red arrows indicate north on each photograph. Red arrows indicate veins described in caption. **A)** Iron-carbonate alteration is folded by an isoclinal F_1 fold that is refolded by S-shaped open F_2 folds. **B)** The S_2 foliation is folded by millimetre- to centimetre-scale Z-shaped asymmetrical F_4 folds and is overprinted by S_4 foliation formed axial planar to F_4 folds. **C)** Early quartz-carbonate veins are surrounded by sericite-carbonate-pyrite alteration halo and are folded by F_1 folds and refolded by F_2 folds. **D)** Bedding-parallel quartz-carbonate veins do not always show F_1 folding; however, they were boudinaged during D_1 deformation and were subsequently folded by F_2 folds. **E)** Northeast to east-northeast-trending tourmaline ± quartz ± carbonate ± sulphide veins cut across F_2 fold hinge. **F)** Northwest-trending quartz-pyrite veins, a few centimetres long, cut across tourmaline-rich veins and are folded by gentle Z-shaped F_4 fold.

to east-trending, locally auriferous quartz-carbonate-sulphide veins (few millimetres to approximately 6 cm), surrounded by 2 to 15 cm thick sericite-carbonate-pyrite alteration halos. Where these veins cut across the banded iron formation, selvages are replaced by a 5 to 15 cm thick semi-massive pyrite. The veins are also locally folded by centimetre-scale Z-shaped F_4 folds or boudinaged during D_4 dextral shear depending on their orientation, and otherwise show similar structural timing relationships as the tourmaline-rich veins, suggesting that they were also emplaced either before or during D_3 deformation. Late northwest-trending quartz-pyrite veins cut across the tourmaline-rich veins and are folded by a gentle Z-shaped F_4 fold (Photo 40.2F), suggesting that they were likely emplaced during D_4 deformation.

CONCLUSIONS

Multiple phases of hydrothermal alteration, vein emplacement and gold mineralization (and/or remobilization) took place during the complex deformation events recorded by the rocks in the Geraldton area. Iron-carbonate alteration and gold-mineralized quartz-carbonate veins surrounded by sericite-carbonate-pyrite alteration halos were emplaced parallel to bedding and folded by F_1 folds, suggesting a pre- or early-D_1 deformation mineralizing event. Another set of bedding-parallel veins were boudinaged during D_1 deformation and then folded during D_2 deformation, supporting a pre- or early-D_1 hydrothermal episode. An auriferous quartz-carbonate vein hosted by quartz-feldspar porphyry is folded by an F_2 fold, indicating that it was emplaced prior to, or early during D_2 deformation. Northeast-striking tourmaline-rich veins cut across F_2 fold hinges and are folded by S-shaped F_3 folds, suggesting a pre- or early-D_3 deformation timing for these veins. East-northeast- to east-trending, auriferous quartz-carbonate-sulphide veins hosted in mudstone and sandstone are associated with a sericite-carbonate-pyrite alteration halo, whereas the same vein system is instead associated with a semi-massive pyrite-sericite alteration halo when hosted in banded iron formation. These auriferous quartz-carbonate-sulphide veins show similar structural features to the tourmaline veins and, thus, are interpreted to have formed prior to or early during D_3 deformation. Sulphide mineralization (or remobilization) occurred along northwest-striking tension gashes composed of quartz-pyrite. The latter cut across tourmaline veins emplaced prior to or early during D_3 deformation and are folded by gentle Z-shaped F_4 folds. Thus, the tension gashes were emplaced prior to, or more likely, during D_4 dextral shear. Even though these sulphide-mineralized northwest-striking veins emplaced during D_4 deformation (i.e., the tension gashes) are not yet proven to carry gold, previous studies described similar, auriferous northwest-striking veins in the western part of the belt (DeWolfe et al. 2007), which suggest the possibility of another gold mineralization (remobilization) event. Sulphides emplaced into D_4 dextral shear bands were described from the Tombill–Bankfield fault exposure, suggesting syn-D_4 emplacement (Lafrance et al. 2012). Based on field relationships described here and the large-scale distribution of gold, the authors infer an early (pre- or early-D_1) gold-bearing hydrothermal event followed by a secondary, plausibly dominant, early- or syn-D_3 mineralizing event.

ACKNOWLEDGMENTS

This project is part of a PhD thesis undertaken by the lead author at Laurentian University, Sudbury, Ontario, with supervision by Bruno Lafrance (Laurentian University) and Benoît Dubé (Geological Survey of Canada). We gratefully acknowledge the funding of the Targeted Geoscience Initiative 4 Lode Gold project of Natural Resources Canada, as well as the support of the Ontario Geological Survey. We thank Premier Gold Mines Ltd. for access to its properties, drill cores and database, particularly Benjamin Cleland, Andrew Hackner, Daniel Grabiec, Thomas Salmi and the entire crew located in Geraldton. In addition, we greatly appreciate all discussions with the previously mentioned geologists including Kenneth Williamson, Dyane Duquette and Tim Twomey. We thank the entire crew of Premier Gold Mines Ltd. for all the technical help they provided during outcrop cleaning and sampling procedures.

REFERENCES

Anglin, C.D. 1987. Geology, structure and geochemistry of gold mineralization in the Geraldton area, northwestern Ontario; unpublished MSc thesis, Memorial University of Newfoundland, St. John's, Newfoundland, 283p.

Devaney, J.R. and Williams, H.R. 1989. Evolution of an Archean subprovince boundary: A sedimentological and structural study of part of the Wabigoon–Quetico boundary in northern Ontario; Canadian Journal of Earth Sciences, v.26, p.1013-1026.

DeWolfe, J.C., Lafrance, B. and Stott, G.M. 2007. Geology of the shear-hosted Brookbank gold prospect in the Beardmore–Geraldton belt, Wabigoon Subprovince, Ontario; Canadian Journal of Earth Sciences, v.44, p.925-946.

Dubé, B., Mercier-Langevin, P., Castonguay, S., McNicoll, V.J., Pehrsson, S.J., Bleeker, W., Schetselaar, E.M. and Jackson, S. 2011. Targeted Geoscience Initiative 4. Lode gold deposits in ancient, deformed and metamorphosed terranes – footprints and exploration implications: A preliminary overview of themes, objectives and targeted areas; *in* Summary of Field Work and Other Activities 2011, Ontario Geological Survey, Open File Report 6270, p.38-1 to 38-10.

Horwood, H.C. and Pye, E.G. 1955. Geology of Ashmore Township; Ontario Department of Mines, Annual Report, 1951, v.60, pt.5, 105p.

Lafrance, B., DeWolfe, J.C. and Stott, G.M. 2004. A structural reappraisal of the Beardmore–Geraldton Belt at the southern boundary of the Wabigoon Subprovince, Ontario, and implication for gold mineralization; Canadian Journal of Earth Sciences, v.41, p.217-235.

Lafrance, B., Tóth, Z., Dubé, B. and Mercier-Langevin, P. 2012. Targeted Geoscience Initiative 4. Lode gold deposits in ancient deformed and metamorphosed terranes: Geological setting of banded iron formation–hosted gold mineralization in the Geraldton area, northern Ontario; *in* Summary of Field Work and Other Activities 2012, Ontario Geological Survey, Open File Report 6280, p.48-1 to 48-10.

Lavigne, M.J. 2009. Distribution of gold with respect to lithologies, metamorphic facies and strain state in the Beardmore–Geraldton greenstone belt; Ontario Geological Survey, Open File Report 6241, 88p.

Macdonald, A.J. 1988. The Geraldton gold camp: The role of banded iron formation; Ontario Geological Survey, Open File Report 5694, 176p.

Pye, E.G. 1952. Geology of Errington Township, Little Long Lac area; Ontario Department of Mines, Annual Report, 1951, v.60, pt.6, 140p.

Tomlinson, K.Y., Hall, R.P., Hughes, D.J. and Thurston, P.C. 1996. Geochemistry and assemblage accretion of metavolcanic rocks in the Beardmore–Geraldton greenstone belt, Superior Province; Canadian Journal of Earth Sciences, v.33, p.1520-1533.

Tóth, Z., Lafrance, B., Dubé, B., McNicoll, V.J. and Mercier-Langevin, P. 2014. Stratigraphic and structural setting of banded-iron-formation-hosted gold mineralisation in the Geraldton area, Ontario; Geological Association of Canada–Mineralogical Association of Canada, Fredericton 2014, Joint Annual Meeting, Program with Abstracts, v.37, p.272-273.

Tóth, Z., Lafrance, B., Dubé, B., Mercier-Langevin, P. and McNicoll, V.J. 2013. Targeted Geoscience Initiative 4. Lode gold deposits in ancient deformed and metamorphosed terranes: Geological mapping and structural re-appraisal of the banded iron formation–hosted gold mineralization in the Geraldton area, Ontario; *in* Summary of Field Work and Other Activities 2013, Ontario Geological Survey, Open File Report 6290, p.58-1 to 58-14.

Williams, H.R. 1987. Structural studies in the Wabigoon and Quetico subprovinces; Ontario Geological Survey, Open File Report 5668, 163p.